RHODES UNIVERSITY
Where leaders learn

Indium (III) porphyrins immobilized on carbon-based supports for the remediation of organic contaminants and bactericidal activity in water

BY

OMONDI JAMES OYIM

G21O1734

A Thesis Submitted in Fulfillment of the Requirements for the Award of the Degree of Doctor of Philosophy (Chemistry) of Rhodes University.

2025

DEDICATION

I dedicate this work to my loving wife, Joy Otuya, my cherished children, Jadah Mor and Jerron Tebello, and my supportive parents, Grace Atieno, Prof. Robert Otuya, and Janet Otuya. To my brothers and sisters, your unwavering support has been my greatest source of strength throughout this journey.

ACKNOWLEDGEMENT

My sincere appreciation goes to my supervisors, Distinguished Prof. Tebello Nyokong and Dr. Edith Amuhaya, for giving me the opportunity to be their student under their mentorship. Their guidance, resilience, and patience have been invaluable.

I would also like to extend my gratitude to Prof. John Mack, Dr. Jonathan Britton, Ms. Gail Cobus, and Mr. Francis Chindeka for their unwavering support and assistance throughout my studies. My thanks also go to the Chemistry Department of Rhodes University, all staff members, and all the postgraduate students.

I am grateful to all past and present members of the Tebello Nyokong Institute for Nanotechnology Innovation research group, especially Mbulelo Jokazi, Mulaudzi Isaac, Thembani Vukeya, and Choonzo Chiyumba, for their friendship and support.

Special thanks to my loving family for their constant love and support, especially during times when it was most needed. I could not have made it without each one of you.

I also acknowledge the financial support provided by the Department of Science and Innovation (DSI) and the National Research Foundation (NRF) of South Africa through the DSTI/NRF South African Research Chairs Initiative for Professor of Medicinal Chemistry and Nanotechnology (UID 62620), the DSI/Mintek Nanotechnology Innovation Centre, Rhodes University, and the United States International University-Africa and Canada's International Development Research Centre (IDRC) (UID 108569-001).

Lastly, I give praise to God, who made it all possible.

ABSTRACT

This thesis investigates the removal of organic contaminants and the deactivation of *E. coli*, a common bacterium in waterborne diseases, using indium (III) porphyrins immobilized on carbon-based supports. Various carbon-based support materials, including activated carbon-related supports, granular activated carbon (GAC), oxygen-functionalized activated carbon (ACO), and polyacrylonitrile/activated carbon (PAN/AC) composites, were evaluated, along with indium-metalated porphyrin-loaded samples (**1a** and **2a**). The study found that the physicochemical nature of these materials significantly influences their efficiency in dye removal through adsorption and combined adsorption-photodegradation processes. The addition of porphyrins improved the photoactivity of the composites without significantly affecting their surface area.

Hydrogen peroxide enhanced the photodegradation of methylene blue (MB) and the deactivation of *E. coli*, especially with colloidal activated carbon (CAC) and porphyrin-loaded CAC samples (**1a**, **2a**, and **3a**). Higher activities were realized with the porphyrin samples, although porphyrin aggregation, as seen with porphyrin **3a**, can interfere with these activities. The study also found that natural sunlight was more effective than a Xe lamp for degrading ciprofloxacin. The effect of porphyrin charge on antimicrobial photodynamic therapy (aPDT) activities was significant, with positively charged porphyrins showing higher antimicrobial efficacy compared to neutral porphyrins. Additionally, the study highlighted the importance of porphyrin functional groups and symmetry in enhancing performance in photodegradation and antimicrobial applications. The antimicrobial potential of the indium metalated pyridinyl-based *trans*-A_2B_2 porphyrin complexes (**4a**, **4b**, **5a**, and **5b**) was investigated. The dicationic porphyrins, **4b** and **5b**, exhibited remarkable aPDT efficacy against both *S. aureus E. coli* and planktonic forms and biofilms.

Further experiments focused on the photodegradation of MB and methyl orange (MO) using porphyrins **1a**, **2a**, **3a**, and **5b** loaded on PAN/nitrogen-doped carbon quantum dot (NCQD) fibers. Overall, the porphyrin-loaded PAN/NCQD composites were effective, especially those loaded with cationic indium porphyrin **5b**, which exhibited higher aPDT effects for *E. coli* and in MB degradation experiments. The unsymmetrical indium porphyrin **3a** showed good activity in both MO and MB, making it the overall better performer during the degradation experiments. The findings reveal that the symmetry of porphyrins can significantly influence their effectiveness in photodegradation and antimicrobial applications.

TABLE OF CONTENTS

LIST OF ABBREVIATIONS

Abs:	Absorbance/Absorption
AC:	Powdered activated carbon
ACO:	Oxygen-functionalised granular activated carbon
aPDT:	Antimicrobial photodynamic therapy
ATCC:	American type culture collection
CAC:	Colloidal activated carbon
CFU:	Colony forming units
CIP:	Ciprofloxacin
DCM:	Dichloromethane
DLS:	Dynamic light scattering
DMA:	9,10 Dimethylanthracene
DMF:	Dimethylformamide
DMSO:	Dimethylsulfoxide
DMSO-d_6:	Deuterated dimethyl sulfoxide
EDX:	Energy-dispersive X-ray spectroscopy
EtOH:	Ethanol
FT-IR:	Fourier-transform infrared spectroscopy
GAC:	Granular activated carbon

IRF: Instrument response function

ISC: Intersystem crossing

LASER: Light amplification by the stimulated emission of radiation

LED: Light-emitting diode

MALDI-TOF MS: Matrix-Assisted Laser Desorption/Ionisation Time-of-Flight Mass Spectrometry

MeOH: Methanol

NaOAc: Sodium acetate

NCQD: Nitrogen-doped carbon quantum dots

Nd-YAG: Neodymium-doped Yttrium Aluminium Garnet

NMR: Nuclear Magnetic Resonance

PBS: Phosphate-buffered saline

Pc: Phthalocyanine

PDT: Photodynamic therapy

PET: Photo-induced electron transfer

PS: Photosensitizer

RB: Rose Bengal

ROS: Reactive oxygen species

rt: Room temperature

SPR:	Surface plasma resonance
TCSPC:	Time-correlated single proton
TGA:	Thermal gravimetric analysis
UV-Vis:	Ultraviolet-visible spectroscopy
ZnTPP:	Zinc tetraphenyl-porphyrin

LIST OF SYMBOLS

α:	Non-peripheral position
β:	Peripheral position
δ:	Chemical shift
J:	Coupling constant
λ_{max}:	Wavelength at maximum absorption
λ_{em}:	Wavelength at maximum emission
λ_{exc}:	Wavelength at maximum excitation
m/z:	Mass to charge ratio
ν:	Frequency
Φ_{Δ}:	Singlet oxygen quantum yield
Φ_F:	Fluorescence quantum yield
Φ_T:	Triplet quantum yield
τ_F:	Fluorescence lifetime
τ_T:	Triplet lifetime

PREAMBLE

The contamination of water sources by organic pollutants and pathogenic bacteria remains a major environmental and public health concern. Conventional water treatment methods frequently face significant challenges such as toxic by-product formation or reliance on costly equipment and processes. Consequently, it is imperative to explore alternative and innovative strategies, such as photocatalysis which involves the use of light and catalysts that absorb light. Solar-driven photocatalysis, particularly when integrated with adsorbent materials, presents a sustainable and highly effective method for water purification. This technology supports global sustainability goals and offers a practical solution to the rising water pollution problem. Porphyrins, with their unique photochemical properties, stand out as highly effective photocatalysts due to their strong absorption of visible light and ability to generate reactive oxygen species. Additionally, their tunable electronic properties and adaptability in various catalytic systems enhance their potential for sustainable and efficient environmental remediation.

This study presents a more promising approach that entails immobilizing novel indium (III) porphyrins onto carbon-based supports. These hybrid materials exhibit dual functionality: adsorption capacity and enhanced photocatalytic activity. As a result, they can efficiently remove organic pollutants—such as dyes and pharmaceutical compounds—and effectively inactivate bacteria in water. By leveraging the synergistic properties of porphyrins and carbon-based matrices, this strategy offers a sustainable and highly effective solution for water purification.

CHAPTER 1: Introduction

This chapter offers a detailed overview of the current water purification technologies, focusing on the role of porphyrin photocatalysts and the unique benefits of carbon-based supports. It underscores the importance of incorporating photocatalysts with antibiofilm properties to enhance the removal efficiency of pathogenic microbes alongside organic pollutants, thereby improving the longevity and effectiveness of water purification systems.

1.1 Background

1.1.1 Mitigating organic contaminants in water

Water contamination by organic pollutants poses a significant threat to the health and ecosystems. Organic pollutants, such as dyes, pharmaceuticals, and pesticides, enter water bodies through industrial, agricultural, and domestic activities [1]. These contaminants often resist conventional water treatment methods, leading to their persistence in the environment. Pharmaceuticals, for example, can disrupt the endocrine system and cause long-term ecological damage, while dyes from textile industries are toxic to aquatic life [2]. Additionally, as agricultural practices intensify, the use of pesticides becomes more prevalent. These chemicals often find their way into water sources, posing significant risks to both human and animal health [2,3].

Most treatment methods today mainly focus on removing solid particles and suspended solids and deactivating microbes. Generally, less focus is placed on emerging pollutants such as pharmaceuticals and organic dyes [4]. Due to their low biodegradability and high solubility in water, organic pollutants are usually not removed by conventional water treatment methods, such as coagulation and flocculation, sedimentation, filtration, and disinfection. This, therefore, calls for the development of alternative approaches to improve the outcome of the water treatment processes. Methods such as photolysis and the degradation of organic pollutants using sunlight are reasonably less expensive but very slow [5,6]. Various conditions must be monitored periodically to achieve good results, such as solar intensity, turbidity, pH, and oxygen content. Moreover, most pollutants in water can undergo photolysis but only to a varying degree, depending on their chemical structures [5]. Some organic pollutants can absorb a photon and become excited when illuminated with solar radiation. Meanwhile, the molecules can undergo chemical transformations

in the higher energy excited state, generating one or more degradation products [5,7,8]. Generally, photolysis is the primary documented mechanism for removing pharmaceuticals and some dyes at low concentrations from the aquatic environment [6,8].

In some cases, photodegradation of organic pollutants in water can also occur by indirect photolysis- the process where a substance is broken down by light, but not directly. Instead, it involves photosensitizers that absorb solar radiation and, in the process, generate reactive oxygen species ($^1O_2$, $HO^{\cdot}$, $ROO^{\cdot}$, $O_2^{\cdot-}$) or transfer the energy to the target substances, leading to their breakdown in water. Photosensitizers, such as humic substances and nitrates, typically found in surface water bodies at low concentrations, can enhance indirect photolysis of the organic compounds in secondary effluent [9]. For instance, nitrate in an aqueous environment can absorb radiation in the UV range and react, as shown in **Scheme 1.1**, to produce hydroxyl radicals [9–11].

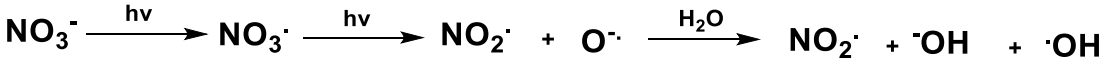

Scheme 1.1: Photogeneration of hydroxide radicals from nitrates in water

The reactive species can also interact with biomolecules in microbes such as bacteria, fungi, and viruses, leading to cell death [9]. However, relying solely on direct and indirect photolysis for degrading organic compounds in wastewater treatment has several limitations, including limited efficiency for resistant compounds, dependence on specific light conditions, incomplete degradation leading to potentially toxic by-products, and scalability challenges. These drawbacks highlight the need for an integrated process involving adsorption, photolysis, and photocatalysis to enhance the effectiveness of wastewater treatment. This work explores the approach that combines absorption and photodegradation mechanisms using novel organic photocatalytic adsorbents for water purification. In addition to removing organic pollutants, the advanced

oxidation approach has also demonstrated the ability to control pathogenic microorganisms, such as antibiotic-resistant bacteria, in water [12].

1.1.2 Antibiotic-resistant bacteria in aquatic ecosystem

The global issue of antibiotic-resistant bacteria (ARB) is a significant public health concern, with aquatic ecosystems acting as reservoirs for these bacteria, which can eventually contaminate water supplies [13]. The rising concentration of antibiotics in sewers contributes to the proliferation of ARB. Unlike other bacteria, ARB is unaffected by most antibiotics. This resistance facilitates the spread of antibiotic resistance by mixing, interacting, and transferring resistant genes to the local microbial community [13,14]. Sludge from water treatment, often used as fertilizer, can release resistant bacteria that survive standard sewage treatment. Consequently, elevated levels of resistance genes have been detected in bacteria downstream of wastewater treatment plants, emphasizing the need to improve water treatment methods to reduce the load of resistant bacteria, particularly from hospitals and farms [15,16]. Incorporating advanced oxidation processes can enhance the effectiveness of water treatment by efficiently eliminating antibiotic residues, pathogenic microbes, and resistance genes without harming humans.

This work addresses a range of pollutants with significant environmental implications. This comprehensive approach helps develop effective strategies for water purification and ensures public health and safety.

1.1.3 Target Pollutants in this study

Methylene blue (MB), methyl orange (MO), ciprofloxacin (CIP) *Staphylococcus aureus* (*S. aureus*) and *Escherichia coli* (*E. coli*) were chosen for this study due to their significant

environmental and health impacts, as well as their relevance in water contamination research. MB is extensively used in textile and paper industries, and its high visibility in water makes it an excellent candidate for evaluating the efficiency of removal processes [17]. Additionally, MB is known for its toxicity to aquatic organisms [17,18], highlighting the importance of its removal from wastewater. MO, another widely used dye in the textile industry, is an anionic dye, which contrasts with the cationic nature of MB [19], allowing for the study of different removal mechanisms. The environmental persistence of MO and its potential health hazards make MO a significant pollutant to address [20]. Conversely, ciprofloxacin is a fluoroquinolone antibiotic frequently detected in water bodies due to its extensive use in human and veterinary medicine [21]. It is primarily excreted in an unmetabolized form, which can lead to the development of antibiotic-resistant bacteria, posing a severe public health risk [22]. Removing ciprofloxacin from water is crucial to prevent ecological and health impacts. Pathogenic bacteria are common in water sources [23], contaminating through sewage discharge, agricultural runoff, and improper waste disposal. This leads to waterborne disease outbreaks [24,25]. Consequently, this necessitates studying effective disinfection methods, such as photocatalysis, which ensures water safety by addressing microbial contaminants and effectively degrades organic pollutants.

1.1.4 Solar-driven photocatalysis and photocatalyst adsorbents

Photocatalysis, which uses light-activated catalysts to break down organic pollutants, such as pesticides, dyes, and pharmaceuticals, is considered a viable alternative for water treatment method [26]. This approach offers higher efficiency in mineralization and minimizes the production of potentially harmful degradation products, all while utilizing sunlight [27,28]. Solar energy, a renewable and abundant resource, makes this method particularly cost-effective for water

purification because it involves harnessing natural sunlight to activate a photocatalyst, which aids in breaking down organic pollutants and deactivating harmful bacteria in water.

Commonly used photocatalysts include semiconductor materials like titanium dioxide (TiO_2) and zinc oxide (ZnO). These materials absorb light and generate electron-hole pairs, initiating reactions that degrade contaminants. However, the main drawback, especially for solar-driven systems, is their limited efficiency under natural sunlight. Many photocatalysts, such as TiO_2 and ZnO, often require UV light to perform optimally, but UV light constitutes only a small portion of the solar spectrum. This limitation necessitates the utilization of porphyrin photocatalysts since they can efficiently utilize visible light. A significant advancement in this field is the combination of photocatalysts with adsorbents, resulting in materials known as photocatalyst adsorbents [29]. These advanced materials integrate the properties of both photocatalysts and adsorbents to enhance water treatment efficiency, capturing and degrading contaminants under light exposure. Examples of adsorbents integrated with photocatalysts include carbon materials, zeolites, and clay [29]. These hybrid materials offer enhanced efficiency, broad-spectrum activity, and reduced byproducts, making them ideal for water treatment, environmental remediation, and air purification applications.

In this work, the photocatalyst adsorbents studied are based on porphyrin as the photocatalyst and carbon materials, such as activated carbon, as one of the adsorbents supports. This combination leverages the unique photochemical properties of porphyrins and the high adsorption capacity of carbon materials to improve water purification processes.

1.2 Porphyrins: Versatile photocatalysts and photosensitizers

Porphyrins are a group of heterocyclic macrocycle compounds that play significant roles in biological systems, including photosynthesis, oxidation, and reduction reactions. For example, porphyrins are part of haemoglobin and myoglobin, which aid in oxygen transfer in vertebrates. The porphyrinic macrocyclic structure, featuring four pyrrole rings connected by methine units, was proposed over a century ago and is remarkably stable (**Fig. 1.1**). The nitrogen atoms within the structure create a central pocket ideally suited for incorporating metal atoms in a tetradentate manner, with iron, cobalt, or magnesium being common in biological systems [30]. These anionic centres are coordinatively unsaturated sites for charge transfer and adduct ligation, which involve reversible changes in electronic configuration, such as oxidation or spin states. Additionally, the structure allows for extensive modification, with a wide range of substituents that can be attached to the pyrrolic β sites or linked to the *meso*-positions at the methine bridges (**Fig. 1.1**).

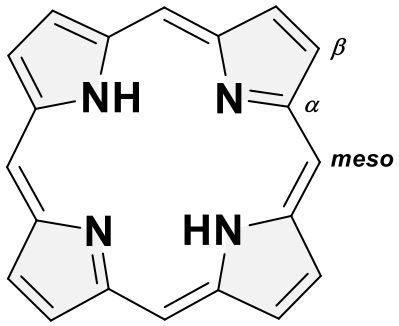

Fig. 1.1: The *β* and *meso* positions in porphyrins.

When exposed to light, porphyrins can generate reactive oxygen species (ROS), such as singlet oxygen and superoxide radicals. These ROS are highly reactive and play a pivotal role in the degradation of organic pollutants and the inactivation of harmful microorganisms in water. The

ability to produce ROS under light irradiation makes porphyrins particularly suitable for environmental remediation applications as photocatalysts. Another significant advantage of porphyrins as photocatalysts is their tunable electronic properties. By altering the peripheral substituents or incorporating different central metal ions into the porphyrin ring, researchers can enhance their photophysical and photochemical behaviours, consequently improving their photocatalytic efficiency [30].

Metalloporphyrins, which incorporate central metal ions such as iron, zinc, gallium, indium, and copper, form stable complexes due to the perfect fit of these ions within the porphyrin ring [31,32]. These metalloporphyrin complexes exhibit high catalytic activity compared to their metal-free counterparts because the central metal significantly influences the electronic properties of the porphyrinato moiety, with both components jointly affecting their electronic levels. This can be observed in the UV-Vis spectra of porphyrins, as illustrated in **Fig. 1.2**, which reveals characteristic absorption bands. The Soret bands (400-450 nm) are strongly allowed π-π^* transitions within the porphyrin ring, while the Q-bands (520-700 nm) are quasi-allowed transitions. Upon metalation, the Q-band shows two distinct bands due to the interaction between the central metal ion and the porphyrin ring, which alters the electronic distribution and symmetry of the complex [33].

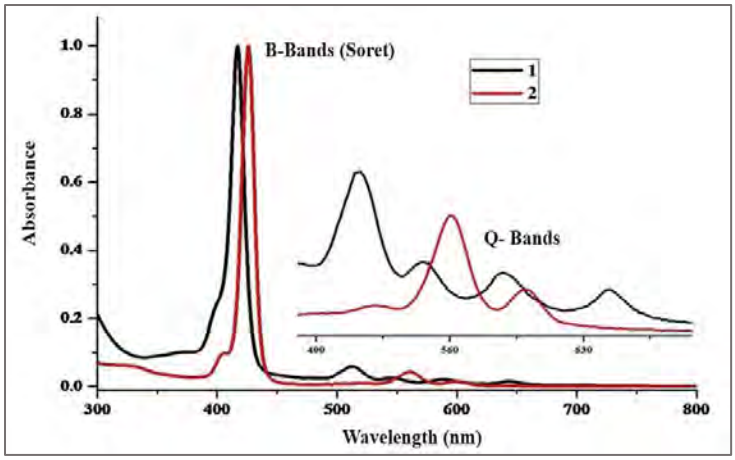

Fig. 1.2: The characteristic absorption spectra (1) of a free-base porphyrin and (2) the metaloporphyrn derivative, Source:[34].

1.2.1 Synthesis of porphyrins

Rothemund first synthesized Porphyrin by reacting benzaldehyde and pyrrole in a sealed bomb for 24 h in pyridine at about 150 °C [35]. Because the yield was relatively low, the Rothemund method was later modified by Adler and Longo by allowing pyrrole and benzaldehyde to react in the open air for just a few minutes (30 min) at around 141 °C with an increased yield of about 20% [36,37]. The Alder-Longo method likewise has its demerits, such as the reaction conditions being relatively harsh, especially when dealing with aldehydes that bear the sensitive functional groups; a high amount of tar is also produced during the reaction and, in most cases, makes the purification process rather tedious, especially for those porphyrin that do not precipitate [37]. Lindsey and co-workers [37,38] showed that porphyrins could be synthesized by condensing aldehydes and pyrroles under argon using a chlorinated solvent such as chloroform or dichloromethane. A Lewis acid such as trifluoroacetic acid (TFA) is the catalyst used. The porphyrinogen intermediate formed is then oxidized to porphyrin by the addition of an oxidant such as 2,3-dichloro-5,6-

dicyanobenzoquinone (DDQ) (**Scheme 1. 2**). After the addition of the oxidant, refluxing for one hour is needed to yield approximately 40-60% [38].

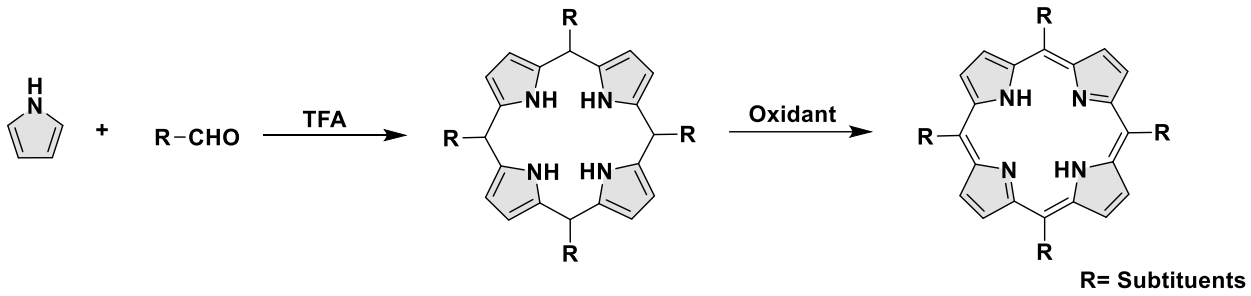

Scheme 1.2: Synthesis of tetraphenyl porphyrin by Lindsey method.

Although Lindsey's one-flask two-step method yields high amounts of porphyrins, it requires large quantities of chlorinated solvents and an expensive oxidizer, 2,3-dichloro-5,6-dicyanobenzoquinone (DDQ), making it costly and less suitable for industrial-scale production. The need for an industrial-scale, cost-effective synthesis of porphyrins is evident, as it would enhance their commercial relevance. To address this, Mondal and co-workers [39] recently proposed a synthesis method based on the concept introduced by Koszarna and Gryko [40], which utilizes a water-methanol (H_2O-MeOH) mixture catalyzed by hydrochloric acid (HCl) to synthesize corroles with high yields. Koszarna and Gryko identified tetrapyrrane as an important intermediate for porphyrin synthesis, which helps reduce the formation of undesired aldehyde–pyrrole oligo-condensates. The first step of this method involves condensing pyrrole and aldehyde in a H_2O-MeOH mixture with HCl. The resulting precipitate is then dissolved in dimethylformamide (DMF) and refluxed, followed by stirring at room temperature in open air [39] and purification through column chromatography or crystallization yields pure porphyrins. This method is advantageous as it does not require expensive oxidizing agents like DDQ, *p*-chloranil, or large volumes of dry-chlorinated solvents. Additionally, it is effective for gram-scale production

of porphyrins, addressing a significant limitation of previous methods [39]. In this thesis, the Alder-Longo method was employed to synthesize the tetra- and mono-substituted porphyrins, while the modified Koszarna and Gryko method was utilized to synthesize the *trans*-A_2B_2-porphyrins.

1.2.2 Mechanism of the use of porphyrins as photocatalysts and photosensitizers

Photodegradation of pollutants and antimicrobial photodynamic therapy (aPDT) involves the use of a combination of light and a light-sensitive material (dye), usually referred to as a photosensitizer (PS) or photocatalyst [41]. aPDT, in particular, is known to be efficient against multi-antibiotic-resistant planktonic and biofilm strains of bacteria with very minimal mutagenic response from bacteria [42]. PS alone usually have a negligible antibacterial effect and must be activated by light. Upon irradiation, photosensitizers transition from the singlet ground state (S_0) to a short-lived singlet excited state (S_1) upon absorbing light of a specific wavelength (**Fig. 1.3**). They then undergo intersystem crossing (ISC) to the long-lived triplet excited state (T_1), where two types of chemical reactions, Type I and Type II, occur to generate reactive oxygen species (ROS) [43]. These ROS are the primary agents responsible for degrading organic pollutants and deactivating microbes [44]. ROS cause DNA damage and cytoplasmic membrane damage in microorganisms, leading to the leakage of cellular contents and, ultimately, cell death [45,46]. In the degradation process, ROS attack the chemical bonds of pollutants, breaking them down into less harmful substances.

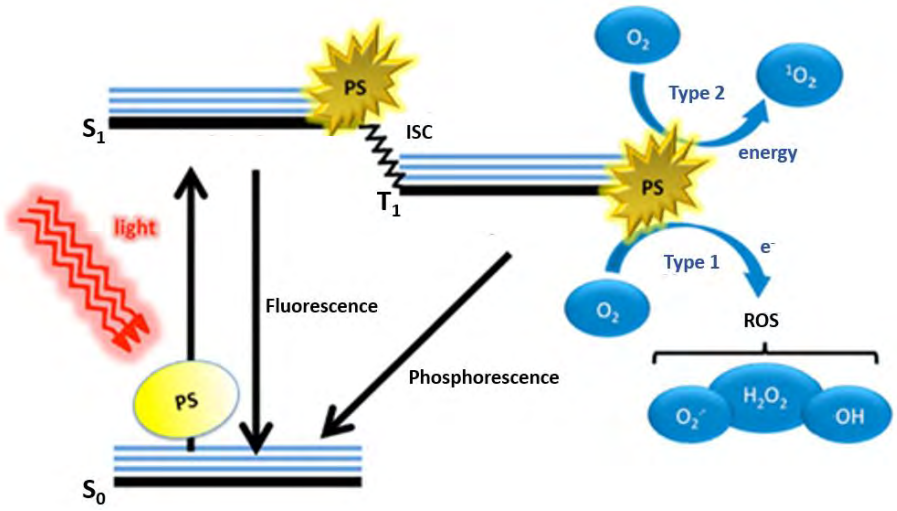

Fig. 1.3: Jablonski diagram indicating Type I and Type II reaction, Source: [43]

In the case of aPDT, ionic photosensitizers (PS), particularly cationic PS, are more effective at inactivating gram-negative bacteria such as *E. coli* than neutral and anionic PS. Gram-negative bacteria have another intricate outer membrane besides the peptidoglycan layer, impervious to most antimicrobial agents [47]. Therefore, to inactivate the gram-negative bacteria using the anionic PS effectively, there is a need to pre-treat the bacteria with $CaCl_2$, polymyxin B nonapeptide, or ethylenediaminetetraacetic acid (EDTA) to disrupt the outer membrane, unlike the case of gram-positive bacteria such as *S. aureus* [32,48]. For this reason, this research aims to synthesize cationic porphyrins and neutral porphyrins to be utilized as PS. The efficacy of some of the porphyrins against planktonic bacteria and biofilms was enhanced by introducing positive charges through methylation of the pyridinyl *meso*-substituents to make them cationic ionic [32,45].

1.2.3 Antimicrobial photodynamic therapy (aPDT) in water treatment

The application of aPDT in water treatment is not a recent concept. For instance, rose bengal bound to polystyrene beads and methylene blue bound to polystyrene were found to be a lethal antimicrobial agent, killing up to 99.99% of *E.coli* under natural sunlight [49,50]. Bonnet and co-workers [51] further industrialized this concept by formulating photosensitizing surfaces of polymeric chitosan membranes bound to 10,15,20-tetrakis(p-aminophenyl) porphyrin, (***p*-TAPP**) ,5,10,15,20-tetrakis(p-hydroxyphenyl)porphyrin (***p*-THPP**) and zinc (II) phthalocyanine tetrasulfonic acid (**ZnPcS**), **Fig 1.4**. They were then applied to a large-scale water flow system to reduce *E. coli* viability [51]. Although they successfully demonstrated the concept of using immobilized photosensitizers for aPDT, their findings indicated that the photomicrobicidal activity achieved was insufficient for practical applications, where a 5-log reduction in microbial levels would be ideal [51]. To make this approach viable for real-world applications, further modifications are necessary to improve and enhance the performance of such systems.

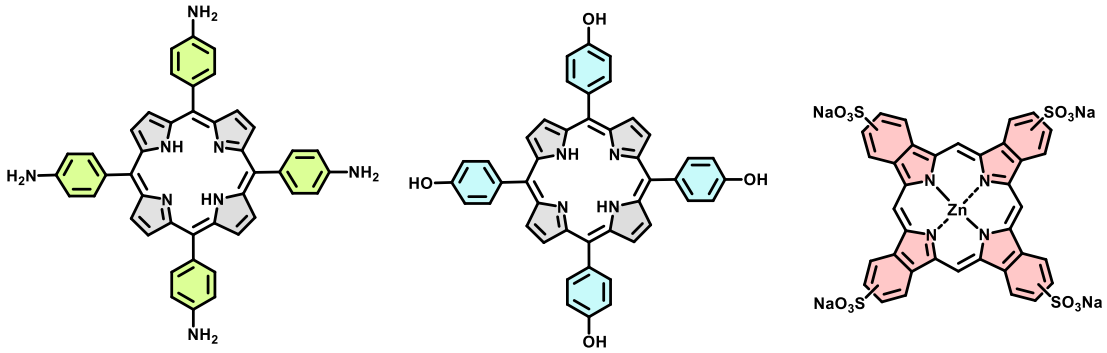

Fig. 1.4: 10,15,20-tetrakis(p-aminophenyl) porphyrin, (**p-TAPP**),5,10,15,20-tetrakis(p-hydroxyphenyl) porphyrin (**p-THPP**) and zinc (II) phthalocyanine tetrasulfonic acid (**ZnPcS**)

The aPDT effect of porphyrins can be highly beneficial in water purification systems due to their ability to deactivate biofilms [52]. Biofilms are complex structures of microorganisms, including bacteria, fungi, and algae, that adhere to surfaces in aqueous environments [53]. These microorganisms produce a slimy, protective matrix that helps them stick together and to surfaces such as pipes, tanks, and filters [53]. Biofilms can contaminate water in various ways: They harbour pathogenic microorganisms, increasing the risk of waterborne diseases [54]. Additionally, biofilms can alter the chemical composition of water, resulting in reduced dissolved oxygen levels, altered taste and odour, and harmful by-products. Physically, biofilms can clog pipes and filters, reducing the efficiency of water distribution and treatment systems [55]. Furthermore, they contribute to the corrosion of metal surfaces, which can release metals into the water, further contaminating it [53].

Integrating photocatalysts with antibiofilm properties to support water purification is crucial for several reasons. The antibiofilm properties of these photocatalysts are essential in preventing and

disrupting biofilm formation on supports. The ROS generated by photocatalysts can penetrate biofilms, killing the microorganisms within and preventing their regrowth. This significantly reduces the presence of waterborne pathogens, including bacteria, viruses, and protozoa, enhancing public health. In this work, the antibiofilm properties of some porphyrins were studied, and the best compound was further investigated as a photocatalyst for water purification.

1.2.4 Supported porphyrin photocatalysts

Porphyrins can easily be distinguished from other photoactive compounds, such as TiO_2, from their high light absorption across a broad spectrum. As discussed previously, this property enables them to generate ROS through a spin-forbidden intersystem crossing mechanism, making them suitable for various catalytic processes. However, their use as homogeneous catalysis faces challenges such as deactivation due to agglomeration/ aggregation, low reusability, and recovery issues [56]. To address these limitations, researchers have explored immobilizing porphyrins on solid supports made from organic and inorganic materials. Commonly used supports include zeolites, polymers, photoactive oxides, and carbon-based materials [57]. Carbon-based materials are increasingly favoured for their availability, biodegradability, and biocompatibility, making them safe and sustainable options for various applications [58]. Consequently, they were employed in this thesis.

1.3 Carbon-based supports and porphyrins for water treatment: A literature study

Carbon-based materials have gained significant attention in water treatment due to their unique properties and versatility [29]. These materials, which include activated carbon, carbon nanotubes (CNTs), graphene, carbon quantum dots (CQD), and nitrogen-doped carbon quantum dots (N-CQD), are preferred for several reasons [59,60]. Firstly, they possess a high surface area, which enhances their adsorption capacity, allowing them to effectively capture a wide range of

contaminants, including dyes and microbial pathogens. Secondly, their chemical stability ensures they remain effective in various environmental conditions, making them suitable for long-term use [61,62]. Additionally, their ability to be functionalized with different chemical groups allows for tailored applications, further enhancing their efficiency in water purification [59].

Beyond serving as mere supports, carbon-based materials have been shown to significantly improve the performance of photocatalysts [63,64]. For instance, when used as support for photocatalysts, these materials can enhance the photocatalytic activity by promoting better dispersion of the photocatalyst and improving light absorption [63]. This synergy between the carbon support and the photocatalyst leads to more efficient degradation of organic pollutants and inactivation of microbial contaminants. Moreover, carbon-based supports can facilitate the transfer of photoelectrons, reducing the recombination of photogenerated electron-hole pairs, a common issue in photocatalysis [64]. Even though porphyrin-carbon nanomaterial composites have demonstrated utility in solar energy conversion, catalysis, and biological applications [65–68], their use in water treatment remains underexplored.

Table 1.1 [69-78] presents the porphyrins on carbon materials studied for the photodegradation of water pollutants and aPDT. The primary carbon materials studied with porphyrins include graphene, graphene oxide (GO), graphitic carbon nitride, and multi-walled carbon nanotubes. Exploring additional, especially low-cost, carbon materials is crucial to expand the scope. This study introduces activated carbon and carbon quantum dots for use as support for porphyrins for the first time.

Table 1.1: Porphyrins Supported on Carbon Materials for Photocatalytic Degradation of Water Pollutants

Porphyrin complex	Carbon Material and interactions	Application and Target pollutants/Microbes	Ref
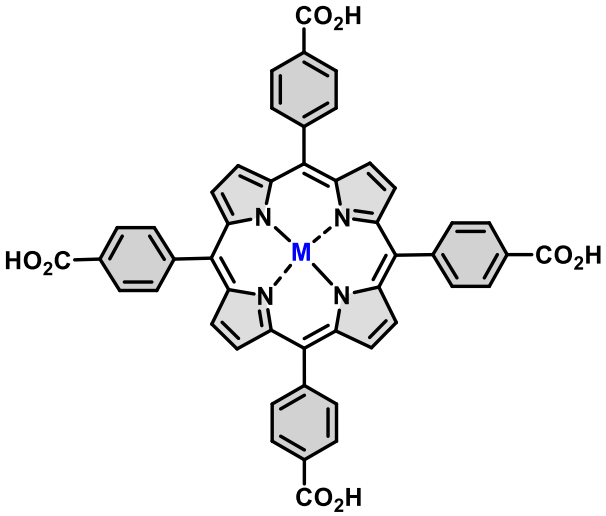 **M = H_2, Co, Ni, Cu, Sn**	Graphitic carbon nitride (g-C_3N_4), Graphite, TiO_2-Graphene Covalent bonding and π–π stacking interaction	<u>Photodegradation</u> Rhodamine B (Rh-B) Methyl orange (MO), Phenol	[69–73]
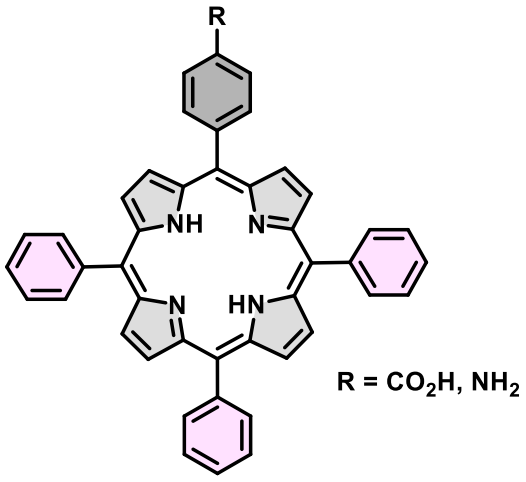 **R = CO_2H, NH_2**	Carboxylic functionalized multi-walled carbon nanotubes (*o*-MWCNTs) Covalent bonding and π–π stacking interaction	<u>Photodegradation</u> Rh-B and Rhodamine-G (RhG)	[74]

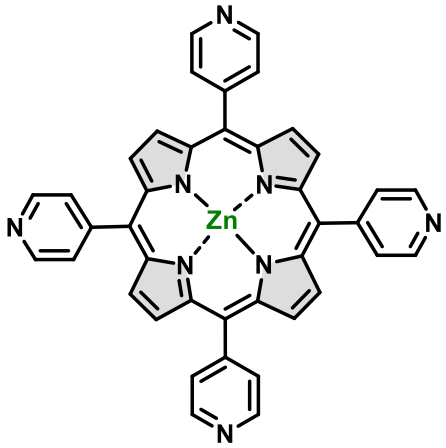	graphene oxide (GO) π–π stacking interaction	Photodegradation Rh-B	[75]
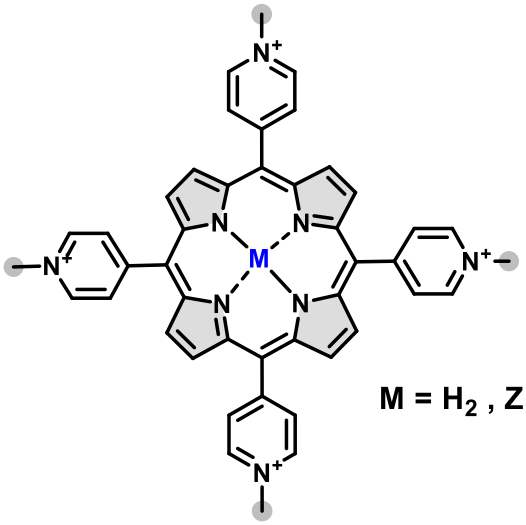	GO π–π stacking interaction and electrostatic interactions	Photodegradation Rh-B	[76]
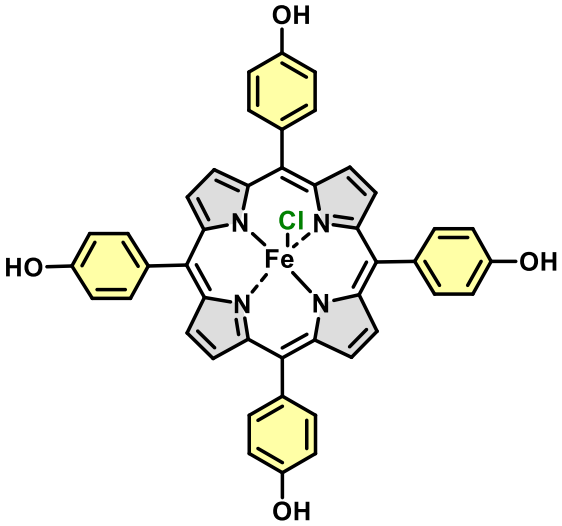	GO Covalent bonding and π–π stacking interaction	Photodegradation Crystal violet	[77]

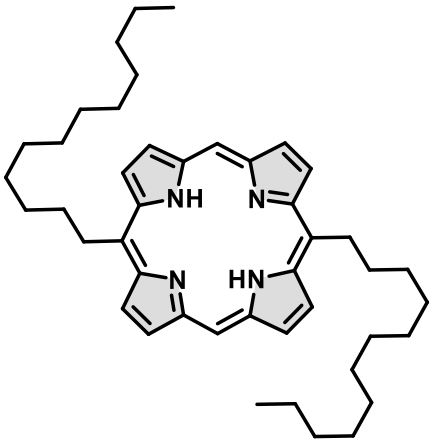	Reduced graphene oxide (rGO) π–π stacking interaction and electrostatic interactions	<u>Photodegradation</u> Congo red <u>aPDT</u> *Candida albicans, Enterococcus faecalis,* and *Staphylococcus aureus*	[78]

1.4 Carbon-based supports used in this work

An exciting advancement in this field, also explored in this work, is the development of photocatalyst-adsorbent composites. These composites merge carbon-based supports' adsorption capabilities with porphyrins' photocatalytic properties. This dual-function approach to water purification allows contaminants to be initially adsorbed onto the carbon support and subsequently degraded by the photocatalyst under light irradiation. This integrated method enhances the overall efficiency of water treatment and offers a comprehensive solution for removing both organic pollutants and microbial contaminants.

This study examines activated carbon in three forms: granulated, powdered (immobilized on polyacrylonitrile fibers), and colloidal forms. Additionally, nitrogen-doped carbon quantum dots immobilized on polyacrylonitrile fibers, are investigated as supports for porphyrins, focusing on their photocatalytic and aPDT properties.

1.4.1 Activated carbon

Activated carbon is a highly porous material with a large surface area, making it ideal for water purification, air filtration, and industrial applications. Its preparation involves two main steps: carbonization and activation. Carbonization converts organic materials (such as coconut shells, wood, coal, and agricultural waste) into carbon by heating them in the absence of oxygen, removing volatile compounds, and leaving a carbon-rich residue [79]. Coconut shells are often preferred due to their high density and hardness, which result in activated carbon with a high surface area and mechanical strength [80]. Activation, which can be physical or chemical, increases the porosity and surface area of the carbonized material. Physical activation uses oxidizing gases like steam or carbon dioxide at high temperatures (800–1100 °C) [81], while chemical activation involves impregnating the carbonized material with chemical agents like potassium hydroxide, phosphoric acid, or zinc chloride before heating. Chemical activation generally takes place at lower temperatures (< 800 °C) compared to physical activation and leads to an increased surface area and pore volume [82].

Activated carbon is particularly effective at removing micropollutants, such as pesticides and pharmaceuticals, and is commonly used in drinking water and wastewater treatment. It can be prepared in various forms, including granulated activated carbon (GAC), powdered activated carbon (AC), and colloidal activated carbon (CAC). CAC comprises very fine carbon particles (1-100 nm) dispersed in a liquid medium, forming a stable colloid [83]. These different forms influence their specific applications and effectiveness in removing various contaminants from water. In this study, oxygen-functionalized granulated activated carbon (ACO), powdered activated carbon (AC), and colloidal activated carbon (CAC) were investigated as potential porphyrin supports for water treatment. For practical application, powdered activated carbon (AC)

was immobilized on polyacrylonitrile (PAN) fibers to form composite fibers, designated as PAN/AC1 and PAN/AC2, with 50% and 100% weight compositions of AC in PAN, respectively.

1.4.2 Carbon quantum dots

Carbon quantum dots (CQD) are tiny carbon nanoparticles, typically less than 10 nm in size, renowned for their unique optical and electronic properties. These properties make CQD highly valuable for sensing, bioimaging, drug delivery, and energy storage [84,85]. The synthesis of CQD can be broadly divided into two main approaches: top-down and bottom-up methods (**Fig. 1.5**) [86]. Top-down methods involve breaking down larger carbon structures into CQD, including arc discharge, laser ablation, and electrochemical oxidation. Bottom-up approaches, on the other hand, involve assembling CQD from smaller molecules and include hydrothermal/solvothermal synthesis, microwave-assisted synthesis, and pyrolysis [87,88].

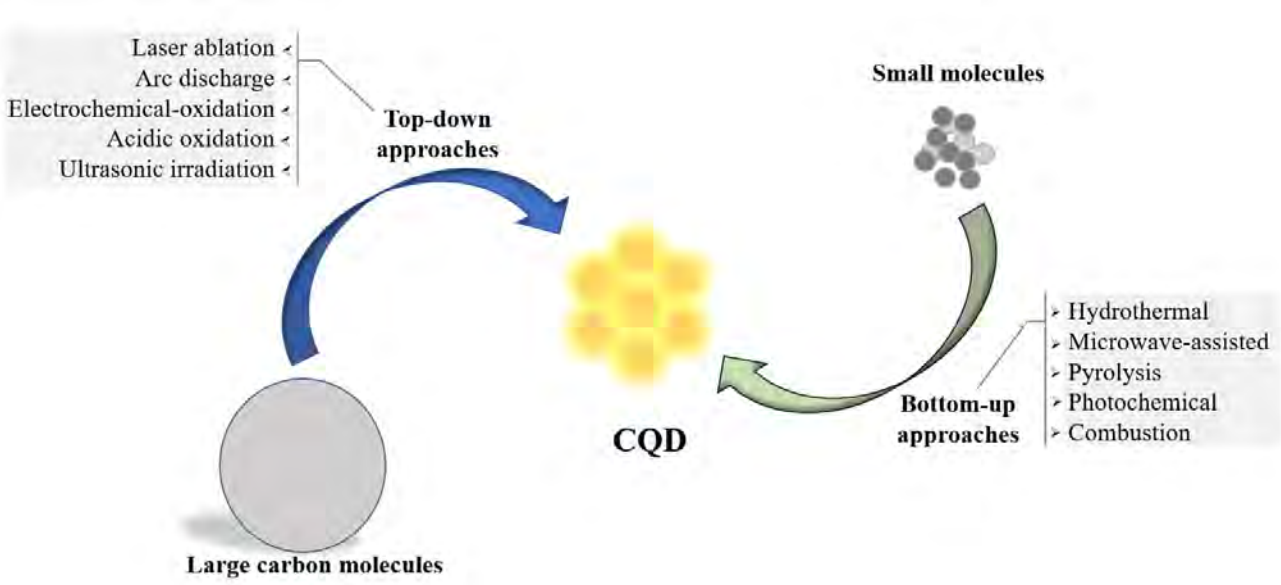

Fig. 1.5: Illustration of top-down and bottom-up CQD synthetic approaches; Source: [86]

Studies have shown that doping CQD with heteroatoms such as nitrogen, sulfur, phosphorus, or boron can significantly enhance their properties. These heteroatoms create active sites on the surface of CQD and introduce new energy levels within their bandgaps, resulting in enhanced photoluminescence, improved catalytic activity, tunable properties, and increased solubility and stability [85].

The synthesis methods for doped CQD are similar to those for undoped CQD but involve adding dopant sources [89]. Hydrothermal/solvothermal synthesis involves heating organic precursors with dopant sources (e.g., urea for nitrogen doping) in a solvent under high pressure. Microwave-assisted synthesis subjects organic precursors and dopant sources to microwave irradiation, rapidly forming doped CQD [84]. Pyrolysis involves the thermal decomposition of organic materials mixed with dopant sources, such as using citric acid and urea to produce nitrogen-doped CQD [90]. Electrochemical synthesis oxidizes carbon electrodes in the presence of dopant-containing electrolytes to produce doped CQD [91]. Chemical vapour deposition involves the deposition of carbon and dopant atoms onto a substrate at high temperatures, forming doped CQD [92].

In this thesis, nitrogen-doped carbon quantum dots (NCQD) were prepared using a bottom-up approach. The NCQD was then supported on polyacrylonitrile (PAN) fibers, and the final composite fibers were used as porphyrin supports.

1.4.3 Immobilization of carbon supports on polyacrylonitrile fibers for improved photocatalytic activity.

Polyacrylonitrile (PAN) fibers were selected for this work to immobilize powdered activated carbon (AC) and nitrogen-doped carbon quantum dots (NCQD) because PAN is chemically stable in water, which ensures that the immobilized AC and NCQD remain intact and functional over

extended periods. PAN also exhibits excellent mechanical strength and durability, further contributing to the longevity and reliability of the immobilized photocatalysts. Moreover, PAN is relatively inexpensive and readily available, making it a cost-effective option for large-scale applications.

PAN fibers are typically prepared using the electrospinning method, which utilizes a high-voltage electric field to draw a polymer solution containing the photocatalyst into fine, porous fibers with a high surface area, thereby enhancing photocatalytic activity [93,94].

Combining smaller-sized carbon supports with porphyrin photocatalysts on PAN fibers creates a synergistic effect. AC increases the surface area of the PAN composite support, enhancing the loading capacity of the photocatalyst. Additionally, NCQD improves light absorption and energy transfer to the loaded porphyrins, leading to a higher production of reactive oxygen species (ROS) within the composite. This synergy results in a more efficient photocatalytic process, making the porphyrin-PAN composite fibers highly effective for water purification and antimicrobial treatments. Additionally, the immobilized supports enhance the chemical and thermal stability, as well as the reusability of the fibers, ensuring consistent performance over multiple cycles.

1.5 Metalloporphyrin complexes in this thesis

This work details the synthesis of indium-metalated porphyrins with various *meso*-meso-substituents, preparing selected supports, and their applications in this study (**Table 1.2**). indium was chosen as the central metal to enhance intersystem crossing to the triplet state, thereby improving singlet oxygen production, which is crucial for aPDT and dye photodegradation. Quaternization of the complexes containing pyridinyl groups enhanced their photophysical properties, improving photocatalytic and aPDT efficiencies. Additionally, quaternization

introduced electrostatic interactions with nitrogen carbon quantum dots (NCQD), complementing the existing π-π interactions.

Table 1.2: Indium-metalated porphyrins and the support materials in this thesis

<table>
<tr><th>Complex structure used with respective support material(s), names, and precursor names</th><th>Support materials</th><th>Application</th></tr>
<tr><td rowspan="4"> 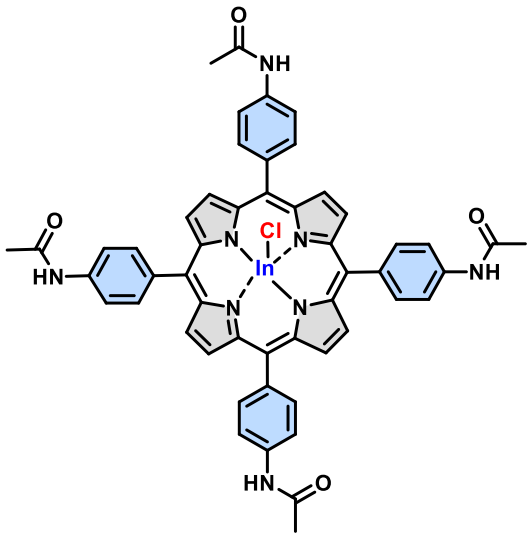

1a: Chloroindium (III) 5,10,15,2-tetrakis (4-acetamidophenyl) porphyrin (NEW)

1: 5,10,15,20-tetrakis(4-aminophenyl) porphyrin (NOT NEW) [95]</td><td>• ACO</td><td><u>Adsorption</u>
MB

<u>Photodegradation</u>
MB</td></tr>
<tr><td>• CAC</td><td>Photodegradation of MB

<u>aPDT</u>
E.coli planktonic cells</td></tr>
<tr><td>• PAN/NCQD fibers</td><td><u>Photodegradation</u>
MB and MO

<u>aPDT</u>
E.coli planktonic cells</td></tr>
<tr><td colspan="2">π-π stacked and electrostatic interactions</td></tr>
<tr><td></td><td>• CAC</td><td><u>Photodegradation</u>
MB

<u>aPDT</u></td></tr>
</table>

<table>
<tr><td rowspan="4"> 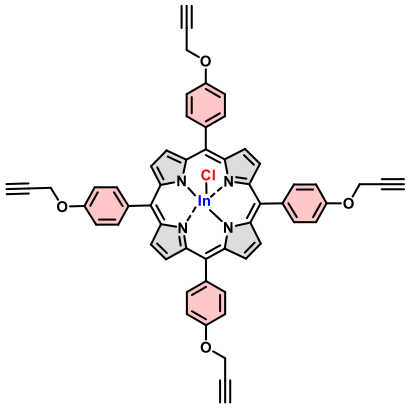
2a : Chloroindium (III) 5,10,15,20-tetrakis[4-(prop-2-yn-1yloxy) phenyl] porphyrin (NEW)

2 : 5,10,15,20-tetrakis[4-(prop-2-yn-1yloxy) phenyl] porphyrin (NOT NEW) [96]</td><td></td><td>E.coli planktonic cells</td></tr>
<tr><td>• PAN/AC2 fibers</td><td><u>Adsorption</u>
MB

<u>Photodegradation</u>
Ciprofloxacin and MB</td></tr>
<tr><td>• PAN/NCQD fibers</td><td><u>Photodegradation</u>
MB

<u>aPDT</u>
E.coli planktonic cells</td></tr>
<tr><td colspan="2">π-π stacked and electrostatic interactions</td></tr>
<tr><td rowspan="2"> 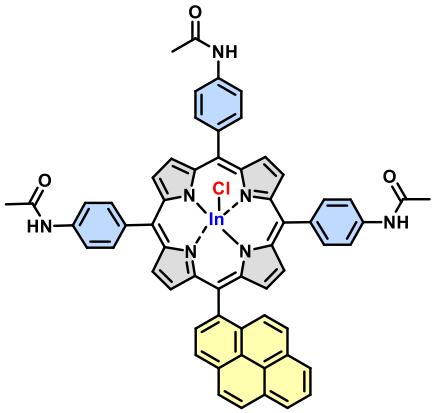
3a : Chloroindium (III) 5,10,15-tri-4-acetamidophenyl 20-(pyren-1-yl) porphyrin</td><td>• CAC</td><td><u>Photodegradation</u>
MB

<u>aPDT</u>
E.coli planktonic cells</td></tr>
<tr><td>• PAN/NCQD fibers</td><td><u>Photodegradation</u>
MB, MO

<u>aPDT</u>
E.coli planktonic cells</td></tr>
</table>

3 : 5,10,15-tri-4-aminophenyl 20-(pyren-1-yl) porphyrin **(ALL NEW)**	π-π stacked and electrostatic interactions	
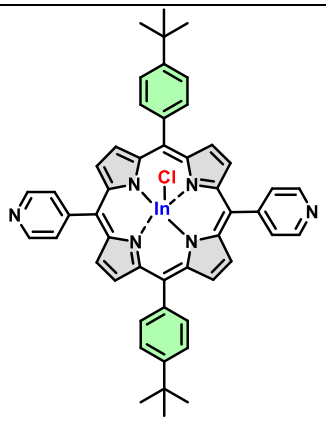 **4a** : Chloroindium (III) 5,15-bis(4-(tert-butyl)phenyl)-10,20-di(pyridin-4-yl) porphyrin **4 :** 5,15-bis(4-(tert-butyl)phenyl)-10,20-di(pyridin-4-yl) porphyrin **(ALL NEW)**	None	<u>aPDT</u> *S. aureus* and *E. coli* planktonic cells
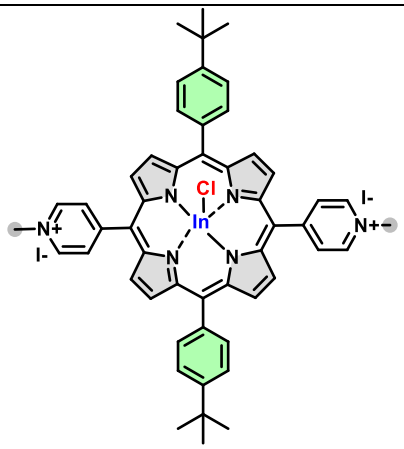 **4b**: Chloroindium (III) 5,15-bis(4-(tert-butyl)phenyl)-10,20-bis(N-methylpyridinyl) porphyrin iodide **(NEW)**	None	<u>aPDT</u> *S. aureus* and *E. coli* planktonic cells and biofilms

<table>
<tr>
<td> 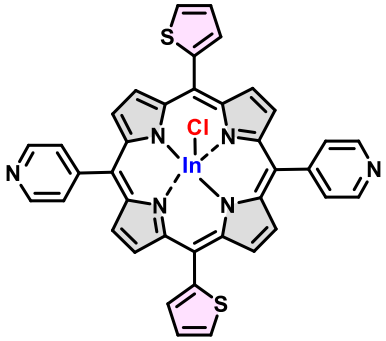
5a: Chloroindium (III) 5,15-di(pyridin-4-yl)-10,20-di(thiophen-2-yl)porphyrin

5 : Chloroindium (III) 5,15-di(pyridin-4-yl)-10,20-di(thiophen-2-yl)porphyrin

(ALL NEW)</td>
<td>None</td>
<td><u>aPDT</u>
S. aureus and E. coli
planktonic cells</td>
</tr>
<tr>
<td rowspan="3"> 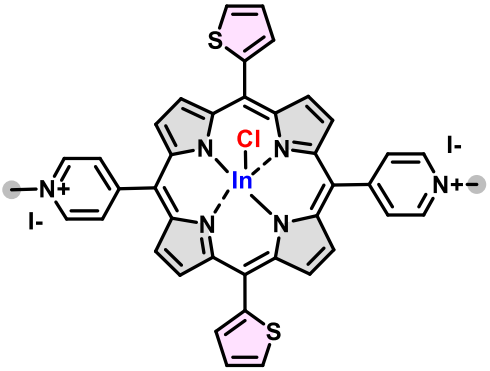
5b: Chloroindium (III) 5,15-bis (N-methylpyridinyl)-10,20-di(thiophen-2-yl) porphyrin iodide
(NEW)</td>
<td>None</td>
<td><u>aPDT</u>
S. aureus and E. coli
planktonic cells and biofilms</td>
</tr>
<tr>
<td>• PAN
• PAN/NCQD fibers</td>
<td><u>Photodegradation</u>
MB, MO

<u>aPDT</u>
E.coli planktonic cells</td>
</tr>
<tr>
<td colspan="2">π-π stacked and electrostatic interactions</td>
</tr>
</table>

1.6 Research gap and justification carbon-based supports

1.6.1 Research gap

Water treatment technologies utilizing photocatalytic systems, especially metal oxides like TiO_2 and ZnO, have been widely studied. These materials are effective in UV-light-activated pollutant removal and antimicrobial applications. However, critical limitations hinder their efficiency and scalability:

- Light absorption range: TiO_2 and ZnO exhibit weak activity under visible light due to their wide band gaps, restricting their use in natural sunlight.
- Photo-corrosion: Metal oxides face chemical degradation under prolonged exposure to photocatalytic conditions, reducing operational stability.
- Limited efficiency due to aggregation: Dut to aggregation, their catalytic performance is constrained under real-world water treatment scenarios where diverse pollutants and conditions exist.

As emerging contaminants such as dyes, pharmaceuticals, and antibiotic-resistant bacteria persist in water, the need for visible-light-active photocatalysts becomes increasingly urgent. Current research trends emphasize multifunctional systems capable of pollutant removal and microbial deactivation under environmentally relevant conditions.

This study addresses these challenges by leveraging the synergistic properties of **indium (III) porphyrins immobilized on carbon-based supports**. These hybrids enable efficient pollutant degradation under visible light while offering dual functionality through enhanced antimicrobial activity. This research stands out by integrating:

- Porphyrins, known for their exceptional visible light absorption and catalytic ability.
- Carbon-based supports, with characteristics such as high surface area, high conductivity, chemical stability, and customizable morphology.

This approach not only expands the operational range of photocatalytic materials into the visible-light spectrum but also tackles the dual challenges of organic pollutant removal and microbial contamination. By addressing limitations of previous works, this study demonstrates the potential for practical water treatment solutions that combine adsorption and photocatalysis mechanisms.

1.6.2 Justification for carbon-based supports

Carbon-based supports are strategically chosen for this study due to the following advantages:

- **Superior photostability**: Carbon materials resist photo-corrosion, improving operational longevity compared to metal oxide counterparts.
- **Reduced electron-hole recombination**: Carbon supports facilitate rapid electron transfer and minimize charge recombination, critical for enhancing photocatalytic efficiency.
- **Multifunctional design**: Carbon-based materials have high surface area and allow seamless immobilization of organic photosensitizers such as porphyrins through π-π stacking.

This study therefore establishes carbon-based materials as viable supports demonstrating enhanced performance and versatility in modern water treatment applications.

1.7 Trends in this thesis

- Effect of Support Materials:
  - ✓ *MB Removal by Adsorption and Photodegradation*: Investigated using activated carbon-related supports, GAC, ACO, PAN/AC1, PAN/AC2, and porphyrin-loaded coposites, **1a**(ACO) and **2a**(PAN/AC2).
  - ✓ *Hydrogen Peroxide Addition*: Enhanced photodegradation of MB and deactivation of *E. coli* using CAC and porphyrin-loaded CAC samples (porphyrins **1a**, **2a**, and **3a**).
- Effect of Light Sources:
  - ✓ *Degradation of ciprofloxacin*: Compared under Xe lamp and sunlight using porphyrin **2a** loaded on PAN/AC2 support fibers.
- Effect of Porphyrin Properties:
  - ✓ *Porphyrin Charge*: Studied aPDT activities of **4a**, **5a**, and their cationic forms **4b** and **5b** against planktonic cells of *S. aureus* and *E. coli*.
  - ✓ *Porphyrin Functional Groups*: Compared **4b** and **5b** in the deactivation of biofilms of *S. aureus* and *E. coli* and in photodegradation of MB and MO studies in water using porphyrins **1a**, **2a**, **3a**, and **5b** loaded on PAN/NCQD fibers.
  - ✓ *Porphyrin Symmetry*: Investigated MB and MO removal using porphyrins **1a** and **3a** loaded on PAN/NCQD fibers.

1.8 Aim and objectives

1.8.1 Aim of the study

The main objective of this study is to synthesize composite materials based on indium porphyrin linked to carbon supports, aimed at enhancing water treatment processes for the removal of organic pollutants and microbial contaminants.

1.8.2 Specific objectives

The specific objectives of this study are:

i. To design, synthesize, and characterize novel porphyrin-based ligands and their corresponding *meso*-indium metallated porphyrin complexes

ii. To synthesize and characterize the carbon supports of interest and non-covalently conjugate (π-π stacking) indium-porphyrins to them.

iii. To examine the photophysical properties of the synthesized porphyrins, the carbon-based supports, and their respective porphyrin/carbon support hybrids

iv. To evaluate the aPDT activity of the pyridinyl-based *trans*-A_2B_2 porphyrins on the *S. aureus* and *E. coli* planktonic and biofilm cells

v. To evaluate the photocatalytic efficiency of porphyrin-carbon support hybrids in degrading methylene blue dye, and selectively methyl orange dye and ciprofloxacin, and to assess their antibacterial activity against *E. coli* (where applicable), for potential application in water treatment systems under visible light irradiation

CHAPTER 2: Experimental

This chapter details the experimental procedures, synthetic methods, and characterization techniques employed for all porphyrins and support materials utilized throughout the study.

2.1 Materials

2.1.1 Solvents

All the organic solvents used were of analytical grade and used as received. Dichloromethane (DCM), chloroform, deuterated chloroform ($CDCl_3$), diethyl ether, dimethyl sulfoxide (DMSO), deuterated dimethyl sulfoxide (DMSO-d_6), N, N-dimethylformamide (DMF), ethyl acetate, toluene, methanol, ethanol, octanol, were purchased from Sigma-Aldrich.

2.1.2 Reagents

1-Pyrene carboxaldehyde, *p*-nitrobenzaldehyde, 2-thiophenecarboxaldehyde, 4-*tert*-butylbenzaldehyde, pyrrole, sodium acetate, propionic acid, glacial acetic acid, hydrochloric acid (32%) , acetic anhydride, potassium hydroxide, pyridine, glutaraldehyde, triethylamine (TEA), sodium hydrogen carbonate, indium (III) chloride, tin (II) chloride, Zn tetraphenyl porphyrin (ZnTPP), and methylene blue (MB), methyl orange (MO), ciprofloxacin, Polyacrylonitrile (PAN, Mw = 150,000), 9,10 dimethylanthracene (DMA), iodomethane, resazurin sodium salt, citric acid and urea were purchased from Sigma-Aldrich. Ammonia (25%) was purchased from Minema Chemicals. Coconut shell waste was collected from the coastal regions of Kenya. *E. coli* (ATCC 25922) and *S. aureus* (ATCC 25923) were purchased from Microbiologic USA. Glucose, agar bacteriological BBL Muller-Hinton broth and nutrient agar were obtained from Merck. Phosphate buffer saline (PBS, 10 mM, pH 7.4) was prepared using appropriate amounts of Na_2HPO_4, KH_2PO_4, NaCl and KCl. The ultrapure water (18.2 MΩ) used in the experiments was obtained from ELGA, Veolia water PURELAB, Flex system (Marlow, UK).

2.2 Equipment

I. The ground-state electronic absorption spectra of the porphyrin samples were measured with a Shimadzu UV-2550 spectrophotometer.

II. Varian Eclipse spectrofluorimeter equipped with a 360-1100 nm filter was used to conduct the fluorescence excitation and emission measurements in solution.

III. Diffuse reflectance spectra (DRS) were obtained using Perkin Elmer Lambda 950 UV–Vis NIR spectrophotometer from 200 nm to 800 nm.

IV. FT-IR spectra were acquired using a Bruker® ALPHA FT-IR spectrometer with a universal attenuated total reflectance (ATR) sampling accessory.

V. Raman spectra were recorded with Bruker vertex 70-Ram II Raman spectrometer (1064 nm Nd:YAG laser and liquid nitrogen cooled germanium detector).

VI. Mass spectral data were collected with a Bruker AutoFLEX III Smartbeam TOF/TOF Mass spectrometer. The instrument was operated in negative ion mode using an m/z range of 400–3000 amu. The voltage of the ion sources was set at 19 and 16.7 kV for ion sources 1 and 2, respectively, while the lens was set at 8.50 kV. The reflector 1 and 2 voltages were set at 21 and 9.7 kV, respectively. The spectra were acquired using α-cyano-4-hydroxycinnamic acid as the MALDI matrix.

VII. Proton nuclear magnetic resonance (^{1}H NMR) spectra were obtained using Bruker AVANCE 400 MHz NMR spectrometers.

VIII. Elemental analysis data were collected from a Vario-Elementar® Microcube ELIII CHNS instrument.

IX. The thermal decomposition profiles of the synthesized material were obtained using a Perkin Elmer TGA 8000 Thermogravimetric Analyzer over a temperature range of 50–800 °C while purging with nitrogen.

X. Dynamic light scattering (DLS) Malvern Zetasizer Nanoseries, Nano-ZS90 particle distribution samples were investigated using dynamic light scattering (DLS) to provide information about the average size distribution in solution

XI. Scanning electron microscope (SEM) images were obtained using a JEOL JSM-840 scanning electron microscope (SEM) operating at an accelerating voltage of 2 kV. An energy-dispersive X-ray spectrometer (EDS, INCA PENTA FET coupled with a VAGA TESCAM operated at 20 kV) was used to determine the elemental compositions qualitatively.

XII. X-ray powder diffraction (XRD) patterns were recorded on a Bruker D8 Discover equipped with a Lynx Eye Detector, using CuK_{α} radiation (λ= 1.5405 Å, nickel filter). Data was collected at 2θ range of 10−100° scanning at 1° min^{-1} with a filter time constant of 2.5 s per step and a slit width of 6.0 mm. Samples were placed on a zero-background silicon wafer slide. The XRD data were treated using Eva (evaluation curve fitting) software.

XIII. Nitrogen adsorption/desorption isotherms were carried out at 77 °K using a Micrometrics ASAP 2020 Surface area and Porosity analyzer. Before each measurement, degassing was carried out at 150 °C for two days. The Brunauer–Emmett–Teller (BET) method was employed to determine surface area and porosity. The micropore volumes ($\mathbf{V_{t\text{-}plot}}$) and micropore surface areas were obtained directly from the t-plot tabular report.

XIV. Fluorescence lifetimes were measured using a time-correlated single photon counting (TCSPC) setup (PicoQuant FluoTime 300). The excitation sources were diode lasers

(LDH-P-C-420 and LDH-P-375, driven by PDL 800-B 20 MHz repetition rate, 44 ps pulse width, Picoquant GmbH). The luminescence decay curve was measured at the maximum emission peak, and the lifetime was obtained by deconvolution of the decay curve using the FluoFit software program (PicoQuant GmbH, Germany). Fig 2.1

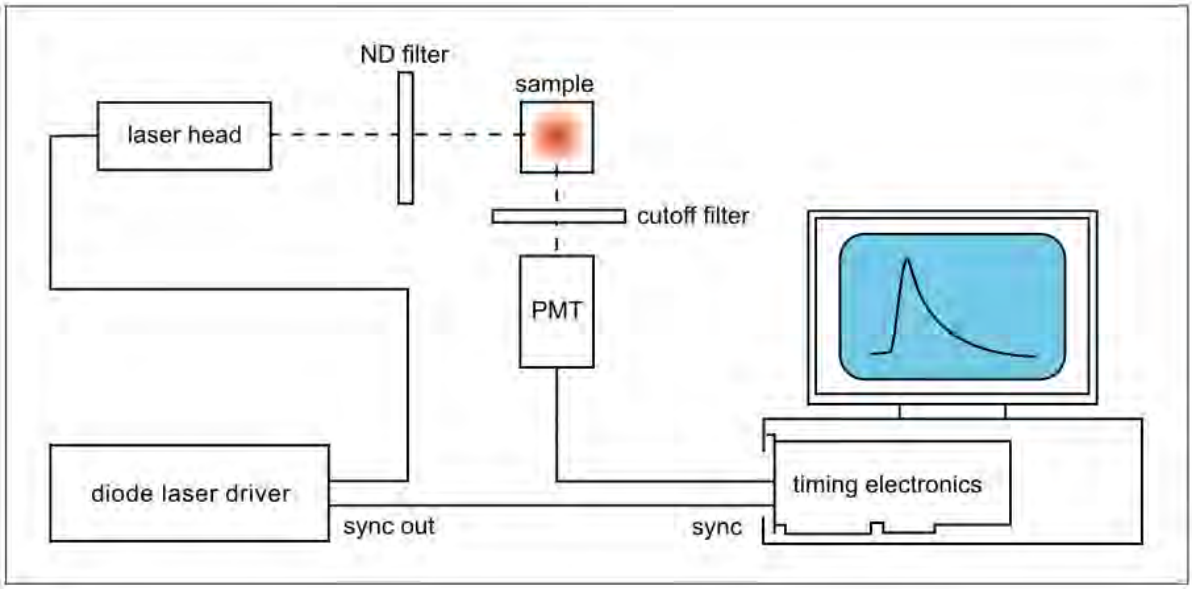

Fig. 2.1: Schematic diagram of TCSPC set-up of PicoQuant FluoTime 300

XV. Triplet state quantum yields were determined using a laser flash photolysis system consisting of an LP980 spectrometer (Edinburgh Instruments) with a PMT-LP detector and an ICCD camera (Andor DH320T-25F03). The signal from a PMT detector was recorded on a Tektronix TDS3012C digital storage oscilloscope. The excitation pulses were produced by a tunable laser system consisting of an Nd: YAG laser (355 nm, 135 mJ/4-6 ns), with a pump beam of 427 nm provided by an Ekspla NT-342B laser (2.0 mJ / 7 ns, 20 Hz) fitted with an OPO. The schematic representation of the setup is shown in Fig.2.2. The

triplet lifetimes were then determined by exponential fitting of the kinetic curves using the program OriginPro 8.0.

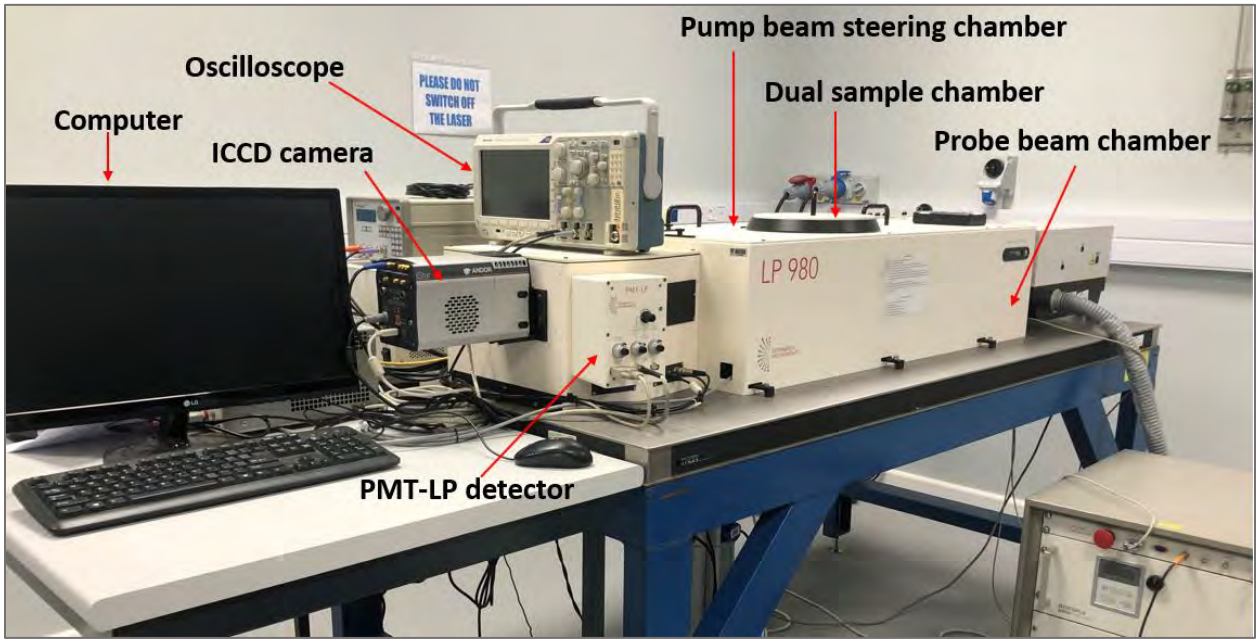

Fig. 2.2: Laser flash photolysis system- Edinburgh Instruments LP980 Spectrometer

XVI. To determine the singlet oxygen production of the compounds, photo-irradiations were done using a Spectra-Physics Quanta Ray Indi-40–10 (118 mJ @ 355 nm, 7 ns, 10 Hz) Nd:YAG laser to pump a Spectra-Physics PrimoScan OPO (405–2855 nm, 39 mJ @ 430 nm). The irradiation wavelength was determined to be the crossover wavelength between the respective samples, and the ZnTPP was used as the standard.

XVII. Time-of-flight-secondary ion mass spectrometer (ToF-SIMS) data were recorded with an ION TOF GmbH TOF SIMS 5 run in positive ion imaging mode using a bismuth ion cluster gun.

XVIII. Thermo Oriel Xe lamp (Model 66902) and Halogen lamp were used as white light beam sources during the photocatalytic degradation experiment.

XIX. The sterilization and autoclaving of nutrient broth, nutrient agar and phosphate buffer, as well as various apparatus for aPDT studies, was done using an Autoclave RAU-530D

XX. The homogenization of the bacteria suspension was done using PRO VSM-3 Lab plus Vortex mixer, while a thermostatic oven was used for incubation processes.

XXI. The optical density of the bacteria was determined using a Ledetect 96 scanner from Interscience.

XXII. Scan® 500 automatic colour colony counter was used to evaluate the colony-forming units CFU/mL of the bacteria, and the BMG CLARIOstar® Plus microplate reader was used during Fluorescence measurements for biofilm assay.

XXIII. Irradiation of porphyrins during the aPDT studies was conducted using Modulight 7710 medical laser system fitted with 415 nm Thorlabs LED (M415L4) of 2.2 mW cm^{-2} for 30 and 60 min, i.e., 3.9 and 7.7 J cm^{-2}, respectively.

XXIV. The Gaussian 09 software package [97] was used for quantum computations to derive information about the electronic structures of the synthesised porphyrins. Optimized geometries were generated using density functional theory (DFT) at the B3LYP/SDD level of theory with no added solvation so that trends across the series of complexes can be identified. The CAM-B3LYP functional was used with SDD basis sets to calculate time-dependent DFT (TD-DFT) UV-visible absorption spectra [98,99] , since it contains a long-range correction.

2.3 Synthesis

2.3.1 Synthesis of indium metalated porphyrins

This thesis reports eight new indium porphyrin complexes for the first time, along with six out of eight of their precursors. The synthesis of the known porphyrin precursors, 5,10,15,20 tetrakis- (4-aminophenyl) porphyrin (**1**) and 5,10,15,20-tetra-(4-propargyloxy phenyl) porphyrin (**2**), was conducted according to literature sources [95,96]. The synthesis of 5-(4-pyridyl) dipyrromethane, used in the preparation of *trans*-A_2B_2 porphyrin, has also been documented in the literature [100].

2.3.1.1 Synthesis of chloroindium (III) 5,10,15,20-tetrakis(4-acetamidophenyl) porphyrin (1a), Scheme 3.1

A mixture of glacial acetic acid (80 mL) and **1** (700 mg, 1.04 mmol) was stirred and brought to reflux. $InCl_3$ (690 mg, 3.12 mmol) and sodium acetate (2 g, 25 mmol) were added, and the mixture was allowed to reflux for 72 h. UV-visible absorption spectroscopy and thin-layer chromatography (TLC) were used to monitor the completion of the reaction. The reaction mixture was cooled to room temperature and added to a separating funnel containing dilute ammonia solution and ethyl acetate. The organic layer was collected and evaporated to obtain the crude **1a**. The crude product was dried and then purified by column chromatography using silica gel and a mixture of methanol/chloroform (2:1) to yield **1a** as green-purple. Yield: 895mg (87%): ^{1}H NMR (400 MHz, DMSO-d_6) δ 9.60 (d, J = 5.2 Hz, 4H, amide), 8.10 (s, 8H, β-pyrrole), 7.23 (d, J = 8.2 Hz, 8H, phenyl-*ortho*), 7.16 (d, J = 8.3 Hz, 8H, phenyl-*meta*), 1.33 (s, 12H, methyl carbonyl). MALDI-TOF-MS m/z calcd: 990.19, Found $[M\text{-}Cl]^-$ 956.72. calcd: 1022.827 [M- Cl]. Anal. Calculated $C_{52}H_{40}ClInN_8O_4$: C 63.01 %, H 3.91 %, N 11.30 %. Found: C 63.11 %, H 4.01%, N 11.34%.

λ_{max}/nm , DMF (log ε): 427 (5.41), 559 (4.1), 600 (4.1) . IR [ν_{max}/cm^{-1}]: 3401(N-H), 1666(C=O) and 1588(C=C).

2.3.1.2 Synthesis of chloroindium (III) 5,10,15,20-tetrakis[4-(prop-2-yn-1yloxy) phenyl] porphyrin (2a), Scheme 3.2

A mixture of glacial acetic acid (100 mL) and **2** (720 mg, 1.08 mmol) was stirred and brought to reflux. $InCl_3$ (719 mg, 3.25 mmol) and sodium acetate (2 g, 25 mmol) were then added, and the mixture was allowed to reflux for 72 h. The completion of the reaction was monitored by thin-layer chromatography (TLC) and UV-Vis spectroscopy. Upon completion, the reaction mixture was cooled to room temperature and added to a separating funnel containing a mixture of distilled water and diethyl ether (500 mL). After a thorough shaking, the separating funnel was left to stand for 30 min, and the organic layer was drained and washed several times with water. The organic layer was then collected, and the solvent evaporated to obtain the crude product, which was later purified by column chromatography using silica gel with chloroform/methanol (4:1) mixture as the eluent to yield **2a** as a green-purple product. Yield: 986 mg (93%). ^{1}H NMR (80 MHz, $CDCl_3$) δ 9.10 (s, 8H; H-porph), 8.11 (dd, 8H; H-Aromatic), 7.40 (d, J = 9.0 Hz, 8H; H-Aromatic), 5.01 (d, J = 2.4 Hz, 8H; OCH_2), 2.71 (t, J = 2.4 Hz, 4H; C≡CH). Calc. for TOF-MS m/z calcd: 979.20, Found, $[M\text{-}Cl]^+$ = 943.904, $[M]^+$ = 978.85. Anal. Calculated $C_{56}H_{39}ClInN_7O$: C 68.69 %, H 3.71 %, N 5.72 %. Found: C 67.78 %, H 3.66%, N 5.62%. λ_{max}/nm , DMF (log ε): 432 (5.7), 563 (4.2), 606 (4.1). IR [ν_{max}/cm^{-1}]: 3283, 2849 and 2119 and 1600.

2.3.1.3 5,10,15-Tri-4-aminophenyl-20-(pyren-1-yl)porphyrin (3), Scheme 3.3

A mixture of *p*-nitrobenzaldehyde (8.1 g, 54 mmol), 1-pyrene carboxaldehyde (4.8 g, 21 mmol) and acetic anhydride (6 mL, 64 mmol) in 150 mL of stirring propionic acid was brought to a reflux. Freshly distilled pyrrole (2.5 ml, 37 mmol) was added dropwise, and the mixture was refluxed for 3 h with stirring. The resultant dark brown solution was allowed to cool overnight, and the precipitate was collected by filtration, washed with 300 mL of water and dried. The powdery solid was dissolved in 40 mL of pyridine and refluxed with stirring for 1 h. Afterwards, the reaction mixture was cooled to room temperature and overnight in an ice bath. The precipitate was filtered and washed several times with acetone to obtain a dark purple crude product, which was dried *in vacuo*. The crude product was redissolved in concentrated HCl solution (50 mL) and stirred while heating at about 75 °C for 2 h in a water bath, followed by the slow addition of a solution of $SnCl_2 \cdot 2H_2O$ (9.0 g, 40 mmol) in concentrated HCl. The solution was heated further at about 75 °C for 2 h, then allowed to cool at room temperature, and then placed in an ice bath. The reaction mixture was neutralized with ammonia solution (100 mL, 25%), and the obtained greenish precipitate was filtered and washed with water. The product was extracted from the crude product by Soxhlet using 250 mL of chloroform, and the solvent evaporated to obtain a dark purple crude product, which was purified by column chromatography using silica gel with dichloromethane/methanol (3:1) mixture as the eluent to yield complex **1** as a dark-purple product. Yield: 879 mg (18%). ^{1}H NMR (600 MHz, $CDCl_3$) δ 8.96 – 8.79 (m, 7H, pyrene), 8.52 – 8.31 (m, 8H, β-pyrrole), 8.10 – 7.99 (m, 7H, phenyl and pyrene-*ortho*), 7.68 (d, *J* = 9.4 Hz, 1H, phenyl-*meta*), 7.45 (d, *J* = 9.4 Hz, 1H, phenyl-*meta*), 7.09 – 7.01 (m, 5H, phenyl-*meta*), 4.01 (s, 6H, amino), −2.50 (s, 2H, inner porphyrin ring). MALDI-TOF-MS m/z calcd: 785.3, found: 785.6 $[M+H]^+$. Anal. Calculated ($C_{54}H_{37}N_7$).$2H_2O$: C 79.10 %, H 5.04 %, N 11.96 %. Found: C 79.60 %,

H 4.95 %, N 11.57%. λ_{max}/nm , DMF (log ε): 430 (4.9), 520 (3.2), 558 (3.1), 600 (3.2), 654 (3.8) in DMF. IR [ν_{max}/cm^{-1}]: 3329-3422 (NH_2 -symmetric and asymmetric stretching), 1583(NH_2 - scissoring) and 1663 (C=C).

2.3.1.4 Chloroindium (III) 5,10,15-tri-4-acetamidophenyl 20-(pyren-1-yl) porphyrin (3a), Scheme 3.3

A mixture of glacial acetic acid (50 mL) and complex **1** (300 mg, 0.38 mmol) was stirred and brought to a reflux. $InCl_3$ (270 mg, 1.14 mmol) and sodium acetate (351 mg, 8.7 mmol) were then added, and the mixture was allowed to reflux for 72 h. The completion of the reaction was monitored by thin-layer chromatography (TLC) and UV-Vis spectroscopy. The reaction mixture was then cooled to room temperature and added to a separating funnel containing a mixture of distilled water and diethyl ether (250 mL). After a gentle shaking, the separating funnel was left to stand for 30 min, and the organic layer was drained and washed several times with concentrated sodium hydrogen carbonate and water solution. The organic layer was then collected, and the solvent evaporated to obtain the crude product, which was later purified by column chromatography using silica gel with dichloromethane/methanol (10:1) mixture as the eluent to yield complex **2** as a green-purple product. Yield: 328 mg (81%). ^{1}H NMR (600 MHz, DMSO) δ 10.70 (s, 3H, amide), 9.15 – 8.93 (m, 9H, pyrene), 8.55 (d, 4H, β-pyrrole), 8.21 (d, 4H, β-pyrrole), 8.10 (d, 6H, phenyl-*ortho*), 7.20 (d, *J* = 13.5 Hz, 2H, phenyl-*meta*), 7.12 (d, *J* = 13.9 Hz, 2H, phenyl-*meta*), 7.03 (d, *J* = 13.9 Hz, 2H, phenyl-*meta*), 1.18 (d, *J* = 7.3 Hz, 9H, methyl carbonyl). MALDI-TOF-MS m/z calcd: 1058.30, found: 1057.841 $[M]^+$; calcd: 1022.827 [M- Cl]. Anal. Calculated ($C_{60}H_{41}ClInN_7$). H_2O: C 66.96 %, H 4.03 %, N 9.11 %. Found: C 66.74 %, H 4.27 %,

N 9.01%. λ_{max}/nm , DMF (log ε): 433 (5.1), 567 (4.2), 612 (4.4). IR [ν_{max}/cm^{-1}]: 3246 (N-H stretch), 1670 (C=O) and 1598(N-H bending).

2.3.1.5 General Procedure for synthesis of the A_2B_2 porphyrins (4 and 5), Scheme 3.4

The two porphyrins (**4** and **5**) were synthesized by adding 5-(4-pyridyl)dipyrromethane and each aldehyde (1 mmol equivalent) to methanol (200 mL) contained in a round-bottomed flask, followed by stirring for 5 min. Separately, 50 mL acid solution was prepared by adding 5 mL of concentrated HCl to 45 mL of water in a beaker, which was then transferred to the round-bottomed flask containing 5-(4-pyridyl)dipyrromethane and the aldehydes. The mixtures were stirred overnight. The mixtures were then neutralized with triethylamine (10 mL) and extracted with chloroform. The extracted products were evaporated, redissolved in DMF (100 mL), and refluxed for 6 h while stirring. After cooling, the mixtures were transferred to a beaker and stirred at room temperature for 12 h in the air. UV-visible absorption spectroscopy was used to monitor the completion of the reaction, after which the solvent was evaporated to dryness, and the crude product was purified by silica gel column chromatography.

5,15-bis(4-(*tert*-butyl)phenyl)-10,20-di(pyridin-4-yl)porphyrin (4): Following the general procedure and using 5-(4-pyridyl)dipyrromethane (1.2 g, 5.4 mmol) and 4-*tert*-butylbenzaldehyde (850 µL, 5.4 mmol), compound **4** was obtained as a dark purple solid, Yield: 826 mg (42%): ^{1}H NMR (400 MHz, DMSO-d_6) δ 8.56 (d, *J* = 59.2 Hz, 2H, β-pyrrole), 8.44 – 8.30 (m, 6H, β-pyrrole), 7.44 (d, *J* = 8.5 Hz, 4H, *-ortho*), 7.35 (d, *J* = 4.9 Hz, 4H, *-ortho*), 7.22 (d, *J* = 8.2 Hz, 4H, *-meta*), 6.51 (d, *J* = 13.7 Hz, 4H, *-meta*), 0.93 (s, 18H, *t-butyl*), -3.40 (s, 1H, N–H). MALDI-MS *m/z*: calcd: 728.94, Found [M+2H]$^{\cdot}$ 730.42. Anal. Calculated $C_{50}H_{44}N_6$: C 82.39 %, H 6.08 %, N 11.53 %. Found: C 81.69 %, H 6.13 %, N 11.31%. λ_{max}/nm (log ε) 418 (5.13), 515 (4.32), 551

(3.13), 592 (3.67), 648 (3.22). IR [ν_{max}/cm^{-1}]: (CH) 2951-2860, (C=N, C=C) 1698-1591, 1464 (CH_3), (C-H) 1406 , (C-C) 1278, (C-H) 791.

5,15-di(pyridin-4-yl)-10,20-di(thiophen-2-yl)porphyrin (5): Following the general procedure and using 5-(4-pyridyl)dipyrromethane (2.0 g, 9.0 mmol) and 2-thiophene carboxaldehyde (846 µL, 9.1 mmol), compound **5** was obtained as a dark purple solid, Yield: 1.3 g (46%):, ^{1}H NMR (400 MHz, DMSO-d_6) δ 8.84 – 8.09 (m, 8H, β-pyrrole), 8.03 – 7.84 (m, 4H, pyridinyl-*ortho*), 7.75 (d, *J* = 53.9 Hz, 2H, pyridinyl-*meta*), 7.31 (d, *J* = 45.2 Hz, 2H, pyridinyl-*meta*), 6.63 (d, *J* = 5.7 Hz, 1H, thienyl), 5.80 (d, *J* = 8.2 Hz, 2H, thienyl), 5.62 (d, *J* = 5.6 Hz, 1H, thienyl), 5.10 (d, *J* = 7.0 Hz, 2H, thienyl), -3.31 (s, 1H, N-H). MALDI-MS *m/z*: calcd: 627.16, Found $[M+2H]^{\cdot}$ 629.32. UV–vis (DMSO). Anal. Calculated $C_{38}H_{24}N_6S$: C 72.59 %, H 3.85 %, N 13.37 %. Found: C 71.38 %, H 3.67 %, N 13.09 %. λ_{max}/nm (log ε) 421 (5.66), 518 (4.36), 554 (3.10), 592 (3.31), 650 (3.33). IR [ν_{max}/cm^{-1}]: (CH) 2916-2848, (C=N, C=C) 1601–1509, (C-H bend) 1464, (C-N) 964, (C-H) 797.

2.3.1.6 General synthesis of chloroindium (III) porphyrins (4a and 5a), Scheme 3.4

Mixtures of glacial acetic acid (100 ml) and porphyrins **4** and **5** (0.38 mmol) were stirred and brought to reflux at 120°C. $InCl_3$ (3 equivalent) and sodium acetate (8.7 mmol) were added, and the mixtures were refluxed for 36 h. UV-visible absorption spectroscopy and thin-layer chromatography (TLC) were used to monitor the completion of the reactions. The reaction mixtures were cooled and added to a 500 mL separating funnel containing saturated sodium hydrogen carbonate solution and chloroform. After a thorough shaking, the separating funnel was allowed to stand for 30 min, and the organic phases were collected and evaporated to dryness. The

resulting crude products were then purified by column chromatography using silica gel with chloroform as the eluent.

Chloroindium (III) 5,15-bis(4-(*tert*-butyl)phenyl)-10,20-di(pyridin-4-yl) porphyrin (4a): Following the general procedure and using **4** (277 mg, 0.38 mmol), $InCl_3$ (270 mg, 1.14 mmol) and sodium acetate (351 mg, 8.7 mmol), compound **4a** was obtained as a dark purple solid, Yield: 280 mg (84%): ^{1}H NMR (400 MHz, DMSO-d_6) δ 8.67 – 8.66 (m, 6H, β-pyrrole), 8.35 (s, 2H, β-pyrrole), 7.88 – 7.84 (m, 4H, -ortho), 7.76 – 7.74 (m, 4H, -*meta*), 7.42 – 7.37 (m, 2H, -*ortho*), 7.31 – 7.27 (m, 2H, -ortho), 7.17 (d, J = 7.5 Hz, 2H, -*meta*), 6.46 (d, J = 13.3 Hz, 2H, -*meta*), 1.14 (s, 18H, t-butyl). MALDI-MS *m/z*: calcd: 877.20, Found [M+H]. 878.72. UV–vis (DMSO), Anal. Calculated ($C_{50}H_{42}ClInN_6$): C 68.46 %, H 4.83 %, N 9.58 %. Found: C 67.06 %, H 4.96 %, N 9.39 %. λ_{max}/ nm (log ε) 428 (4.85), 563 (3.28), 604 (2.91). IR [νmax/cm−1]: (C-H) 2959-2850, (C=N, C=C) 1721-1594, 1460(CH3), (C-C) 1276, (C-N) 1007, (C-H) 797.

Chloroindium (III) 5,15-di(pyridin-4-yl)-10,20-di(thiophene-2-yl)porphyrin (5a): Following the general procedure and using **5** (239 mg, 0.38 mmol), $InCl_3$ (270 mg, 1.14 mmol) and sodium acetate (351 mg, 8.7 mmol), compound **5a** was obtained as a dark purple solid, Yield: 268 mg (92%): ^{1}H NMR (400 MHz, DMSO-d_6) δ 8.99 – 8.54 (m, 8H, β-*pyrrole*), 7.90 (s, 4H, pyridinyl -*ortho*), 7.77 (d, *J* = 57.1 Hz, 4H, pyridinyl-*meta*), 7.38 – 7.20 (m, 2H, thienyl-H), 6.61 (d, *J* = 43.8 Hz, 2H, thienyl-H), 6.41 (s, 2H, thienyl-H). MALDI-MS *m/z*: calcd: 776.04, Found $[M\text{-}Cl]^-$ 741.29. UV–vis (DMSO), Anal. Calculated ($C_{38}H_{22}ClInN_6S_2$): C 58.74 %, H 2.85 %, N 14.78 %. Found: C 59.43 %, H 2.78 %, N 14.64 %. λ_{max}/ nm (log ε) 429 (5.02), 565 (3.97), 604 (3.32). IR [ν_{max}/cm^{-1}]: (C-H) 2918-2848, ν(C=N, C=C) 1590–1505, (C-H) 1404, (C-N) 1011, (C-H) 791.

2.3.1.7 General procedure for N-methylation of porphyrins 4b and 5b, Scheme 3.4

An excess of iodomethane was added to a solution of each porphyrin, **4a** and **2a,** in anhydrous DMF (10 mL per 50 mg of porphyrin) under a nitrogen atmosphere and then stirred at room temperature for 24 h with a magnetic stirrer. The solutions were evaporated under vacuum, and the desired products (reddish brown precipitate) were washed with diethyl ether (100 mL) and recrystallized in acetone.

Chloroindium (III) 5,15-bis(4-(*tert*-butyl)phenyl)-10,20-bis(*N*-methylpyridinyl) porphyrin iodide (4b): Following the general procedure and using **4a** (60 mg, 68 μmol) and iodomethane (43 μL, 0.7 mmol), compound **4b** was obtained as a reddish brown crystalline product, Yield: 57 mg (72%): ^{1}H NMR (400 MHz, DMSO-d_6) δ 9.20 (s, 4H, β-pyrrole), 9.03 (d, J = 4.7 Hz, 4H, pyridinyl-*ortho*), 8.91 (d, J = 4.6 Hz, 4H, -*ortho*), 8.75 (s, 4H, β-pyrrole), 7.73 – 7.56 (m, 8H, pyridinyl -*meta*), 4.47 (s, 6H, CH_3), 1.34 (s, 18H, *t-butyl*). MALDI-MS *m/z*: calcd: 1161.07, Found $[(M\text{-}Cl)\text{-}I]^+$ 998.71. UV–vis (DMSO) λ_{max}/ nm (log ε) 433 (4.55), 564 (3.15), 616 (2.78). IR [ν_{max}/cm^{-1}]: (CH) 2956-2806 m, (N^+-CH) 2750 m, (N^+-C) 2413, (C=N, C=C) 1705-1576, 1460 (CH_3), (C-C) 1255, (CN) 1013, (CH) 852.

Chloroindium (III) 5,15-bis(*N*-methylpyridinyl)-10,20-di(thiophen-2-yl) porphyrin iodide (5b): Following the general procedure and using **5a** (60 mg, 77 μmol) and iodomethane (50 μL, 0.8 mmol), compound **5b** was obtained as reddish brown crystalline product, Yield: 76 mg (92%): ^{1}H NMR (400 MHz, DMSO-d_6) δ 9.53 (d, J = 5.9 Hz, 4H, β-*pyrrole*), 9.36 (d, J = 34.5 Hz, 6H, pyridinyl-*ortho* and thienyl), 9.06 (d, J = 6.0 Hz, 4H, β-*pyrrole*), 7.71 (s, 3H, thienyl-H), 6.81 (s, 4H, pyridinyl-*meta*), 5.75 (s, 1H, thienyl-H), 4.75 (s, 6H, CH_3). MALDI-MS *m/z*: calcd: 1061.90, Found $[(M\text{-}Cl)\text{-}I]^+$ 898.71. UV–vis (DMSO) λ_{max}/ nm (log ε) 437 (4.83), 568 (3.44), 613 (3.03).

IR [ν_{max}/cm^{-1}]: (CH) 2957-2811 m, (N^+-CH) 2747 m, (N^+-C) 2412, (C=N, C=C) 1698–1505 m, (CH_3) 1462 m, (C-H) 1405 m, (CN) 1013 m, (C-H) 848 m.

2.3.2 Synthesis of granulated activated carbon and porphyrin 1a conjugate

2.3.2.1 Preparation of coconut-based granulated activated carbon (GAC and ACO)

Note: *Granulated activated carbon (GAC) was used to prepare oxygen-functionalized granular activated carbon (ACO), without combining it with porphyrin.*

To prepare GAC, coconut shells were carbonized using the traditional way of making charcoal in a drum under limited oxygen conditions [101]. After carbonization, the pyrolyzed coconut shells were sorted to remove the partially carbonized shells and then crushed into smaller pieces to a maximum of 50 mm.

Chemical activation was employed using KOH as the activating agent [102] as follows: granular carbon samples (500 g) were washed with 0.1 M HCl to neutralize the ash (formed during carbonization) and then rinsed with Millipore water until the rinse water reached pH 7. Afterwards, the samples were dried in the oven for 12 h at 110 °C. Separately, 500 mL of 50% KOH solution was prepared and then added to a separate 1000 mL beaker containing 300 g of dry carbon granules. The mixture was allowed to soak for complete impregnation of KOH into the inner parts of the carbon granules. After 12 h, the carbon samples were removed from the solution, placed in a nitrogen-purged furnace, and then heated continuously at 800 °C for 4 h under a limited oxygen supply. The samples were allowed to cool overnight and soaked in 0.1 M HCl the next day before washing with Millipore water until the rinse solution reached pH 7. The now-activated carbon granules (GAC) were then placed in an oven to dry for 24 h at 110 °C and finally stored in an airtight container.

Chemical surface modification of activated carbon granules (GAC) to form oxygen-functionalized carbon granules (ACO) was performed as follows: GAC (200 g) was added to 500 mL nitric acid (70%) and refluxed for 4 h. After cooling, the ACO granules were filtered from the acid solution and washed with warm Millipore water until the pH of the rinse water reached the 6−7 range. The ACO granules were then dried in an oven at 110 °C for 48 h and later stored in a sealed glass container.

2.3.2.2 Immobilization of porphyrin 1a on ACO

The porphyrin solution was prepared in a 250 mL flask by dissolving **1a** in ethanol to a final concentration of 0.5 mM. Then, ACO (2 g) was added, followed by refluxing until the solution turned clear (about 45 min). The granules were filtered from the solution, washed several times with water, and dried in the oven overnight at 110 °C. The dried conjugate (represented as **1a** (ACO)) granules were finally stored in an airtight glass container.

2.3.3 Preparation of PAN electrospun fibers decorated with powdered activated carbon (AC) and porphyrin 2a-immobilized composite

Note: *Porphyrin was only combined with PAN/AC2*.

Powdered activated carbon (AC) was prepared by powdering granulated activated carbon (GAC). Homogeneous solutions for electrospinning were then prepared by mixing and sonicating (for 24 h) polyacrylonitrile (10 wt %) with different amounts of activated carbon powder (5% for PAN/AC1 and 10% for PAN/AC2) separately in DMF (20 mL). A separate homogeneous solution was also prepared by sonicating (for 24 h at room temperature) a mixture of PAN (10% wt), AC (10% wt), and **2a** (200 mg) (for **2a**(PAN/AC2) in DMF (20 mL). Unmodified PAN fibers were prepared as described above but without AC or **2a**. Electrospun fibers were obtained under the

following conditions: 0.9 mL/h flow rate, +35 kV applied voltage, and 15 cm tip-to-collector distance. The resulting PAN, PAN/AC1, PAN/AC2, and **2a**(PAN/AC2) fibers were deposited on the collector to form a fibrous mat.

2.3.4 Preparation of colloidal activated carbon (CAC) and porphyrin/CAC composites

AC (2 g) was transferred to a 250 mL flask containing DMF (200 mL) and sonicated for 6 h. The undissolved powder was removed by centrifugation at 4000 rpm for 15 min, and the supernatant was drawn from the centrifuge tubes. Subsequently, the DMF solution was evaporated, and the precipitate was resuspended in DMF to make 150 mL (1 mg/mL) of CAC suspension. The porphyrin/CAC composite solutions of complexes **1a, 2a** or **3a** were prepared by dissolving them in DMF (10 mL) to make a final concentration of 0.5 mM. To each flask, 20 mL of CAC suspension (1 mg/mL in DMF) was added, followed by sonication for 60 min. The porphyrin/CAC composites were then separated from the DMF solution by centrifugation at 15,000 rpm for 15 min and washed with DMF until the solution became clear after centrifugation, indicating the removal of the unbound porphyrin. The precipitates were then dried in the oven, resuspended in DMF, and separately in water.

2.3.5 Preparation of PAN fibers decorated with nitrogen-doped carbon quantum dots and their porphyrin-immobilized composites

2.3.5.1 Synthesis of nitrogen-doped carbon quantum dots (NCQD and NCQD1)

The nitrogen-doped carbon quantum dots (NCQD and NCQD1) was synthesised by varying the quantities of urea and citric acid. This method followed a bottom-up approach involving carbonising organic precursors [103]. Briefly, a 10 mL mixture containing 0.38 g (1 mmol) of citric

acid (CA) and 0.6 g (5 mmol) of urea in water at a ratio of 1:5 was prepared. The mixture was heated on a hot plate at 120 °C until all the solvent evaporated, resulting in a dark brown solid product. After cooling to room temperature, the solid was washed with ethanol, and the resulting brown material (NCQD) was dried in an oven. A similar method was employed to synthesize NCQD1, but with a citric acid to urea ratio of 1:3, yielding a dark brown product.

2.3.5.2 Preparation of PAN and PAN/NCQD electrospun fibers and their porphyrin-loaded composite forms.

Note: *Porphyrins were only combined with NCQD.*

NCQD at 0.5% wt were dispersed in DMF using magnetic stirring for 1 h. PAN powder was dissolved at 10 wt.% in the NCQD/DMF dispersion by stirring and sonication for 24 h at room temperature. A separate homogeneous solution was also prepared by sonicating (for 24 h at room temperature) only PAN (10% wt) powder in DMF. The dispersions were loaded into 20 mL plastic syringes. The applied voltage was kept constant at +35 kV, the flow rate used was 0.9 mL/h, and the distance between the needle and the collector was 15 cm during the electrospinning process. After the stable jet formation, electrospun PAN and PAN/NCQD nanofibrous membranes were collected on aluminium foil, which was removed for fiber characterization.

The porphyrin-loaded PAN/NCQD composites were prepared by first dissolving porphyrins (**1a**, **2a**, **3a**, and **5b**) in 50 mL of ethanol, followed by stirring to ensure homogeneity. The PAN/NCQD fibers were then placed in a round-bottom flask containing the porphyrin-ethanol solution, which was refluxed overnight at 80°C to encourage interaction between the porphyrin and PAN/NCQD fibers. After refluxing, the mixtures were cooled and sonicated for 1 h to disperse the porphyrins evenly throughout the fibers. Subsequently, the composites were washed using a Soxhlet setup

with ethanol and water to remove unattached porphyrin. Additionally, porphyrin **5b** was explicitly used to dye PAN fibers and served as a control material, using a similar method used for all porphyrin (PAN/NCQD) to form **5b**(PAN) composites. Finally, the composites were dried in an oven at 90°C and characterized.

2.4 Photophysical and photochemical parameters

The photophysicochemical properties of the excited states of porphyrins are influenced by their chemical structures, including factors such as the nature of the central metal ion, peripheral substituents, axial ligands, and nonplanar distortions [104]. These properties include fluorescence quantum yields, fluorescence lifetimes, triplet quantum yields, triplet lifetimes, and singlet-oxygen quantum yields.

The porphyrin complexes' fluorescence quantum yields (Φ_F) were calculated in DMF using a comparative method, **Eq. 2.1** by comparing the area of integrated fluorescence of the samples (F_s) with that of a reference (F_{ref}) with known Φ_F, the absorbance values of the sample (A_s) and reference (A_{ref}) at the excitation wavelength (spectral crossover wavelength between the standard and the sample) and refractive indices of the solvents used with the sample (n_s) and reference (n_{ref}) solutions. ZnTPP (Φ_F = 0.034) standards in DMF [105].

$$\Phi_F = \Phi_F^{ref} \cdot \frac{F_s A_{ref} n_s^2}{F_{ref} A_s n_{ref}^2} \qquad (2.1)$$

The singlet oxygen quantum yields (Φ_Δ) of the porphyrin complexes alone were calculated in DMF using a comparative method, **Eq. 2.2**.

$$\Phi_\Delta = \Phi_\Delta^{Std} \cdot \frac{B.I^{Std}}{B^{Std}.I} \qquad (2.2)$$

Where Φ_{Δ}^{std} is the singlet oxygen quantum yield of the standard; B and B^{Std} represent the photobleaching rates of the sample and the standard, respectively; I and I^{Std} represent the rates of light absorption by the sample and standard, respectively. DMA was used as the singlet oxygen quencher in DMF and ZnTPP (Φ_{Δ}^{Std} = 0.53 in DMF) [106].

2.5 Antimicrobial photodynamic therapy (aPDT) Studies

2.5.1 Antimicrobial assays on planktonic bacteria

The aPDT studies were carried out against planktonic cells of Gram-(+) *S. aureus* (ATCC® 25923TM) and Gram-(-) *E. coli* bacteria (ATCC® 25922TM) strains. *S. aureus* and *E. coli* bacteria strains were grown anaerobically on agar plates to obtain colonies of each by following the manufacturer's specifications. A single colony of each strain to be studied was inoculated into a 5 mL freshly prepared Lura nutrient broth. The culture mixture was vortexed and incubated at 37 °C with agitation (*ca.* 200 rpm) in a rotary shaker incubator for 18h and 48 h for *S. aureus* and *E. coli*, respectively. Aliquots from the bacteria culture mixtures were taken regularly to measure their optical densities until the bacterial growth reached a mid-logarithmic phase (OD 620 nm, 0.6-0.8). The bacteria pellets were then harvested through centrifugation for 15 min at 3000 rpm and washed three times with sterile PBS to remove residual nutrient broth. The bacteria pellets were re-suspended in 4 mL PBS and diluted to 1:1000 (*v*/*v*) in PBS to obtain the working bacteria culture stock solutions. The viable colonies count of the freshly prepared *S. aureus* and *E. coli* bacteria stock cultures were determined by serial dilution of the bacteria culture stock solutions by factors of 10^{-4}, 10^{-5}, 10^{-6}, $10^{-7}$and 10^{-8}. 100 µL aliquots of each sample solution were aseptically inoculated on the agar plates in triplicate and incubated at 37 °C for 24 h to determine the optimum bacteria count. The viable bacteria colonies were counted on a Scan 500® series Automatic Colony Counter.

Optimized bacteria solutions of colony-forming units (CFU/mL) about 2.9×10^8 and 1.6×10^8 CFU/mL for *S. aureus* and *E. coli*, respectively, were used in the subsequent studies

The disk diffusion method was used to investigate the bactericidal activity of CAC and the porphyrin/CAC (**1a, 2a** and **3a**) composites. Only the gram-negative *E. coli* was used in the experiments to evaluate the aPDT activities of the colloidal suspensions with and without 0.5 % H_2O_2 solutions. Agar plates were prepared in triplicates for both dark and light experiments. 100 μL of bacterial solution were inoculated on each agar plate, and the CAC and porphyrin/CAC composites (50 μL in water) were individually placed in the respective pre-labelled wells. Plates for light studies were irradiated using a broad-spectrum halogen lamp (range 350 nm to 3500 nm, centred at 552 nm) for 30 min, while the plates for the dark experiment were placed in a dark for the same amount of time. Afterwards, all the plates were incubated for 24 h at 37 °C, and the diameters of the zones of inhibitions were determined.

The colony counting method was used to investigate the aPDT activities of *trans*-A_2B_2 porphyrins (**4a**, **5a**, **4b** and **5b**). 5 mL bacteria suspension ($\approx 10^8$ CFU/mL) of *S. aureus* or *E. coli* bacteria strains in 1% DMSO/PBS solution was incubated with appropriate concentrations of the porphyrin dyes at 37 °C in a rotary shaking incubator at 200 rpm for 30 min in the dark. Half (2.5 mL) of the dye-incubated bacteria suspension was transferred into a 24-well plate for light studies, and the remaining half (2.5 mL) was kept in another 24-well plate in the dark for *in vitro* dark cytotoxicity studies.

During light studies, the porphyrin-treated bacteria suspensions were irradiated with M415L4 Thorlabs LEDs mounted onto a Modulight 7710-680 medical laser system housing for 30 min. 2.5, 5, 10, 20, and 40 μM of the dye concentrations were administered against *S. aureus* and *E.*

coli bacteria suspensions. After light and dark treatments, a 100 μL aliquot of the samples was aseptically inoculated on the agar plate and incubated for 18 h at 37 °C.

Viable bacteria colonies were counted with a Scan 500® series Automatic Colony Counter to determine colony-forming unit (CFU/mL) values. The controls were *S. aureus* and *E. coli* bacteria suspensions (colony-forming units ≈ 10^8 CFU/mL) with no porphyrin dye. The cell survival fractions were calculated by comparing the porphyrin-treated bacteria with the control. The $\log_{10}$ reductions were calculated using **Eq. 2.3**

$$\text{Log reduction} = \text{Log (A)} - \text{Log (B)} \quad (\mathbf{2.3})$$

A and B are the number of viable colonies (CFU/mL) of bacteria for the untreated and treated samples. All the experiments were carried out in three independent triplicates, and data were analyzed statistically using student *t*-tests and ANOVA.

The colony counting method was also used to evaluate the bacteriocidal and aPDT activities of the PAN, PAN/NCQD and porphyrin/NCQD composite fibers (**1a, 2a, 3a** and **5b**). Bacterial cell solutions (50 μL) were dropped to the surface of two 24-well plates containing PAN composites and incubated for 30 min. One plate was placed under a halogen lamp for 30 min, while the other plate remained in darkness (dark treatment) for the same duration. Pure PAN fibers served as control samples. After the treatment, each sample was placed into a 1.5 mL centrifuge tube containing 950 μL PBS. The tubes were subjected to vigorous shaking followed by vortexing in the dark for 3 min to facilitate cell release. Ten-fold serial dilutions were made in PBS (pH 7.4) to test viable cell numbers, and the cells were aseptically inoculated triplicate on the agar plates. The colony numbers were counted after 18 h at 37 °C using the Scan 500® series Automatic Colony Counter.

2.5.2 Anti-biofilm Assay

Antibiofilm activity was evaluated exclusively for the cationic *trans*-A_2B_2 porphyrins (**4a** and **5b**). Freshly prepared planktonic *S. aureus* and *E. coli* bacteria cultures were diluted to 1×10^6 CFU/mL in Mueller–Hinton broth with 1% glucose to stimulate biofilm formation. The nutrient broth-supplemented bacteria cultures (200 µL/well) were added to sterile 96-microwell plates and incubated for 18 h (37 °C, 200 rpm). Following the incubation, the planktonic solution was discarded, and the wells were rinsed with sterile PBS to remove the residual broth and the non-adherent planktonic bacteria cells. The biofilms were then treated with porphyrin samples (4 µL) of different concentrations (25, 50, 100 and 200 µM). Two sets of 96-well plates were prepared for light and dark studies, and untreated samples of only biofilm were also included. In the light studies, 96-well plates were exposed to a 415 nm light from a Thorlabs LED (M415L4) at constant irradiance levels of 2.2 mW cm^{-2} for 30 and 60 min, i.e., 3.9 and 7.7 J cm^{-2}, respectively. The light was integrated into the housing of a Modulight 7710 medical laser system. In contrast, the dark study sets were kept in the absence of irradiation (in the dark) for 30 or 60 min to assess the effect of porphyrins under dark conditions or explore their inherent antimicrobial properties. Afterwards, nutrient broth (196 µL/well) was added to the wells and then incubated for 18 h (37 °C, 200 rpm). Following the incubation, the solution was discarded, and the wells were rinsed with sterile PBS to remove the residual dissolved porphyrin, broth, and non-adherent planktonic bacteria cells. 200 µL of resazurin solution (20 µM/ well) was added to the biofilm plate and incubated for 20 min until the controls were evenly pink (**Fig 2.3**). Fluorescence measurements were taken (λ_{ex} = 560 nm, λ_{em} = 590 nm) using the BMG CLARIOstar® Plus microplate reader. Triplicate measurements were made to ensure accuracy, and the results were compared using a 3-way factorial ANOVA.

The data were presented as means ± standard deviation (SD) of cell survival for the biofilms. A *p*-value of 0.05 was considered statistically significant.

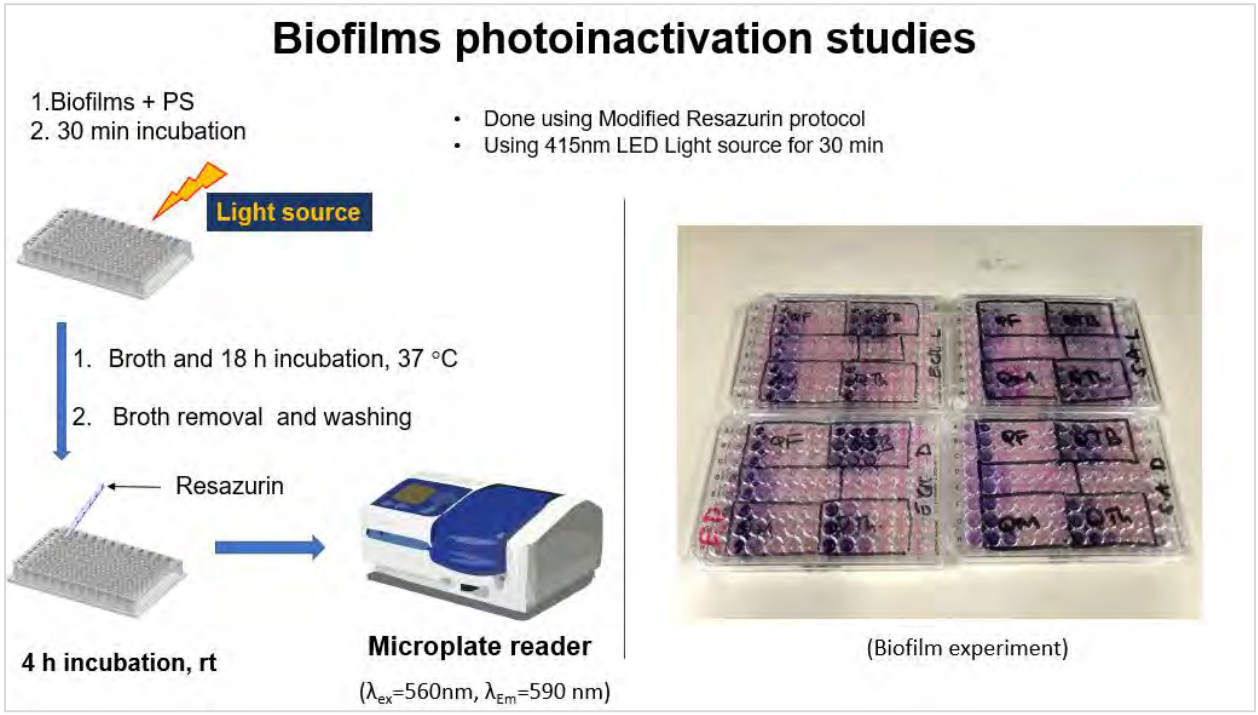

Fig. 2.3: Biofilm photoinactivation studies using modified resazurin method

The cell morphology of *E. coli* biofilms on treated and untreated glass slides was assessed by scanning electron microscopy (SEM). Before observations, biofilm samples were fixed using 3% wt—glutaraldehyde in phosphate buffer pH 7.2 for 8 h at 4°C. After extra washing, the samples were incubated using an increasing percentage of ethanol in water (25, 50, 75, 90, and 100% v/v) for 10 min and dried at room temperature. Finally, the materials were coated with Au-Pd and examined under a JSM 840 scanning electron microscope (JEOL, Tokyo, Japan).

CHAPTER 3: Synthesis and characterization

This chapter details the experimental procedures, synthetic methods, and characterization techniques for all porphyrins and support materials studied in this thesis.

Publications

Chapters **3-6** present findings published or accepted in peer-reviewed journals. The corresponding articles are listed below.

[1] **Oyim, J**.; Amuhaya, E.; Matshitse, R.; Mack, J.; Nyokong, T. Integrated Photocatalyst Adsorbents Based on Porphyrin Anchored to Activated Carbon Granules for Water Treatment. *Carbon Trends*, **2022**, *8*, 100191.

[2] **Oyim, J**.; Amuhaya, E.; Nyokong, T. Activated Carbon-Decorated Polyacrylonitrile Fibers and Their Porphyrin-Immobilized Composites for Removal of Methylene Blue Dye and Ciprofloxacin in Water. *J. Macromol. Sci. Part A*, **2023**, *60*, 192–206.

[3] **Oyim, J**.; Jokazi, M.; Mack, J.; Amuhaya, E.; Nyokong, T. Indium Porphyrin - Colloidal Activated Carbon Composites for Photocatalytic Activity against an Organic Pollutant and Bacteria. *Polyhedron*, **2024**, *253*, 116918.

[4] **Oyim, J**.; Magadla, A.; Mack, J.; Amuhaya, E.; Nyokong, T. Expanding the Horizons of Photodynamic Therapy: Indium Metalated Pyridinyl-Based *Trans*-A_2B_2 Porphyrin as Novel Anti-Biofilm Agents. *Dyes Pigments*, **2025**, *232*, 112448.

[5] **Oyim, J**.; Britton, J.; Amuhaya, E.; Nyokong, T. Photodegradation of organic pollutants and antimicrobial efficacy of porphyrins supported on polyacrylonitrile fibers containing carbon quantum dots: The effect porphyrin functional groups., **In preparation**.

Additional publications not directly related to this thesis

[6] **Oyim, J**.; Omolo, C.A.; Amuhaya, E.K. Photodynamic Antimicrobial Chemotherapy: Advancements in Porphyrin-Based Photosensitize Development. *Front. Chem.*, **2021**, *9*, 123.

[7] **Oyim, J**.; Matshitse, R.; Malomane, N.; Openda, Y.I.; Nyokong, T.; Managa, M. In Vitro Photoinactivation of *S. Aureus* and *E. Coli* Using 5,10,15,20-Tetrakis[4-(Benzyloxy) Phenyl] Porphyrin and Its Metal Derivatives Conjugated to Pristine Graphene Quantum Dots. *J. Porphyr. Phthalocyanines*, **2023**, *27*, 634–644.

[8] Nobatana, V.; **Oyim, J**.; Nwahara, N.; Prinsloo, E.; Nyokong, T. The Potential of Photodynamic Therapy Combined with Hyperthermia Using Porphyrin-Nanomaterial Hybrids against the Triple-Negative Breast Cancer Cell Line. *Polyhedron*, **2024**, 117341.

[9] Nobatana, V.; **Oyim, J**.; Nwahara, N.; Sindelo, A.; Nyokong, T. The photodynamic anti-cancer and anti-bacterial behaviour of *meso*-substituted *trans*-A_2B_2 porphyrin conjugated silica-gold nanoparticles. *Inorganica Chim. Acta*, **2025**, *579*, 122584

[10] Welegergs, G.G.; **Oyim, J**.; Chindeka, F.; Brotton, J.; Yenus, Z.; Maaza, M.; Nyokong, T. Room-temperature synthesized mesoporous Cu_7S_4@Cu-foam hollow nanostructures for photodegradation of organic pollutants. *Optik.*, **Submitted.**

[11] Benise, E.; Centane, S**.; Oyim, J**.; Mashazi, P.; Nyokong, TV. The development of composites of cobalt phthalocyanine with graphene oxide nanomaterials as biosensors for the detection of prostate-specific antigen. *Polyhedron*, **Submitted**

3.1 Synthesis and characterization of the target porphyrins

The precursors **1**, **2** and 5-(4-pyridyl) dipyrromethene used during the synthesis of the *trans*-A_2B_2 porphyrins have been previously reported [95,96,100], and their characterization will thus not be discussed in this work. The characterization of the rest of the new 10 porphyrin and porphyrin complexes is discussed in detail in the following subsections. The respective spectra can be found in the **APPEDICES** section.

3.1.1 Synthesis and characterization of 1a

The procedure to add the acetyl groups along with the In (III) central metal ion to **1** was carried out as illustrated in **Scheme 3.1.** From the ^{1}H NMR spectral data of **1a**, the characteristic broad singlet peak at 9.60 can be ascribed to amide groups. The singlet signal at 8.10 was assigned to the protons on the ß-position of the pyrrolic groups, and the doublets signals at 7.16 and 7.23 were assigned to the protons on *ortho* and *meta*-positions of the benzene rings, respectively. Mass spectra showed M-Cl peak at m/z = 956.72. In the infrared spectra for **1a**, the peak at 3401 cm^{-1} is assigned to stretching vibrations of the N-H groups on the amide groups, while the peaks at 1666 cm^{-1} were assigned to C=O stretching modes of the secondary amide groups of the **1a**. The vibration band at 1588 cm^{-1} was assigned to the C=C stretching modes of the cyclic alkene groups of the porphyrin. (See the respective spectra in **Appendix A**)

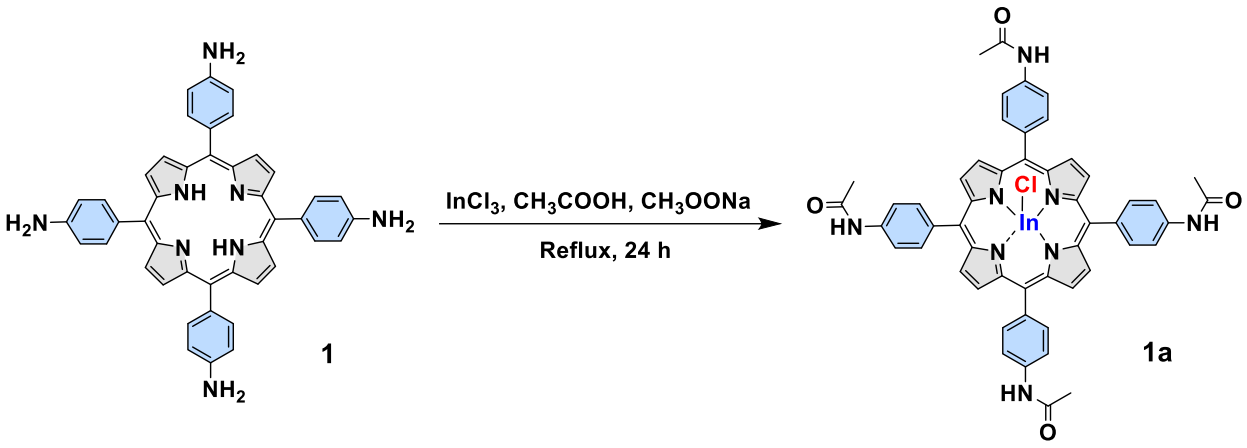

Scheme 3.1: Synthetic route for **1a**

3.1.2 Synthesis and characterization of 2a

Synthesis of **2a** was carried out as illustrated in **Scheme 3.2.** From the ^{1}H NMR spectral data of **2a**, the triplet peak at 2.71 was assigned to the alkyl proton, while the peak doublet peak at 5.01 was assigned to the protons attached to the oxygen group. The singlet signal at 9.10 was assigned to the protons on the ß-position of the pyrrolic groups, while the doublets signals at 8.11 and 7.40 were assigned to the protons on *ortho* and *meta*-positions of the benzene rings, respectively. Mass spectra showed $[M]^{+}$ peak at m/z = 978.85. In the infrared spectra for **2a**, the appearance of the strong, distinct vibration band at 2849 cm^{-1} corresponds to the C-O-C [107], while the peak at 2119 cm^{-1} is assigned to the carbon-carbon triple bond stretch. The peak at 3283 cm^{-1} was assigned to C–H stretch of the C–H bond adjacent to the carbon-carbon triple bonds, indicating the presence of terminal alkyne groups on porphyrin [108]. The vibration band at 1600 cm^{-1} was assigned to the C=C stretching modes of the cyclic conjugated alkene groups on the porphyrin. (See the respective spectra in **Appendix B**)

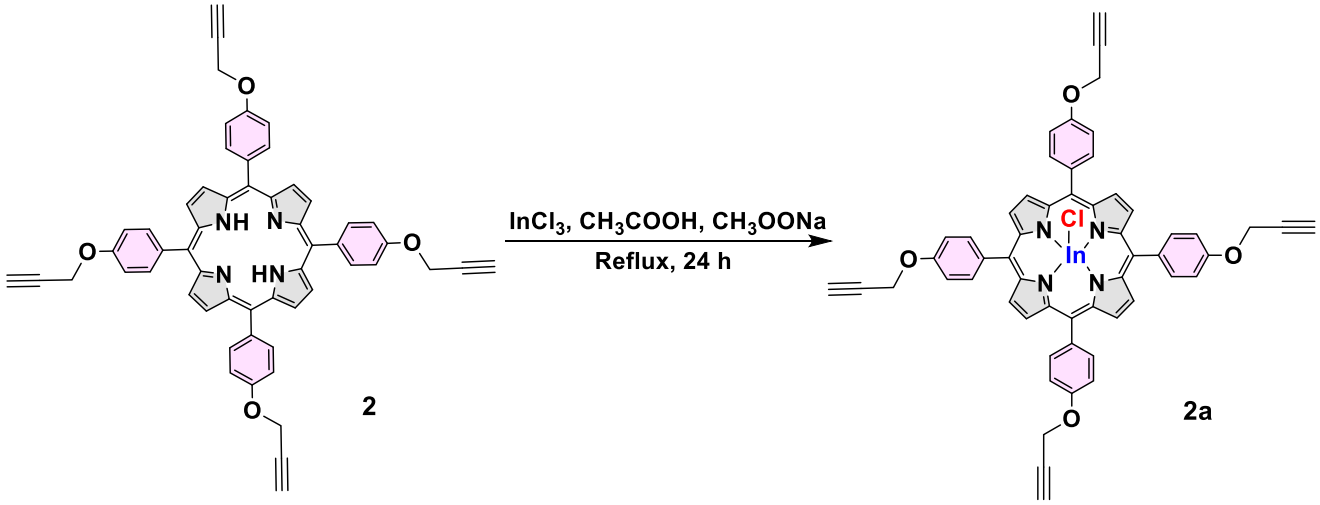

Scheme 3.2: Synthetic route for **2a**

3.1.3 Synthesis and characterization of 3 and 3a

The procedure for porphyrin **3** and complex **3a** is illustrated in **Scheme 3.3**, with the respective NMR and infrared spectra shown in **Appendix C**. From the ^{1}H NMR spectral data of **3**, the peaks at 8.79−8.96 ppm are assigned to the protons of the pyrene group, while the peaks at 8.52−8.31 ppm are assigned to the protons on the ß-positions of the pyrrolic groups. The peaks between 7.99−8.10 ppm are assigned to the protons *ortho* to the benzene rings and position 2 of the pyrene, while the peaks between 7.01−7.68 ppm are assigned to protons *meta*-positions of the benzene rings. The characteristic broad peak at 4.01 ppm is assigned to the NH_2 protons, while the peak at −2.50 ppm is assigned to N-H protons within the porphyrin core.

The disappearance of the N-H protons in the ^{1}H NMR spectrum for complex **3a** is due to the direct bonding of indium metal with the nitrogen groups within the porphyrin core. For complex **3a**, the peak at 10.70 ppm is assigned to the N-H proton of the amide group, while the peaks around 9.15−8.93 ppm are assigned to the pyrene moiety. The peaks between 8.21−8.55 ppm are assigned

to the ß-positions of the pyrrolic groups. The peaks at 8.10 ppm are assigned to protons *ortho* to the phenyl groups, while those between 7.03−7.20 ppm are assigned to protons *meta*-positions of the benzene rings. The singlet peak at 1.18 ppm is assigned to the protons on the acetyl groups. The overall down-field shift of the chemical shifts for complex **3a** relative to **3** can be attributed to the electron-withdrawing effect of the acetyl groups on complex **3a**. The mass spectra of **3** showed $[M+2H]^+$ peak at m/z = 785.62, while complex **3a** showed $[M]^+$ peak at m/z = 1057.84 and fragmentation peaks form $[M-Cl]^+$ at m/z= 1022.83. Elemental analysis confirms that porphyrins are isolated as hydrates [109].

In the infrared spectrum for **3**, the characteristic strong peak at 1583 cm^{-1} is attributed to the in-plane NH_2 scissoring vibration modes, while the vibration band at 1663 cm^{-1} is assigned to the C=C stretching modes of the cyclic conjugated alkene groups on the porphyrin. The vibrational due to the N-H within the porphyrin rings (usually around 3327 cm^{-1}) are masked by the stronger vibrations around 3422 and 3329 cm^{-1}, attributed to the symmetric and asymmetric vibrations of NH_2 groups. In the infrared spectra for **3a**, the peak at 3246 cm^{-1} is assigned to stretching vibrations of the N-H groups of the amide groups, while the characteristic strong peak at 1670 cm^{-1} is assigned to C=O stretching modes of the secondary amide groups of the **3a**. The vibration band at 1598 cm^{-1} is assigned to the N-H bending modes of the amide groups.

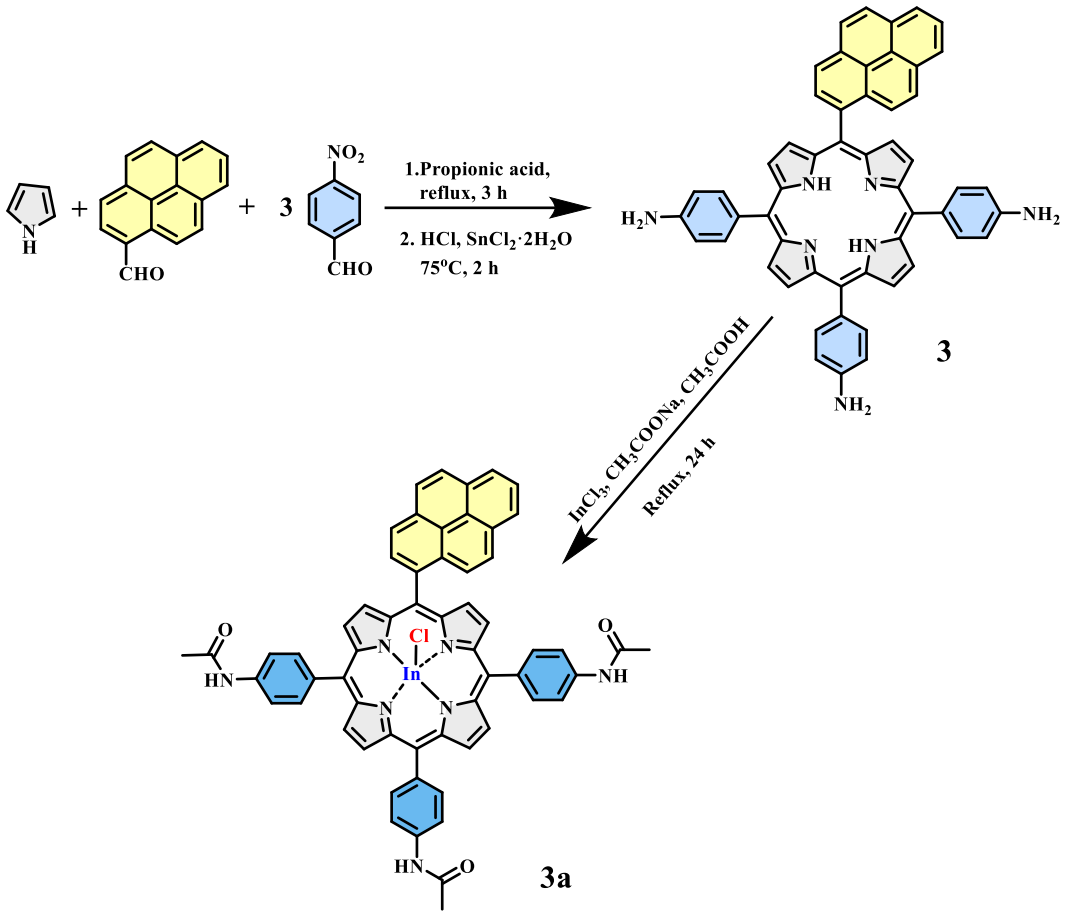

Scheme 3.3: Synthetic route for **3** and **3a**

3.1.4 Synthesis and characterization of the *trans*-A_2B_2 porphyrins (4, 5, 4a, 4b, 5a, 5b)

The free-base pyridinyl-based A_2B_2 porphyrins were synthesized using the green synthesis approach [39], with few modifications for improved yields. The primary step involved the condensation of 5-(4-pyridyl)dipyrromethane with the appropriate aldehyde in water–methanol mixture in the presence of HCl. The mixture was neutralized with TEA, extracted with chloroform, and dried under vacuum. The crude product was then redissolved dimethylformamide (DMF), and refluxed for 6 h, followed by stirring overnight (12 h) in air at room temperature to obtain the respective A_2B_2 porphyrins. Purification of porphyrin was done using column chromatography,

and the porphyrin was obtained in high yields, 46% and 42%, for porphyrin **5** and **4**, respectively. Their indium metal complexes and the methylated forms were synthesized using literature methods [110,111]. **Scheme 3.4** summarizes the synthesis procedure used and the reaction conditions.

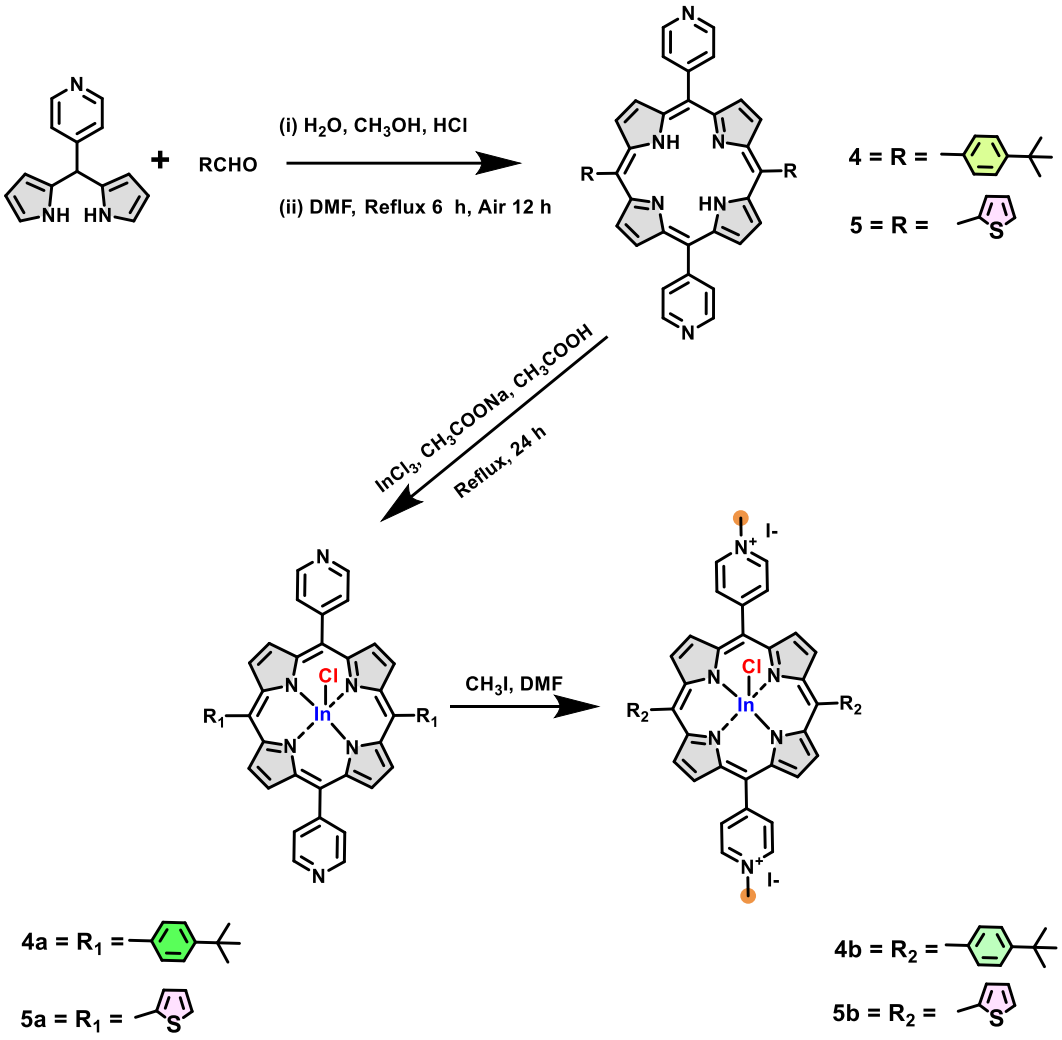

Scheme 3.4: Synthesis of the Indium metalated *meso*-substituted *trans*-A_2B_2-Porphyrins

The compounds were characterized by NMR, IR, UV-Vis and MALDI-TOF MS (See the respective spectra in **Appendix D**), and the acquired data were consistent with the predicted structures. From the ^{1}H NMR, the anticipated protons can be readily assigned for all the complexes.

For the free base porphyrins, the inner protons did not integrate properly. These protons are sometimes not even seen on NMR spectra because of the fast exchange with deuterated solvents.

The β-pyrrole and aromatic protons are for the synthesised porphyrins and the aromatic protons lie between 7.84 to 9.53 ppm. The ^{1}H NMR spectrum of **4**, **4a**, and **4b** have additional peaks in the aliphatic region between 0.93-1.34 ppm from the -CH_3 groups on the *tert*-butyl groups, while the cationic porphyrins **4b and 5b** displayed additional peaks between 4.76-4.25 ppm due to CH_3 groups on the pyridinyl groups. The mass spectral data observed closely matched the expected parent peaks**.** The MALDI-TOF MS data for compounds **4a,b,** and **5a,b** aligned with their respective target structures.

The FTIR spectra of all porphyrins showed strong absorption bands around ~2960 -2850 cm^{-1}, which were assigned to CH stretching modes of the aromatic and aliphatic groups, while vibration bands around ~1405 are due to CH bending vibrations [112]. Additionally, the intense bands observed around ~852–791 cm^{-1} were attributed to the C-H bonds on the pyrrolic rings and more specifically due to vibrations involving deformation of the pyrrole ring with a contribution from the in-plane bending of pyrrolic CH [113]. The spectra were also characterized by the several overlapping bands related to the porphyrin rings modes (C=C, C=N) of the phenyls and pyrrolic groups between ~1721-1490 cm^{-1} [114–116]. The important differences noted included the spectra for cationic porphyrins **4b/5b** which displayed additional strong absorption around ~2750 cm^{-1} assigned to N^{+}C-H. In contrast, porphyrins **4** and **4a** displayed intense absorption bands around ~1278 cm^{-1}, assigned to C-C stretching vibrations of the *tert*-butyl groups [116].

3.1.5 Ground state absorption and fluorescence spectra of the synthesised porphyrins

Fig. 3.1 presents the UV-visible absorption spectra of free-base porphyrins (**1-5**), their metalated counterparts (**4a-5a**), and the metalated-cationic forms (**4b** and **5b**). The corresponding data are summarized in **Table 3.1.** The collapse of the four Q-bands of the free base porphyrins into two Q bands (**Fig. 3.1**) following the metalation confirms the successful insertion of indium metals into the porphyrin core. The spectra of the complexes reveal prominent bands between 418 and 437 nm (the Soret or B band) and weaker absorp tions (the Q or α bands) in the 515–654 nm range, **Table 3.1**. The Soret and Q bands are distinctive signatures in porphyrin absorption spectra [33,117]. Methylation of porphyrins **4a** and **5a** to yield **4b** and **5b** resulted in a noticeable red shift of their Soret and Q (0,0) bands, **Table 3.1**. This spectral alteration can be attributed to the increased nonplanar structural deformation within the porphyrin macrocycles after the quaternization of nitrogen groups [118].

The fluorescence emission spectra of the porphyrins (**Fig. 3.2**) exhibit two distinct bands: a generally intense Q(0,0) band at higher energy and a weaker Q(0,1) band at lower energy. Notably, porphyrin **2a** displayed a more intense Q(0,0) band compared to the Q(0,1) band, in contrast to the other porphyrins, where the Q(0,1) bands were more intense, indicating enhanced vibrational relaxation and internal conversion processes in porphyrin **2a**. All porphyrins showed reduced Stokes shifts upon metalation with indium, suggesting stabilization of the excited states. Acetylation of porphyrins resulted in the highest reduction of Stokes shifts and blue-shifted emissions, highlighting the stabilizing effect of electron-withdrawing groups. Quaternization of **4b** and **5b** led to increased Stokes shifts, attributed to the electron-donating and withdrawing effects of thiophene, tert-butyl, and pyridinium groups [119].

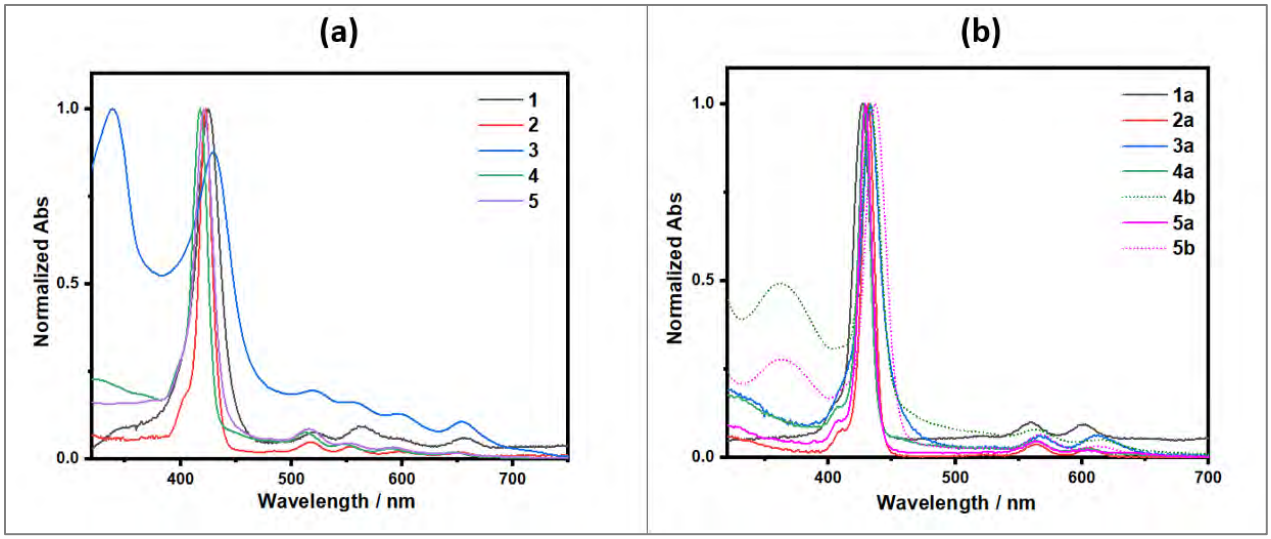

Fig. 3.1: UV-Vis spectra of the synthesised porphyrins

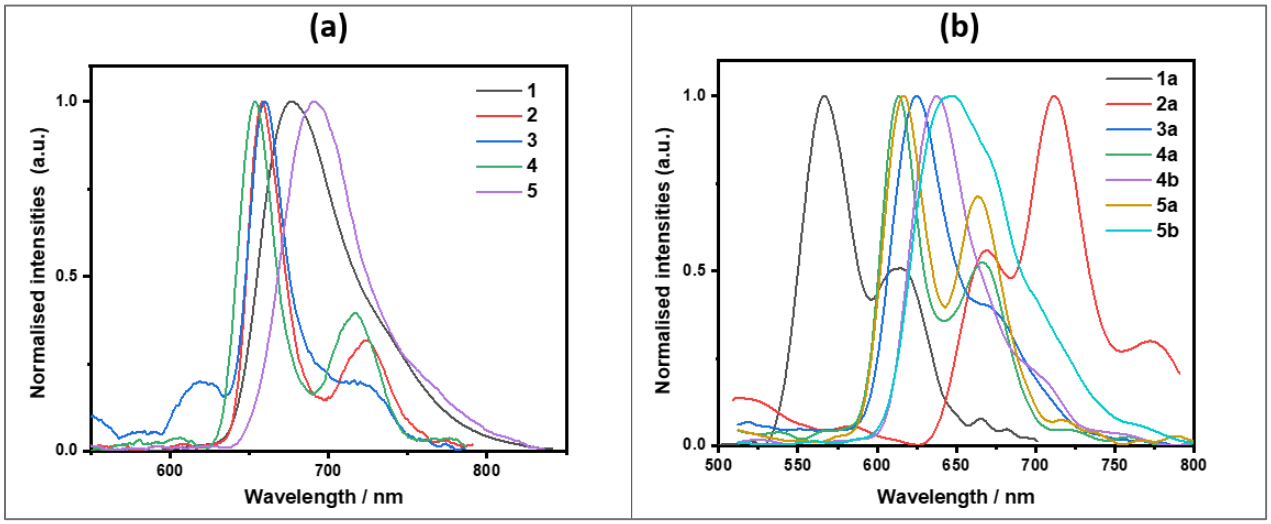

Fig. 3.2: Fluorescence spectra of the synthesized porphyrins

Table 3.1: Photo-physicochemical parameters of synthesized porphyrins in DMF

Compounds	B-bands (nm)	Q-bands (nm)		Stokes shifts
	λ_{Abs} (nm)	λ_{Abs} (nm)	λ_{Em}	(cm^{-1})
1	426	522, 564, 596, 654	676, 715_{Sh}	8681
1a	427	559, 600	567, 614	5783
2	423	518, 555, 599, 651	660, 721	8489
2a	432	566, 606	669,712	8200
3	430	520, 558, 600, 654	660, 720	8104
3a	433	567, 612	625, 673	7095
4	418	515, 551, 592, 648	654, 717	8633
4a	428	563, 604	614, 667	7078
4b	433	564, 616	638, 703_{Sh}	7421
5	421	518, 554, 592, 650	692, 759_{Sh}	9302
5a	429	565, 604	617, 664	7103
5b	437	568, 614	647, 714_{Sh}	7427

Gouterman's four-orbital model [33,120] can be used to explain trends in the electronic excitation spectra of porphyrins. In this case, the model is applied to the indium metalated *trans*-A_2B_2 porphyrins (**4a** and **5a**) and their quaternized complexes (**4b** and **5b**), using a four-orbital arrangement with angular nodal properties (**Fig. 3.3-3.4**), to investigate the effects of quaternization. The highest occupied molecular orbital (HOMO) and lowest unoccupied molecular orbital (LUMO) have M_L values of ±4 and ±5, resulting in four and five angular nodal planes, respectively. The model predicts allowed B transitions ($\Delta M_L = \pm 1$) at high energy and forbidden

Q transitions ($\Delta M_L = \pm 9$) at lower energy. Michl's comparison of MOs [121] uses **a** and **-a** for π-MOs with nodal planes on the y-axis and **s** and **-s** for corresponding MOs with significant coefficients on the y-axis.

The porphyrin orbitals in complexes **4a** and **5a** resemble the widely recognized four Gouterman orbitals that are delocalized across all four pyrrole rings. In the case of complexes **4b and 5b**, the **s** and **-a** orbitals are distributed over the four pyrrole rings and extend to the *tert*-butyl and thiophene groups and on the two-opposing methyl-pyridinyl rings, respectively (**Fig. 3.3-3.4**).

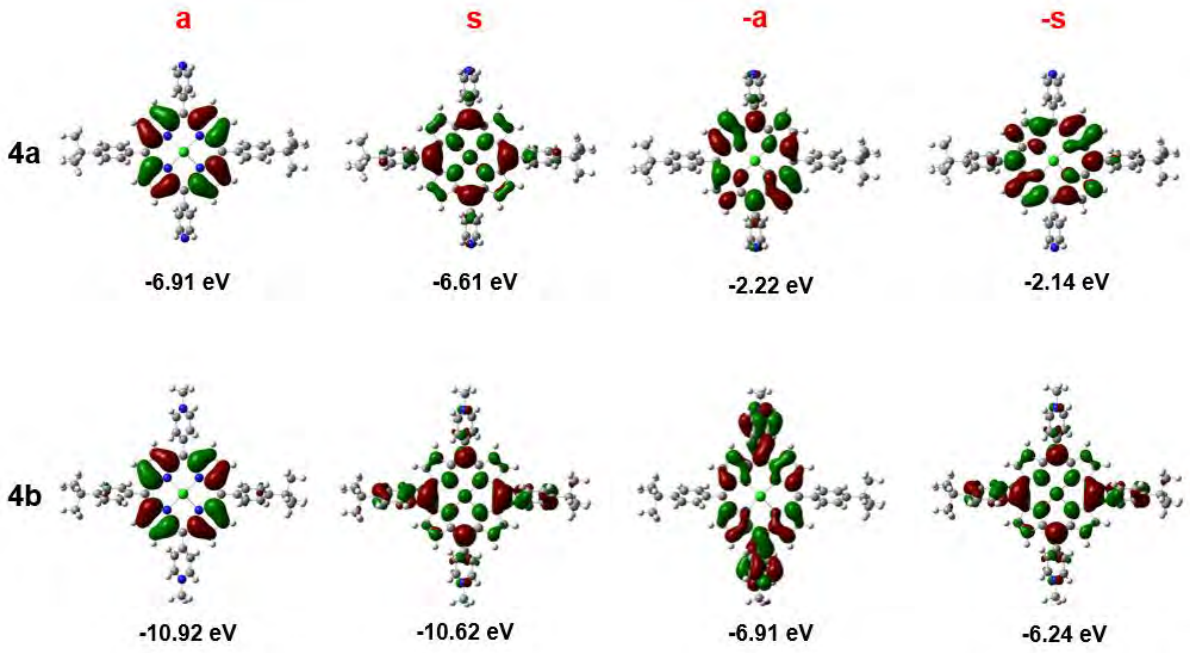

Fig. 3.3: The angular nodal patterns of the **a**, **s**, **-a** and **-s** MOs of **4a,b** at an isosurface value of 0.022 a.u**.**

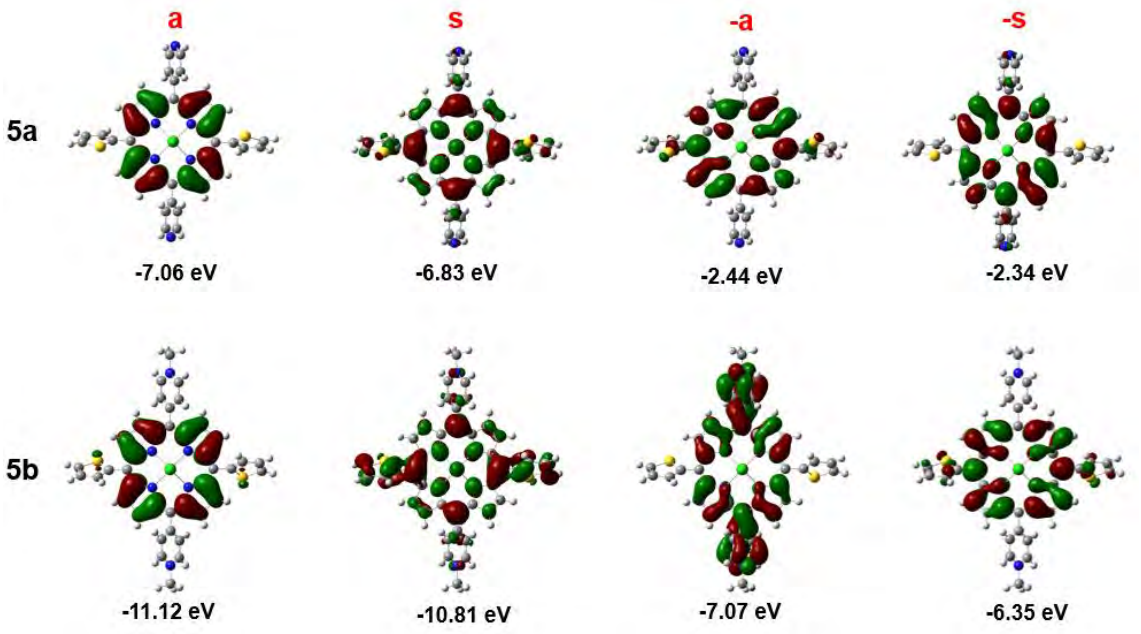

Fig. 3.4: The angular nodal patterns of the **a**, **s**, **-a** and **-s** MOs of **5a,b** at an isosurface value of 0.024 a.u

In the context of the TD-DFT calculations, the frontier π-MOs of **4b/5b** were more stabilized than those of **4a/5a** (**Fig. 3.3-3.4**). In the context of the **4a/5a**, the average HOMO−LUMO gap energies based on a consideration of the **a**, **s**, **-a**, and **-s** MOs associated with the **Q** and **B** transitions are reasonably similar (approximately 4.6 eV) (**Fig. 3.5**). The values for **4a/5a** were also similar to that of the chloroindium (III) tetraphenyl porphyrin (**InTPP**). The choice of **InTPP** as a model complex is due to its similarity to zinc tetraphenylporphyrin (**ZnTPP**), a widely used benchmark molecule in various photochemical studies due to its ease of synthesis and structural resemblance to chlorophyll [122].

In the **4a** and **5a** (**Fig. 3.6, Table 3.2**), the calculated Q and B band maxima are very similar while the main spectral bands of the **4b**/**5b** are red-shifted compared to those of **4a**/**5a** in a manner consistent with the experimental UV-Vis spectra. This shift can be attributed to their lower

HOMO−LUMO gap energies. Additionally, the slightly more intense Q bands observed in complexes **4b** and **5b** are attributed to a slight relative destabilization of their **s** molecular orbitals (**Fig. 3.5**). This results in a larger ΔHOMO value (the energy gap between the **a** and **s** MOs in Michl's terminology [121]), leading to a slight mixing of the allowed and forbidden properties of the B and Q bands. The appearance of charge transfer bands around 30,000 cm^{-1} (**Fig. 3.6**) in the **4b/5b** porphyrins aligns with the experimental UV-Vis spectra. Studies conducted by Cai and coworkers have revealed that non-Gouterman transitions are remarkably responsive to chemical environments, including solvents [123]. The solvent environment significantly modulates the electronic structure and transition energies associated with non-Gouterman transitions, providing valuable insights into the spectroscopic behavior of such complex molecular systems.

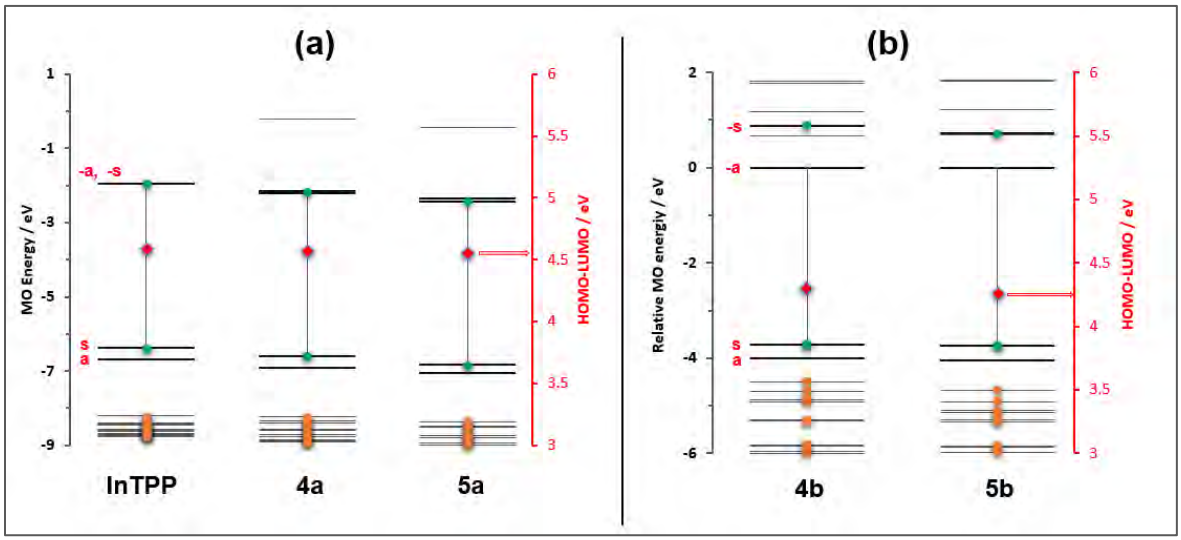

Fig. 3.5: MO energies of (**a**) **InTPP** and **4a** and **5a,** and (**b**) relative MO energies with the LUMO set to 0 eV for **4b** and **5b**. The ΔHOMO−ΔLUMO gap energies are highlighted with red diamonds and are plotted against a secondary axis.

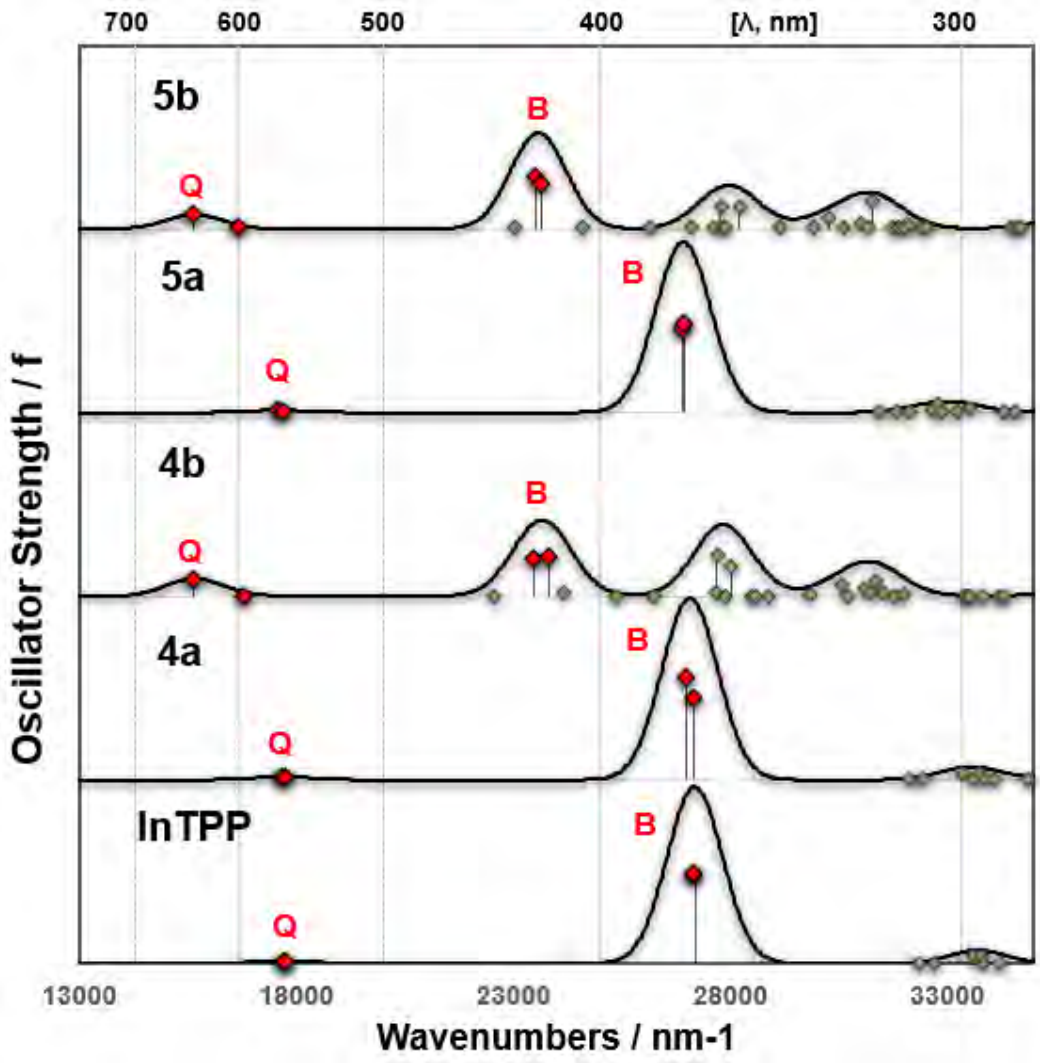

Fig. 3.6: TD-DFT spectra for **InTPP, 4a,b** and **5a,b** using the CAM-B3LYP functional with SDD basis. Red diamonds highlight the Q and B bands of Gouterman's 4-orbital model [33,120]. Spectral simulations were carried out using the Chemcraft software package with a fixed bandwidth of 1500 cm^{-1}. Details of the spectra are provided in **Table 3.2**.

Table 3.2: Electronic excitation bands of **4a,b** and **5a,b** porphyrins at the TD-DFT level of theory using the CAM-B3LYP functional with SDD basis sets.

			Calc.[c]			Exp.[d]		
	Band[a]	#[b]	ν (10^3 cm^{-1})	λ (nm)	f	ν (10^3 cm^{-1})	λ (nm)	Wave Function [c]
4a	Q	1	17.6	567	0.03	16.6	604	**s** → **-a** (61%), **a** → **-s** (37%); …
		2	18.0	563	0.02			**s** → **-s** (57%), **a** → **-a** (41%); …
	B	3	27.0	371	1.55	23.4	428	**a** → **-a** (55%), **s** → **-s** (40%); …
		4	27.2	368	1.91			**a** → **-s** (60%), **s** → **-a** (36%); …
5a	Q	1	17.6	569	0.03	16.6	604	**s** → **-a** (60%), **a** → **-s** (39%); …
		2	17.7	566	0.01			**s** → **-s** (53%), **a** → **-a** (45%); …
	B	3	26.9	372	1.35	23.3	429	**a** → **-s** (34%), **a** → **-a** (23%), **s** → **-a** (22%), **s** → **-s** (19%); …
		4	27.0	371	1.43			**a** → **-a** (31%), **s** → **-s** (26%), **a** → **-s** (25%), **s** → **-a** (16%); …
4b	Q	1	15.7	638	0.29	16.2	616	**s** → **-a** (77%), **a** → **-s** (17%); …
		2	16.8	595	0.01			**a** → **-a** (64%), **s** → **-s** (29%); …
	B	4	23.5	425	0.61	23.1	433	**a** → **-s** (33%), **s** → **-a** (17%); …
		5	23.8	419	0.63			**s** → **-s** (49%), **a** → **-a** (31%); …
5b	Q	1	15.6	639	0.23	16.3	613	**s** → **-a** (75%), **a** → **-s** (20%); …
		2	16.7	600	0.00			**a** → **-a** (59%), **s** → **-s** (36%); …
	B	4	23.5	425	0.85	22.9	437	**a** → **-s** (34%), **s** → **-a** (16%), **a** → **-a** (11%), **s** → **-s** (14%); …
		5	23.6	423	0.76			**s** → **-s** (37%), **a** → **-a** (27%), **a** → **-s** (13%); …

[a] Band assignment referred to in this work. [b] Energy states are assigned in ascending order within the TD-DFT calculation. **B**and energies (**ν**), wavelengths (**λ**), and oscillator strengths are in brackets (f). [c] The wave functions are based on the eigenvectors predicted by TD-DFT. One-electron transitions between the **a**, **s**, **-a,** and **-s** MOs are highlighted in bold. Only contributions greater than 10% are provided.

3.2 Synthesis and characterization of supports and their porphyrin-loaded composites

This section discusses the synthesis and characterization of carbon-based supports and their porphyrin-loaded composites. The focus will be on the methods used to create these support materials and the processes and techniques employed to functionalize carbon supports with porphyrin molecules, primarily through π-π stacking. The analysis techniques used are also discussed.

3.2.1 Anchoring of porphyrin 1a on activated carbon granules

The coconut shells were washed with water to remove the dirt and mud and dried under the sun. The dry shells were carbonized and then crushed into granules (**Fig. 3.7).**

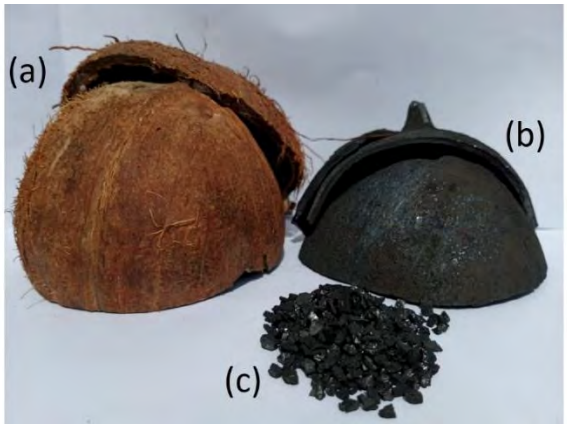

Fig. 3.7: Transformation stages of coconut shell starting from (a) the raw coconut shells to (b) carbonized shells and (c) the granulated form

The granules were transformed into activated carbon by chemical activation to form GAC and afterwards oxidized using nitric acid to increase the amount of oxygen surface groups (to form ACO) and introduce hydrophilic sites on the hydrophobic activated carbon structure, which was deemed essential for improving the adsorption properties of the activated carbon supports.

The synthesized metalloporphyrins were then anchored to the ACO and analyzed. Since the bulk composition of ACO is carbon, hydrophobic interaction (π-π interactions) with the hydrophobic groups of the porphyrin is anticipated for surface adsorption (**Fig. 3.8**). Functionalization of the granulated activated carbon with oxygen groups created hydrophilic centers, presumed essential for anchoring porphyrins through hydrogen bonding.

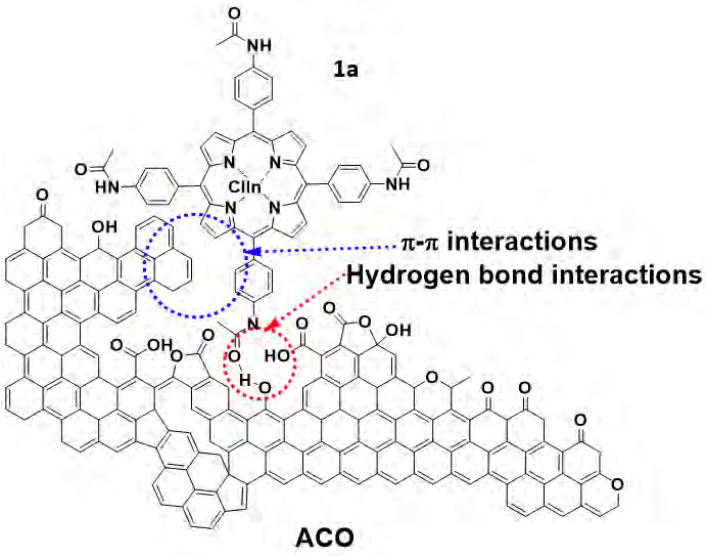

Fig. 3.8: Schematic representation of the possible interactions aiding in the anchoring of **1a** porphyrins

3.2.1.1 Scanning electron microscopy (SEM) and Energy-dispersive X-ray spectrometer (EDS) analysis

Scanning electron microscopy (SEM) was used to study the surface morphology of the activated carbon supports and the porphyrin hybrids. **Fig. 3.9** shows the detailed surface characteristics of the samples. The GAC sample images display different pore structures, including tube-like structures along the surface and the cross-sectional areas of GAC that reveal the porous

characteristics of the GAC structures, **Fig. 3.9(A)**. When GAC samples were oxidised with the acid to form ACO, there was a collapse of most macropores due to the prodding / degrading effects of the acid, which then transformed the GAC surface into a more rugged texture with even more micropore formations, **Fig. 3.9(B)**. The increase of the oxygen peaks (**Fig. 3.10**) and estimated atomic percentage (**Table 3.3**) in the EDS analysis for ACO samples compared to GAC illustrate the successful oxidation process during the oxygen functionalization process. Additionally, the presence of porphyrin molecules is shown by the appearance peaks for elements such as Cl (axial ligand) and In in the **1a**(ACO) spectrum.

Fig. 3.9(C) shows no noticeable changes in the SEM images of ACO samples loaded with **1a** except for some dispersed crystalline clusters around the ACO surface.

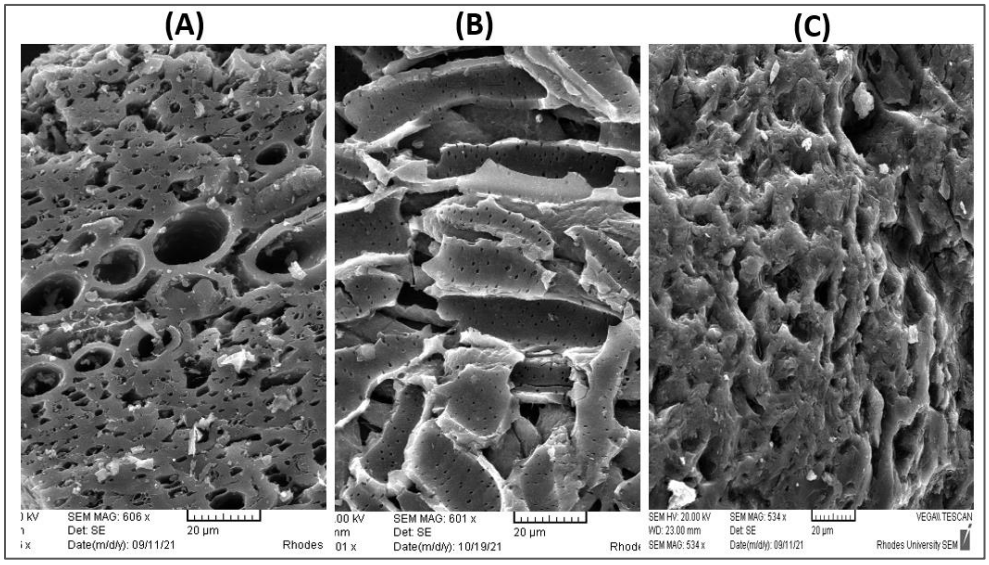

Fig. 3.9: SEM images of the (**A**) GAC, (**B**) ACO and (**C**) **1a**(ACO)

Table 3.3: EDS semiquantitative analysis of samples: GAC, ACO, and **1a**(ACO)

	Samples		
Atomic %	**GAC**	**ACO**	**1a(ACO)**
C	95.01	77.75	83.54
O	4.07	22.25	15.4
In	-	-	0.69
Cl	-	-	0.37

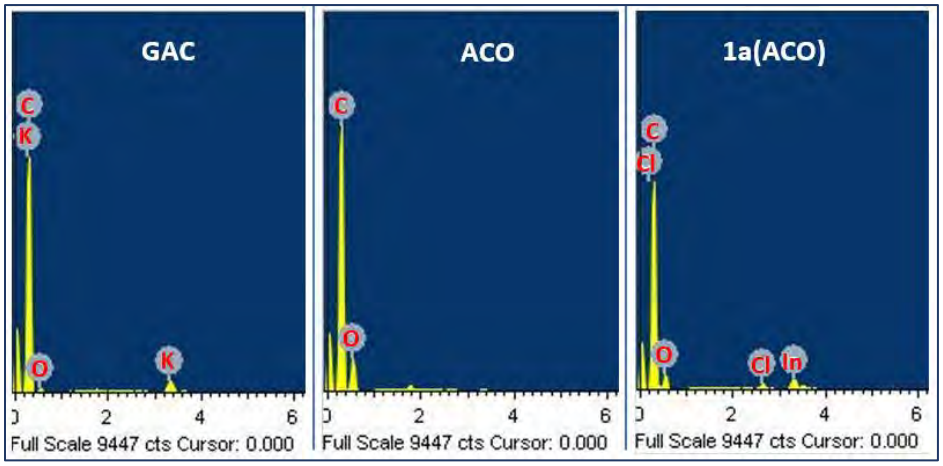

Fig. 3.10: EDS spectra of the samples: GAC, ACO, and **1a**(ACO)

3.2.1.2 Surface Area Analysis

The Brunauer-Emmett Teller (BET) analysis technique was used to monitor the surface changes in surface area (**Fig. 3.11**). The presence of low-pressure hysteresis loops for all the samples, at $P/P_0 < 0.2$, is attributed to possible void-like structures within the carbon structures coupled with narrow pore constrictions that interferes with outgassing [124]. Likewise, the nitrogen adsorption-desorption isotherms displayed blended hysteresis characteristics of H3 and H4 types for all the

samples. The H4 type observed in the GAC is primarily due to nano-porosity, which is common with most activated carbon adsorbents [125]. The acid treatment of GAC introduced oxygen functional groups and increased pore structures, as evidenced by changes in the isotherm plot (**Fig. 3.11**). This plot also shows a slight shift from H4 to H3-type hysteresis loops as the material transitions from AC to functionalized ACO granules. The increased pore structures for ACO also resulted in increased BET surface area, as shown in **Table 3.3**.

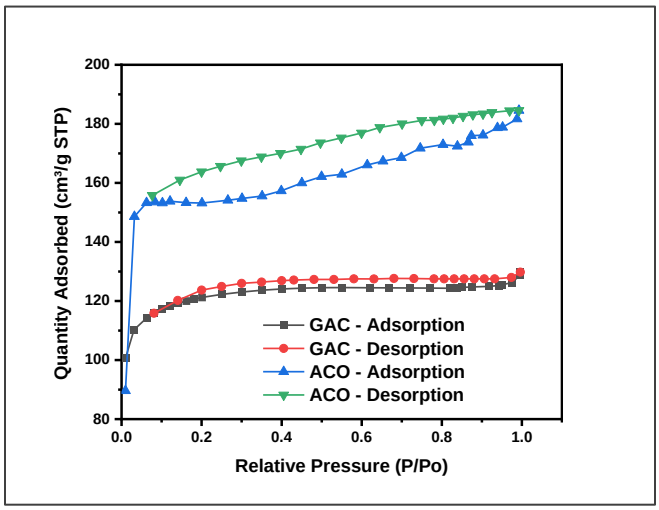

Fig. 3.11: BET Isotherms plots for GAC and ACO granules. P = partial pressure, P_0 = saturation pressure

The BET isotherm plots in the presence of porphyrin did not differ much from the ACO (figure not shown). With the addition of porphyrins, there was an increase in the external surface area and a reduction in the micropore volume (**Table 3.4**). The porphyrin molecules might occupy most of the micropores, thus reducing the micropore volumes and the total surface area of **1a**(ACO).

Table 3.4: BET surface area analysis of GAC, ACO, and **1a**(ACO)

	BET Total Surface Area	**Micropore Volume**	**Micropore Area**	**External Surface Area**
	(m^2/g)	**(cm^3/g)**	**(m^2/g)**	**(m^2/g)**
GAC	369.0	0.15	285.3	83.7
ACO	502.5	0.25	475.1	27.4
1a(ACO)	342.6	0.12	242.5	100.1

3.2.1.3 FTIR Analysis

The Fourier transform infrared (FT-IR) spectroscopy determined the samples' functional groups. The appearance of the strong, distinct absorption peaks around 1716, 1180 and 1080 cm^{-1} (**Fig. 3.12**), corresponding to C=O and C-O and C-O-C groups, respectively [112,126], on the ACO samples confirmed the successful oxygen-group functionalization of GAC, which was also observed on the porphyrin attached-ACO samples. No noticeable changes were observed in respective FTIR spectra of **1a**(ACO), possibly due to the masking of the respective porphyrin functional groups (such as the $-NH_2$) by the much stronger peaks from the bulkier activated carbon supports.

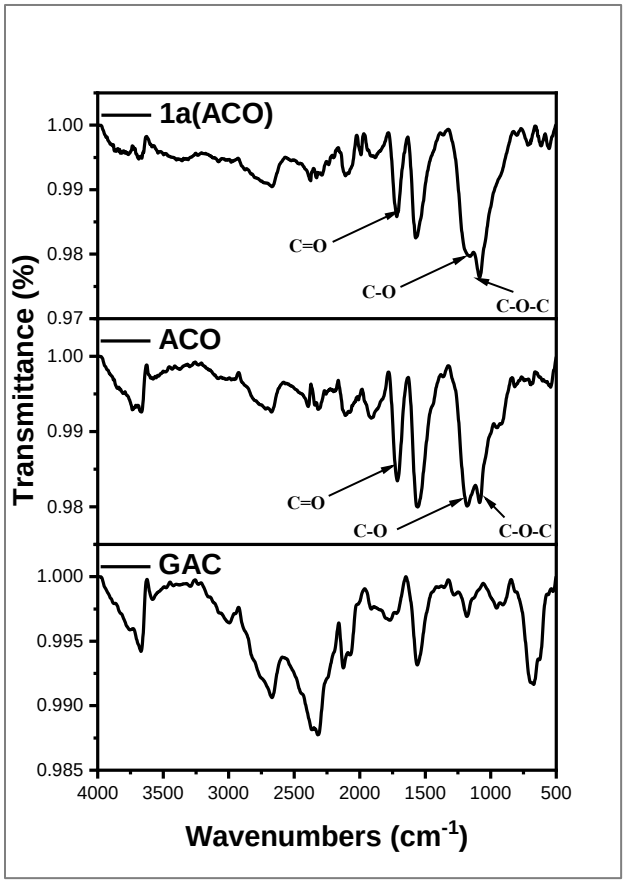

Fig. 3.12: FTIR spectra of AC, ACO, and **1a**(ACO)

3.2.1.4 Raman spectra Analysis

Raman spectroscopy is highly sensitive to structural changes in carbon-based materials, producing characteristic Raman peaks that typically range from 800 to 1200 cm^{-1} [127,128]. Only one first-order graphite band (G band) at ~1580 cm^{-1} is generally observed for highly oriented pure polycrystalline graphitic samples. This band corresponds to the graphitic lattice vibration mode or zone centre phonons of E_{2g} symmetry, involving the in-plane stretching motion of carbon sp^2 atom pairs. However, in disordered graphitic structures, the first-order spectra usually display additional defect bands (D bands) [129]. The D1 band, typically around 1350 cm^{-1}, corresponds to the K-point phonons of A_{1g} breathing mode symmetry and is only active when disorder arises. Other

bands observed in this region include the D2 peak near 1620 cm^{-1}, the D3 peak near 1500 cm^{-1}, and the D4 peak near 1180 cm^{-1} [130].

As shown in **Fig. 3.13**, upon deconvolution of each spectrum, a set of four Lorentzian-shaped bands, denoted by G, D1, D2, and D4) at *ca.* 1580, 1325, 1610 and 1200 cm^{-1}, respectively, were obtained. In the GAC and **1a**(ACO) spectra, the additional D3 bands (*ca.* 1500 cm^{-1}) were also observed, which characterizes first-order Raman spectra for most amorphous carbon. In the ACO spectrum, however, the D3 band seemed masked by the more broadened G band. As anticipated for most amorphous carbon, other peaks around 1400−1500 and 1100−1200 cm^{-1} were also observed in individual Raman spectra. These peaks have recently been associated with other sp^2-bonded configurations with much lower band gaps, such as the *trans*-polyacetylenes types, as opposed to other sp^3-bonded phases [129].

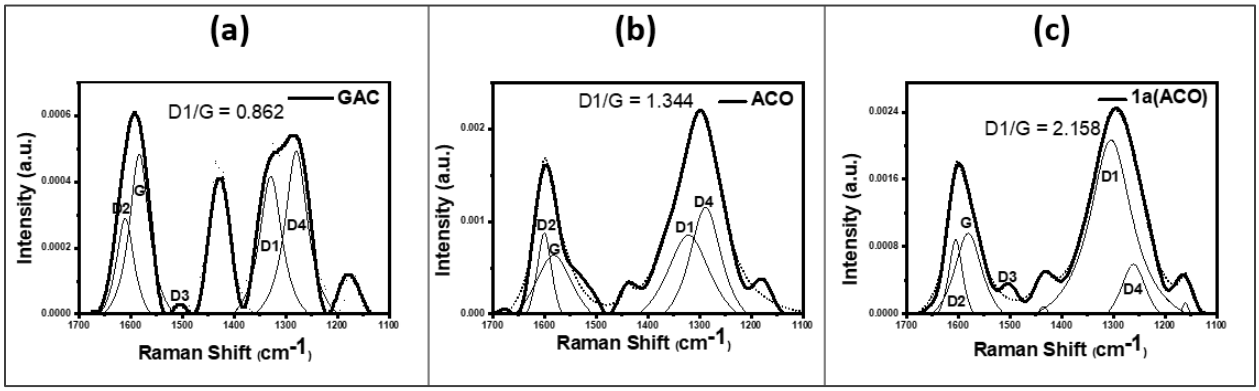

Fig. 3.13: The Raman spectra for (a) GAC, (b) ACO and (c) **1a**(ACO)

The oxygen functional groups introduced some sp^3 (C-O) and sp^2 (C=O) sites, which eventually increased IR Raman activity when moving from GAC to ACO, notably by the increased intensities of the D and G peaks in ACO. Computation calculations have demonstrated that introducing carbonyl groups disrupts electron distribution across aromatic ring systems, constraining the A_{1g} breathing modes of adjacent carbons at *ca.* 1350 cm^{-1}. The significance of such constrictions in

Raman spectra for carbon is the emergence of stronger secondary D peaks and the broadening of the D1 band [131], as observed in this work, where the D2 and D4 peaks are much more intense in the ACO when comparing the intensities. Raman spectrum for porphyrin attached to activated carbon granules showed reduced intensities of D2 and D4 relative to those of ACO. With the introduction of porphyrin compounds, increased disordering was observed, notably from the increased D1/G intensity ratios of **Fig. 3.13c**, attributed to the increased sp^2 sites.

Moreover, since the D mode is solely connected to the presence of six-fold aromatic rings, its intensity is directly proportional to the probability of finding the six-fold aromatic rings in a cluster. The occurrence of other folds results in a broadening of the D mode and a decrease in its intensity [128]. In this case, both events are observed simultaneously: increased intensity and broadening of the D1 mode. These observations are attributed to the increased probability of finding six-fold rings and five-membered rings in the porphyrin compounds.

3.2.1.5 X-ray diffraction (XRD) analysis

XRD analyzed the crystallization degrees of the activated carbon support and porphyrin-loaded activated carbon supports. As expected [132], the two characteristic diffraction peaks of GAC appeared at $2\theta = 22°$ and 43°, corresponding to 002 and 100 surface planes (**Fig. 3.14**). The weak broad 002 peak of the GAC indicated the amorphous nature of its structure. The shift of the 002 diffraction of ACO to higher angles may be attributed to uniform stresses and strains caused by the oxygen functional groups on ACO, which then affect the lattice parameters. The introduction of porphyrin molecules reduced existing strains on the ACO surface because of the interactions between the **1a** porphyrin and ACO supports, as noted in the improved peak symmetry of **1a**(ACO).

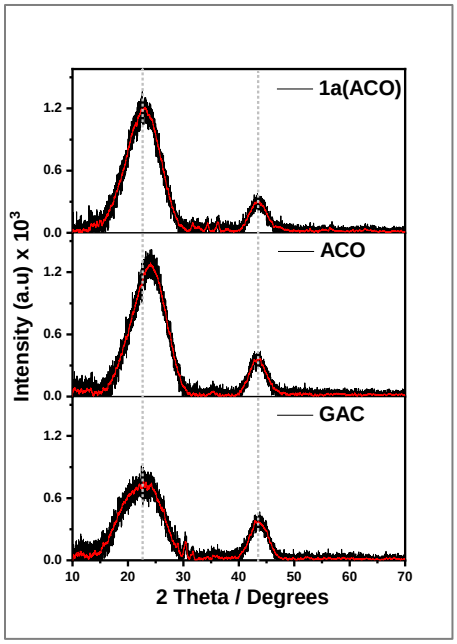

Fig. 3.14: XRD spectra for GAC, ACO, and **1a**(ACO)

3.2.2 Activated carbon-decorated polyacrylonitrile electrospun fibers and their porphyrin-immobilized composites

For application purposes and to eliminate any secondary contamination, all the materials selected to prepare the fibers were insoluble in water, including the photocatalyst porphyrin (**2a**), to prevent leaching or any possible secondary contamination. The electrospinning process of the fibers used in this study was done as shown in **Fig. 3.15**, and the resultant fibers were dried in the oven at 120°C overnight. The **2a**(PAN/AC2) fibers were washed further using chloroform in a Soxhlet setup for 24 h (to remove the unbound porphyrin dye) and then dried in the oven.

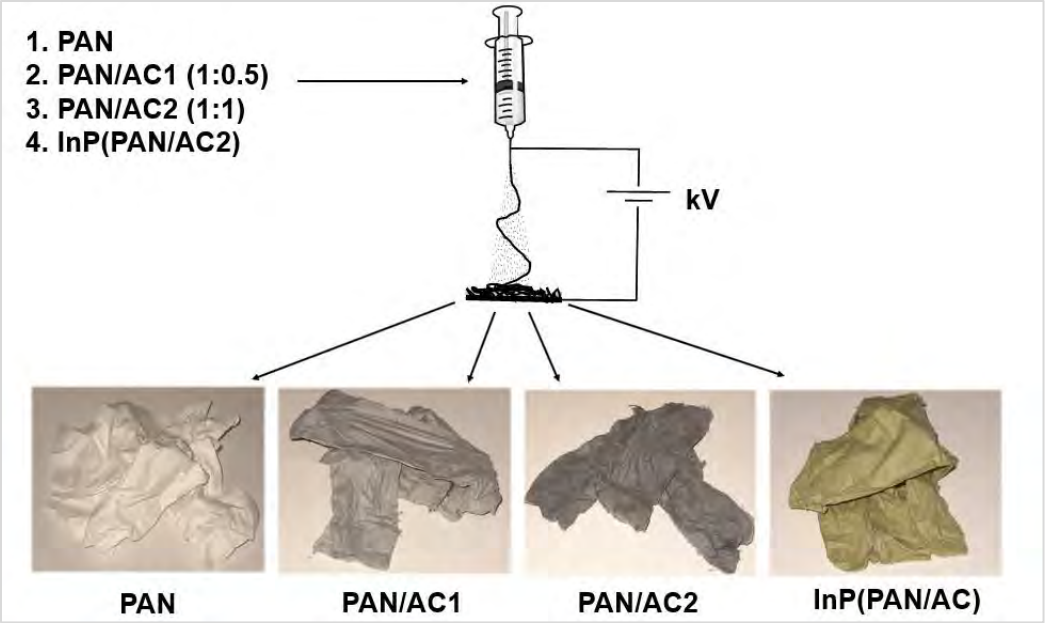

Fig. 3.15: Representation of the electrospinning of PAN, PAN/AC1, PAN/AC2 and **2a**(PAN/AC2) fibers

The PAN fibers displayed the characteristic white colour; however, the ones with activated carbon were grey, with the PAN/AC2 showing a darker shade of grey due to the higher activated carbon percentage. On the contrary, the **2a**(PAN/AC2) displayed a dark green due to the indium porphyrin (**2a**), bound firmly by **π-π** interactions.

3.2.2.1 SEM and BET Surface area analysis

Scanning electron microscopy (SEM) was used to study the surface morphology of the PAN composites (**Fig. 3.16**). The fibers were generally unbranched, smooth, and cylindrical. From SEM images of the PAN fibers with activated carbon (**Fig. 3.16b,c**), the individual spherical activated carbon particles were nested tightly within the PAN fibers, leaving out large surface areas of exposed surfaces of the activated carbon. The fact that the individual carbon particles are held up

tightly explains why no residual AC particles came off the fibers at any point. For **2a**(PAN/AC2), no visible evidence of the presence of porphyrin molecules was observed in the SEM images due to the small size of the porphyrin, and other characterization techniques were further explored and discussed.

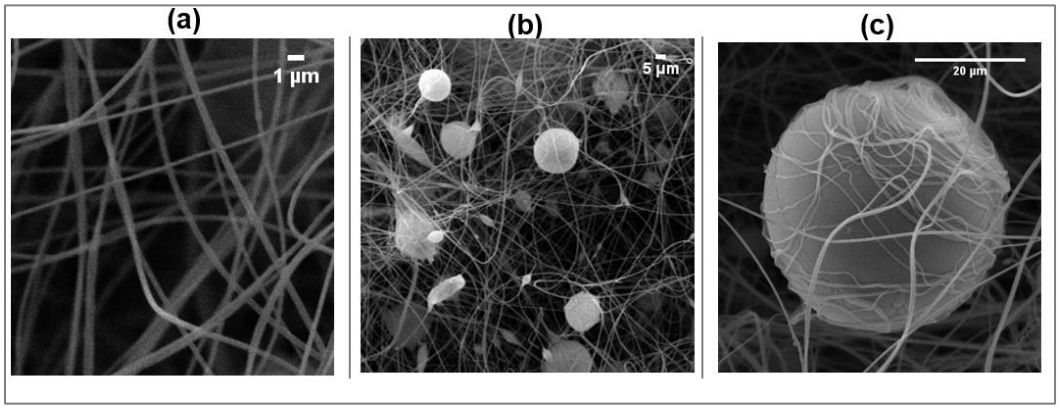

Fig. 3.16: SEM images of the (a) PAN fibres, (b) activated carbon decorated PAN fibres (PAN/AC2) and (c) **2a**(PAN/AC2) fibres

The Brunauer-Emmett Teller (BET) analysis technique was used to determine the surface area and pore sizes (**Fig. 3.17**). Notably, the AC isotherm exhibited a steep increase at relative pressure P/P0 <0.02, typical of type II - type IV combination of isotherms and H3 hysteresis loop, characteristic of particles with both well-developed micropores and mesopores (**Fig. 3.17**). The PAN, PAN/AC1, PAN/AC2, and InP(PAN/AC2) samples (**Fig. 3.17**) displayed type IV isotherms with high-pressure H1 type-hysteresis loops at P/P_0 >0.7, as typical of materials with spherical structures and cylindrical pore geometry.

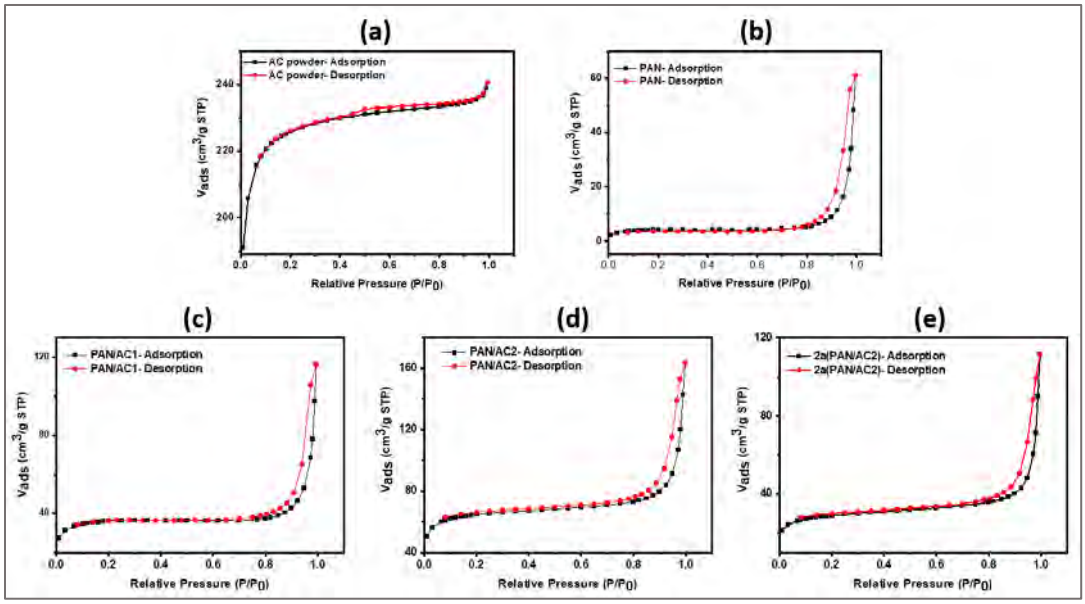

Fig. 3.17: BET Isotherms plots for (a) AC, (b) PAN fibers, (c) PAN/AC1, (d) PAN/AC2 and (e) **2a**(PAN/AC2) fibers. P = partial pressure, P0 = saturation pressure

The activated carbon powder (AC) sample displayed the highest surface area (**Table 3.5**). BET surface area of the PAN fibers increased drastically when activated carbon powder was incorporated within the PAN fabric, **Table 3.5**. The values for BET surface area followed the order: AC > PAN/AC2 > PAN/AC1 > **2a**(PAN/AC2) > PAN. The direct effect of AC powder incorporation is seen by increasing the surface area of PAN/AC composites with increasing activated carbon composition (**Table 3.5)**.

The average pore diameters for the materials are as follows: AC powder (2.5 nm), PAN (28.8 nm), PAN/AC1 (16.1 nm), PAN/AC2 (12.1 nm), and **2a**(PAN/AC2) (16.1 nm), **Table 3.5**. The average pore sizes for the materials show significant variations, with AC powder having the smallest average pore size and PAN the largest. The large pore size in PAN is attributed to interfiber distances. The composite materials, PAN/AC1 and PAN/AC2 have intermediate average pore sizes, reflecting the impact of AC powder on PAN. Notably, PAN/AC2, which contains double

the amount of AC compared to PAN/AC1, has a slightly lower average pore size. The **2a**(PAN/AC2) sample shows a similar average pore diameter to PAN/AC1 despite having double the amount of AC, suggesting that porphyrin is present within the AC pores.

Table 3.5: Specific surface areas (S_{BET}) and pore parameters of PAN, PAN/AC1, PAN/AC2 and **2a**(PAN/AC2)

	AC	PAN	PAN/AC1	PAN/AC2	**2a**(PAN/AC2)
Surface area, S_{BET} / m^2g^{-1}	681.6	12.7	110.0	199.0	91.3
Average pore diameter/nm	2.5	28.8	16.1	12.1	16.1

3.2.2.2 UV-Vis diffuse reflectance analysis.

From the UV-Vis diffuse reflectance spectra of the PAN and composite fibers (**Fig. 3.18**), all samples exhibited absorption in the UV region, at 274 nm, due to polyacrylonitrile polymer [133]. The PAN/AC samples showed weak broad absorbances between 200-650 nm, characteristic of most carbon samples [134]. In contrast, the **2a**(PAN/AC2) sample exhibited strong absorption bands in the visible region, similar to porphyrin spectra, which is evidence of the presence of a high concentration coating of **2a** on the **2a**(PAN/AC2 fibers for efficient visible light photocatalysis application.

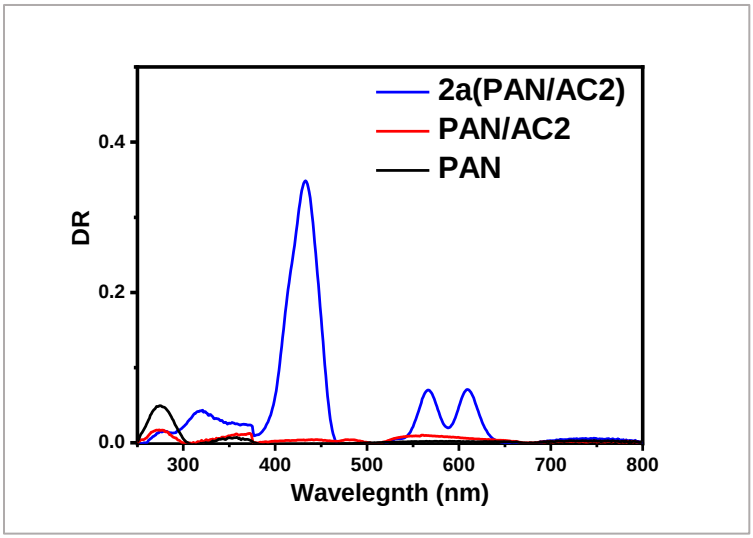

Fig. 3.18: Diffuse reflectance (DR) spectra of PAN, PAN/AC2 and **2a**(PAN/AC2) fibers

3.2.2.3 FT-IR and Raman spectra Analysis

The FTIR spectra of PAN fibers are shown in **Fig 3.19(a)**, with the characteristic peaks at 2938 cm^{-1} (-CH_2 asymmetric stretch), 2243 cm^{-1} from the stretching vibrations of the nitrile group of acrylonitrile, and 1453 cm^{-1} (-CH_2 bending) of the aliphatic vibrations of acrylonitrile [135]. A strong IR band at 1730 cm^{-1}, was also observed, primarily from the carbonyl groups of the methyl acrylate units in the polyacrylonitrile [135,136]. These bands mainly dominated the FTIR spectra of all the PAN composites due to the PAN fiber polymer, which masked all other vibrations from the AC and porphyrin.

The Raman spectrum for AC has been discussed before **(Section 3.2.1.4)**. The Raman spectra pure PAN fiber displayed the characteristic strong peak at 1453 cm^{-1}, which is assigned to CH_2 bending (scissoring), while the peak at 1302 cm^{-1} is assigned to CH_2 twisting mode, thus indicating the presence of a polymer chain (**Fig 3.19b**). The peak at 1357 cm^{-1} is assigned to CH_3 bending (umbrella), while the peaks at 1602 cm^{-1} and 1520 cm^{-1} are assigned to C-C stretching bands. The

characteristic peak around 1114 cm^{-1} is mainly associated with the C-C skeletal stretching [137,138].

As seen in **Fig 3.19b**, the Raman spectra of the PAN/AC2 composites are shifted compared to AC and PAN. For PAN/AC2 sample, the peak at 1583 cm^{-1} is assigned to the G-band peaks, while the characteristic bands at 1342 cm^{-1} and 1280 cm^{-1} are assigned to the carbon disorder bands (D1 and D4) of AC [139]. The peak at 1476 cm^{-1} is assigned to the C=C stretches, and the 1149 cm^{-1} band is assigned to the nanocrystalline structures with sp^3 -diamond bonding [140,141], which are sparsely distributed within the PAN fibers. The presence of porphyrin compounds in the **2a**(PAN/AC2 is evidenced by the porphyrin ring modes; 1594 cm^{-1}, 1483 cm^{-1}, 1373 cm^{-1} [142,143]. According to Parthasarathi and coworkers, the dominant peak at 1373 cm^{-1} is attributed to ν_4 mode (C-N breathing mode), while the bands at 1594 cm^{-1} and 1483 cm^{-1} are attributed to the ν_2 and ν_3 symmetric (A_{1g}) modes [143]. So intense are these peaks that all other peaks have been masked, thus supporting the idea of the possibility of complete porphyrin coverage over the PAN/AC2 support.

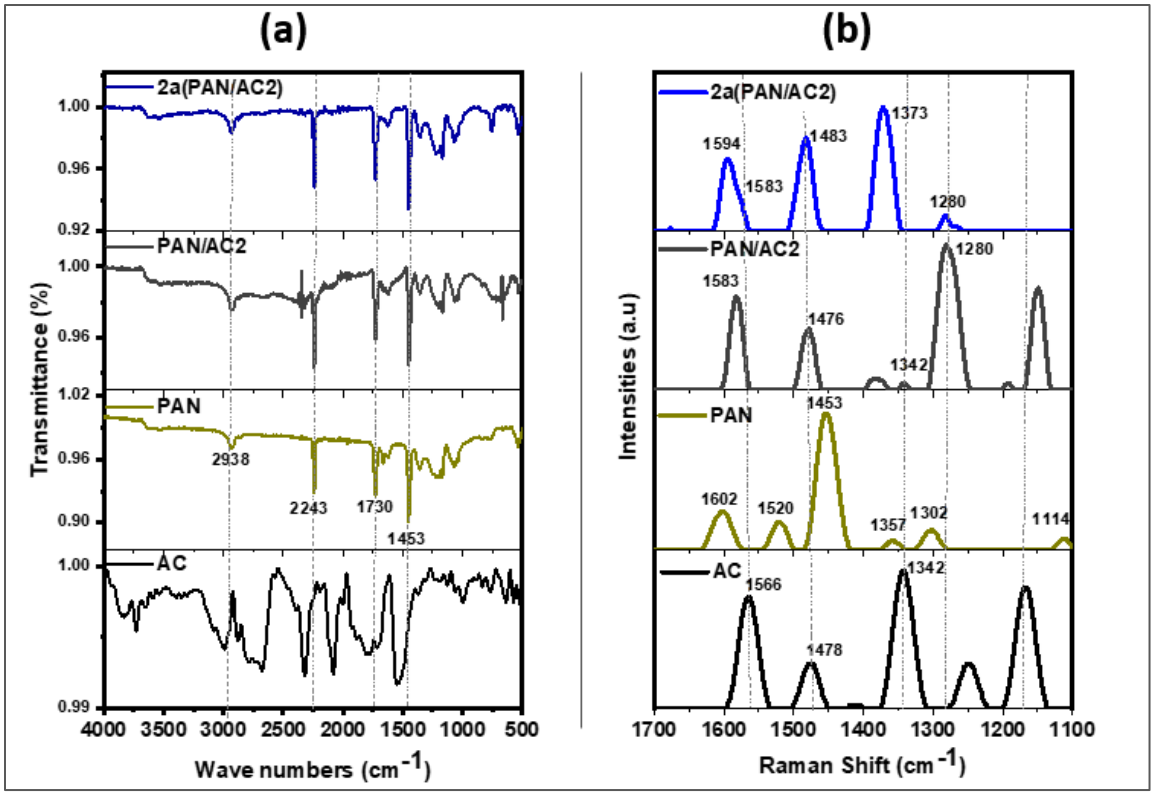

Fig. 3.19: FTIR and Raman spectra of PAN, PAN/AC2 and **2a**(PAN/AC2)

3.2.2.4 X-ray Diffraction analysis (XRD)

The crystal structures of the activated carbon powder, the PAN fibers, and the composites were analyzed by XRD, where the AC powder sample displayed the diffraction pattern with two strong-broad bands at 2θ = 23°, 43° and 78° (**Fig. 3.20**), characteristic of (002), (100) and (110) graphite-type reflections, respectively, of amorphous carbon structure [144,145]. The strong diffraction peaks from the AC sample are due to more disordered graphitic crystallites [146].

The pure PAN fibers diffractograms displayed a strong peak at 2θ = ∼17°, characteristic of the pan (100) crystallographic plane of PAN fibers [147]. Moving from PAN/AC1 to **2a**(PAN/AC2) through PAN/AC2, the respective AC and PAN XRD diffraction peaks diminish to total

disappearance. At the same time, the amount of background scattering increases due to increased amorphization, particularly with **2a**(PAN/AC2) fibers.

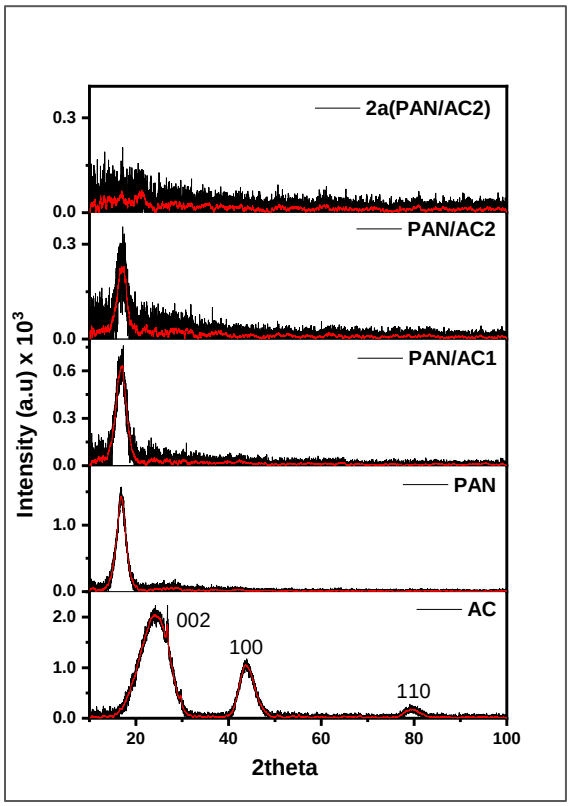

Fig. 3.20: XRD spectra for AC, PAN, PAN/AC1, PAN/AC2 and **2a**(PAN/AC2

3.2.2.5 Thermogravimetric (TGA) analysis

TGA analysis was used to determine the ideal pre-oxidation temperatures and the overall thermal stability of the PAN composites. The TGA curve **Fig. 3.21** shows that the chemical and thermal properties of the PAN fibers were unchanged after impregnation with activated carbon powder and porphyrin. The starting degradation temperature of the PAN fibers and the respective composites ranged from ~289 to ~323 °C. The residual weights of PAN/AC1 (65%), PAN/AC2 (72%), and **2a**(PAN/AC2) (76%) were much higher than the PAN (55%) fibers at 500 °C due to the presence

of the more thermally stable activated carbon. The weight loss between 50 and 150 °C by the activated carbon powder (AC) was mainly due to moisture loss, with a similar trend also observed with the PAN/AC composites.

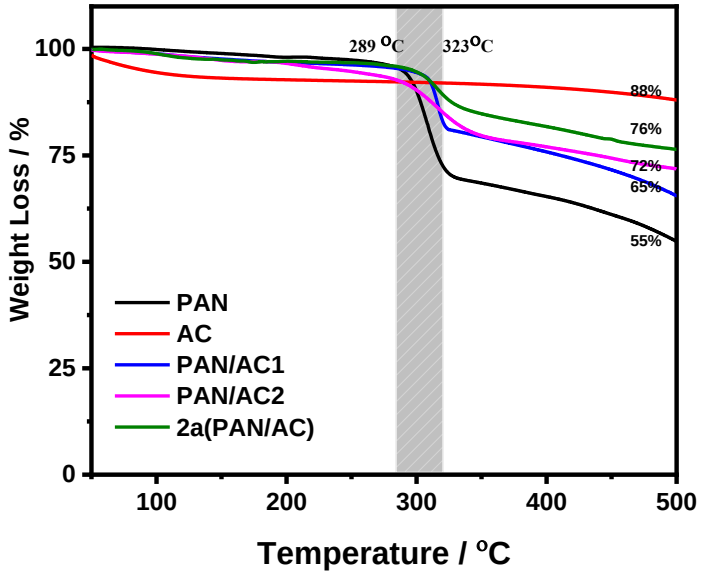

Fig. 3.21: TGA curves for PAN, AC, PAN/AC1, PAN/AC2 and **2a**(PAN/AC2)

3.2.3 Colloidal activated carbon (CAC) and porphyrin-loaded CAC

The CAC and the porphyrin-loaded CAC were prepared as described in the previous chapter (**Chapter Two**). The CAC and the porphyrin/CAC suspension generated from the AC were very stable in DMF after more than 48 h (**Fig. 3.22**). There was no noticeable change in colour between the unloaded CAC and the porphyrin-loaded CAC samples. The porphyrin composition was determined using UV-Vis spectroscopy by comparing the initial porphyrin solutions with the supernatants. The percentage composition of porphyrins loaded (w/w) on the composites was thus calculated as 1.0%, 1.4%, and 1.2% in **1a**/CAC, **2a**/CAC and **3a**/CAC, respectively. UV-Vis

spectra for the porphyrin/ CAC showed no differences in the Soret band maxima of the three complexes in DMF, **Fig 3.22b.**

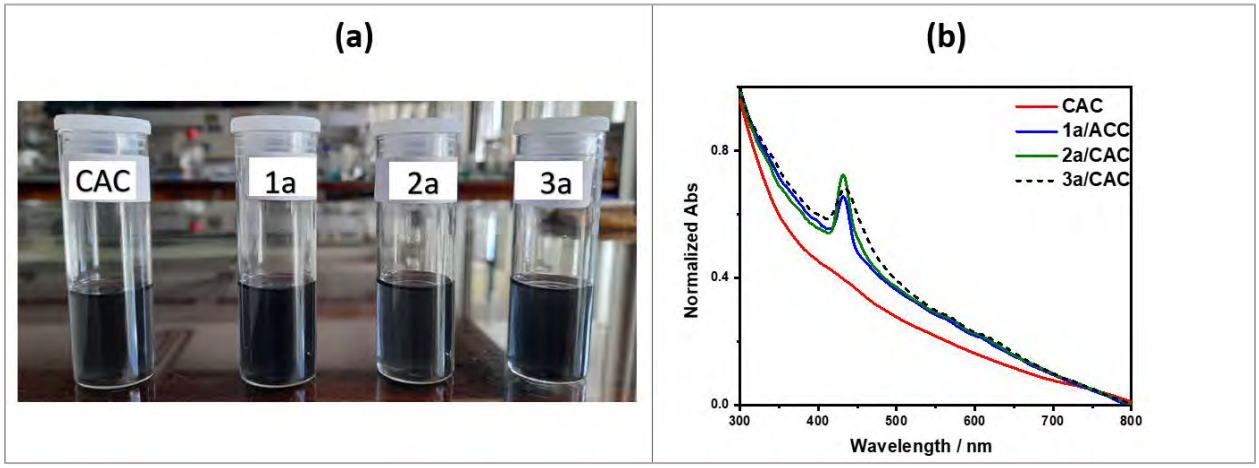

Fig. 3.22: (a) CAC and Porphyrin/CAC suspensions in DMF after 48 h, and (b) absorption spectra of CAC, **2**/CAC, **3**/CAC, and **4**/CAC suspended in DMF

The surface morphology of the CAC composites was studied using scanning electron microscopy (SEM) (**Fig. 3.23a,b**). The colloidal activated carbon particles had irregular forms because of the numerous micropores and cracks within their structures. Due to the small size of the porphyrin, no visible indication of their presence was seen in the SEM of porphyrin/CAC composites (figure not shown). SEM analysis revealed that the particle sizes of CAC were mainly less than 1 μm (**Fig. 3.23a,b**). The dynamic light scattering (DLS) analysis further corroborated the SEM results, which revealed that the particle size distribution of CAC and porphyrin/CAC composites had an average of 140 nm. The polydispersity indexes (PDI) of CAC, **1a**/CAC, **2a**/CAC and **3a**/CAC were determined as 0.25, 0.18, 0.21 and 0.19, respectively, indicating a broad particle size distribution of the colloids [148].

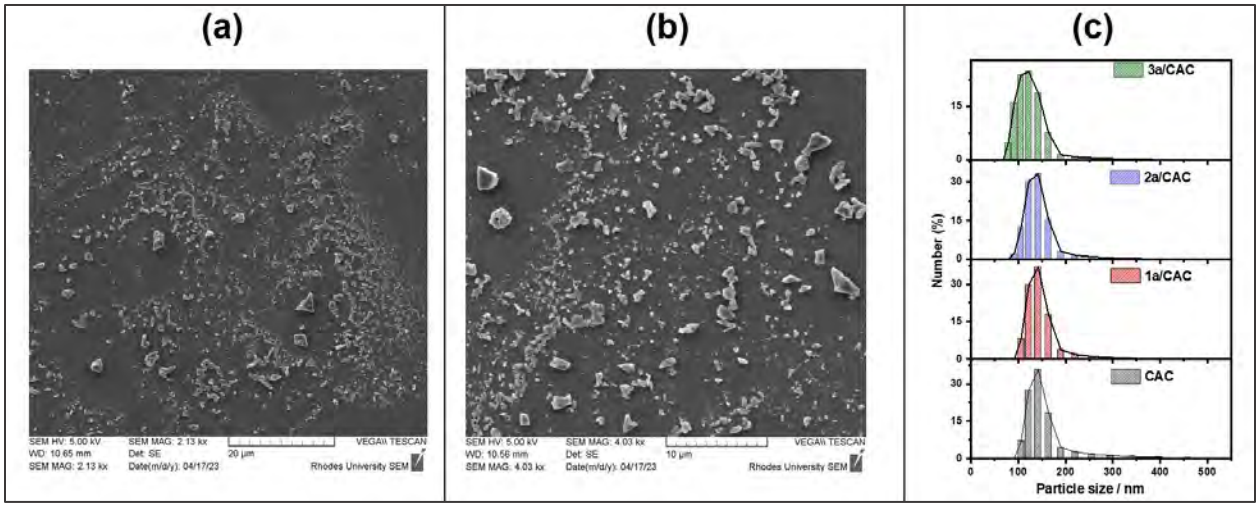

Fig. 3.23: SEM images of CAC on a glass substrate; (a) wider view, (b) expanded view (samples for SEM prepared as explained in the Supporting Information), and (c) DLS particle size distribution of the CAC, **1a**/CAC, **2a**/CAC, and **3a**/CAC suspended in water.

3.2.4 Anchoring of porphyrins on polyacrylonitrile fibers containing carbon quantum dots (PAN/NCQD)

3.2.4.1 Synthesis and characterization of nitrogen-doped carbon quantum dots

The N-doped carbon quantum dots, NCQD and NCQD1, was synthesised using a bottom-up synthesis method as demonstrated in **Fig. 3.24**, using citric acid as a source of carbon and urea as a nitrogen source.

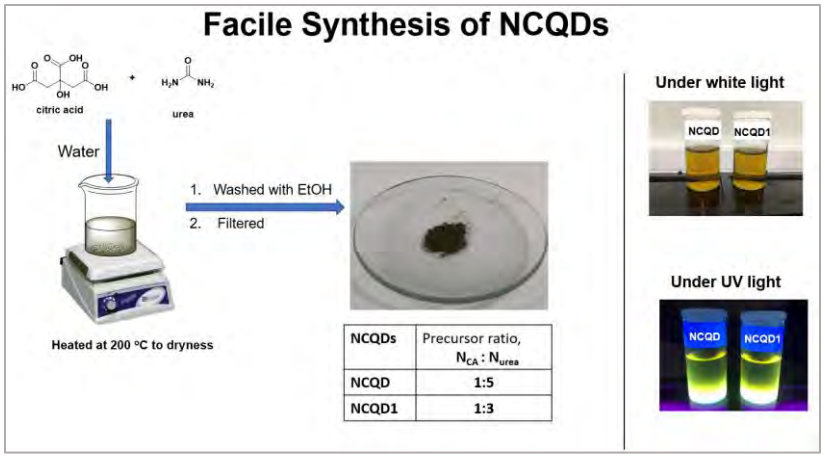

Fig. 3.24: Representation the bottom-up synthesis of nitrogen-doped carbon dots (NDCQD) employed in this work. EtOH = ethanol

The X-ray diffraction (XRD) pattern of N-doped carbon quantum dots (NCQD and NCQD1) exhibited broad peaks centred around 2θ = ~27° (002 plane) [149]. These peaks correspond to the coherent and parallel stacking of graphene-like sheets. The broadness of these peaks confirms the amorphous nature of NCQD and NCQD1. Generally, heteroatom (N) doping in graphene introduces defect sites and disrupts the carbon lattice, reducing crystallinity [150]. Consequently, the XRD peak associated with NCQD is less intense than NCQD1 due to the higher concentration of nitrogen atoms within the carbon core lattice of the former (as observed in **Fig. 3.25a**).

The Raman spectrum of NCQD and NCQD1 (**Fig. 3.25c**) reveal distinct sp^2 carbon characteristics with notable disorder. The disordered D band appears prominently at 1379 cm^{-1} for NCQD and NCQD1, while the crystalline G bands are observed at 1581 cm^{-1} and 1585 cm^{-1} for NCQD and NCQD1, respectively. The intensity of the G band is not affected by defects, whereas the defects enhance the D band, increasing the intensity ratio between D and G (I_D: I_G ratio). The I_D: I_G ratio for NCQD is 5.2, while the value is 2.1 for NCQD1. As stated above, introducing heteroatom (N) in graphene introduces defect sites; hence, NCQD with more N atoms has more defects. Nitrogen doping of carbon compounds results in the appearance of additional peaks [151], as observed in

Fig. 3.25c. According to Ayiana and coworkers, heteroatoms induce active vibrations in the region between 1400 and 1550 cm^{-1}, explaining the presence of Raman peaks at 1480-1496 cm^{-1} in both NCQD and NCQD1. The region between 1250 and 1320 cm^{-1} is fundamentally associated with the breathing mode of defective polycyclic aromatic hydrocarbons (PAHs) [151]. These vibrations are typically intense in the presence of functional groups like graphitic nitrogen, which accounts for the observed peaks at 1270-1280 cm^{-1} in both NCQD and NCQD1. Specifically, the Raman bands at ~1270 cm^{-1} have been attributed to trans-polyacetylene and N-doped polyacetylene-like systems [129,152]. These bands exhibited higher intensities in NCQD than NCQD1, suggesting a greater presence of π-conjugated units in NCQD. Additionally, NCQD exhibited an intense Raman band at approximately 1167 cm^{-1}, attributed to the breathing mode of 8-membered-like nitrogen-containing rings, which typically appear between 1150 and 1200 cm^{-1} [151].

The chemical and structural characteristics of the NCQD (NCQD and NCQD1) were further elucidated using Fourier-transform infrared (FTIR) spectroscopy. Several key vibrational modes were observed in the FTIR spectrum (**Fig. 3.25b**): Peaks centred near 3433 cm^{-1} correspond to the stretching vibrations of –OH and –NH groups. The peaks around 3008-3184 cm^{-1} are due to the C–H stretching vibrations of sp^2 hybridized carbons, while peaks at 2772 cm^{-1} correspond to C–H stretching vibrations of sp^3 hybridized carbons. The successful surface passivation and nitrogen doping were confirmed by C-N/N-O stretching vibrations at 1360 cm^{-1}. Additionally, vibration peaks at 1701, 1582, and 1184 cm^{-1} are assigned to C=O vibration, C=C stretching/N-H bending of a primary amine, and C–O stretching of an ester or ether, respectively.

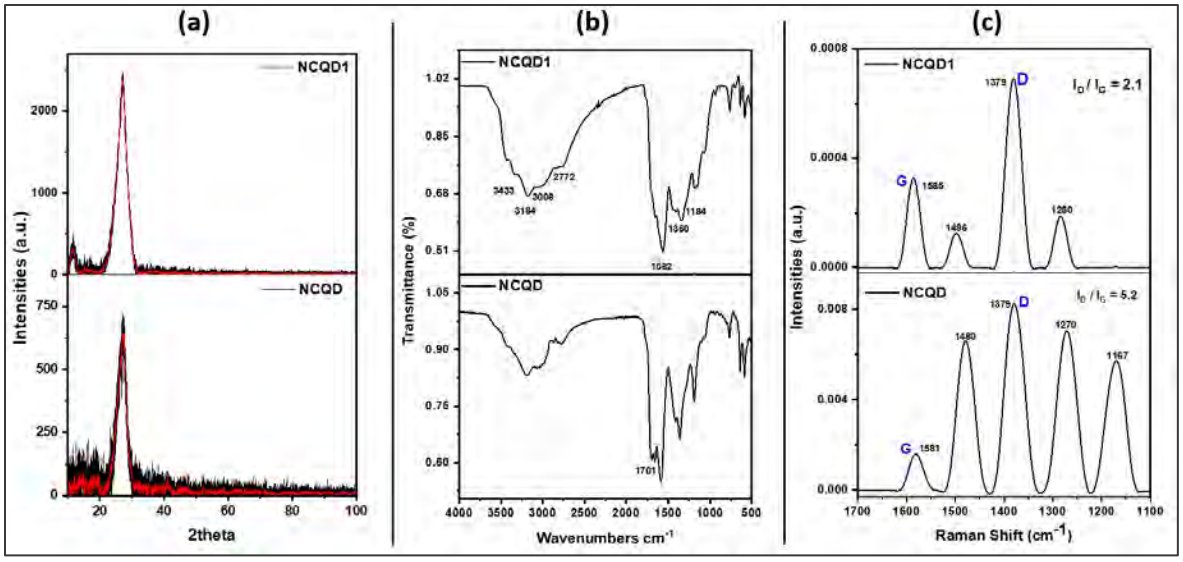

Fig. 3.25: (a) XRD, (b) FT-IR and (c) Raman spectra of NCQD and NCQD1

Fig. 3.26. shows the UV-visible absorption, emission, and excitation spectra for NCQD (**Fig. 3.26a-b**) and NCQD1 (**Fig. 3.26c-d**), which differ according to the citric acid to urea ratio (**Fig. 3.24**). The spectra reveal two distinct absorption peaks at ~335 nm and ~430 nm, corresponding to the n→π* transitions of C=O and C=N bonds, respectively [153]. Additionally, a shoulder peak at ~270 nm is characteristic of π–π* transitions of the graphitic core (C=C or C–C) of sp^2 domains in the sp^3 environment [90]. Increasing the nitrogen content in NCQD by adding a larger quantity of urea during the synthesis process resulted in the absorption spectrum becoming dominated by the C=N bond transitions. The changes in the chemical compositions cause significant changes in the photoluminescence emission, resulting in the transition from blue (~450 nm) to green (~532 nm) wavelengths, as illustrated in **Fig. 3.26**. These findings are consistent with the previous work by Xue and colleagues, who investigated similar effects in nitrogen-doped quantum dots [154].

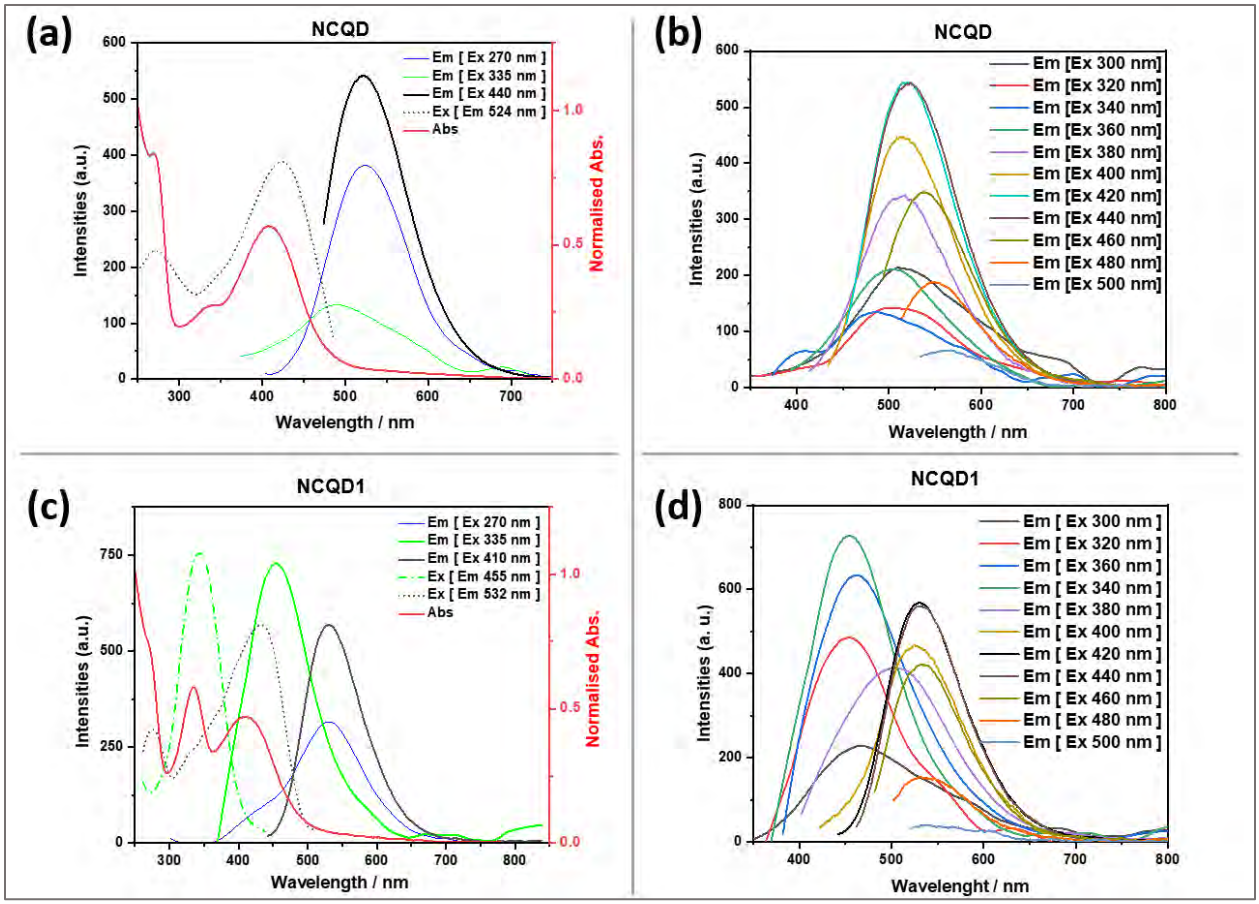

Fig. 3.26: Absorption and fluorescence analysis of NCQD: (a) NCQD and (c) NCQD1, and excitation-dependent photoluminescence (PL) spectra: (b) NCQD and (d) NCQD1, measured using excitation wavelengths in the range of 300 to 500 nm.

3.2.4.2 Preparation of PAN/NCQD and porphyrin-loaded PAN/NCQD electrospun fibers

The fabrication of fibers was carried out by electrospinning. Incorporating NCQD rather than NCQD1 into the PAN matrix was based on their distinct absorption properties within the visible spectrum of the electromagnetic spectrum (**Fig. 3.26**). This property makes NCQD particularly suitable as a photosensitizer, including application under sunlight as an inexpensive light source. The PAN/NCQD fibers exhibited a light brown colour, while the porphyrin-loaded PAN/NCQD fibers (loaded with porphyrins **1a**, **2a**, **3a** and **5b**) displayed a yellow-green colour (**Fig. 3.27**)

under normal white light. Notably, the fluorescence emission properties of the quantum dots (NCQD) were well-preserved within the PAN/NCQD solid fibers, as demonstrated in **Fig. 3.27** for the PAN/NCQD composites under UV (365 nm) illumination. This observation signifies a uniform dispersion of the NCQD within the PAN fabric.

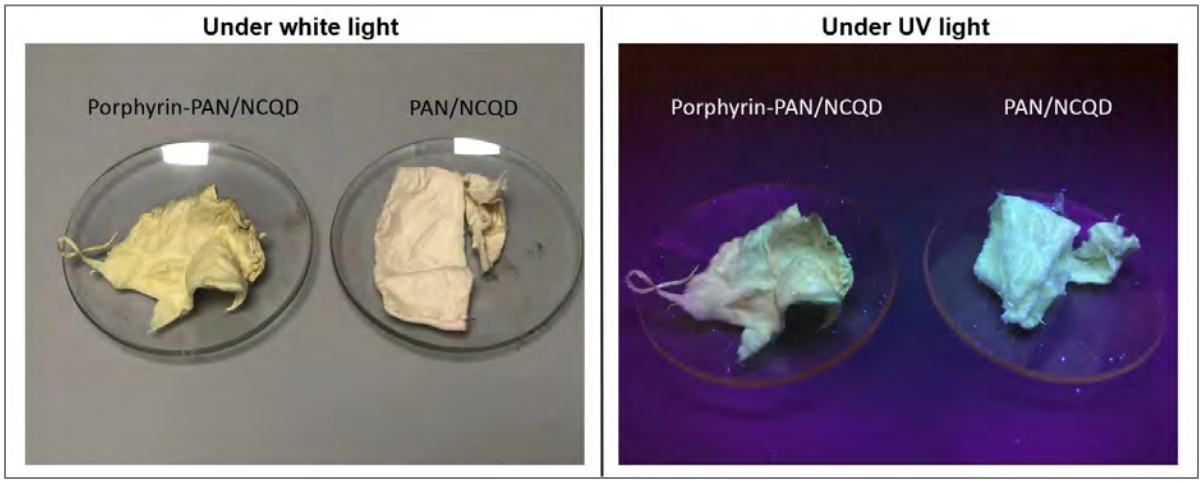

Fig. 3.27: Digital photos of the PAN/NCQD and porphyrin-loaded PAN/NCQD fluorescent fibers under white (normal) and UV light (365 nm)

3.2.4.3 SEM analysis

Scanning electron microscopy (SEM) was employed to investigate the surface morphology of the PAN and PAN/NCQD composite fibers (**Fig. 3.28**). PAN fibers exhibit unbranched and cylindrical structures (**Fig. 3.28a**) while PAN/NCQD fibers had some branched fibers. Some fibers also exhibit rough aggregated coatings, attributed to the presence of NCQD **(Fig. 3.28b)**. No visible evidence of porphyrin molecules was detected in the SEM images of any PAN composites due to the small size of the porphyrins, hence the SEM image is not shown.

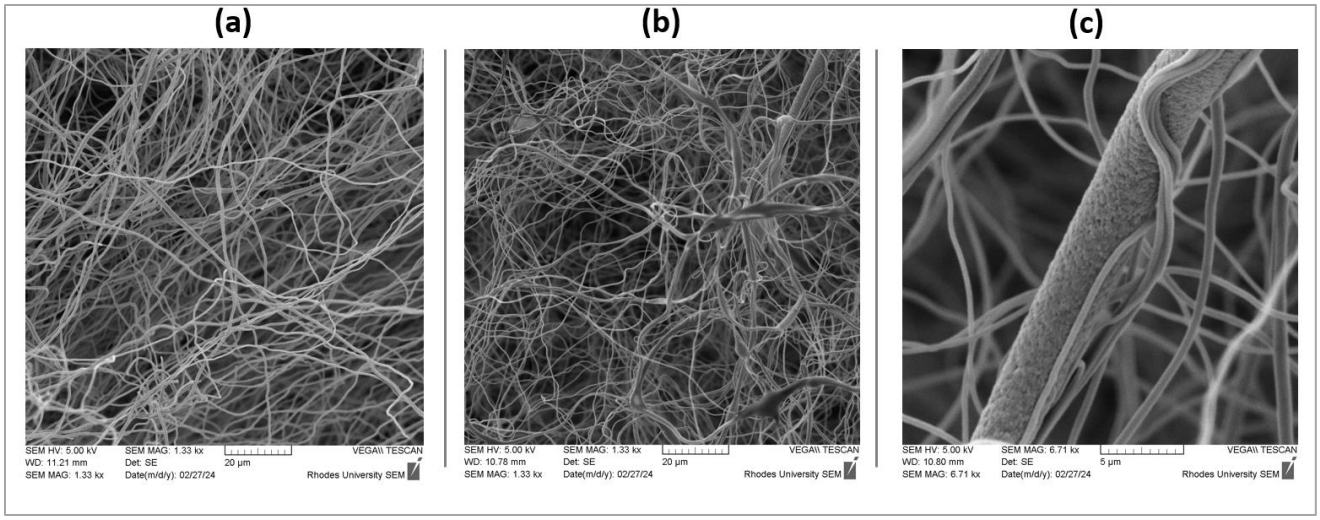

Fig. 3.28: SEM micrographs obtained for (a) PAN fibers (b) PAN/NCQD, and (c) close view image of the PAN/NCQD fibers

3.2.4.4 UV-Vis diffuse reflectance analysis

Distinct absorption features emerge in the UV-Vis diffuse reflectance spectra of PAN and the PAN/NCQD composite fibers (**Fig. 3.29**). The pure PAN fibers exhibit UV absorption band at ≈274 nm (**Fig. 3.29a**) due to polyacrylonitrile polymer [133]. However, in PAN/NCQD and its porphyrin composites, acrylonitrile absorption is slightly blue-shifted (to around ≈266 nm). Porphyrin-loaded PAN and PAN/NCQD composites possess prominent porphyrin peaks, which are more pronounced in **5b**, followed by **2a**, **3a**, and **1a** (**Fig. 3.29b**). When comparing the Soret band values of porphyrins in DMF with those on the PAN/NCQD composites in the solid state (**Table 3.6**), we observe red-shifted spectral bands, typical of porphyrins in the solid state [155].

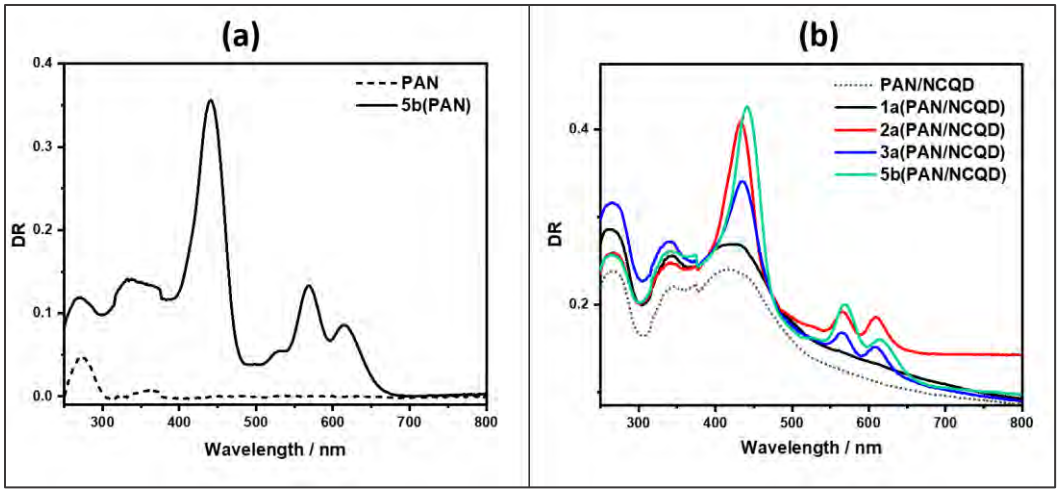

Fig. 3.29: The UV-Vis diffuse reflectance (DR) spectra of the following samples: (a) PAN and P(PAN) and (b) PAN/NCQD and its porphyrin composites

Table 3.6: Solid state spectral data (spectra of the porphyrin alone in DMF in brackets) of porphyrin (PAN) and porphyrin (PAN/NCQD) composites

Composites	λ_{Abs} (Soret-bands)/nm	λ_{Abs} (Q-bands)/nm
1a(PAN/NCQD)	**433 (433)**	**-**
2a(PAN/NCQD)	**434 (432)**	**567, 611**
3a(PAN/NCQD)	**437 (433)**	**567, 611**
5b(PAN/NCQD)	**441 (437)**	**569, 614**
5b(PAN)	**441 (437)**	**568, 614**

3.2.4.5 FT-IR and Raman spectra analysis

The Fourier-transform infrared (FTIR) spectra of polyacrylonitrile (PAN) fibers were analyzed (**Fig. 3.30**). In FT-IR PAN alone has been discussed in section **3.2.2.3**. When examining PAN/NCQD and porphyrin-loaded composites, their FTIR spectra primarily show bands from PAN and NCQD (discussed earlier). In the porphyrin-loaded composites, the porphyrin bands are entirely masked by the PAN and NCQD peaks (**Fig. 3.30b**).

Apart from the 1453 cm^{-1} peak due to CH_2 bending observed in pure PAN fiber (**Fig. 3.19**, 1100-1700 cm^{-1}), the full Raman spectra (between 1000-3500 cm^{-1}) of pure PAN fiber shows additional strong peaks at 2916 cm^{-1}, 2244 cm^{-1}, and 1093 cm^{-1}, corresponding to CH stretching, C≡N mode, and C-C skeletal stretching, respectively (**Fig. 3.31a**) [137,138,156,157]. These characteristic peaks were also observed in all PAN composites (**Fig. 3.31b**). In the PAN/NCQD composites (**Fig. 3.31a**), previously discussed, the characteristic Raman peaks due to quantum dots (NCQD) were observed in the full Raman spectra. These include the **D** band at 1379 cm^{-1} and the **G** band at 1581 cm^{-1}. Additionally, other peaks were observed at 2403, 2200, 2125, 1986, 1780, 1685, 1470-1480, 1270, 1165, and 1065 cm^{-1}, assigned to N-H stretching, N=C=O, C-N, C≡C, C=O(ketone), C=O(amide), C=N stretching, C=C in trans-polyacetylene-like systems, C-O, and C-C bonds, respectively [156,158–162]. Similar to the FTIR spectra, no new Raman peaks were observed in the spectra for porphyrin PAN/NCQD composites (**Fig. 3.31b)**.

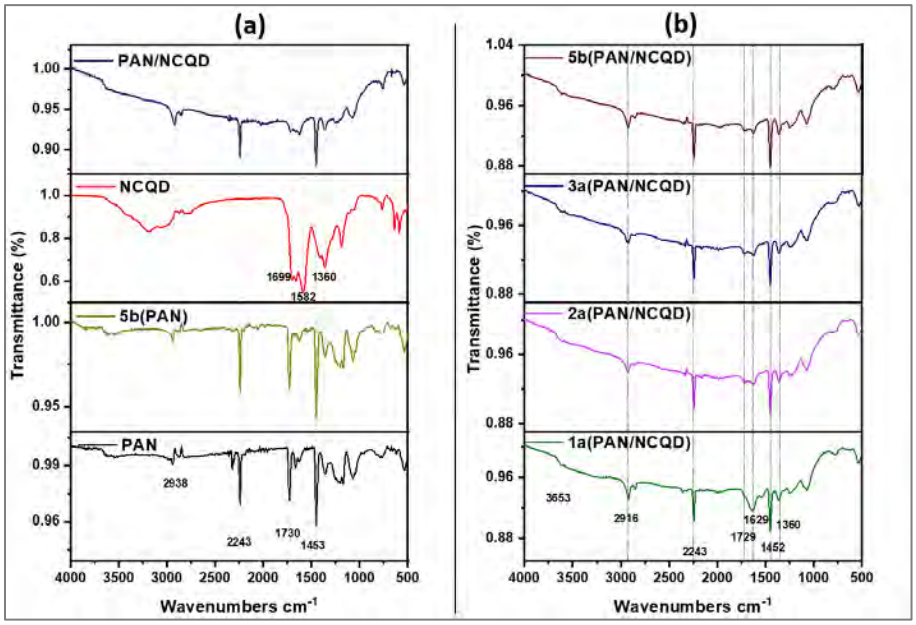

Fig. 3.30: FTIR spectra of (a) PAN, **5b**(PAN), NCQD (as powder), and PAN/NCQD, and (b) porphyrin-loaded PAN/NCQD fibers

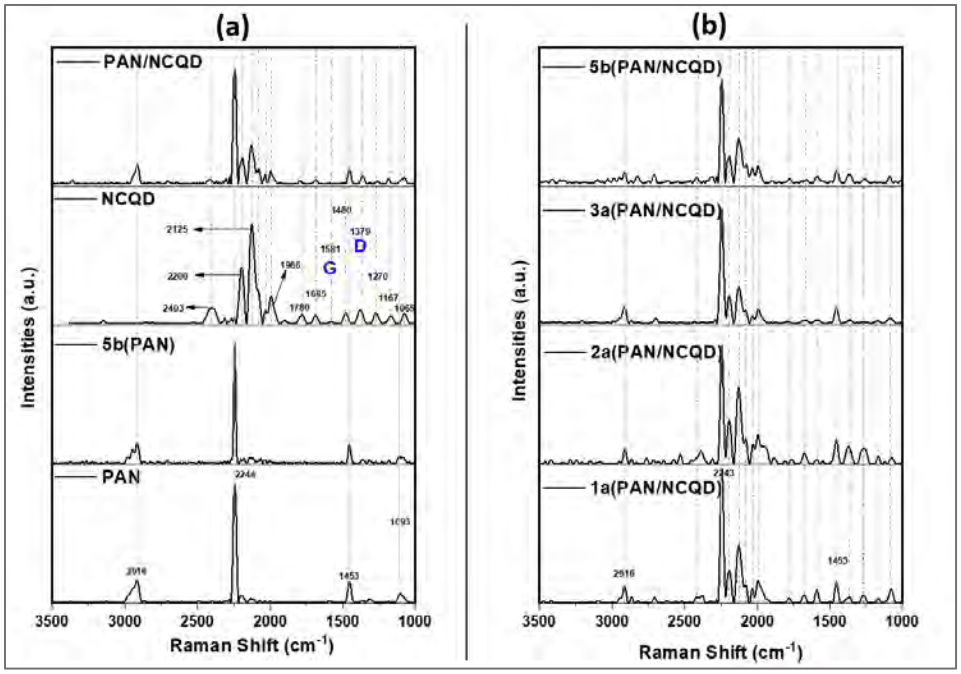

Fig. 3.31: Raman spectra of (a) PAN, **5b**(PAN), NCQD, and PAN/NCQD, and (b) porphyrin-loaded PAN/NCQD fibers

3.2.4.6 X-ray Diffraction analysis (XRD)

The pristine polyacrylonitrile (PAN) fibers and the PAN/NCQD composites diffractograms exhibited distinct peaks at $2\theta \approx 17°$ (**Fig 3.32**), corresponding to the (100) crystallographic plane of PAN fibers [147]. The porphyrin-loaded PAN and PAN/NCQD composites displayed additional broad and weak amorphous peaks centered at $2\theta \approx 27°$ (002 plane) due to the presence of porphyrins. In the X-ray diffraction (XRD) spectra of the PAN composites, the intense diffraction peaks from **PAN** gradually decreased with the addition of NCQD and porphyrins, attributed to increased background scattering caused by enhanced amorphization.

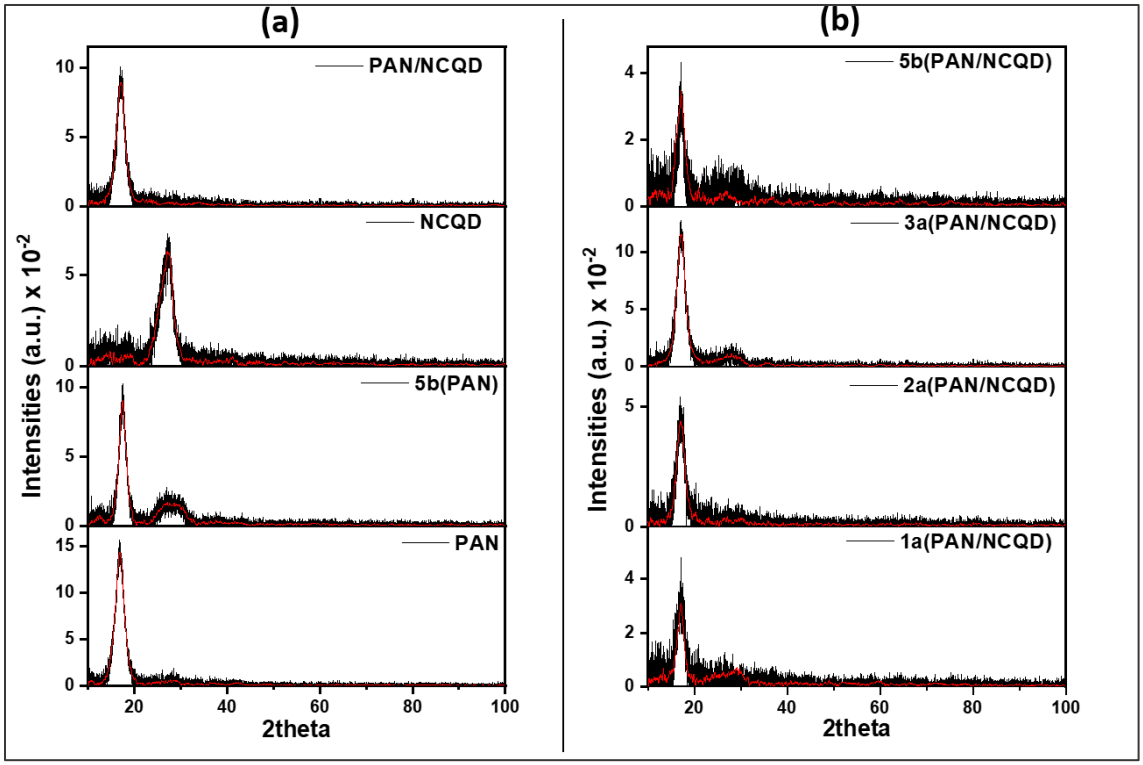

Fig. 3.32: XRD spectra of (a) PAN, **5b**(PAN), NCQD, and PAN/ NCQD, and (b) porphyrin-loaded PAN/ NCQD fibers

3.2.4.7 Thermogravimetric (TGA) analysis

We utilized thermogravimetric analysis (TGA) to evaluate the overall thermal stability of the PAN composites. As shown by the TGA curve in **Fig. 3.33**, the thermal properties of PAN fibers improved upon impregnation with NCQD and porphyrin. The degradation for both PAN fibers and their respective composites started near 310 °C. At 700 °C, the residual weight of PAN/NCQD (21%) significantly exceeded that of pure PAN fibers (2%), thanks to the presence of the more thermally stable NCQD (as powder). In comparison to PAN, NCQD (as powder) exhibited a higher residual weight (38%) at 700 °C, resulting in the improved thermal stability of PAN/NCQD composites. Furthermore, the increased thermal stability observed in porphyrin-loaded composites is attributed to porphyrins. Among the porphyrins loaded samples studied, **5b**(PAN) displayed the

highest residual weight at 700 °C (61%), followed by **5b**(PAN/NCQD) (52%), **2a**(PAN/NCQD) (48%), **3a**(PAN/NCQD) (43%), and **1a**(PAN/NCQD) (39%), in that order.

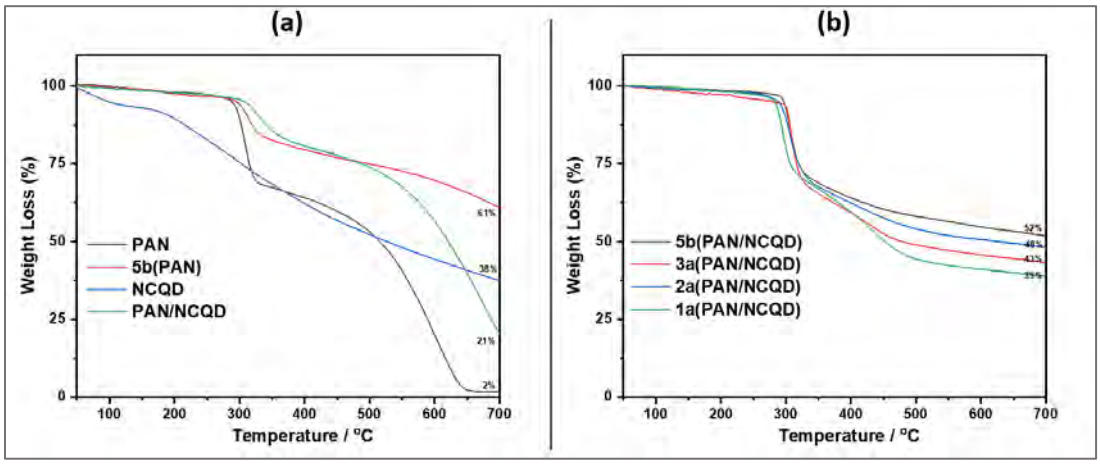

Fig. 3.33: TGA curves for (a) PAN, **5b**(PAN), NCQD (powder), PAN/NCQD, and (b) porphyrin (PAN/NCQD) composite fibers

3.2.4.8 TOF-SIMS analysis

Time-of-Flight Secondary Ion Mass Spectrometry (TOF-SIMS) was employed to assess the uniformity of NCQD and porphyrin distribution on the surfaces of PAN composite fibers (**Fig. 3.34**). The analysis revealed distinct chemical compositions among the individual fibers. In the TOF-SIMS overlays, the positive mass signals $C_3H_9N^+$ (Red), $C_4H_{11}N^+$ (Green), and $C_6H_5^+$ (Blue) were attributed to porphyrin **5b**, PAN, and NCQD, respectively.

The distribution of NCQD on the surface of PAN is shown by overlays of NCQD (Blue) ion fragments on PAN (Green) ion fragments. Similarly, the distribution of porphyrin **5b** on the surface of **5b**(PAN/NCQD) fibers is depicted by overlays of porphyrin **5b** (Red) ion fragments on PAN/NCQD ion fragments (**Fig. 3.34**). The green ion signals corresponding to PAN were observed in both the PAN and PAN/NCQD sample images, respectively, confirming their presence in both samples. The blue signal, corresponding to NCQD, was the dominant signal in the

PAN/NCQD sample image. This signal dominance indicates a significant degree of coverage of the PAN fibers by the NCQD. In the **5b**(PAN/NCQD) sample image, the red signal, corresponding to porphyrin **5b**, is the only dominant signal present, signifying complete coverage of the PAN/NCQD fibers by porphyrin **5b**.

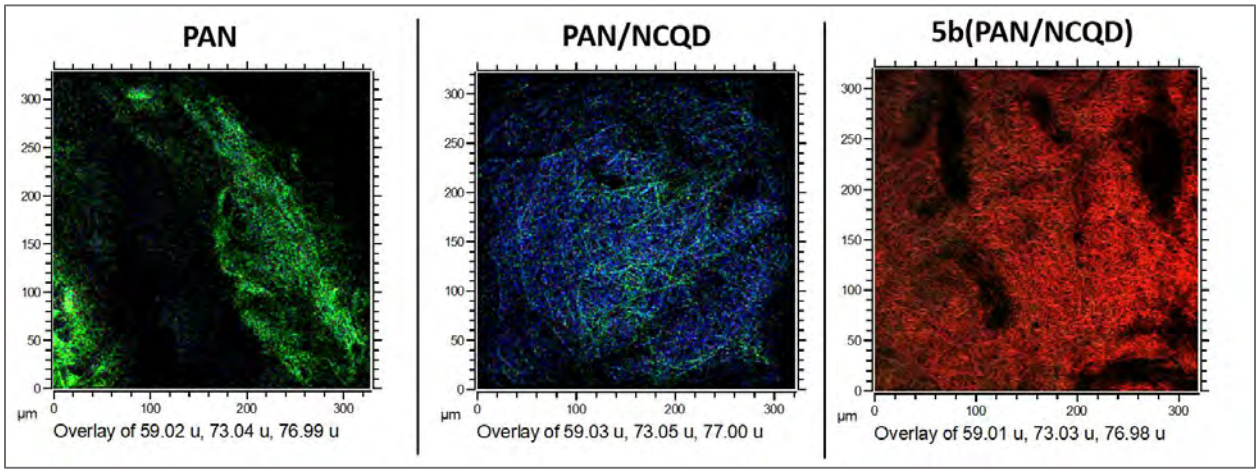

Fig. 3.34: Red-Green-Blue TOF-SIMS mass ion overlay images showing distribution of positive ions on the PAN, PAN/NCQD and **5b**(PAN/NCQD) fibers, obtained with Bi liquid metal ion gun (LMIG) source.

3.3 Closing remarks

This chapter details the synthesis and characterization of various materials. The indium complexes **1a**, **2a**, **3a**, **4a**, **4b**, **5a**, and **5b** were successfully synthesized and characterized using mass spectrometry, UV-Vis, FT-IR, NMR spectroscopy, and elemental analysis. The FT-IR, NMR, and mass spectra, along with elemental analysis, confirmed the structure, composition, and functionality of the target complexes.

Activated carbon supports in the form of granular (GAC), oxygen-functionalized GAC (ACO), powdered (AC), and colloidal activted carbon (CAC), as well as PAN-based composites consisting

of AC and NCQD, were also prepared and characterized. Their porphyrin composites were characterized using additional techniques such as UV-Vis, FT-IR, Raman, XRD, and TGA. FT-IR and XPS confirmed the successful anchoring of photosensitizers to the supports for some conjugates. SEM was used to confirm the porous nature of the AC samples, while their solid-state UV-Vis spectra confirmed photosensitizer immobilization. Additionally, TOF-SIMS was used to analyze the porphyrin-loaded PAN/NCQD sample, providing insights into the porphyrin coverage on the support.

CHAPTER 4: Photophysical and Photochemical Properties

This chapter discusses the photochemical and photophysical properties of the synthesized porphyrins and their composites

4.1 Fluorescence quantum yields (Φ_f),

The fluorescence quantum yields (Φ_f) of all the indium porphyrins obtained using **Eq 2.1** were very low, that is (<0.01) compared to the Zinc tetraphenyl porphyrin (ZnTPP), which is commonly used as a standard [105], hence were not shown in **Table 4.1**. This low quantum yield is attributed to the heavy atom effect of the In(III) central metal atom, which promotes non-radiative electronic relaxation mechanisms, such as intersystem crossing to the triplet states.

4.2 Fluorescence lifetimes (τ_f)

Due to the low fluorescence of indium porphyrins and the non-fluorescent nature of the carbon supports, except for the nitrogen-doped carbon quantum dots, lifetime experiments were not conducted for these samples. The fluorescence lifetimes for NCQD and NCQD1 were measured using Time-Correlated Single Photon Counting (TSCPC), and fluorescence decay curves were obtained at an excitation wavelength of 375 nm (**Fig. 4.1**). The average fluorescence lifetimes were determined as very close, 7.58 and 7.84 ns for NCQD and NCQD1, respectively. Subsequently, NCQD was selected for the application because of their strong absorption in the visible region.

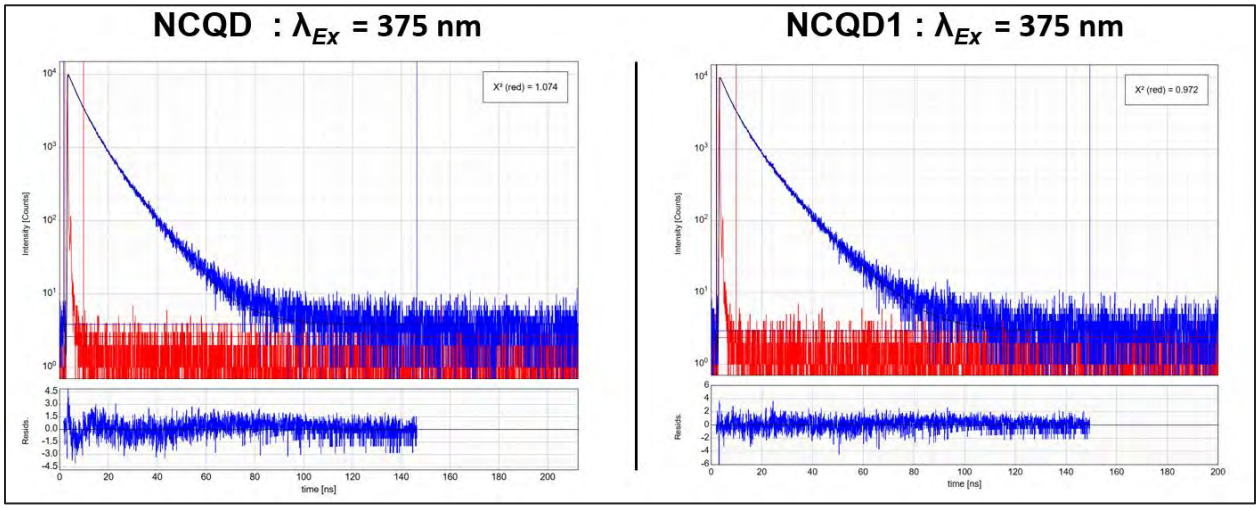

Fig. 4.1: TCSPC spectra of NCQD and NCQD1 in water

4.3 Triplet lifetimes (τ_T) and singlet oxygen quantum yields ($\Phi\Delta$)

The triplet lifetime decay kinetics of porphyrins **1a-5a** followed simple exponential models (**Fig. 4.2**), with porphyrin **2a** exhibiting the longest triplet lifetime (τ_T) of 44 μs (**Table 4.1**) compared to the rest of the porphyrins within the **1a-5a** series. This observation can be attributed to enhanced internal conversion processes, as evidenced by the intense Q(0,1) emission bands relative to the Q(0,0) bands in porphyrin **2a (Fig. 3.2)**. However, the triplet lifetime curves of complexes **4b** and **5b** exhibited biexponential decay profiles (**Fig. 4.2**), where the τ_{T2} triplet state lifetimes were significantly longer than the τ_{T1}. This can attributed to the push-pull effect, which modifies the electronic distribution and molecular geometries of these porphyrins, creating intramolecular charge transfer (ICT) states that mix with locally excited (LE) states, resulting in multiple singlet excited states, which lowers the energy gap between the ground and excited states, leading to red-shifted emission spectra. The evidence of this is the observed broadened emission spectra of **4b** and **5b** , attributed to multiple low-energy emission bands from ICT states [119], **Fig. 4.2b**.

The singlet oxygen quantum yield values were determined using DMA as a quencher in DMF, with ZnTPP as the standard. **Fig. 4.3** illustrates the spectral changes observed during the degradation of DMA by the ZnTPP standard and complexes **4a** and **4b** (as examples). The Soret band intensities remained unchanged, while the peaks corresponding to DMA decreased with irradiation, demonstrating that the porphyrins remained stable during the photoirradiation process used for singlet oxygen detection.

The high singlet quantum yield of complex **2a** (0.55) using **Eq 2.2**, which also displayed the longest triplet lifetimes, highlights its efficient photophysical properties. For complex **1a**, the good singlet oxygen-generating ability is likely due to the stabilizing properties of the acetyl substituent.

Although complex **3a** also contains acetyl groups, its lower singlet oxygen generation is likely due to aggregation effects. Pyrene molecules are known to display a strong tendency for self-association through an excited-state process known as excimer formation, which strongly limits energy conversion capabilities and migration [163,164]. Thus, although pyrene derivatives have strong light-harvesting abilities [165], their applications are limited by aggregation.

Despite having longer triplet lifetimes, the cationic porphyrins **4b** and **5b** exhibited slightly lower singlet oxygen quantum yields than their unquaternized precursors, **4a** and **5a**. The quenching of singlet oxygen is likely due to its reaction with iodide anions (I^-) introduced into the solution by cationic porphyrins [166,167].

For the porphyrin-loaded CAC samples, **2a**/CAC exhibited the highest singlet oxygen quantum yields (Φ_Δ), followed by **1a**/CAC and **3a**/CAC, respectively. The conjugates showed higher singlet oxygen quantum yields than the porphyrins in solution, likely due to the reduced rate of recombination of electron-hole pair upon conjugation. Additionally, no fluorescence emission peaks were observed for **1a**/CAC, **2a**/CAC, and **3a**/CAC at an excitation wavelength of 432 nm, confirming the interactions between the porphyrins and the CAC, similar to other carbon-related materials [168–170].

Table 4.1: Photo-physicochemical parameters of synthesized indium porphyrins and the CAC conjugates in DMF

Complexes	λ_{Abs} (B-band)	Φ_{Δ}	τ_{T1}	τ_{T2}
	nm		µs	µs
1a	427	0.51	16	-
2a	432	0.55	44	-
3a	433	0.40	17	-
4a	428	0.46	17	-
4b	433	0.41	8	37
5a	429	0.46	8	-
5b	437	0.44	12	83
1a/CAC	433	0.78	-	-
2a/CAC	432	0.94	-	-
3a/CAC	433	0.54	-	-

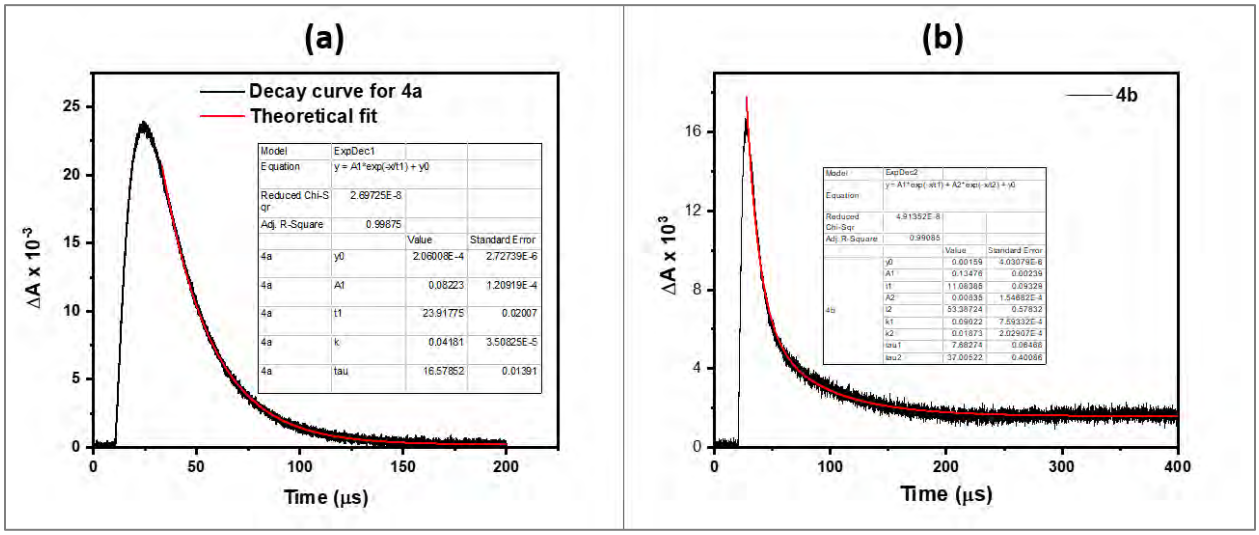

Fig. 4.2: Representative triplet-state lifetimes decay curves of (a) **5a** and (b) **5b** in nitrogen-saturated DMF

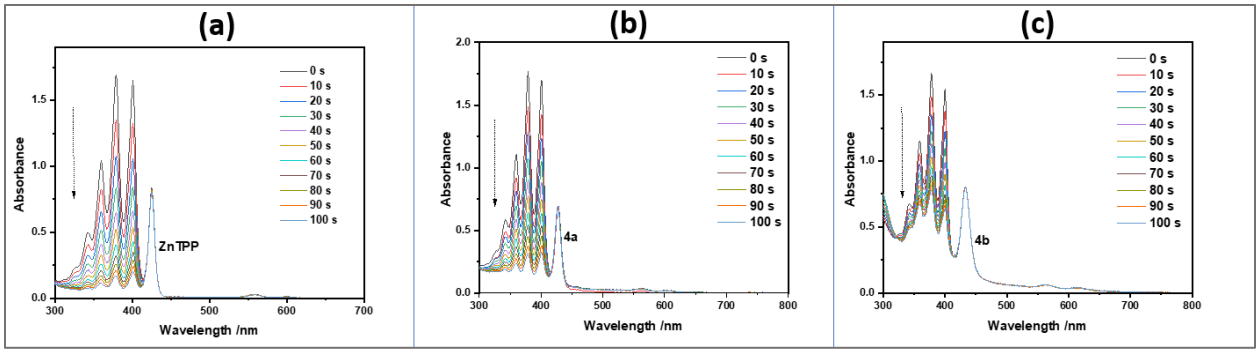

Fig. 4.3: Representative absorption spectral changes during the determination of singlet oxygen quantum yield of complex (a) ZnTPP standard, (b) **4a** and (c) **4b** in DMF

4.4 Closing remarks

This chapter highlights the distinct photophysical properties of indium porphyrins and their composites. The low fluorescence quantum yields of indium porphyrins are attributed to the heavy atom effect of the In(III) central metal atom, which promotes non-radiative relaxation mechanisms. The fluorescence lifetimes of NCQD and NCQD1 were measured, with NCQD selected for further applications due to its strong visible absorption. The triplet lifetimes and singlet oxygen quantum yields of the porphyrins were also investigated, revealing efficient photophysical properties, particularly for complex **2a**. The porphyrin-loaded CAC samples displayed higher singlet oxygen quantum yields than in solution, indicating successful conjugation and reduced recombination of electron-hole pairs. These provide valuable insights that can guide the design and application of porphyrin-based materials in a wide range of photophysical and photochemical applications

CHAPTER 5: Indium metalated pyridinyl-based *trans*-A_2B_2 porphyrin in solution as novel aPDT agents against planktonic cells and biofilms

This chapter presents the activity of novel pyridinyl-based t*rans*-A_2B_2 porphyrin photosensitizers (PS) with antimicrobial photodynamic therapy (aPDT) properties against both planktonic and biofilms of *S. aureus* and *E. coli*, highlighting their potential for use in both medical and environmental applications.

5.1 The effect of charge on antimicrobial photodynamic therapy (aPDT)

The **4** and **5** series of porphyrin complexes investigated in this study were deliberately designed to incorporate pyridinyl moieties. Upon methylation, these moieties are known to enhance water solubility and bioavailability within bacterial cells, thereby augmenting the overall antimicrobial photodynamic activity, particularly against gram-negative bacteria

5.1.1. In vitro antibacterial activity on planktonic cells of *S. aureus* and *E. coli* bacteria

Fig. 5.1 displays the cytotoxicity plots of *S. aureus* and *E. coli* bacteria treated with gradient doses of **4a-5a** and **4b-5b** in the dark and under 30 min of illumination using a 415 nm LED (2.2 mW cm^{-2}, i.e., 3.9 J cm^{-2}). **Table 5.1** summarizes the log reduction and cell viability values for **4a-5a** and **4b-5b** at the lowest concentration (2.5 μM) in the dark and under light. Antimicrobial PDT activity data also show that the quaternized forms (**4b-5b**) had a higher aPDT activity than the neutral complexes (**4a** and **5a**) against both *S. aureus* and *E. coli*. Notably, Gram-(-) *E. coli* bacteria have a permeability barrier that prevents photosensitizer dyes from entering the cells and his behavior is expected in the context of neutral photosensitizer dyes toward Gram-(-) *E. coli* [171,172].

Hurst *et al*. examined the impact of charge in cationic porphyrin on photodynamic inactivation (aPDT) of *E. coli* [173]. They tested photosensitizers with varying positive charges (1–4 charges) and found a correlation between number of charges and aPDT effectiveness. The study highlighted differences in aPDT mechanisms, particularly with the tetra-cationic porphyrin. Live-cell microscopy showed varied interactions: porphyrins with 1–3 charges bound to the cell membrane, while the tetra-cationic version penetrated the membrane [173]. This suggests distinct inactivation mechanisms for cationic porphyrins. In a separate study, Alves and co-workers [174] found that,

apart from charge distribution, adding *meso*-substituent groups possessing inherent antimicrobial properties to pyridinyl porphyrins can significantly influence the aPDT activity of porphyrins. Their study revealed that the tri-cationic porphyrin, 5-(pentafluorophenyl)-10,15,20-tris(1-methylpyridinium-4-yl)porphyrin, exhibited higher aPDT activity compared to the tetra-cationic 5,10,15,20-tetrakis(1-methylpyridinium-4-yl) porphyrin [174]. Dicationic compound **4b**, which features tert-butyl groups, and compound **5b**, which features thiophenyl groups, exhibit high efficacy in aPDT. **5b** showed significant antimicrobial properties even without light, against both *E. coli* and *S. aureus*, **Table 5.1.** These findings illustrate the influence of different meso-aryl substitutions on the aPDT effectiveness of A_2B_2 cationic porphyrins.

Moreover, it is evident that both hydrophilic and amphiphilic interactions play essential roles, and any imbalance can significantly affect the activity of photosensitizers, as demonstrated by the aPDT results of the cationic porphyrins (**4b/5b**), which exhibit both properties. This phenomenon corresponds to similar findings in similar studies, highlighting that moderately hydrophobic molecules can sometimes exhibit an increased propensity to accumulate within cell membranes. Consequently, this enhanced accumulation facilitates improved cellular uptake, leading to elevated intracellular concentrations of the photosensitizer [175–177]. However, it is important to note that highly hydrophobic molecules are prone to aggregation in an aqueous environment, which can negatively impact cellular uptake [178,179].

A**s** stated above, **4b** displayed remarkable aPDT activity compared to **5b** against the planktonic cells of *E. coli* and *S. aureus*. This enhanced activity can be attributed to the presence of tert-butyl groups, which increase the hydrophobicity of the porphyrin and reduce the tendency of the molecules to aggregate due to steric effects [180]. This reduction in aggregation enhances the solubility, bioavailability, and uptake of the porphyrins, ensuring their aPDT effectiveness. While

the singlet oxygen studies indicated lower singlet oxygen production with cationic porphyrins, it is evident that enhanced uptake upon quaternization leads to improved activity. This improvement arises from increased interaction between the bacteria and porphyrins, resulting in higher concentrations of ROS at the cellular level.

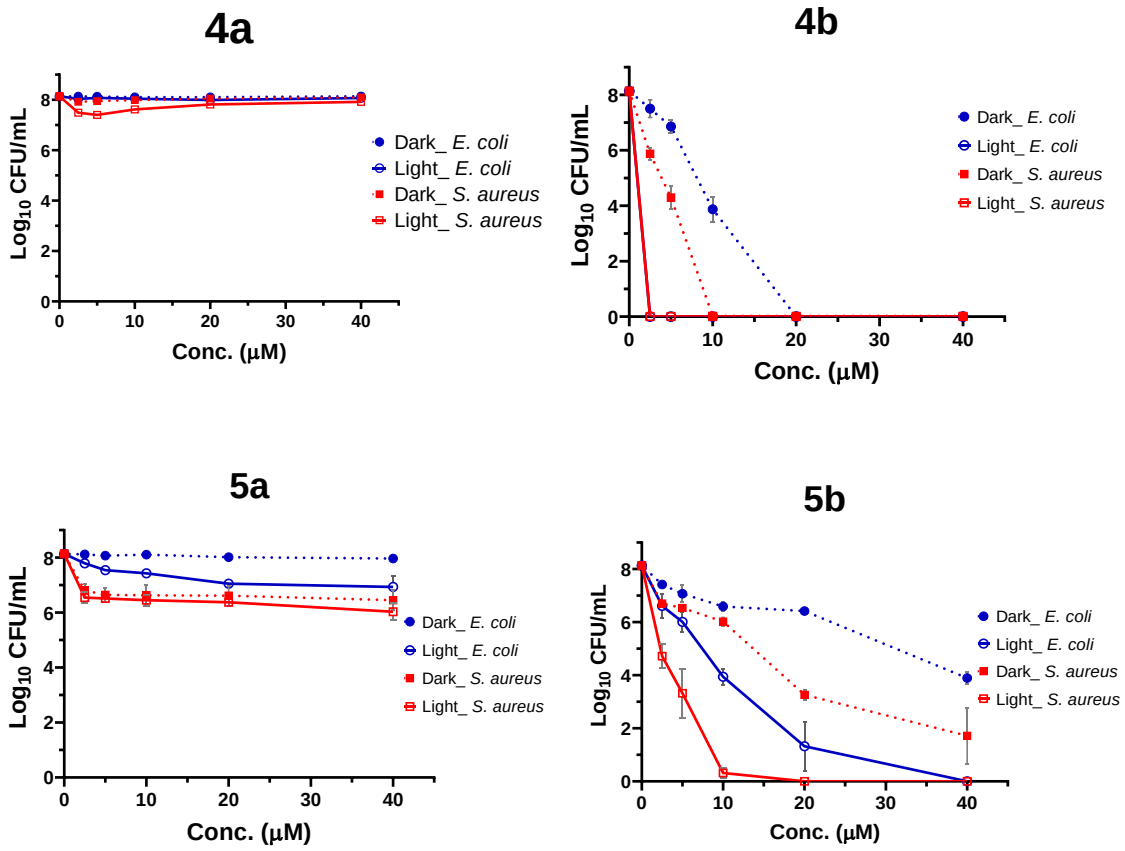

Fig. 5.1: The cell viability plots for planktonic cells of (a) *E. coli* and (b) *S. aureus* upon treatment with gradient concentrations of **4a,b** and **5a,b** after illumination with 415 nm LED light at a constant irradiance for 30 min.

Table 5.1: Log reduction and cell survival values at 2.5 µM concentrations of **4a,b** and **5a,b** against planktonic cells of *S. aureus* and *E. coli* in DMSO/PBS (1 : 99 v/v) after illumination with 415 nm LED light at a constant irradiance for 30 min.

Complex	*E. coli*				*S. aureus*			
	Log Reduction		Cell Survival (%)		Log Reduction		Cell Survival (%)	
	(Dark)	(Light)	(Dark)	(Light)	(Dark)	(Light)	(Dark)	(Light)
4a	<0.01	0.10	99.9	79.3	0.22	0.65	61.2	11.5
5a	0.03	0.35	92.8	38.9	1.34	1.59	5.2	2.4
4b	0.62	8.14	21.9	<0.1	2.25	8.12	0.5	<0.1
5b	0.71	1.52	18.5	2.8	3.32	3.41	<0.1	<0.1

5.1.2. In vitro antibacterial activity on biofilms of *S. aureus* and *E. coli* bacteria

In an *in vitro* study, the antimicrobial against *E. coli* and *S. aureus* was investigated using cationic porphyrins **4b** and **5b**. These porphyrins were chosen due to their demonstrated effective antimicrobial properties, as observed during the study involving planktonic cells. The preparation of the biofilm bacteria cells was performed as reported in the literature [181] and is outlined in the experimental section. The studies were conducted with gradient concentrations of 10, 20, 40, 80 and 160 µM of **4b**/**5b** porphyrins for both *S. aureus* and *E. coli* biofilms.

Metabolically active cells reduce resazurin, causing it to transition from a blue, nonfluorescent state to a highly fluorescent pink compound known as resorufin (**Fig. 2.3**). This transformation primarily occurs within live cells, specifically in the mitochondria [182]. Fluorescence technique was employed to determine the percentage metabolism based on the resorufin fluorescence. Since metabolic activity is closely linked to cell viability, the experimental results revealed that both **4b** and **5b** exhibited substantial activity at concentrations of 160 µM, **Fig**. **5.2**.

From the dose-response bar graphs (**Fig. 5.2**), complex **5b** showed an increase in aPDT activity with an increase in concentration with *E. coliI* bifilms, while in **4b**, there was a slight reduction and then an increase in aPDT activity with an increase in concentration. The underlying mechanism likely involves an intricate interplay involving biofilm structure, photosensitizer (PS) penetration, and bacterial physiology [183,184]. The PS efficiently penetrates the outer biofilm layers at very low concentrations, impacting matrix integrity. When bacteria within biofilms are exposed to high concentrations of the photosensitizer, they can persist and re-establish a more resistant biofilm, hindering penetration [185,186], hence the observed irregular variation of % metabolism in the *E. coli* biofilms, in this case at 10-20μM with porphyrin **4b Fig. 5.2**. Under light conditions or extremely high PS concentrations, disruption of the extracellular matrix takes place which exposes bacterial cells, enhancing aPDT activity. Based on aPDT percentage contribution, compound **5b** demonstrated the highest activity against both *E. coli* (61%) and *S. aureus* (87%) biofilms at a low concentration of 10 μM, **Table 5.2**. Compound **4b** also showed significant efficacy against *S. aureus* biofilms, achieving a 72% reduction and extending the irradiation time to 60 min enhanced aPDT activity for both porphyrins (**4b** and **5b**), as detailed in **Table 5.2**.

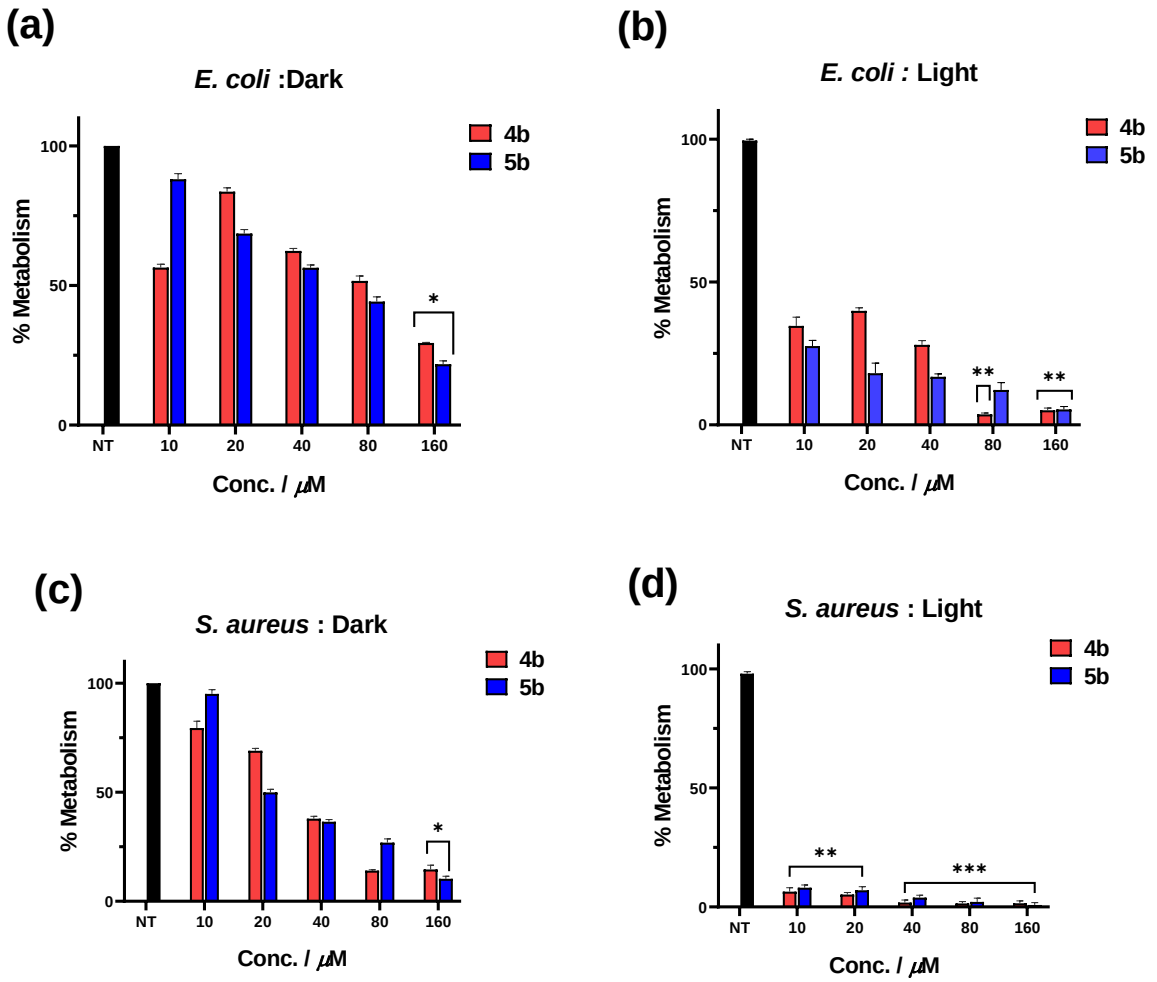

Fig. 5.2: Biofilm viability of (**a**/**b**) *E. coli* and **(c**/**d**) *S. aureus* upon treatment with gradient concentrations of **4b** and **5b**, and after illumination with 415 nm LED light at a constant irradiance for 30 min, with cell viability done using resazurin stain. **NT**: Non-treated samples

Table 5.2: Cell survival (%) values and aPDT activity for 10 μM concentrations of **4b** and **5b** against biofilms of *S. aureus* and *E. coli* after illumination with 415 nm LED light at a constant irradiance for 30 min and 60 min (the latter in brackets).

Complex	*E. coli*			*S. aureus*		
	Cell survival Dark (%)	Cell survival Light (%)	aPDT Contribution (%)	Cell survival Dark (%)	Cell survival Light (%)	aPDT Contribution %
4b	56	34 (5.7)	22	79	6 (2.4)	72
5b	88	27 (2.5)	61	95	8 (0.9)	87

aPDT Contribution (%) = % Cell survival in dark – % Cell survival in the presence of Light (30 min)

5.2. Investigating the effects of aPDT on *E. coli* biofilms using SEM

To investigate the effects of aPDT on biofilms, the cell morphology of untreated *E. coli* biofilms was studied on glass slides, those treated with complex **5b** (10 μM) alone, and those treated with **5b** (10 μM) under 60 min of light exposure using SEM. The SEM images in **Fig. 5.3** depict treated and untreated *E. coli* biofilm samples. The untreated sample (**Fig. 5.3a**) shows clusters of *E. coli* cells attached to the surface, connected via an extracellular polysaccharide matrix, with some cells stacked on each other. After treatment with **5b**, *E. coli* biofilms exhibit intricate interconnected networks of cells (**Fig. 5.3b**). These patterns reflect the biofilm's adaptive response [185], which is mediated by the quorum-sensing molecules such as autoinducer-2 (AI-2) [187]. Chemotaxis-driven aggregation enhances AI-2-mediated signalling, providing physical protection against oxidative stress and contributing to surface-attached biofilm development [187]. When *E. coli* biofilms were treated with a photosensitizer and exposed to light, they exhibited a remarkable change in morphology, with cells appearing flatter due to their disrupted cell membranes and altered matrix. Similar observations have also been made elsewhere [188]. Notably, from this study, aPDT emerges as an attractive strategy for controlling biofilms, particularly in cases of

recurrent and chronic biofilm-related issues. Thus, **5b** displayed potent aPDT activity, leading to significant changes in *E. coli* cell shape, as evidenced by SEM images. These alterations are likely attributed to the disruption of cell membranes.

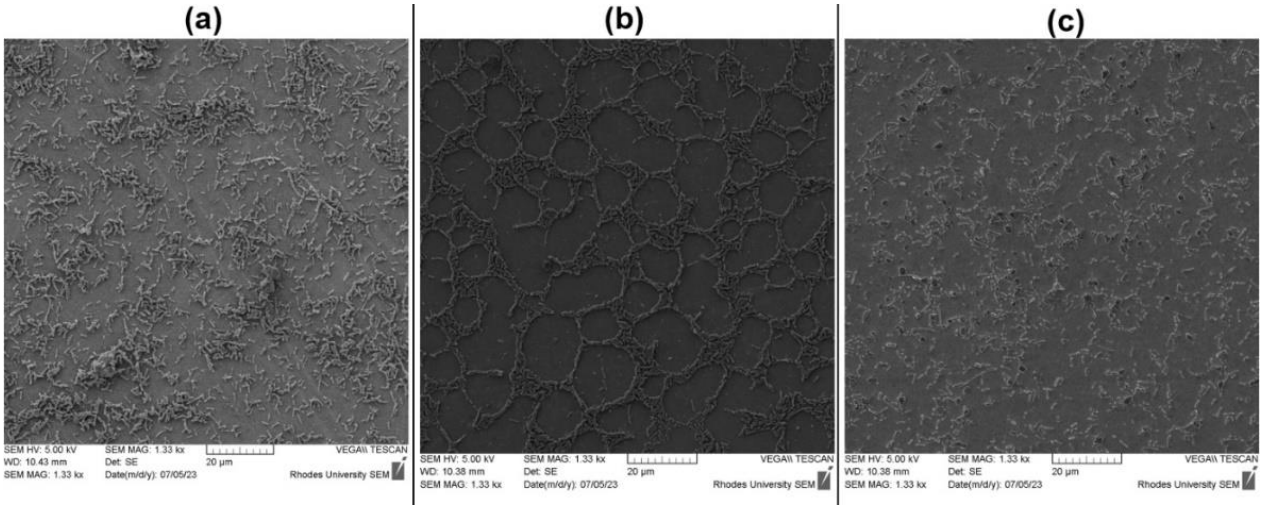

Fig. 5.3: SEM images of *E. coli* biofilms illustrating the effect of aPDT: (a) untreated sample, (b) treated with only **5b** (in the dark) and (c) treated with **5b** and light (irradiation time = 60 min). Concentration of **5b** at 10 μM.

5.3. Closing remarks

This chapter explored the activity of novel pyridinyl-based trans-A_2B_2 porphyrin photosensitizers with aPDT properties. The work demonstrated the significant effect of charge, particularly positive charges, in deactivating gram-negative bacteria. Additionally, aPDT proved effective in eradicating biofilms. Consequently, this chapter highlights the potential applications of cationic porphyrin photosensitizers in medical treatments for antibiotic-resistant infections, environmental remediation, and, within this thesis, antimicrobial decontamination of water.

CHAPTER 6: Removal of organic pollutants in water using porphyrin-loaded composite carbon materials and their antimicrobial activity against planktonic *E. coli* bacteria

---

This chapter presents the results of studies on the removal of organic pollutants from water through adsorption, photodegradation, or a combined process and the antimicrobial properties of selected composite materials against *E. coli* bacteria

---

6.1 Methylene blue (MB) removal in water

6.1.1. The effect of support material on MB adsorption

From this work, the nature of the support material for removing organic pollutants is a key determinant when choosing the appropriate support. A crucial factor to consider is the surface area, which affects the removal efficiency through enhanced adsorption, where pollutants interact favourably with the adsorbent support. Additionally, support with a higher surface area will likely result in higher porphyrin loading. This thesis focuses on developing integrated photocatalyst adsorbents, and for this reason, the activated carbon composite supports and their porphyrin-loaded composites were investigated.

Methylene blue (MB) adsorption studies were conducted in a darkroom for 5 h at 20 °C in 30 mL glass vials. Each vial contained approximately 20 mL of 20 mg/L MB solution. For these studies, 200 mg of either **1a**(ACO), GAC, or ACO, and 15 mg of either PAN, PAN/AC1, PAN/AC2, or **2a**(PAN/AC2) fibers were separately added to the vials. Samples of 3 mL were taken at 30-min intervals, and the residual MB concentration was determined using a UV-Vis spectrometer by monitoring the absorbance at 664 nm. The adsorption capacities (Q_t, mg/g) were calculated using **Eq. 6.1** [189], and plot of Q_t vs time (min) obtained (**Fig. 6.1** and **6.2**).

$$Q_t = \frac{(C_0 - C_t)V}{m} \qquad \textbf{(6.1)}$$

Where: C_0 and C_t are the initial MB concentration (mg/L)and MB concentrations at time t (mg/L), respectively, in water, V = MB volume and m = mass of adsorbent (g) (**sample**).

As shown in **Fig. 6.1** and **6.2**, the adsorption capacity (Q_t) of methylene blue was significantly higher with the fibers compared to the granulated samples. For the granulated samples, the adsorption capacities were higher with the ACO supports and **1a**(ACO) than with GAC, **Fig. 6.1**. This observation has been corroborated by several researchers, who attribute it to the increased interactions between methylene blue and the oxygen-functionalized carbon surfaces [102,190,191]. Oxygen functionalization also increased external surface area (**Table 3.4**), which likely contributed to the enhanced adsorption capacity of ACO. Similarly, **1a**(ACO) exhibited excellent adsorption properties, presumably due to the ACO support.

In the case of the fibers, the adsorption capacity (Q_t) of methylene blue was much higher with PAN/AC2 (10% AC). The **2a**(PAN/AC2) fibers with the porphyrin dye, also displayed remarkably high methylene blue dye adsorption capacity, followed by the PAN/AC1 samples (5% AC). Considering that **2a**(PAN/AC2) was essentially obtained by completely dyeing PAN/AC2 with the **2a** dye, there was only a slight loss in the adsorption capacity of the resultant composite, as shown in **Fig. 6.2**. Notably, PAN fibers exhibited appreciable adsorption properties. However, fibers with activated carbon demonstrated superior methylene blue adsorption capabilities compared to pure PAN fibers. Equilibrium adsorption was achieved with pure PAN fibers after approximately 3 h. In contrast, the composite fibers (PAN/AC1, PAN/AC2, and **2a**(PAN/AC2)) continued to increase their adsorption capacities even after 6 hours, and by 12 h, all the methylene blue was removed from the solutions with PAN/AC1, PAN/AC2, and 2a(PAN/AC2), but not from

the solution with pure PAN fibers (**Fig 6.2b**). This may be attributed to two different but competing adsorption processes, given the varying physicochemical properties of PAN and AC.

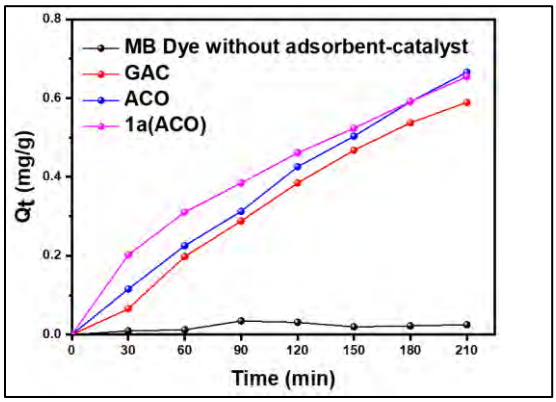

Fig. 6.1: GAC, ACO, and **1a**(ACO) adsorption capacities. Experimental conditions, pH = 6.5, (m) mass photocatalyst used = 200 mg, MB solution (~20 mg/L, 20 mL) temperature= 20 °C

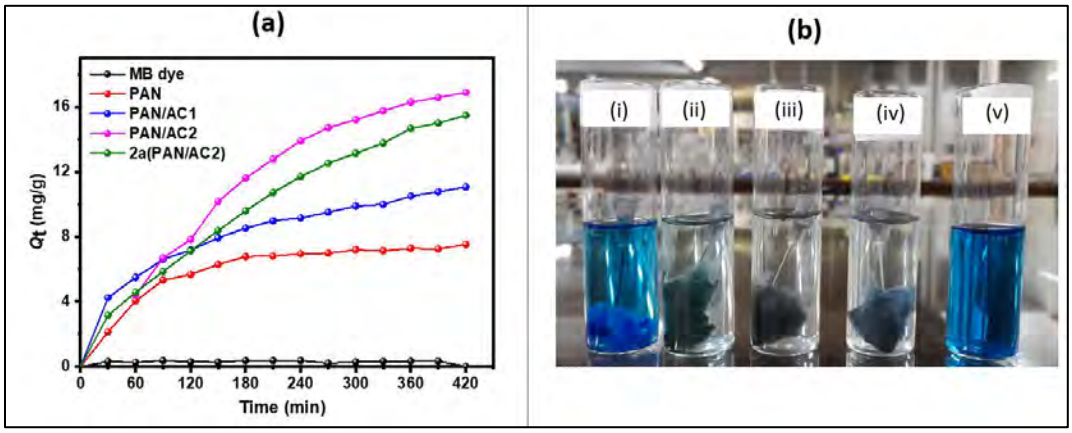

Fig. 6.2: (a) Adsorption capacities for PAN, PAN/AC1, PAN/AC2 and **2a**(PAN/AC2), Experimental conditions, pH = 6.5, (m) mass photocatalyst used = 15 mg, MB solution (~20 mg/L, 20 mL) temperature= 20 °C. (b) Photograph of MB solution after 12 h in the dark, (i) PAN, (ii) **2a**(PAN/AC2), (iii) PAN/AC2, and (iv) PAN/AC1 and (v) MB dye alone.

To further study the adsorption process, the data were fitted using the two common adsorption kinetic models: pseudo-first-order kinetic and pseudo-second-order kinetic models. The best model was evaluated based on the correlation coefficient (R^2). The pseudo-first-order kinetic model (**Eq. 6.2**) assumes that diffusion primarily controls adsorption, and adsorption rates are thus proportional to the number of methylene blue molecules remaining in the solution [192].

$$\ln(Q_e - Q_t) = \ln Q_e - k_1 t \qquad (6.2)$$

where k_1 = rate constant for adsorption (min^{-1}), Q_t and Q_e = are the adsorption capacities per unit mass of sorbent (mg/g) at any time (t), and equilibrium (where very minimal changes in concentration are observed), respectively. Q_e was obtained by calculating Q_t when the equilibrium concentration was reached; in this case, after about 3 h for PAN fibers which had reached equilibrium at this time. The rest of the fibers did not attain the equilibrium concentration, and by 12 h all the MB dye had been completely removed from the water. The pseudo-second-order kinetic model was also used to explain the adsorption of methylene blue. The pseudo-second-order kinetic model mainly assumes the chemisorption steps to control adsorption. Therefore, adsorption rates are proportional to the concentrations of two reactants, as expressed by (**Eq. 6.3**) [102,117].

$$\frac{t}{Q_t} = \frac{1}{k_2 Q_e^2} + \frac{t}{Q_e} \qquad (6.3)$$

The fitting parameters are summarized in **Table 6.1**, with the representative plots shown in **Fig. 6.3**. The first-order model was more effective in explaining the adsorption process for the granulated samples (GAC, ACO and **1a**(ACO)) and the PAN composites with the activated carbon and porphyrin (PAN/AC1, PAN/AC2, and **2a**(PAN/AC2)), judging by the calculated correlation coefficients (R^2) values obtained from the fittings. In contrast, the second-order model was more effective in explaining the adsorption process for the pure PAN samples, from the R^2 values (**Table**

6.1). Similar observation has been reported for PAN-based activated carbon fibers by Ibupoto and co-workers who studied the efficiency of methylene blue removal by pyrolyzed PAN fibers for their removal in water, where they suggested that the adsorption process is mainly due to chemical interaction between MB and the adsorbent [193].

Even though these studies indicate that the second-order model best explains methylene blue (MB) adsorption on pure PAN (**Table 6.1**), the PAN-AC composites are better described by the first-order model due to the presence of AC. The fit to the second-order model decreases with increasing amounts of AC in the PAN/AC composite samples. This suggests that PAN fibers favour the second-order model, as indicated by the R^2 values, while the activated carbon-related samples predominantly followed the first-order model, **Fig 6.3 and Table 6.1**.

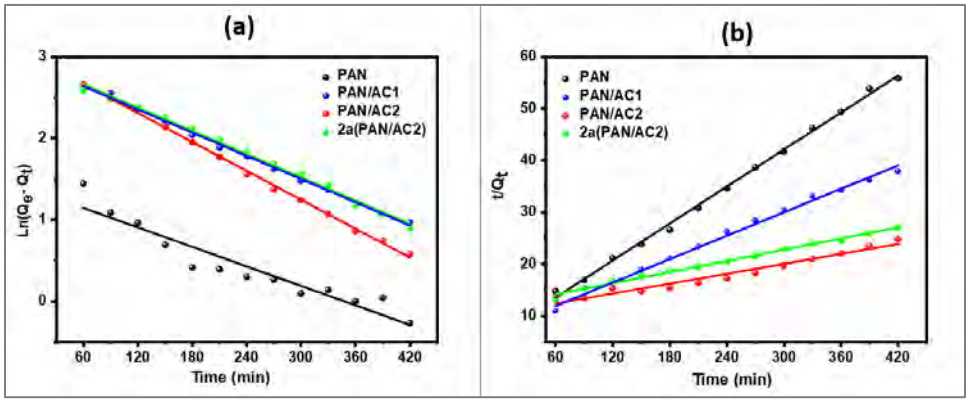

Fig. 6.3: (a) Pseudo-First-Order model and (b) Pseudo-Second-Order model for methylene blue adsorption on PAN, PAN/AC1, PAN/AC2, and **2a**(PAN/AC2), pH = ~7, T = 20 °C. (Used as an example)

Table 6.1: Pseudo-First-Order model and Pseudo-Second-Order model for methylene blue adsorption by AC, ACO, **1a**(ACO), PAN/AC1, PAN/AC2 and **2a**(PAN/AC2).

Samples	Pseudo-First Order Model			Pseudo-Second Order Model		
	k_1 (min^{-1}) x 10^{-3}	R^2	Q_e Exp (mg g^{-1})	Q_e, Cal (mg g^{-1})	K_2 (g mg^{-1} min^{-1}) x 10^{-4}	R^2
GAC	5.3	0.994	0.9	3.0	3.9	0.893
ACO	4.1	0.996	1.2	3.3	3.6	0.917
1a(ACO)	3.9	0.991	1.1	1.2	45.0	0.973
PAN	4.0	0.897	7.8	8.4	22.0	0.997
PAN/AC1	4.8	0.998	-	13.3	7.7	0.994
PAN/AC2	6.1	0.998	-	31.4	1.0	0.957
2a(PAN/AC2)	5.2	0.994	-	27.8	1.1	0.982

6.1.2. The effect of support material on the photodegradation of MB

Photocatalytic degradation experiments of methylene blue were conducted using both granular (GAC, ACO, and **1a**(ACO)) and fiber (PAN, PAN/AC1, PAN/AC2, and **2a**(PAN/AC2) samples under a white light source provided by a halogen lamp (set at approximately 70 W). The percentage removal (photodegradation) efficiencies, *Re* (%), were calculated using **Eq. 6.4** [194]**.**

$$\% \text{ Removal } = \left(\frac{C_0 - C_t}{C_0} \times 100\right) \qquad (\mathbf{6.4})$$

Where C_t is the dye concentration in solution at time *t,* C_o is the initial dye concentration. The kinetics of the degradation experiments were then evaluated using the first-order model (**Eq. 6.5**) [195,196].

$$\ln \frac{C_0}{C_t} = k_{app} t \qquad (6.5)$$

where C_0 = The starting concentration of methylene blue at the beginning of the experiment, C_t = the concentration of methylene blue at a given time ***t***, k_{app} = apparent rate constant

For the granulated samples, after 5 h of irradiation, **1a**(ACO) exhibited high photocatalytic activity, resulting in a much lighter solution compared to the other samples (**Fig. 6.4a**). The linear plots of $\ln(C_0/C_t)$ versus time were obtained (**Fig. 6.4b**). In terms of k_{app}, GAC showed relatively high catalytic activity (**Table 6.2**), considering that the adsorption capacity of ACO, as discussed above, is much higher than that of GAC. The increased methylene blue (MB) removal rate is thus most likely due to photodegradation. A similar observation was made by Velasco and co-workers when studying the degradation of phenol using TiO_2 anchored on activated carbon, where they also observed the formation of different degradation intermediates with activated carbon compared to those formed with just TiO_2 photocatalysts [197].

On the other hand, the functionalization of GAC with oxygen groups to form ACO resulted in a significant reduction in the apparent reaction rate constant (k_{app}) (**Table 6.2**). However, **1a**(ACO) showed more than a 100% increase in photocatalytic activity. Additionally, all the R^2 values were higher than 0.99, indicating that the degradation of methylene blue by **1a**(ACO), ACO, and GAC is consistent with the first-order model.

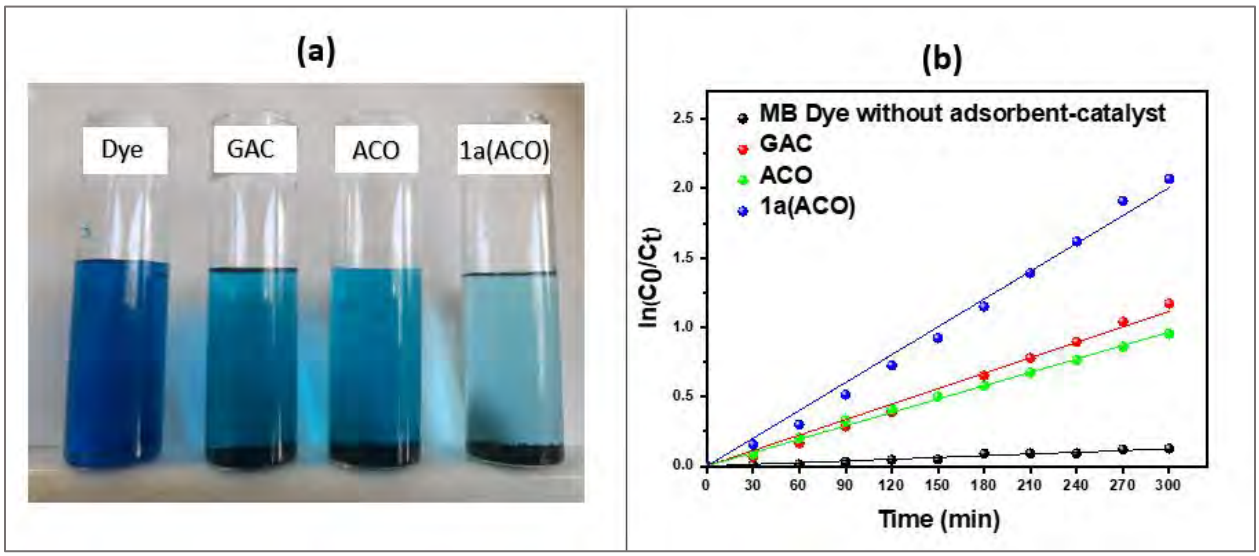

Fig. 6.4: (a) Photograph of MB solution after 5 h of irradiation with filtered visible light. (i) MB alone, (ii) MB with GAC, (iii) MB with ACO, and (iv) MB with **1a**(ACO), (b) kinetic linear simulation curves for degradation of methylene blue.

When comparing the granulated and fiber samples, the composite fibers samples displayed superior photocatalytic activity, judging by the k_{app} values in **Table 6.2**, despite only 15 mg of the fiber samples being used. Conversely, among the fibers, **2a**(PAN/AC2) exhibited the highest methylene blue (MB) removal efficiency (~93%), followed by PAN/AC2 (~90%), PAN/AC1 (~87%), pure PAN (~41%), and photolysis (due to photodegradation by light without a photocatalyst) at ~12% (**Table 6.2**)

Overall, PAN fibers alone exhibited the lowest photocatalytic activity and removal efficiency compared to all the samples (**Table 6.2, Fig. 6.5a**). All the activated carbon-based PAN composites (PAN/AC2 and PAN/AC1) showed high methylene blue (MB) removal efficiency during the first cycle (**Fig. 6.5b**) due to their high adsorptive properties. To further verify this, the fibers were rinsed with water, dried in the oven, and reused in subsequent cycles. There was a drastic reduction

in activity for all the fibers, likely due to clogging of the active sites, except for **2a**(PAN/AC2), which remained high. By the 5th cycle, the photocatalyst-adsorbent retained 75% of its photocatalytic activity compared to the rest of the fibers, which lost more than 25% of their activity (**Fig. 6.5b**). Thus, the photocatalyst adsorbents based on **2a**(PAN/AC2) are much more reusable under light, as they seem to regenerate during photocatalysis.

The final products of photocatalytic degradation of methylene blue have been identified elsewhere as CO_2, SO_4^{2-}, NO_3^- and NH_4^+ [198], which are generally non-toxic to humans but are also readily adsorbed by AC [199–202], thus making complete elimination of MB through the sequential adsorption/photocatalysis process feasible.

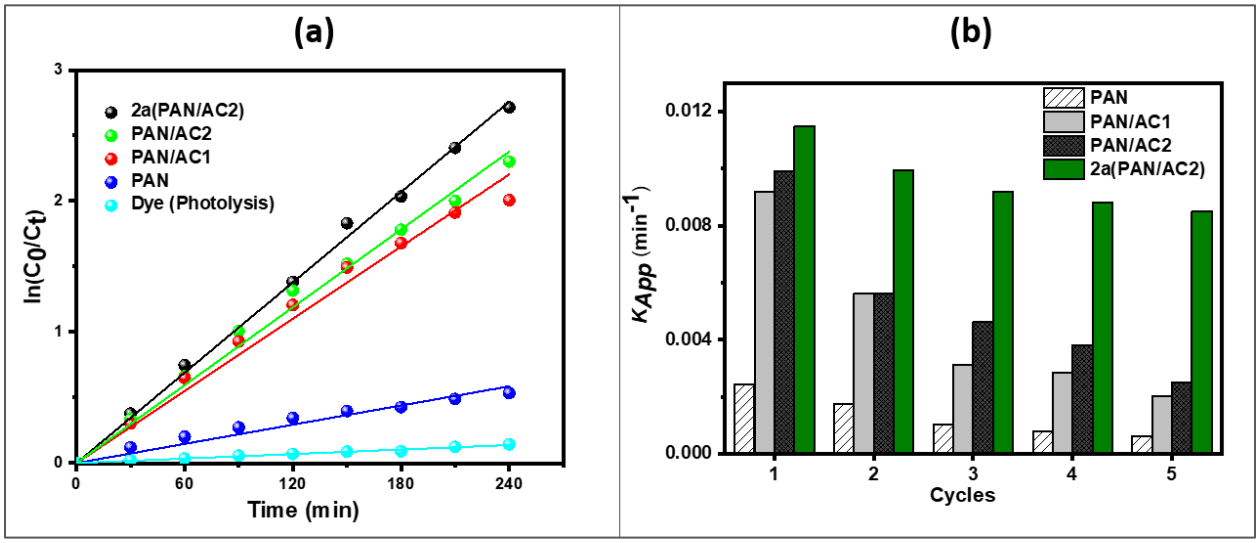

Fig. 6.5: (a) kinetic linear simulation curves for degradation of methylene blue and (b) Reusability studies of removal of MB dye by PAN, PAN/AC1, PAN/AC2 and **2a**(PAN/AC2) under light

[Experimental conditions: volume of solution (20 mL), time (4 h), adsorbent dosage (15 mg), temperature (298 K), agitation rate (200 rpm), concentration (~20 mg/L), pH(6.5)]. Photolysis = administering light to MB without any photocatalysts.

Table 6.2: First-order Kinetic parameters of methylene blue degradation.

Samples	% Removal efficiency	k_{app} (min $^{-1}$) x 10^{-3}	R^2
GAC	69.0	3.7	0.996
ACO	61.5	3.2	0.999
1a(ACO)	87.4	6.7	0.996
PAN	41.1	2.4	0.985
PAN/AC1	86.5	9.2	0.997
PAN/AC2	89.9	9.9	0.994
2a(PAN/AC2)	93.4	11.5	0.998
Photolysis (No photocatalyst)	11.8	0.6	0.995

6.1.3. The effect of hydrogen peroxide on photodegradation of MB using carbon-based and porphyrin-loaded materials

This study examined the impact of hydrogen peroxide on the photodegradation of methylene blue using carbon-based and porphyrin-loaded materials. Experiments were conducted with colloidal activated carbon and porphyrin-loaded colloidal activated carbon to evaluate their photocatalytic efficiency. The selection of colloidal activated carbon was based on its small size and unique optical properties, which contribute to an enhanced photodegradation process.

The experiments were conducted as follows: 200 µL of CAC and porphyrin/CAC suspensions (1 mg/L in water) were added to 3 mL of methylene blue solution (20 mg/L) in the cuvette. In a separate system, H_2O_2 (50 µL of 30% H_2O_2) was added to the similarly prepared mixture to

evaluate the effect of peroxide in the photodegradation process. It has been shown elsewhere that H_2O_2 displays high catalytic activity (as a Fenton-like catalyst) in degrading organic compounds in the dark by forming free radicals such as $^{\bullet}OH$ [203,204]. The spectral changes observed are shown in **Fig. 6.6** with **1a**/CAC, as an example, and the kinetics of the degradation experiment are then evaluated using the commonly used first-order model. After 1 h of irradiation, **1a**/CAC showed the highest photocatalytic activity with 31.8 % removal efficiency, followed by **2a**/CAC (30.2 %), CAC (27.0 %) and lastly **3a**/CAC (24.0 %), **Table 6.3** (**Fig 6.7** and **Fig. 6.8**).

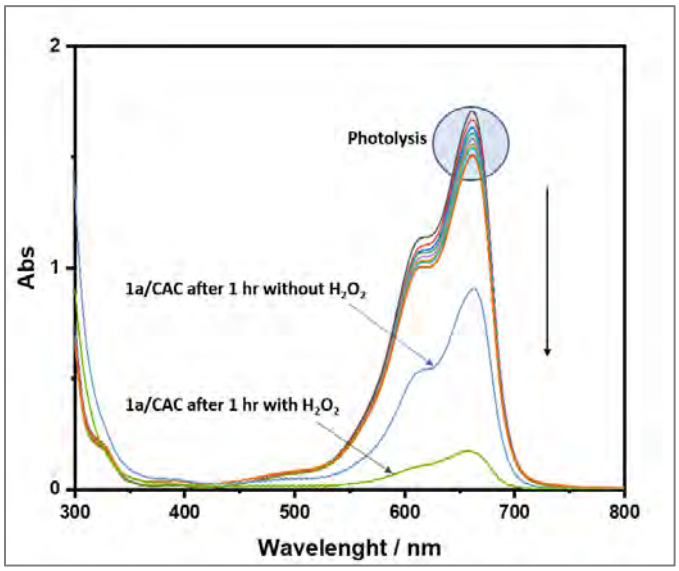

Fig. 6.6: UV-visible absorption spectral changes observed during degradation of MB using **1a**/CAC. [MB] = 20 mg/L, [catalyst] = 1 mg/L in water.

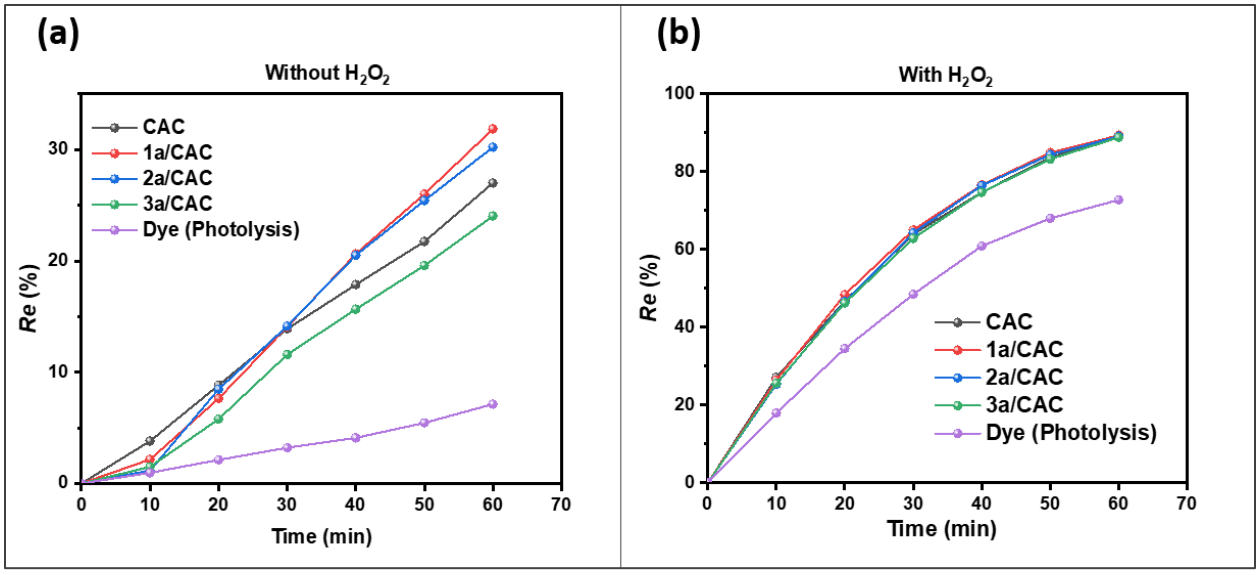

Fig. 6.7: Percentage removal efficiency of methylene blue (under Xe lamp), and with no photocatalyst in water (labelled as photolysis). [MB] = 20 mg/L, [catalyst] = 1 mg/L in water.

The higher efficiency of **1a**/CAC compared to **2a**/CAC does not agree with the singlet oxygen quantum yield values (**Table 6.3**). The differences will be explained below using zeta potential. Overall, in the presence of hydrogen peroxide, all the composites displayed very high photocatalytic activity (*ca.* 89 %). However, the **1a**/CAC displayed slightly higher photocatalytic activity at 89.3 % efficiency, followed by **2a**/CAC (89.0 %), CAC (88.9%) and lastly, **3a**/CAC (88.8%), **Table 6.3** (**Fig. 6.7, 6.8**), and follow the same trend as observed in the absence of hydrogen peroxide. The current study affirms that porphyrin aggregation is detrimental to photocatalytic activity, and aggregation overrides the advantages of low symmetry. The k_{app} values were also lowest for **3a**/CAC, for reasons given above. The increased removal efficiency in the presence of H_2O_2 peroxide, both in the presence and the absence of photocatalysts, in comparison to the peroxide-free experiment, is attributed to the action of the hydroxyl radicals [205].

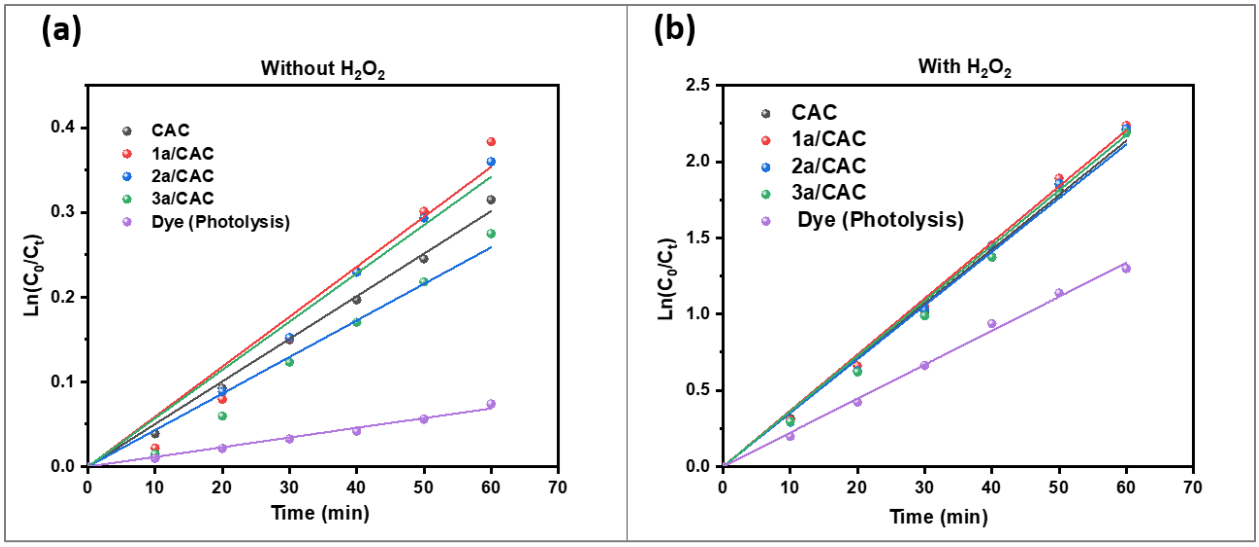

Fig. 6.8: Kinetic plots for degradation of methylene blue (under Xe lamp) and with no photocatalyst in water (labelled as photolysis). [MB] = 20 mg/L, [catalyst] = 1 mg/L in water.

Table 6.3: First-order kinetic parameters of degradation of methylene blue, [MB] = 20 mg/L, [catalyst] = 1 mg/L in water.

	[c]Φ_Δ	% Removal efficiency (%)[a]	MB Degradation under Xe lamp $k_{App}(min^{-1}) \times 10^{-3}$ (R^2)[b]	MB degradation using 1.5 % H_2O_2 and under Xe lamp $k_{App}(min^{-1}) \times 10^{-3}$ (R^2)[b]
CAC	-	27.0 (88.9)	5.0 (0.998)	35.6 (0.998)
1a/CAC	0.78	31.8 (89.3)	5.9 (0.984)	36.8 (0.998)
2a/CAC	0.94	30.2 (89.0)	5.7 (0.987)	36.3 (0.998)
3a/CAC	0.54	24.0 (88.8)	4.3 (0.988)	35.2 (0.998)
Dye (alone)	-	7.1 (72.7)	1.1 (0.995)	22.3 (0.999)

[a]Values in brackets are in the presence of H_2O_2; [b]R^2 values in brackets.[c]Values in DMF

The degradation experiments were carried out at neutral pH 7 in water since this provides the ideal photodegradation conditions, as reported in the literature [206]. **Fig. 6.9** shows the Zeta potentials versus the material tested at a pH of ~7. A negative zeta potential indicates that the dispersed

particles in the suspension are negatively charged. It has been demonstrated that activated carbon contains negative dissociative groups at pH > 4 due to carboxyl groups that are often present on the surface [207]. Zeta potential indicates the stability of colloidal dispersion [208], high zeta potential (positive or negative) as an indication of stability and the ability of the dispersion to resist aggregation [208]; low values indicate that attractive forces exceed repulsion, which results in aggregation. **1a**/CAC had the highest negative zeta potential (−22.1), followed by CAC (−20.6), **3a**/CAC (−19.4), and finally **2a**/CAC (−16.9). The high photocatalytic performance of **1a**/CAC (31.8% removal efficiency without H_2O_2, **Table 6.3**, **Fig. 6.7a**), in comparison to **2a**/CAC (30.2% removal efficiency without H_2O_2, **Fig. 6.7a**) can be attributed to the zeta potential. This observation indicates that the presence of **1a** on CAC results in the formation of a more stable colloidal dispersion. Moreover, the increased propensity for aggregation observed for **3a**/CAC is in accordance with the findings from UV-visible spectroscopy analysis.

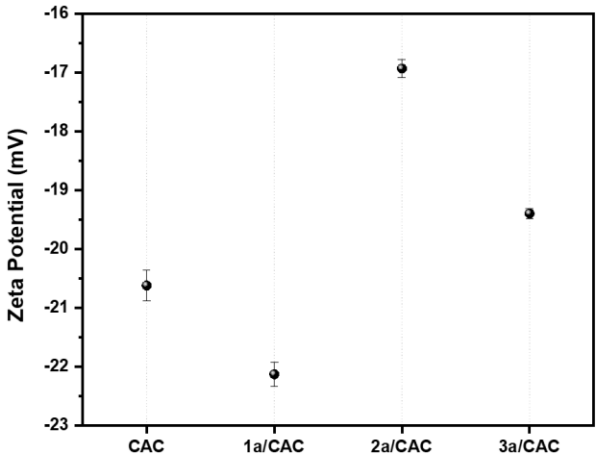

Fig. 6.9: Zeta potential measurements at pH ~7 in water.

6.2 Removal of ciprofloxacin in water using 2a(PAN/AC2) fibers under Xe lamp and sunlight irradiation

The combined adsorption/photocatalysis process for removing organic pollutants, such as pharmaceutical compounds like ciprofloxacin, using activated carbon fibers with deposited TiO_2 has been studied under UV light irradiation by Triquet and co-workers [209]. They demonstrated that the combined process is more efficient and only releases non-toxic aliphatic acids as degradation products, along with a significant amount of dissolved fluorine produced during a photochemical reaction on the surface of the adsorbent with the already adsorbed ciprofloxacin molecules.

This study aimed to evaluate whether similar or improved results could be achieved by using **2a**(PAN/AC2) fibers under visible light. Photodegradation was investigated using a Xe lamp (set at ~70 W) as the light source, with measurements taken at 30-min intervals for 5 h. Additionally, the effects using the Xe lamp were compared with those of sunlight irradiation. The sunlight irradiation was conducted to assess the practicality of using porphyrin-loaded PAN/AC fibers for the removal of organic pollutants, including pharmaceuticals such as ciprofloxacin, under real-life conditions. The studies were thus repeated under sunlight irradiation to demonstrate the viability of the porphyrin photocatalyst supported on PAN/AC fibers for the degradation of fluoroquinolones in water and to compare the effects of the two light sources.

Initially, **2a**(PAN/AC2) fibers were soaked in two separate vials containing ciprofloxacin solution, where one vial was placed in the dark and another under the Xe lamp or sunlight. A control vial with only ciprofloxacin solution (no photocatalyst) was sequentially added to the experiment under the Xe lamp or sunlight. **Fig 6.10** shows the experimental setup under sunlight irradiation (between 10.00 a.m. to 3.00 p.m., South Africa Time) on a bright sunny day.

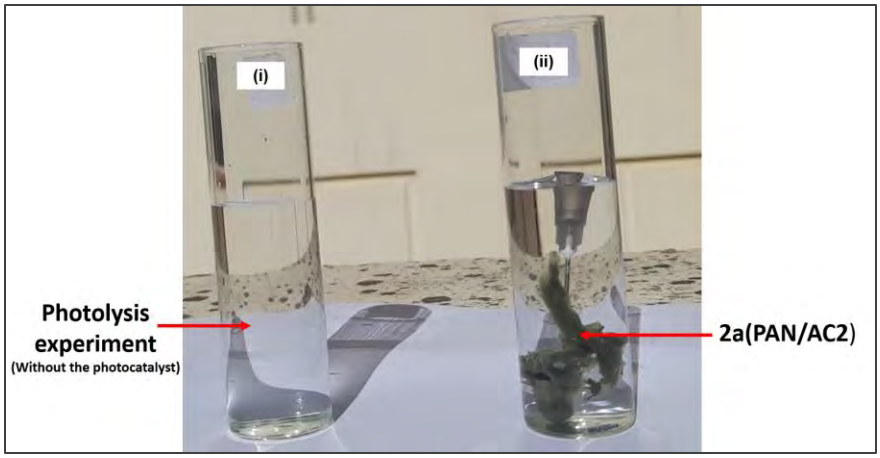

Fig. 6.10: Ciprofloxacin removal experimental setup in water under sunlight irradiation: (i) photolysis experiment, (ii) Photocatalytic degradation experiment [Experimental conditions: volume of solution (20 mL), time (5 h), Photocatalyst-adsorbent dosage (15 mg), drug concentration (20 mg/L), pH (6.5)].

All the ciprofloxacin degradation experiments were done under a neutral natural pH of ~7 in water since this provides the ideal photodegradation conditions as reported in the literature [210], and the changes of ciprofloxacin absorbance were recorded using UV-visible spectroscopy at 60 min intervals. **Fig. 6.11** shows the UV-Vis spectra obtained during the ciprofloxacin removal experiments by adsorption in the dark, photolysis, and photocatalytic degradation under Xe lamp and sunlight irradiation. The maximum wavelength of ciprofloxacin (λ_{max} 276 nm in water) was used to obtain measurement values from the spectra, which were then used to calculate the percentage removal efficiency (*%Re*) using **Eq. 6.4.**

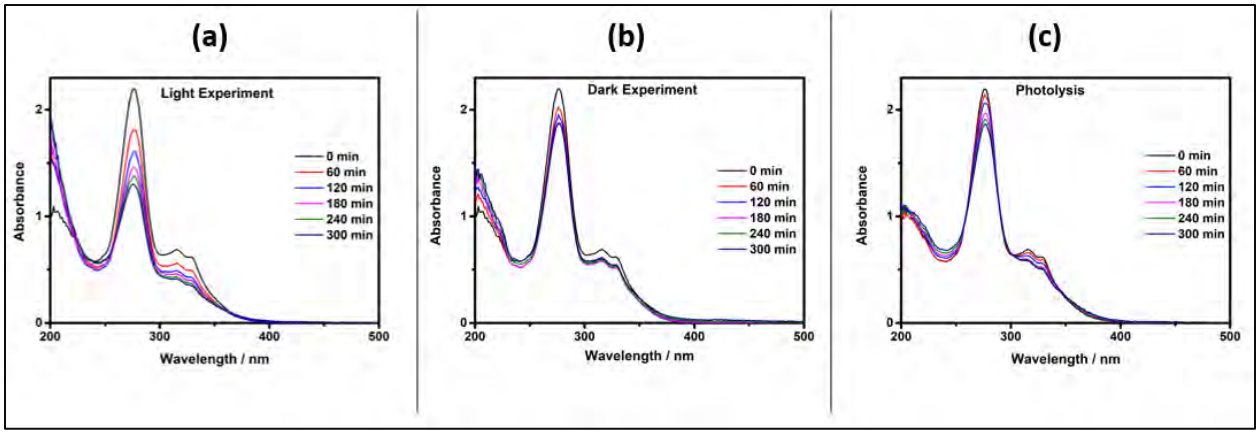

Fig. 6.11: Ciprofloxacin removal in water using **2a**(PAN/AC2) fibers: (a) photocatalysis experiment under sunlight irradiation, (b) adsorption experiment in the dark and (c) photolysis experiment (under solar irradiation and with no photocatalyst).

Fig. 6.12 (a) shows that after 5 h and using **2a**(PAN/AC2), ciprofloxacin removal efficiencies of ~14% in the dark (via adsorption) and ~42% and ~41% under Xe lamp and sunlight, respectively, were obtained (after 300 min). Removal efficiencies of ~4% and ~15% were obtained using Xe lamp and sunlight alone, respectively, without the photocatalyst adsorbent. Notably, adsorption equilibrium was reached after 3 h during the dark studies, as evidenced by the plateauing curve for the dark experiment curve. Conversely, both photocatalysis (using **2a**(PAN/AC2) with light) and photolysis (using light only) processes continued after 3 h. **Fig. 6.12b** illustrates the degradation kinetics for **2a**(PAN/AC2), with data plotted after omitting the first 60 min. The adsorption rate during this initial period was significantly higher than in subsequent intervals, hence the omission. According to the first-order model kinetics for the degradation, the apparent rate constant (k_{app}) of degradation under sunlight was ~2 times higher compared to Xe lamp due to the high photolysis rate (~3 times higher) of ciprofloxacin under sunlight irradiation than under UV-filtered light from the Xe lamp **Table 6.4**.

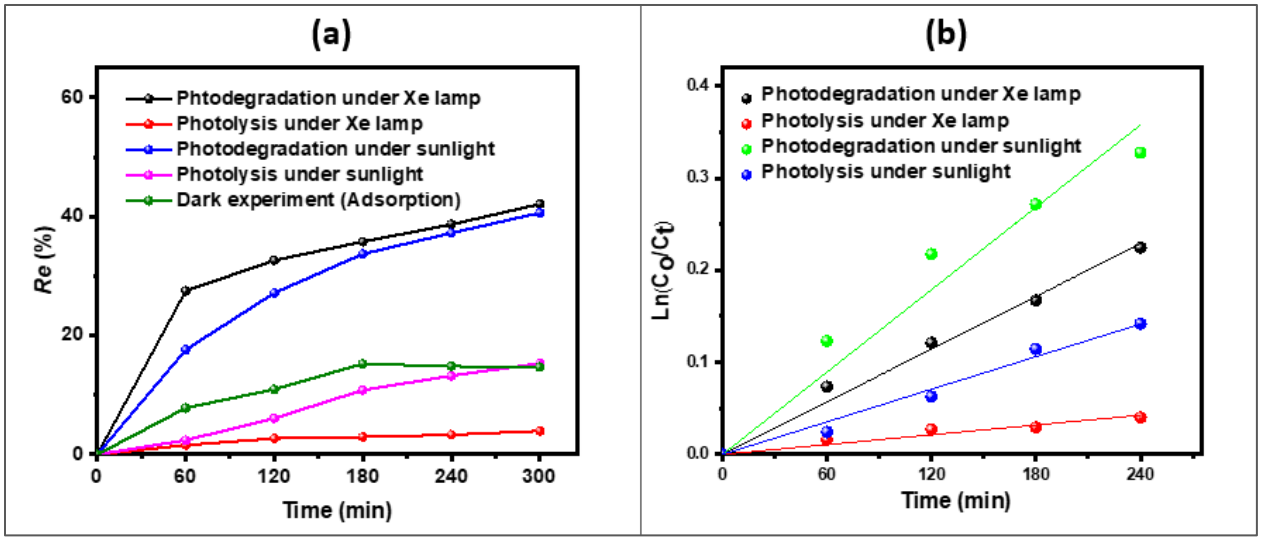

Fig. 6.12: (a) Percentage removal efficiency and (b) kinetic plots for degradation of ciprofloxacin in the presence of **2a**(PAN/AC2) (in the dark, under Xe lamp, and under sunlight) and with no photocatalyst (labeled as photolysis). *Re* (%) = % Removal efficiency.

Table 6.4: First-order kinetic parameters of ciprofloxacin degradation.

Samples	**Ciprofloxacin degradation under Xe lamp**		**Ciprofloxacin degradation under sunlight**	
	k_{App}(min^{-1}) x 10^{-4}	R^2	k_{App}(min^{-1}) x 10^{-4}	R^2
2a(PAN/AC2)	9.5	0.996	14.9	0.982
Photolysis (No photocatalyst)	1.8	0.975	5.9	0.992

According to this study, high photolysis of ciprofloxacin occurs under sunlight irradiation. Other researchers have made similar observations under simulated sunlight irradiation [5]. Photocatalysis of ciprofloxacin utilizing a porphyrin photocatalyst under both Xe lamp and sunlight conditions exhibited significantly higher removal rates (k_{App}) of 9.5 and 14.9, respectively, compared to photolysis values of 1.8 under Xe lamp and 5.9 under sunlight. This demonstrates that the

photocatalytic process is approximately 5 times more efficient under Xe lamp irradiation and 2.5 times more efficient under sunlight irradiation than photolysis,**Table 6.4**. Thus, indium porphyrin photocatalysts immobilized on PAN/AC2 composites are promising candidates for removing pharmaceutical compounds like ciprofloxacin from water through photocatalytic degradation.The higher removal rate under sunlight irradiation might be attributed to the broader spectrum of light from the sun, which includes ultraviolet (UV) radiation.

6.3 Optimizing nitrogen-doped carbon quantum dot-loaded polyacrylonitrile fibers with porphyrins for removal of MB and MO dyes in water: The effect of porphyrin functional groups and symmetry

This study investigates the interactions and photodegradation of cationic-methylene blue (MB) and anionic-methyl orange (MO) dyes with composite materials, specifically polyacrylonitrile (PAN) fibers embedded with nitrogen-doped carbon quantum dots (NCQD) and loaded with porphyrins. The unique properties of these composites offer a dual-benefit approach to water remediation, combining light-harvesting for photocatalysis and high adsorption capacity. By examining the effects of various porphyrin functional groups and their symmetry, this research aims to optimize the performance of these materials for environmental applications, enhancing their efficiency and sustainability in water purification processes.

The photodegradation experiments were conducted using a 70 W halogen lamp at various time intervals for 4 h. The main spectral changes observed are shown in **Fig. 6.13** for PAN, **5b**(PAN), PAN/NCQD, and **5b**(PAN/NCQD). The degradation kinetics were assessed using the first-order model. For methylene blue (MB) removal studies, **3a**(PAN/NCQD) gave the highest efficiency at 46%, followed by **1a**(PAN/NCQD1) (43%), **2a**(PAN/NCQD) (40%), PAN (34%), PAN/NCQD

(30%), **5b**(PAN) (27%), and **5b**(PAN/NCQD) (22%) **Fig. 6.14**, **Table 6.5**. The highest activity (high k_{App} and removal efficiency, **Table 6.5**) was obtained for **3a**(PAN/NCQD). This can be attributed to the presence of low-symmetry porphyrin **3a** and its favourable interaction with MB. Photolysis refers to the process by which the dye is broken down or transformed by light without a catalyst. In the case of methylene blue, removal efficiency through photolysis was 11%, **Table 6.5**. The high removal efficiency of PAN composites with porpyrin **1a**, **2a** and **3a** can be attributed to their strong adsorption properties and favourable interactions with MB, which is cationic. Cationic porphyrin **5b** on these supports reduced MB removal efficiency in the PAN and PAN/NCQD composite materials due to electrostatic repulsion between the porphyrin and MB molecules.

From the methyl orange (MO) removal studies, the **5b**(PAN/NCQD) fibers exhibited the highest removal efficiency (56%), followed by **5b**(PAN) (32%), **3a**(PAN/NCQD) (21%), **2a**(PAN/NCQD) (9%), **1a**(PAN/NCQD) (6%), PAN (4%), and PAN/NCQD (0.8%), **Fig 6.15, Table 6.5**. Thus, the PAN/NCQD composite, without porphyrin, exhibited very low photocatalytic activity compared to those with porphyrin photocatalysts. This low activity is attributed to high electron-hole recombination. Similar observations were reported by Xue and colleagues, where related quantum dots (nitrogen-doped graphene quantum dots) also exhibited minimal photocatalytic activity [154]. However, when combined with TiO_2, a significant improvement was achieved, up to 16 times more than TiO_2 alone [154]. The removal of MO dyes by photolysis was only 0.7%, compared to 11% for MB, indicating that MO is more photostable than MB.

The high activity of porphyrin **5b** for MO removal, as demonstrated by the apparent rate (k_{App}) values (**Fig. 6.13**, **Table 6.5**), but not for MB, can be attributed to charge interactions. MO, being negatively charged, interacts closely with the positively charged porphyrin **5b**, resulting in better

photocatalytic activity. The PAN and PAN/NCQD composites exhibited very low adsorption of MO in dark studies, in contrast to the high adsorption observed during the MB studies (**Fig. 6.13**). This may be attributed to the low interaction with the MO dye.

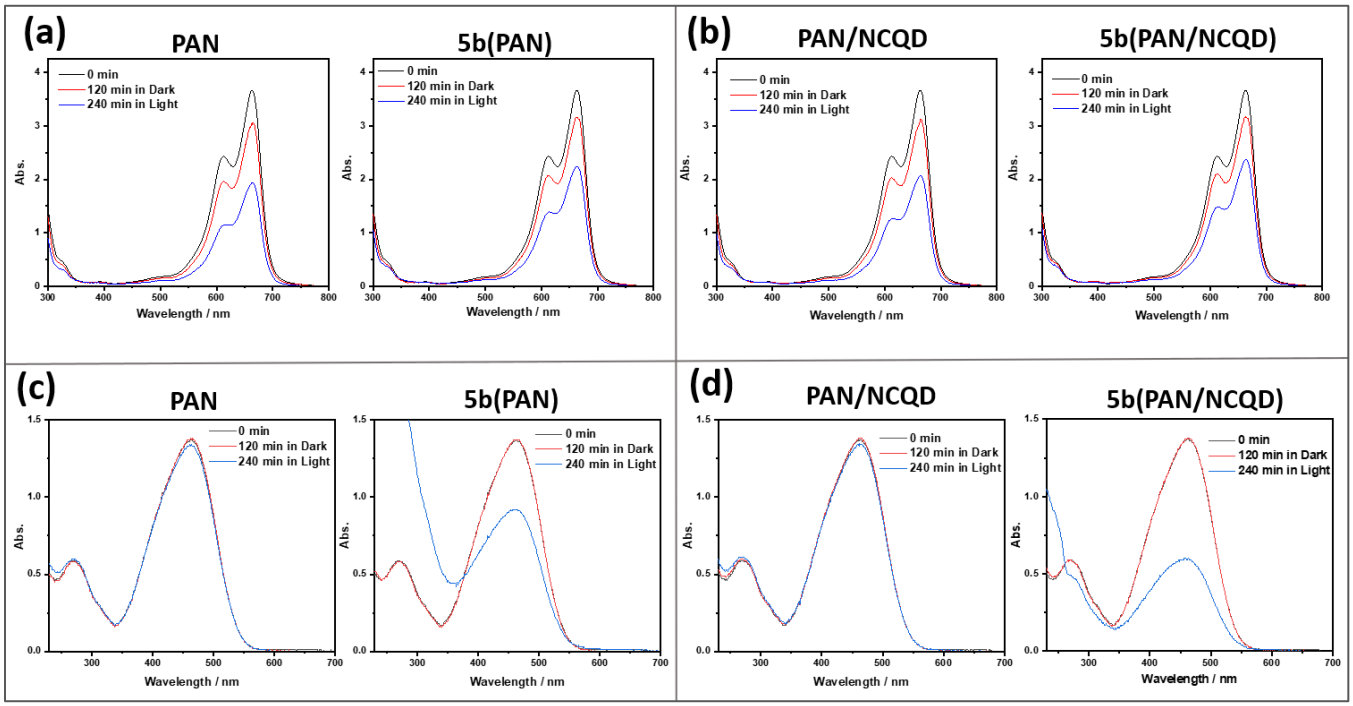

Fig. 6.13: UV-Vis spectral changes observed at the beginning and end of the (**a,b**) methylene blue and (**c,d**) methyl orange removal experiments using PAN, **5b**(PAN), PAN/NCQD and **5b**(PAN/NCQD).

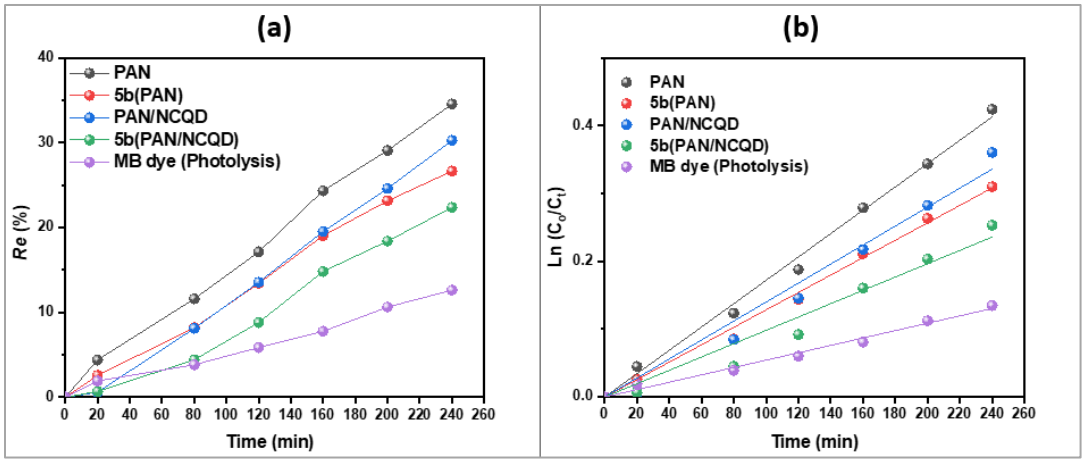

Fig. 6.14: (a) Percentage removal efficiency and (b) kinetic plots for degradation of MB in the presence of PAN composites, under a Halogen lamp and with no photocatalyst (labelled as photolysis). [Experimental conditions: volume of solution (20 mL), time (4 h), adsorbent dosage (15 mg), temperature (298 K), agitation rate (200 rpm), concentration (20 mg/L), pH(6.5)]. Photolysis = administering light to MB without any photocatalysts.

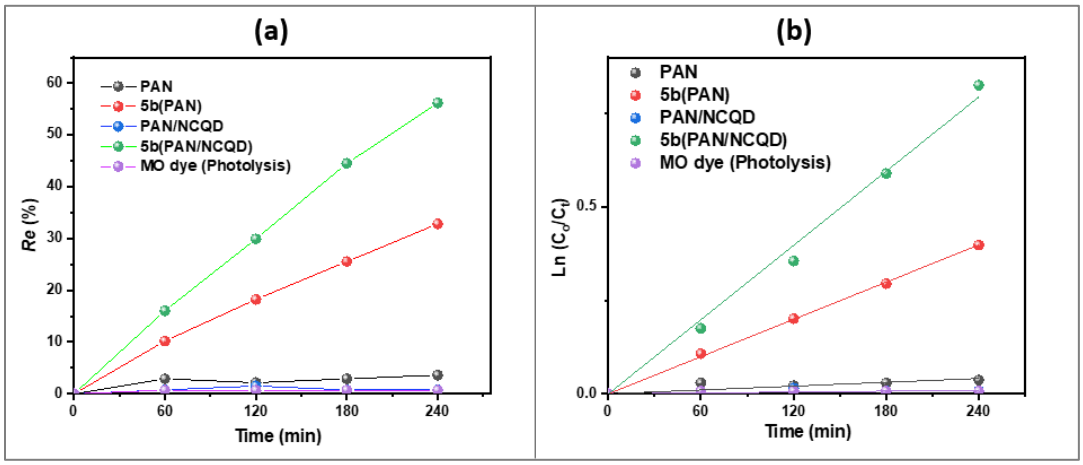

Fig. 6.15: (a) Percentage removal efficiency and (b) kinetic plots for degradation of MO in the presence of PAN composites (in the dark, under Xe lamp, and under sunlight) and with no photocatalyst (labelled as photolysis). [Experimental conditions: volume of solution (20 mL), time (4 h), adsorbent dosage (15 mg), temperature (298 K), concentration (20 mg/L), pH = (6.5)]. Photolysis = administering light to MO without any photocatalysts.

Table 6.5: First-order Kinetic parameters of methylene blue and methyl orange degradation with the prepared PAN composites.

	MB Degradation				MO degradation		
Samples	**% Removal efficiency**	k_{App} **(min^{-1}) x 10^{-3}**	R^2		**% Removal efficiency**	k_{App} **(min^{-1}) x 10^{-3}**	R^2
1a(PAN/NCQD)	43	2.30	0.995		6	0.28	0.971
2a(PAN/NCQD)	40	2.09	0.993		9	0.42	0.964
3a(PAN/NCQD)	46	2.60	0.999		21	1.01	0.999
PAN	34	1.72	0.998		4	0.17	0.864
5b(PAN)	27	1.28	0.998		32	1.66	0.999
PAN/NCQD	30	1.40	0.999		0.8	0.05	0.606
5b(PAN/NCQD)	22	0.98	0.981		56	3.31	0.997
Photolysis (No photocatalyst)	11	0.54	0.995		0.7	0.04	0.792

6.4 Antimicrobial efficacy testing

6.4.1 Antimicrobial efficacy of CAC and porphyrin-loaded CAC Composites with and without hydrogen peroxide

To investigate the antimicrobial effects of CAC and porphyrin-loaded CAC composites, both with and without H_2O_2, the zone of inhibition technique (**Fig. 6.16**) was used. This approach allowed further exploration of the potential of these systems in disinfection and sterilization processes, ultimately contributing to improved public health and environmental safety. From these studies, no inhibition zones were formed in the peroxide-free experiments. This is not surprising since Gram-negative bacteria are less susceptible to photodynamic inactivation than Gram-positive bacteria when using neutral or negatively charged photosensitizers [211]. The wells with only

0.5% H_2O_2 showed antimicrobial activity in both dark and light (under 415 nm light) studies against *Escherichia coli*. However, the zone of inhibition of the light studies was slightly higher than that of dark studies, **Fig. 6.16B**. The dark toxicity in **Fig. 6.16B** is due to the antimicrobial effects of hydrogen peroxide. The inhibition diameters from the light studies with the CAC and the porphyrin/CAC samples and with peroxide were larger than those with just peroxide alone. **3a**/CAC showed a slightly lower diameter in the light than the rest due to aggregation. Interestingly, **2a**/CAC has a higher antibacterial activity than **1a**/CAC, yet the latter had better photocatalytic activity against MB. This could be due to the antibacterial activities of alkynyl groups [212].

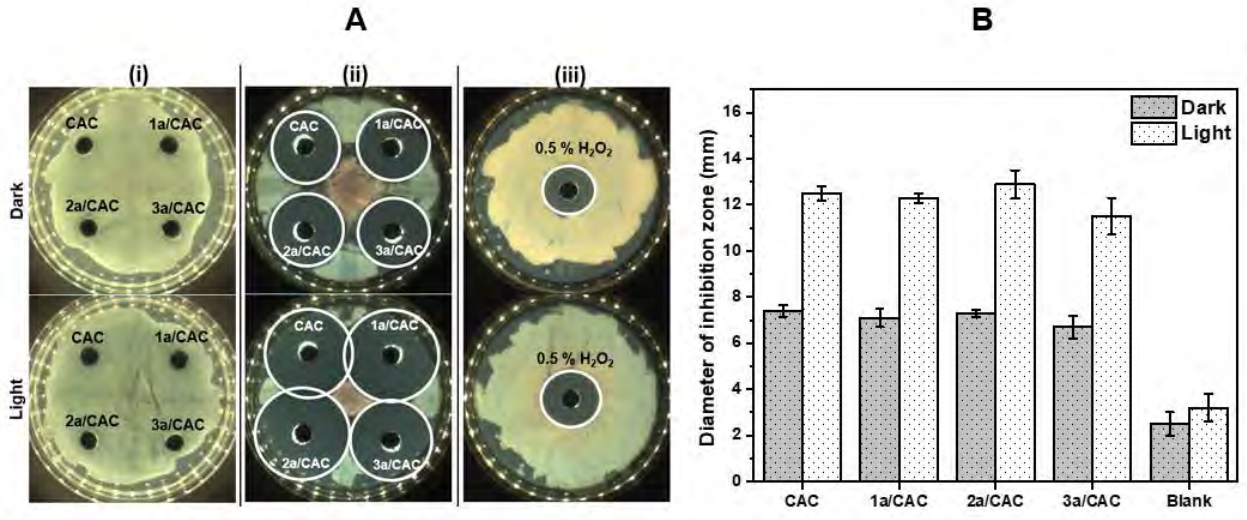

Fig. 6.16: (A) Illustrative images of bacterial culture plates of *E. coli*; (i) Composites suspension (without H_2O_2), (ii) Composites plus 0.5% H_2O_2 and (iii) blank wells with only 0.5% H_2O_2 solution, (B) Bar graph showing diameters of the zone of inhibitions. The circles in (A) represent the zone of inhibition.

6.4.2 Antimicrobial efficacy of PAN/NCQD and porphyrin-loaded PAN/NCQD composites

To investigate the antimicrobial and photodynamic therapy (aPDT) properties of the PAN/NCQD composites, including those loaded with porphyrins, Gram-(-) *E. coli* bacterial cells were subjected to treatment with the composites. This treatment occurred either under illumination for 30 and 60 min or in darkness.

The pure PAN fibers, without NCQD, did not exhibit significant alterations in viable cell numbers after 30 min of treatment, suggesting that PAN alone (control) lacks inherent antimicrobial activity against *E. coli* cells), **Fig. 6.17**. This behaviour underscores the need for additional antimicrobial agents to enhance the efficacy of PAN-based materials. In contrast, PAN/NCQD composites demonstrated appreciable antimicrobial efficacy. This effect was observed both in the presence and absence of light. Nitrogen-doped carbon quantum dots (NCQD) within the composite likely contributed to this enhanced antimicrobial activity. Previous studies have highlighted the inherent antimicrobial properties of CQD [213,214], making them promising candidates for bioactive materials.

The effect of different porphyrins (**1a**, **2a**, **3a**, and **5b**) on the antimicrobial and aPDT activities of PAN/NCQD composites was also investigated (**Fig 6.17** and **Table 6.6**). All porphyrin-loaded composites showed lower dark toxicity than PAN/NCQD. **5b**(PAN/NCQD showed high aPDT activity. It effectively inactivated *E. coli* cells, achieving 10% and 2% cell viability at 30 min and 60 min irradiation, respectively, highlighting the potent antimicrobial effect of this specific composite. The high aPDT activity of PAN/NCQD in the absence of porphyrins is due to high dark toxicity. The excellent performance of complex **5b** is due to its positive charge. Positively

charged porphyrins can electrostatically interact with the negatively charged bacteria cell wall [215,216], improving aPDT effects

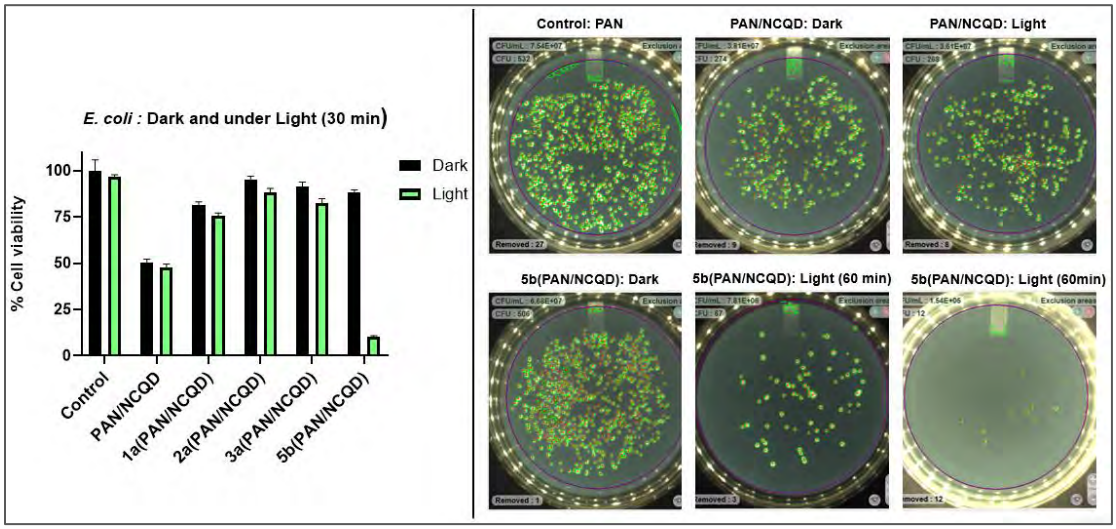

Fig. 6.17: Antibacterial and antimicrobial photodynamic therapy properties of PAN/NCQD1 and **5b**(PAN/NCQD1) fibers against *E. coli*: (**Right**) Cell viability plot with data presented as mean values of triplicate measurement with SD bars, (**Left**) Sample of *E. coli* colonies obtained during the experiment.

Table 6.6: % Cell survival values using 0.5 mg/mL of PAN, PAN/NCQD, and porphyrin-loaded PAN/NCQD composites against *E. coli* in water in the dark and after irradiation with white light for 30 and 60 min.

Sample	**% Cell survival**		
	Dark for 30 min	**Light for 30 min**	**Light for 60 min**
Control (PAN)	99	98	96
PAN/NCQD	51	48	37
1a(PAN/NCQD)	81	76	70
2a(PAN/NCQD)	95	88	81
3a(PAN/NCQD)	91	82	79
5b(PAN/NCQD)	89	10	2

6.5 Proposed degradation mechanisms of pollutants

The proposed degradation mechanism by the activated carbon-based supports is illustrated in **Fig. 6.18**. When illuminated with visible light, the porphyrins generate electron-hole pairs [72,217], which are dispersed on the surface of the activated carbon (ACO). This dispersion minimizes recombination, increasing the lifetimes of the charge carriers and enhancing the formation of singlet oxygen and hydroxyl radicals. Dye molecules are degraded on the porphyrin(ACO) surface by active species, such as hydroxyl radicals (·OH) and singlet oxygen ($^1O_2$), formed through reactions between photogenerated electrons and dissolved oxygen, as well as photogenerated holes and water (OH^- or H_2O) [72].

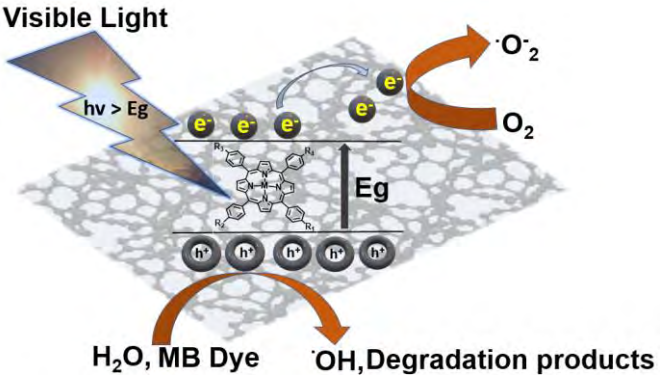

Fig. 6.18: Possible mechanism of the photocatalytic degradation of MB by **1a**(ACO) photocatalyst, used as an example.

For the porphyrin-loaded (PAN/NCQD) composites, a different degradation mechanism is proposed due to the fluorescent nature of the composite fibers, **Fig 6.19**. Both porphyrins and nitrogen-doped carbon quantum dots (NCQD) are involved in the photocatalytic process. When exposed to visible light, they generate electron-hole pairs. The excited electrons within the NCQD are transferred to the porphyrins, preventing charge recombination. Reactive oxygen species (ROS), including hydroxyl radicals (·OH) and superoxide radicals ($O_2{\cdot}^-$), as well as

photogenerated holes, degrade MB/MO/ciprofloxacin molecules on the surface porphyrin (PAN/NCQD) fibers. Additionally, sensitized porphyrins produce singlet oxygen ($^1O_2$), effectively degrading water dyes. The combination of NCQD and porphyrins enhances photocatalytic activity, making the composite material efficient for visible-light-driven pollutant degradation.

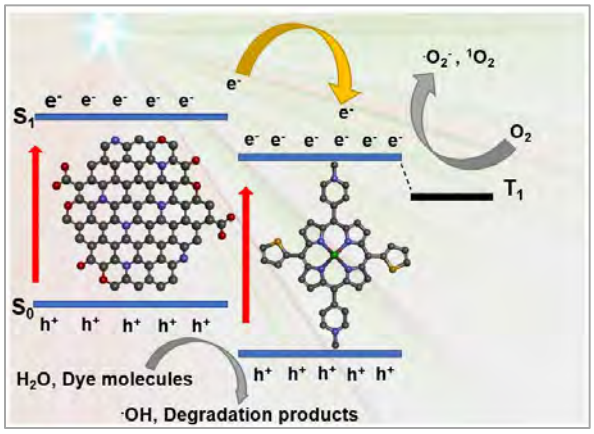

Fig. 6.19: Possible mechanism of the photocatalytic degradation of MB and MO dyes by **5b**(PAN/NCQD), used as an example.

6.6 Closing remarks

The porphyrin-loaded composite carbon materials have demonstrated significant potential in removing organic pollutants from water. Their enhanced photocatalytic activity and antimicrobial properties against *E. coli* bacteria, particularly in the presence of hydrogen peroxide, highlight the effectiveness of these materials in disinfection and water treatment applications. The synergistic effect from the combination of porphyrins and carbon-based supports, especially nitrogen-doped carbon quantum dots (NCQD), not only improves pollutant degradation but also offers a promising approach to addressing microbial contamination.

CHAPTER 7: Conclusions and recommendations

This chapter presents the conclusions and the future perspectives of this work

7.1 General conclusions

In this thesis, porphyrin-loaded carbon-based support materials, including activated carbon-related supports and nitrogen-doped carbon quantum dots (NCQD), were evaluated for removing organic pollutants in water. Their bactericidal and antimicrobial photodynamic therapy (aPDT) properties were also assessed, mainly using *E. coli*, the most common bacterium associated with waterborne diseases.

The activated carbon-related supports included oxygen-functionalized granular activated carbon (ACO), colloidal activated carbon (CAC), and polyacrylonitrile/activated carbon (PAN/AC) composites, as well as those loaded with porphyrins (**1a**, **2a**, and **3a**). These materials were evaluated for their efficiency in dye removal through adsorption and combined adsorption-photodegradation processes, using methylene blue (MB) as a model dye. The findings demonstrate that the physicochemical properties of the activated carbon support materials significantly influence their efficiency in dye removal. Notably, adding porphyrins did not significantly affect the surface area of the composites but markedly improved their photoactivity.

Adding hydrogen peroxide enhanced the photodegradation of MB and the deactivation of *E. coli*, mainly when using CAC and porphyrin-loaded CAC samples (porphyrins **1a**, **2a**, and **3a**). This highlights the role of hydrogen peroxide in improving the effectiveness of the photodegradation process. Higher activities were realized with the porphyrin samples, although porphyrin aggregation, as seen with porphyrin **3a**, can interfere with these activities. The study also compared the degradation of ciprofloxacin under different light sources, specifically a Xe lamp and natural sunlight, using porphyrin **2a** loaded on PAN/AC2 supports. The findings indicate that removal in natural sunlight was higher than under the Xe lamp, with significant implications for practical

applications. Both MB and ciprofloxacin were used to represent organic compounds in these experiments.

Furthermore, the effect of porphyrin charge on antimicrobial photodynamic therapy (aPDT) activities was investigated. The activities of porphyrins **4a** and **5a** and their cationic forms **4b** and **5b** were tested against planktonic cells of *S. aureus* and *E. coli*. The results indicate that the charge of porphyrins plays a crucial role in determining their antimicrobial efficacy. Additionally, the effect of porphyrin functional groups was studied by comparing the deactivation of biofilms of *S. aureus* and *E. coli* using porphyrins **4b** and **5b**. Further experiments focused on the photodegradation of MB and methyl orange (MO), as well as the deactivation of *E. coli* in water, using porphyrins **1a**, **2a**, **3a**, and **5b** loaded on PAN/nitrogen-doped carbon quantum dot (NCQD) fibers. Overall, the porphyrin-loaded PAN/NCQD composites were effective, especially those loaded with cationic indium porphyrin **5b**, which exhibited higher aPDT effects for *E. coli* and in MB degradation experiments. These studies underscore the importance of functional groups in enhancing the performance of porphyrins as photocatalysts in water treatment applications.

Finally, the effect of porphyrin symmetry on the removal of MB and MO was investigated by comparing the activities of porphyrins **1a**, **2a**, **3a**, and **5b** loaded on PAN/NCQD fibers. The unsymmetrical indium porphyrin **3a** showed promising activity in MO and MB removal studies, making it a better performer during the degradation experiments. The findings reveal that the symmetry of porphyrins can significantly influence their effectiveness in photodegradation and antimicrobial applications

7.2 Recommendations and future perspectives

To build on these findings, future research should optimize support materials by exploring various options, including novel composites and hybrid materials. Investigating the optimal concentrations and application methods of hydrogen peroxide and exploring alternative oxidizing agents and competing ions could provide more effective and sustainable options for enhancing photodegradation and antimicrobial activities, particularly for treating industrial and hospital effluents. Additionally, it would be beneficial to test the most promising materials and methods under real-world conditions. This could involve using flow systems that combine granulated samples and fibers in natural water bodies or industrial wastewater. Such testing will help evaluate the practical applicability and effectiveness of these materials on a larger scale.

REFERENCES

[1] Morin-Crini, N.; Lichtfouse, E.; Liu, G.; Balaram, V.; Ribeiro, A.R.L.; Lu, Z.; Stock, F.; Carmona, E.; Teixeira, M.R.; Picos-Corrales, L.A.; Moreno-Piraján, J.C.; Giraldo, L.; Li, C.; Pandey, A.; Hocquet, D.; Torri, G.; Crini, G. Worldwide Cases of Water Pollution by Emerging Contaminants: A Review. *Environ. Chem. Lett.*, **2022**, *20*, 2311–2338.

[2] Gonsioroski, A.; Mourikes, V.E.; Flaws, J.A. Endocrine Disruptors in Water and Their Effects on the Reproductive System. *Int. J. Mol. Sci.*, **2020**, *21*, 1929.

[3] Hassaan, M.A.; El Nemr, A. Pesticides Pollution: Classifications, Human Health Impact, Extraction and Treatment Techniques. *Egypt. J. Aquat. Res.*, **2020**, *46*, 207–220.

[4] Bai, X.; Ma, X.; Xu, F.; Li, J.; Zhang, H.; Xiao, X. The Drinking Water Treatment Process as a Potential Source of Affecting the Bacterial Antibiotic Resistance. *Sci. Total Environ.*, **2015**, *533*, 24–31.

[5] Babić, S.; Periša, M.; Škorić, I. Photolytic Degradation of Norfloxacin, Enrofloxacin and Ciprofloxacin in Various Aqueous Media. *Chemosphere*, **2013**, *91*, 1635–1642.

[6] Challis, J.K.; Hanson, M.L.; Friesen, K.J.; Wong, C.S. A Critical Assessment of the Photodegradation of Pharmaceuticals in Aquatic Environments: Defining Our Current Understanding and Identifying Knowledge Gaps. *Environ. Sci. Process. Impacts*, **2014**, *16*, 672–696.

[7] Fernández, L.; Esteves, V.I.; Cunha, Â.; Schneider, R.J.; Tomé, J.P.C. Photodegradation of Organic Pollutants in Water by Immobilized Porphyrins and Phthalocyanines. *J. Porphyr. Phthalocyanines*, **2016**, *20*, 150–166.

[8] Yan, S.; Song, W. Photo-Transformation of Pharmaceutically Active Compounds in the Aqueous Environment: A Review. *Environ. Sci. Process. Impacts*, **2014**, *16*, 697–720.

[9] Wang, Y.; Roddick, F.A.; Fan, L. Direct and Indirect Photolysis of Seven Micropollutants in Secondary Effluent from a Wastewater Lagoon. *Chemosphere*, **2017**, *185*, 297–308.

[10] Warneck, P.; Wurzinger, C. Product Quantum Yields for the 305-nm Photodecomposition of Nitrate in Aqueous Solution. *J. Phys. Chem.*, **1988**, *92*, 6278–6283.

[11] Mack, J.; Bolton, J.R. Photochemistry of Nitrite and Nitrate in Aqueous Solution: A Review. *J. Photochem. Photobiol. Chem.*, **1999**, *128*, 1–13.

[12] Azuma, T.; Usui, M.; Hayashi, T. Inactivation of Antibiotic-Resistant Bacteria in Wastewater by Ozone-Based Advanced Water Treatment Processes. *Antibiotics*, **2022**, *11*, 210.

[13] Xi, C.; Zhang, Y.; Marrs, C.F.; Ye, W.; Simon, C.; Foxman, B.; Nriagu, J. Prevalence of Antibiotic Resistance in Drinking Water Treatment and Distribution Systems. *Appl. Environ. Microbiol.*, **2009**, *75*, 5714–5718.

[14] Samrot, A.V.; Wilson, S.; Sanjay Preeth, R.S.; Prakash, P.; Sathiyasree, M.; Saigeetha, S.; Shobana, N.; Pachiyappan, S.; Rajesh, V.V. Sources of Antibiotic Contamination in Wastewater and Approaches to Their Removal—An Overview. *Sustainability*, **2023**, *15*, 12639.

[15] Manaia, C.M.; Macedo, G.; Fatta-Kassinos, D.; Nunes, O.C. Antibiotic Resistance in Urban Aquatic Environments: Can It Be Controlled? *Appl. Microbiol. Biotechnol.*, **2016**, *100*, 1543–1557.

[16] Mutuku, C.; Gazdag, Z.; Melegh, S. Occurrence of Antibiotics and Bacterial Resistance Genes in Wastewater: Resistance Mechanisms and Antimicrobial Resistance Control Approaches. *World J. Microbiol. Biotechnol.*, **2022**, *38*, 152.

[17] Oladoye, P.O.; Ajiboye, T.O.; Omotola, E.O.; Oyewola, O.J. Methylene Blue Dye: Toxicity and Potential Elimination Technology from Wastewater. *Results Eng.*, **2022**, *16*, 100678.

[18] Cheng, J.; Zhan, C.; Wu, J.; Cui, Z.; Si, J.; Wang, Q.; Peng, X.; Turng, L.-S. Highly Efficient Removal of Methylene Blue Dye from an Aqueous Solution Using Cellulose Acetate Nanofibrous Membranes Modified by Polydopamine. *ACS Omega*, **2020**, *5*, 5389–5400.

[19] Neethu, N.; Choudhury, T. Treatment of Methylene Blue and Methyl Orange Dyes in Wastewater by Grafted Titania Pillared Clay Membranes. *Recent Pat. Nanotechnol.*, **2018**, *12*, 200–207.

[20] Wu, L.; Liu, X.; Lv, G.; Zhu, R.; Tian, L.; Liu, M.; Li, Y.; Rao, W.; Liu, T.; Liao, L. Study on the Adsorption Properties of Methyl Orange by Natural One-Dimensional Nano-Mineral Materials with Different Structures. *Sci. Rep.*, **2021**, *11*, 10640.

[21] Shen, M.; Hu, Y.; Zhao, K.; Li, C.; Liu, B.; Li, M.; Lyu, C.; Sun, L.; Zhong, S. Occurrence, Bioaccumulation, Metabolism and Ecotoxicity of Fluoroquinolones in the Aquatic Environment: A Review. *Toxics*, **2023**, *11*, 966.

[22] Kümmerer, K. Antibiotics in the Aquatic Environment – A Review – Part I. *Chemosphere*, **2009**, *75*, 417–434.

[23] Devane, M.L.; Moriarty, E.; Weaver, L.; Cookson, A.; Gilpin, B. Fecal Indicator Bacteria from Environmental Sources; Strategies for Identification to Improve Water Quality Monitoring. *Water Res.*, **2020**, *185*, 116204.

[24] Pandey, P.K.; Kass, P.H.; Soupir, M.L.; Biswas, S.; Singh, V.P. Contamination of Water Resources by Pathogenic Bacteria. *AMB Express*, **2014**, *4*, 51.

[25] Uluseker, C.; Kaster, K.M.; Thorsen, K.; Basiry, D.; Shobana, S.; Jain, M.; Kumar, G.; Kommedal, R.; Pala-Ozkok, I. A Review on Occurrence and Spread of Antibiotic Resistance in Wastewaters and in Wastewater Treatment Plants: Mechanisms and Perspectives. *Front. Microbiol.*, **2021**, *12*.

[26] Al-Nuaim, M.A.; Alwasiti, A.A.; Shnain, Z.Y. The Photocatalytic Process in the Treatment of Polluted Water. *Chem. Pap.*, **2023**, *77*, 677–701.

[27] Ohko, Y.; Iuchi, K.-I.; Niwa, C.; Tatsuma, T.; Nakashima, T.; Iguchi, T.; Kubota, Y.; Fujishima, A. 17 Beta-Estradiol Degradation by TiO_2 Photocatalysis as a Means of Reducing Estrogenic Activity. *Environ. Sci. Technol.*, **2002**, *36*, 4175–4181.

[28] Jenks, W.S. Photocatalytic Reaction Pathways – Effects of Molecular Structure, Catalyst, and Wavelength. In: *Photocatalysis and Water Purification*; Pichat, P., Ed.; John Wiley & Sons, Ltd: Weinheim, Germany, **2013**; Vol. 1, pp. 25–51.

[29] Yahya, N.; Aziz, F.; Jamaludin, N.A.; A. Mutalib, M.; Ismail, A.F.; W. Salleh, W.N.; Jaafar, J.; Yusof, N.; A. Ludin, N. A Review of Integrated Photocatalyst Adsorbents for Wastewater Treatment. *J. Environ. Chem. Eng.*, **2018**, *6*, 7411–7425.

[30] Auwärter, W.; Écija, D.; Klappenberger, F.; Barth, J.V. Porphyrins at Interfaces. *Nat. Chem.*, **2015**, *7*, 105–120.

[31] Makarska, M.; Radzki, S. Water-Soluble Porphyrins and Their Metal Complexes. *ChemInform*, **2004**, *35*.

[32] Malik, Z.; Hanania, J.; Nitzan, Y. Bactericidal Effects of Photoactivated Porphyrins—An Alternative Approach to Antimicrobial Drugs. *J. Photochem. Photobiol. B*, **1990**, *5*, 281–293.

[33] Gouterman, M. Spectra of Porphyrins. *J. Mol. Spectrosc.*, **1961**, *6*, 138–163.

[34] Makola, L.C.; Managa, M.; Nyokong, T. Enhancement of Photodynamic Antimicrobialtherapy through the Use of Cationic Indium Porphyrin Conjugated to Ag/$CuFe_2O_4$ Nanoparticles. *Photodiagnosis Photodyn. Ther.*, **2020**, *30*, 101736.

[35] Rothemund, P. Formation of Porphyrins from Pyrrole and Aldehydes. *J. Am. Chem. Soc.*, **1935**, *57*, 2010–2011.

[36] Adler, A.D.; Longo, F.R.; Finarelli, J.D.; Goldmacher, J.; Assour, J.; Korsakoff, L. A Simplified Synthesis for Meso-Tetraphenylporphine. *J. Org. Chem.*, **1967**, *32*, 476–476.

[37] Lindsey, J.S.; Schreiman, I.C.; Hsu, H.C.; Kearney, P.C.; Marguerettaz, A.M. Rothemund and Adler-Longo Reactions Revisited: Synthesis of Tetraphenylporphyrins under Equilibrium Conditions. *J. Org. Chem.*, **1987**, *52*, 827–836.

[38] Lindsey, J.S. The Synthesis of Meso-Substituted Porphyrins. In: *Metalloporphyrins Catalyzed Oxidations*; Montanari, F.; Casella, L., Eds.; Catalysis by Metal Complexes; Springer: Dordrecht, Netherlands, **1994**; Vol. 17, pp. 49–86.

[39] Mondal, S.; Pain, T.; Sahu, K.; Kar, S. Large-Scale Green Synthesis of Porphyrins. *ACS Omega*, **2021**, *6*, 22922–22936.

[40] Koszarna, B.; Gryko, D.T. Efficient Synthesis of Meso-Substituted Corroles in a H_2O−MeOH Mixture. *J. Org. Chem.*, **2006**, *71*, 3707–3717.

[41] Wainwright, M. Photodynamic Antimicrobial Chemotherapy (PACT). *J. Antimicrob. Chemother.*, **1998**, *42*, 13–28.

[42] Jori, G.; Fabris, C.; Soncin, M.; Ferro, S.; Coppellotti, O.; Dei, D.; Fantetti, L.; Chiti, G.; Roncucci, G. Photodynamic Therapy in the Treatment of Microbial Infections: Basic Principles and Perspective Applications. *Lasers Surg. Med.*, **2006**, *38*, 468–481.

[43] Tegos, G.; Dai, T.; Fuchs, B.B.; Coleman, J.J.; Prates, R.A.; Astrakas, C.; St. Denis, T.G.; Ribeiro, M.S.; Mylonakis, E.; Hamblin, M.R. Concepts and Principles of Photodynamic Therapy as an Alternative Antifungal Discovery Platform. *Front. Microbiol.*, **2012**, *3*.

[44] Carvalho, C.M.B.; Tomé, J.P.C.; Faustino, M.A.F.; Neves, M.G.P.M.S.; Tomé, A.C.; Cavaleiro, J.A.S.; Costa, L.; Alves, E.; Oliveira, A.; Cunha, Â.; Almeida, A. Antimicrobial Photodynamic Activity of Porphyrin Derivatives: Potential Application on Medical and Water Disinfection. *J. Porphyr. Phthalocyanines*, **2009**, *13*, 574–577.

[45] Huang, H.; Song, W.; Rieffel, J.; Lovell, J.F. Emerging Applications of Porphyrins in Photomedicine. *Front. Phys.*, **2015**, *3*.

[46] Ryskova, L.; Buchta, V.; Slezak, R. Photodynamic Antimicrobial Therapy. *Open Life Sci.*, **2010**, *5*.

[47] Almeida, A.; Faustino, M.A.; Tomé, J.P. Photodynamic Inactivation of Bacteria: Finding the Effective Targets. *Future Med. Chem.*, **2015**, *7*, 1221–1224.

[48] Jori, G.; Brown, S.B. Photosensitized Inactivation of Microorganisms. *Photochem. Photobiol. Sci.*, **2004**, *3*, 403–405.

[49] Bezman, S.A.; Burtis, P.A.; Izod, T.P.; Thayer, M.A. Photodynamic Inactivation of *E. Coli* by Rose Bengal Immobilized on Polystyrene Beads. *Photochem. Photobiol.*, **1978**, *28*, 325–329.

[50] Cooper, A.T.; Goswami, D.Y. Evaluation of Methylene Blue and Rose Bengal for Dye Sensitized Solar Water Treatment. *J. Sol. Energy Eng.*, **2002**, *124*, 305–310.

[51] Bonnett, R.; Krysteva, M.A.; Lalov, I.G.; Artarsky, S.V. Water Disinfection Using Photosensitizers Immobilized on Chitosan. *Water Res.*, **2006**, *40*, 1269–1275.

[52] Beirão, S.; Fernandes, S.; Coelho, J.; Faustino, M.A.F.; Tomé, J.P.C.; Neves, M.G.P.M.S.; Tomé, A.C.; Almeida, A.; Cunha, A. Photodynamic Inactivation of Bacterial and Yeast Biofilms with a Cationic Porphyrin. *Photochem. Photobiol.*, **2014**, *90*, 1387–1396.

[53] Liu, S.; Gunawan, C.; Barraud, N.; Rice, S.A.; Harry, E.J.; Amal, R. Understanding, Monitoring, and Controlling Biofilm Growth in Drinking Water Distribution Systems. *Environ. Sci. Technol.*, **2016**, *50*, 8954–8976.

[54] Wingender, J.; Flemming, H.-C. Biofilms in Drinking Water and Their Role as Reservoir for Pathogens. *Int. J. Hyg. Environ. Health*, **2011**, *214*, 417–423.

[55] Nguyen, T.; Roddick, F.A.; Fan, L. Biofouling of Water Treatment Membranes: A Review of the Underlying Causes, Monitoring Techniques and Control Measures. *Membranes*, **2012**, *2*, 804–840.

[56] Branch, K.L.; Johnson, E.R.; Nichols, E.M. Porphyrin Aggregation under Homogeneous Conditions Inhibits Electrocatalysis: A Case Study on CO_2 Reduction. *ACS Cent. Sci.*, **2024**, *10*, 1251–1261.

[57] Silvestri, S.; Fajardo, A.R.; Iglesias, B.A. Supported Porphyrins for the Photocatalytic Degradation of Organic Contaminants in Water: A Review. *Environ. Chem. Lett.*, **2022**, *20*, 731–771.

[58] Daneshmandi, L.; Barajaa, M.; Tahmasbi Rad, A.; Sydlik, S.A.; Laurencin, C.T. Graphene-Based Biomaterials for Bone Regenerative Engineering: A Comprehensive Review of the Field and Considerations Regarding Biocompatibility and Biodegradation. *Adv. Healthc. Mater.*, **2021**, *10*, 2001414.

[59] Nasrollahzadeh, M.; Sajjadi, M.; Iravani, S.; Varma, R.S. Carbon-Based Sustainable Nanomaterials for Water Treatment: State-of-Art and Future Perspectives. *Chemosphere*, **2021**, *263*, 128005.

[60] Piaskowski, K.; Zarzycki, P.K. Carbon-Based Nanomaterials as Promising Material for Wastewater Treatment Processes. *Int. J. Environ. Res. Public. Health*, **2020**, *17*, 5862.

[61] Lam, E.; Luong, J.H.T. Carbon Materials as Catalyst Supports and Catalysts in the Transformation of Biomass to Fuels and Chemicals. *ACS Catal.*, **2014**, *4*, 3393–3410.

[62] Das, A.; Mondal, S.; Hansda, K.M.; Adak, M.K.; Dhak, D. A Critical Review on the Role of Carbon Supports of Metal Catalysts for Selective Catalytic Hydrogenation of Chloronitrobenzenes. *Appl. Catal. Gen.*, **2023**, *649*, 118955.

[63] Thambiliyagodage, C. Efficient Photocatalysis of Carbon Coupled TiO_2 to Degrade Pollutants in Wastewater – A Review. *Environ. Nanotechnol. Monit. Manag.*, **2022**, *18*, 100737.

[64] Sandanayaka, A.S.D.; Chitta, R.; Subbaiyan, N.K.; D'Souza, L.; Ito, O.; D'Souza, F. Photoinduced Charge Separation in Ion-Paired Porphyrin−Single-Wall Carbon Nanotube Donor−Acceptor Hybrids. *J. Phys. Chem. C*, **2009**, *113*, 13425–13432.

[65] Santos, C.I.M.; Rodríguez-Pérez, L.; Gonçalves, G.; Dias, C.J.; Monteiro, F.; Faustino, M. do A.F.; Vieira, S.I.; Helguero, L.A.; Herranz, M.Á.; Martín, N.; Neves, M.G.P.M.S.; Martinho, J.M.G.; Maçôas, E.M.S. Enhanced Photodynamic Therapy Effects of Graphene Quantum Dots Conjugated with Aminoporphyrins. *ACS Appl. Nano Mater.*, **2021**, *4*, 13079–13089.

[66] Rabiee, N.; Bagherzadeh, M.; Ghadiri, A.M.; Fatahi, Y.; Baheiraei, N.; Safarkhani, M.; Aldhaher, A.; Dinarvand, R. Bio-Multifunctional Noncovalent Porphyrin Functionalized Carbon-Based Nanocomposite. *Sci. Rep.*, **2021**, *11*, 6604.

[67] Monteiro, A.R.; Neves, M.G.P.M.S.; Trindade, T. Functionalization of Graphene Oxide with Porphyrins: Synthetic Routes and Biological Applications. *ChemPlusChem*, **2020**, *85*, 1857–1880.

[68] Orellana, W.; Loyola, C.Z.; Marco, J.F.; Tasca, F. Evidence of Carbon-Supported Porphyrins Pyrolyzed for the Oxygen Reduction Reaction Keeping Integrity. *Sci. Rep.*, **2022**, *12*, 8072.

[69] Chen, D.; Wang, K.; Hong, W.; Zong, R.; Yao, W.; Zhu, Y. Visible Light Photoactivity Enhancement via CuTCPP Hybridized G-C_3N_4 Nanocomposite. *Appl. Catal. B Environ.*, **2015**, *166–167*, 366–373.

[70] Liu, S.; Zhou, S.; Hu, C.; Duan, M.; Song, M.; Huang, F.; Cai, J. Coupling Graphitic Carbon Nitrides with Tetracarboxyphenyl Porphyrin Molecules through π–π Stacking for Efficient Photocatalysis. *J. Mater. Sci. Mater. Electron.*, **2020**, *31*, 10677–10688.

[71] Zhang, J.; Wang, A.; Zhao, W.; Li, C.; Chen, X.; Wang, Y.; Zhu, W.; Zhong, Q. Influence of Metal-Porphyrins on the Photocatalysis of Graphitic Carbon Nitride. *Dyes Pigments*, **2018**, *153*, 241–247.

[72] La, D.D.; Hangarge, R.V.; V. Bhosale, S.; Ninh, H.D.; Jones, L.A.; Bhosale, S.V. Arginine-Mediated Self-Assembly of Porphyrin on Graphene: A Photocatalyst for Degradation of Dyes. *Appl. Sci.*, **2017**, *7*, 643.

[73] Zargari, S.; Rahimi, R.; Ghaffarinejad, A.; Morsali, A. Enhanced Visible Light Photocurrent Response and Photodegradation Efficiency over TiO_2–Graphene Nanocomposite Pillared with Tin Porphyrin. *J. Colloid Interface Sci.*, **2016**, *466*, 310–321.

[74] Spencer, M.G.; Sacchi, M.; Allam, J.; Silva, S.R.P. Porphyrin–Nanocarbon Complexes to Control the Photodegradation of Rhodamine. *ACS Omega*, **2022**, *7*, 41304–41313.

[75] Guo, P.; Chen, P.; Liu, M. One-Dimensional Porphyrin Nanoassemblies Assisted via Graphene Oxide: Sheetlike Functional Surfactant and Enhanced Photocatalytic Behaviors. *ACS Appl. Mater. Interfaces*, **2013**, *5*, 5336–5345.

[76] Larowska, D.; O'Brien, J.M.; Senge, M.O.; Burdzinski, G.; Marciniak, B.; Lewandowska-Andralojc, A. Graphene Oxide Functionalized with Cationic Porphyrins as Materials for the Photodegradation of Rhodamine B. *J. Phys. Chem. C*, **2020**, *124*, 15769–15780.

[77] Raveena; Singh, M.P.; Sengar, M.; Kumari, P. Synthesis of Graphene Oxide/Porphyrin Nanocomposite for Photocatalytic Degradation of Crystal Violet Dye. *ChemistrySelect*, **2023**, *8*, e202203272.

[78] El-Khawaga, A.M.; Tantawy, H.; Elsayed, M.A.; Abd El-Mageed, A.I.A. Synthesis and Applicability of Reduced Graphene Oxide/Porphyrin Nanocomposite as Photocatalyst for Waste Water Treatment and Medical Applications. *Sci. Rep.*, **2022**, *12*, 17075.

[79] Lewoyehu, M. Comprehensive Review on Synthesis and Application of Activated Carbon from Agricultural Residues for the Remediation of Venomous Pollutants in Wastewater. *J. Anal. Appl. Pyrolysis*, **2021**, *159*, 105279.

[80] Heidarinejad, Z.; Dehghani, M.H.; Heidari, M.; Javedan, G.; Ali, I.; Sillanpää, M. Methods for Preparation and Activation of Activated Carbon: A Review. *Environ. Chem. Lett.*, **2020**, *18*, 393–415.

[81] Bouchelta, C.; Medjram, M.S.; Bertrand, O.; Bellat, J.-P. Preparation and Characterization of Activated Carbon from Date Stones by Physical Activation with Steam. *J. Anal. Appl. Pyrolysis*, **2008**, *82*, 70–77.

[82] Serafin, J.; Dziejarski, B. Activated Carbons—Preparation, Characterization and Their Application in CO_2 Capture: A Review. *Environ. Sci. Pollut. Res.*, **2024**, *31*, 40008–40062.

[83] Georgi, A.; Schierz, A.; Mackenzie, K.; Kopinke, F.-D. Colloidal Activated Carbon for In-Situ Groundwater Remediation — Transport Characteristics and Adsorption of Organic Compounds in Water-Saturated Sediment Columns. *J. Contam. Hydrol.*, **2015**, *179*, 76–88.

[84] Wang, Y.; Hu, A. Carbon Quantum Dots: Synthesis, Properties and Applications. *J. Mater. Chem. C*, **2014**, *2*, 6921–6939.

[85] Miao, S.; Liang, K.; Zhu, J.; Yang, B.; Zhao, D.; Kong, B. Hetero-Atom-Doped Carbon Dots: Doping Strategies, Properties and Applications. *Nano Today*, **2020**, *33*, 100879.

[86] Krishna Saraswat, S.; Ahmed Mustafa, M.; Kamil Ghadir, G.; Kaur, M.; Guamán Lozada, D.F.; Hasen shuhata alubiady, M.; Muzahem Al-Ani, A.; Alshahrani, M.Y.; Kadhem Abid, M.; Salih Jumaa, S.; Yahaia Alhameedi, D.; huseen Redhee, A. Carbon Quantum Dots: A Comprehensive Review of Green Synthesis, Characterization and Investigation Their Applications in Bioimaging. *Inorg. Chem. Commun.*, **2024**, *162*, 112279.

[87] Chauhan, D.S.; Quraishi, M.A.; Verma, C. Carbon Nanodots: Recent Advances in Synthesis and Applications. *Carbon Lett.*, **2022**, *32*, 1603–1629.

[88] Kumar, P.; Dua, S.; Kaur, R.; Kumar, M.; Bhatt, G. A Review on Advancements in Carbon Quantum Dots and Their Application in Photovoltaics. *RSC Adv.*, **2022**, *12*, 4714–4759.

[89] Yadav, P.K.; Chandra, S.; Kumar, V.; Kumar, D.; Hasan, S.H. Carbon Quantum Dots: Synthesis, Structure, Properties, and Catalytic Applications for Organic Synthesis. *Catalysts*, **2023**, *13*, 422.

[90] Nguyen, K.G.; Baragau, I.-A.; Gromicova, R.; Nicolaev, A.; Thomson, S.A.J.; Rennie, A.; Power, N.P.; Sajjad, M.T.; Kellici, S. Investigating the Effect of N-Doping on Carbon Quantum Dots Structure, Optical Properties and Metal Ion Screening. *Sci. Rep.*, **2022**, *12*, 13806.

[91] Lim, S.Y.; Shen, W.; Gao, Z. Carbon Quantum Dots and Their Applications. *Chem. Soc. Rev.*, **2014**, *44*, 362–381.

[92] Lai, L.; Huang, X.; Sun, W.; Chen, X.; Pei, S.; Chai, S.; Chen, J. One-Step Synthesis of Carbon Quantum Dots with Antibacterial Activity Based on Andrographolide. *Russ. J. Gen. Chem.*, **2022**, *92*, 2178–2185.

[93] Ademola Bode-Aluko, C.; Pereao, O.; Kyaw, H.H.; Al-Naamani, L.; Al-Abri, M.Z.; Tay Zar Myint, M.; Rossouw, A.; Fatoba, O.; Petrik, L.; Dobretsov, S. Photocatalytic and Antifouling Properties of Electrospun TiO2 Polyacrylonitrile Composite Nanofibers under Visible Light. *Mater. Sci. Eng. B*, **2021**, *264*, 114913.

[94] Abdel-Mottaleb, M.M.; Khalil, A.; Karim, ShroukA.; Osman, T.A.; A.Khattab. High Performance of PAN/GO-ZnO Composite Nanofibers for Photocatalytic Degradation under Visible Irradiation. *J. Mech. Behav. Biomed. Mater.*, **2019**, *96*, 118–124.

[95] Bettelheim, A.; White, B.A.; Raybuck, S.A.; Murray, R.W. Electrochemical Polymerization of Amino-, Pyrrole-, and Hydroxy-Substituted Tetraphenylporphyrins. *Inorg. Chem.*, **1987**, *26*, 1009–1017.

[96] Cecioni, S.; Faure, S.; Darbost, U.; Bonnamour, I.; Parrot-Lopez, H.; Roy, O.; Taillefumier, C.; Wimmerová, M.; Praly, J.-P.; Imberty, A.; Vidal, S. Selectivity among Two Lectins: Probing the Effect of Topology, Multivalency and Flexibility of "Clicked" Multivalent Glycoclusters. *Chem. - Eur. J.*, **2011**, *17*, 2146–2159.

[97] Frisch, M.J.; Trucks, G.W.; Schlegel, H.B.; Scuseria, G.E.; Robb, M.A.; Cheeseman, J.R.; Scalmani, G.; Barone, V.; Petersson, G.A.; Nakatsuji, H.; Li, X.; Caricato, M.; Marenich, A.; Bloino, J.; Janesko, B.G.; Gomperts, R.; Mennucci, B.; Hratchian, H.P.; Ortiz, J.V.; Izmaylov, A.F.; Sonnenberg, J.L.; Williams-Young, D.; Ding, F.; Lipparini, F.; Egidi, F.; Goings, J.; Peng, B.; Petrone, A.; Henderson, T.; Ranasinghe, D.; Zakrzewski, V.G.; Gao, J.; Rega, N.; Zheng, G.; Liang, W.; Hada, M.; Ehara, M.; Toyota, K.; Fukuda, R.; Hasegawa, J.; Ishida, M.; Nakajima, T.; Honda, Y.; Kitao, O.; Nakai, H.; Vreven, T.; Throssell, K.; Montgomery, J.A.; Peralta, Jr., J.E.; Ogliaro, F.; Bearpark, M.; Heyd, J.J.; Brothers, E.; Kudin, K.N.; Staroverov, V.N.; Keith, T.; Kobayashi, R.; Normand, J.; Raghavachari, K.; Rendell, A.; Burant, J.C.; Iyengar, S.S.; Tomasi, J.; Cossi, M.; Millam, J.M.; Klene, M.; Adamo, C.; Cammi, R.; Ochterski, J.W.; Martin, R.L.; Morokuma, S.S.; Farkas, O.; Foresman, J.B.; Fox, D.J. Gaussian 09, Revision A.02. *Inc Wallingford CT*, **2016**.

[98] Mack, J.; Wildervanck, M.; Nyokong, T. TD-DFT calculations and MCD spectroscopy of porphyrin and phthalocyanine analogues: rational design of photosensitizers for PDT and NIR region sensor applications. *Turk. J. Chem.*, **2014**, *38*, 1013–1026.

[99] Li, L.; Hu, J.; Shi, X.; Ruan, W.; Luo, J.; Wei, X. Theoretical Studies on Structures, Properties and Dominant Debromination Pathways for Selected Polybrominated Diphenyl Ethers. *Int. J. Mol. Sci.*, **2016**, *17*, 927.

[100] Susmel, S.; Comuzzi, C. 5-Phenyl-Dipyrromethane and 5-(4-Pyridyl)-Dipyrromethane as Modular Building Blocks for Bio-Inspired Conductive Molecularly Imprinted Polymer (cMIP). An Electrochemical and Piezoelectric Investigation. *RSC Adv.*, **2015**, *5*, 78379–78388.

[101] Tintner, J.; Fierlinger, R.; Gerzabek, H.; Pfeifer, C.; Smidt, E. Pyrolysis Profiles of a Traditional Circular Kiln in Austria and a Drum Kiln in Namibia. *J. Anal. Appl. Pyrolysis*, **2020**, *150*, 104865.

[102] Hou, J.; Liu, Y.; Wen, S.; Li, W.; Liao, R.; Wang, L. Sorghum-Waste-Derived High-Surface Area KOH-Activated Porous Carbon for Highly Efficient Methylene Blue and Pb(II) Removal. *ACS Omega*, **2020**, *5*, 13548–13556.

[103] Wang, C.; Yang, M.; Shi, H.; Yao, Z.; Liu, E.; Hu, X.; Guo, P.; Xue, W.; Fan, J. Carbon Quantum Dots Prepared by Pyrolysis: Investigation of the Luminescence Mechanism and Application as Fluorescent Probes. *Dyes Pigments*, **2022**, *204*, 110431.

[104] Röder, B.; Büchner, M.; Rückmann, I.; Senge, M.O. Correlation of Photophysical Parameters with Macrocycle Distortion in Porphyrins with Graded Degree of Saddle Distortion. *Photochem. Photobiol. Sci.*, **2010**, *9*, 1152–1158.

[105] Zheng, W.; Li, X.; Chen, H.; Xie, Q.; Li, H. Synthesis and Photophysical Properties of Porphyrin–Arylimidazole Heterodyads. *J. Heterocycl. Chem.*, **2017**, *54*, 1522–1528.

[106] Venkatesan, R.; Periasamy, N.; Srivastava, T.S. Singlet Molecular Oxygen Quantum Yield Measurements of Some Porphyrins and Metalloporphyrins. *Proc. Indian Acad. Sci. - Chem. Sci.*, **1992**, *104*, 713–722.

[107] Degen, I.A. Detection of the Methoxyl Group by Infrared Spectroscopy. *Appl. Spectrosc.*, **1968**, *22*, 164–166.

[108] Huang, X.; Yang, L.; Emanuelsson, R.; Bergquist, J.; Strømme, M.; Sjödin, M.; Gogoll, A. A Versatile Route to Polythiophenes with Functional Pendant Groups Using Alkyne Chemistry. *Beilstein J. Org. Chem.*, **2016**, *12*, 2682–2688.

[109] Ribeiro, M.G.; Azzellini, G.C. Synthesis of New Cationic Metalloporphyrins and Heterodimer Formation with Anionic Metallophthalocyanines. *J. Braz. Chem. Soc.*, **2003**, *14*, 914–921.

[110] Hong, T.-N.; Sheu, Y.-H.; Jang, K.-W.; Chen, J.-H.; Wang, S.-S.; Wang, J.-C.; Wang, S.-L. A New Synthesis of Acetato Porphyrinato Indium(III) from Indium(III) Oxide and X-Ray Crystal Structures of In(Tpyp)(OAc) and In(Tmpp)(OAc). *Polyhedron*, **1996**, *15*, 2647–2654.

[111] Openda, Y.I.; Ngoy, B.P.; Nyokong, T. Photodynamic Antimicrobial Action of Asymmetrical Porphyrins Functionalized Silver-Detonation Nanodiamonds Nanoplatforms for the Suppression of Staphylococcus Aureus Planktonic Cells and Biofilms. *Front. Chem.*, **2021**, *9*.

[112] Hadjiivanov, K.I.; Panayotov, D.A.; Mihaylov, M.Y.; Ivanova, E.Z.; Chakarova, K.K.; Andonova, S.M.; Drenchev, N.L. Power of Infrared and Raman Spectroscopies to Characterize Metal-Organic Frameworks and Investigate Their Interaction with Guest Molecules. *Chem. Rev.*, **2021**, *121*, 1286–1424.

[113] Oshio, H.; Ama, T.; Watanabe, T.; Kincaid, J.; Nakamoto, K. Structure Sensitive Bands in the Vibrational Spectra of Metal Complexes of Tetraphenylporphine. *Spectrochim. Acta Part Mol. Spectrosc.*, **1984**, *40*, 863–870.

[114] Thomas, D.W.; Martell, A.E. Absorption Spectra of Para-Substituted Tetraphenylporphines1,2. *J. Am. Chem. Soc.*, **1956**, *78*, 1338–1343.

[115] El-Nahass, M.M.; Zeyada, H.M.; Aziz, M.S.; Makhlouf, M.M. Optical Absorption of Tetraphenylporphyrin Thin Films in UV–Vis–NIR Region. *Spectrochim. Acta. A. Mol. Biomol. Spectrosc.*, **2005**, *62*, 11–15.

[116] Dinache, A.; Nistorescu, S.; Tozar, T.; Smarandache, A.; Boni, M.; Prepelita, P.; Staicu, A. Spectroscopic Investigations of Porphyrin-TiO_2 Nanoparticles Complexes. *Molecules*, **2022**, *28*, 318.

[117] Kee, H.L.; Bhaumik, J.; Diers, J.R.; Mroz, P.; Hamblin, M.R.; Bocian, D.F.; Lindsey, J.S.; Holten, D. Photophysical Characterization of Imidazolium-Substituted Pd(II), In(III), and Zn(II) Porphyrins as Photosensitizers for Photodynamic Therapy. *J. Photochem. Photobiol. Chem.*, **2008**, *200*, 346–355.

[118] Haddad, R.E.; Gazeau, S.; Pécaut, J.; Marchon, J.-C.; Medforth, C.J.; Shelnutt, J.A. Origin of the Red Shifts in the Optical Absorption Bands of Nonplanar Tetraalkylporphyrins. *J. Am. Chem. Soc.*, **2003**, *125*, 1253–1268.

[119] Prakash, K.; Manchanda, S.; Sudhakar, V.; Sharma, N.; Sankar, M.; Krishnamoorthy, K. Facile Synthesis of β-Functionalized "Push-Pull" Zn(II) Porphyrins for DSSC Applications. *Dyes Pigments*, **2017**, *147*, 56–66.

[120] Gouterman, M.; Wagnière, G.H.; Snyder, L.C. Spectra of Porphyrins: Part II. Four Orbital Model. *J. Mol. Spectrosc.*, **1963**, *11*, 108–127.

[121] Michl, J. Magnetic Circular Dichroism of Aromatic Molecules. *Tetrahedron*, **1984**, *40*, 3845–3934.

[122] Taniguchi, M.; Lindsey, J.S.; Bocian, D.F.; Holten, D. Comprehensive Review of Photophysical Parameters (ε, Φf, Ts) of Tetraphenylporphyrin (H_2TPP) and Zinc Tetraphenylporphyrin (ZnTPP) – Critical Benchmark Molecules in Photochemistry and Photosynthesis. *J. Photochem. Photobiol. C Photochem. Rev.*, **2021**, *46*, 100401.

[123] Cai, Z.-L.; Crossley, M.J.; Reimers, J.R.; Kobayashi, R.; Amos, R.D. Density Functional Theory for Charge Transfer: The Nature of the N-Bands of Porphyrins and Chlorophylls

Revealed through CAM-B3LYP, CASPT2, and SAC-CI Calculations. *J. Phys. Chem. B*, **2006**, *110*, 15624–15632.

[124] Silvestre-Albero, A.; Juarez-Galan, J.; Silvestre-Albero, J.; Rodriguez-Reinoso, F. Low-Pressure Hysteresis in Adsorption: An Artifact? *J. Phys. Chem. C*, **2012**, *116*, 16652.

[125] Sing, K.; Williams, R. Physisorption Hysteresis Loops and the Characterization of Nanoporous Materials. *Adsorpt. Sci. Technol.*, **2004**, *22*.

[126] *Metal-Free Functionalized Carbons in Catalysis: Synthesis, Characterization and Applications*; Villa, A.; Dimitratos, N., Eds.; Catalysis series; Royal Society of Chemistry: Cambridge, UK, **2018**.

[127] Couzi, M.; Bruneel, J.-L.; Talaga, D.; Bokobza, L. A Multi Wavelength Raman Scattering Study of Defective Graphitic Carbon Materials: The First Order Raman Spectra Revisited. *Carbon*, **2016**, *107*, 388–394.

[128] Ferrari, A.C.; Robertson, J. Resonant Raman Spectroscopy of Disordered, Amorphous, and Diamondlike Carbon. *Phys. Rev. B*, **2001**, *64*, 075414.

[129] Ferrari, A.C.; Robertson, J. Origin of Dispersive Effects of the Raman D Band in Carbon Materials. *Phys. Rev. B*, **2001**, *63*, 121405.

[130] Sadezky, A.; Muckenhuber, H.; Grothe, H.; Niessner, R.; Pöschl, U. Raman Microspectroscopy of Soot and Related Carbonaceous Materials: Spectral Analysis and Structural Information. *Carbon*, **2005**, *43*, 1731–1742.

[131] Smith, M.W.; Dallmeyer, I.; Johnson, T.J.; Brauer, C.S.; McEwen, J.-S.; Espinal, J.F.; Garcia-Perez, M. Structural Analysis of Char by Raman Spectroscopy: Improving Band Assignments through Computational Calculations from First Principles. *Carbon*, **2016**, *100*.

[132] Zhao, J.; Yu, L.; Zhou, F.; Ma, H.; Yang, K.; Wu, G. Synthesis and Characterization of Activated Carbon from Sugar Beet Residue for the Adsorption of Hexavalent Chromium in Aqueous Solutions. *RSC Adv.*, **2021**, *11*, 8025–8032.

[133] Morales, M.S.; Ogale, A.A. Wet-Spun, Photoinitiator-Modified Polyacrylonitrile Precursor Fibers: UV-Assisted Stabilization. *J. Appl. Polym. Sci.*, **2013**, *130*, 2494–2503.

[134] Huang, H.-B.; Wang, Y.; Cai, F.-Y.; Jiao, W.-B.; Zhang, N.; Liu, C.; Cao, H.-L.; Lü, J. Photodegradation of Rhodamine B over Biomass-Derived Activated Carbon Supported CdS Nanomaterials under Visible Irradiation. *Front. Chem.*, **2017**, *5*, 123.

[135] Karacan, I.; Erdogan, G. The Influence of Thermal Stabilization Stage on the Molecular Structure of Polyacrylonitrile Fibers Prior to the Carbonization Stage. *Fibers Polym.*, **2012**, *13*, 295–302.

[136] Loginova, E.V.; Mikheev, I.V.; Volkov, D.S.; Proskurnin, M.A. Quantification of Copolymer Composition (Methyl Acrylate and Itaconic Acid) in Polyacrylonitrile Carbon-Fiber Precursors by FTIR-Spectroscopy. *Anal. Methods*, **2016**, *8*, 371–380.

[137] Huang, Y.S.; Koenig, J.L. Raman Spectra of Polyacrylonitrile. *Appl. Spectrosc.*, **1971**, *25*, 620–622.

[138] Jin, Y.; Kotula, A.P.; Snyder, C.R.; Hight Walker, A.R.; Migler, K.B.; Lee, Y.J. Raman Identification of Multiple Melting Peaks of Polyethylene. *Macromolecules*, **2017**, *50*, 6174–6183.

[139] Coccato, A.; Jehlicka, J.; Moens, L.; Vandenabeele, P. Raman Spectroscopy for the Investigation of Carbon-Based Black Pigments: Investigation of Carbon-Based Black Pigments. *J. Raman Spectrosc.*, **2015**, *46*, 1003–1015.

[140] Chen, Z.Y.; Zhao, J.P.; Yano, T.; Ooie, T.; Yoneda, M.; Sakakibara, J. Observation of Sp3 Bonding in Tetrahedral Amorphous Carbon Using Visible Raman Spectroscopy. *J. Appl. Phys.*, **2000**, *88*, 2305–2308.

[141] An, J.-H.; El-Said, W.A.; Yea, C.-H.; Kim, T.-H.; Choi, J.-W. Surface-Enhanced Raman Scattering of Dopamine on Self-Assembled Gold Nanoparticles. *J. Nanosci. Nanotechnol.*, **2011**, *11*, 4424–4429.

[142] Spiro, T.G.; Strekas, T.C. Resonance Raman Spectra of Heme Proteins. Effects of Oxidation and Spin State. *J. Am. Chem. Soc.*, **1974**, *96*, 338–345.

[143] Parthasarathi, N.; Hansen, C.; Yamaguchi, S.; Spiro, T.G. Metalloporphyrin Core Size Resonance Raman Marker Bands Revisited: Implications for the Interpretation of Hemoglobin Photoproduct Raman Frequencies. *J. Am. Chem. Soc.*, **1987**, *109*, 3865–3871.

[144] Jurkiewicz, K.; Pawlyta, M.; Burian, A. Structure of Carbon Materials Explored by Local Transmission Electron Microscopy and Global Powder Diffraction Probes. *C*, **2018**, *4*, 68.

[145] Sevilla, M.; Fuertes, A.B. Fabrication of Porous Carbon Monoliths with a Graphitic Framework. *Carbon*, **2013**, *56*, 155–166.

[146] Dai, C.; Wan, J.; Yang, J.; Qu, S.; Jin, T.; Ma, F.; Shao, J. H_3PO_4 Solution Hydrothermal Carbonization Combined with KOH Activation to Prepare Argy Wormwood-Based Porous Carbon for High-Performance Supercapacitors. *Appl. Surf. Sci.*, **2018**, *444*, 105–117.

[147] Park, S.; Yoo, S.H.; Kang, H.R.; Jo, S.M.; Joh, H.-I.; Lee, S. Comprehensive Stabilization Mechanism of Electron-Beam Irradiated Polyacrylonitrile Fibers to Shorten the Conventional Thermal Treatment. *Sci. Rep.*, **2016**, *6*, 27330.

[148] Mudalige, T.; Qu, H.; Van Haute, D.; Ansar, S.M.; Paredes, A.; Ingle, T. Chapter 11 - Characterization of Nanomaterials: Tools and Challenges. In: *Nanomaterials for Food Applications*; López Rubio, A.; Fabra Rovira, M.J.; martínez Sanz, M.; Gómez-Mascaraque, L.G., Eds.; Micro and Nano Technologies; Elsevier: Amsterdam, **2019**; Vol. 1, p. 318.

[149] Jabeen, G.; Hassan Ahmad, M.; Aslam, M.; Riaz, S.; Hayat, A.; Hasnain Nawaz, M. N-Doped Graphene Quantum Dots (N-GQDs) as Fluorescent Probes for Detection of UV Induced DNA Damage. *RSC Adv.*, **2022**, *12*, 22458–22464.

[150] Ariharan, A.; Viswanathan, B.; Nandhakumar, V. Nitrogen Doped Graphene as Potential Material for Hydrogen Storage. *Graphene*, **2017**, *06*, 41–60.

[151] Ayiania, M.; Weiss-Hortala, E.; Smith, M.; McEwen, J.-S.; Garcia-Perez, M. Microstructural Analysis of Nitrogen-Doped Char by Raman Spectroscopy: Raman Shift Analysis from First Principles. *Carbon*, **2020**, *167*, 559–574.

[152] Lefrant, S.; Mulazzi, E.; Mathis, C. Raman Spectra of N-Doped Trans-Polyacetylene Systems: Experiments and Theory. *Phys. Rev. B*, **1994**, *49*, 13400–13407.

[153] Bankole, O.M.; Britton, J.; Nyokong, T. Photophysical and Non-Linear Optical Behavior of Novel Tetra Alkynyl Terminated Indium Phthalocyanines: Effects of the Carbon Chain Length. *Polyhedron*, **2015**, *88*, 73–80.

[154] Xue, Z.; Gao, H.; Li, X. A Green and Lower-Temperature Synthesis of Two-Color Fluorescent Nitrogen Doped Graphene Quantum Dots. *Dyes Pigments*, **2018**, *156*, 379–385.

[155] Evans, J.S.; Musselman, R.L. Red Shifting Due to Nonplanarity in Alkylporphyrins: Solid-State Polarized UV−Vis Spectra and ZINDO Calculations of Two Nickel(II)Octaethylporphyrins. *Inorg. Chem.*, **2004**, *43*, 5613–5629.

[156] Movasaghi, Z.; Rehman, S.; Rehman, D.I.U. Raman Spectroscopy of Biological Tissues. *Appl. Spectrosc. Rev.*, **2007**, *42*, 493–541.

[157] Mojica, E.-R.E.; Abbas, N.; Wyan, L.O.; Vedad, J.; Desamero, R.Z.B. Solvent Sensitivity of the −C≡N Group: A Raman Spectroscopic Study. In: *ACS Symposium Series*; Sonntag, M.D., Ed.; American Chemical Society: Washington, DC, **2018**; Vol. 1305, pp. 181–197.

[158] Bower, D.M.; McAdam, A.C.; Yang, C.S.C.; Millan, M.; Arevalo, R.; Achilles, C.; Knudson, C.; Hewagama, T.; Nixon, C.A.; Fishman, C.B.; Johnson, S.S.; Bleacher, J.; Whelley, P. Spectroscopic Comparisons of Two Different Terrestrial Basaltic Environments: Exploring the Correlation between Nitrogen Compounds and Biomolecular Signatures. *Icarus*, **2023**, *402*, 115626.

[159] Si, Y.; Li, L.; Qin, X.; Bai, Y.; Li, J.; Yin, Y. Porous SiO_2-Coated Au-Ag Alloy Nanoparticles for the Alkyne-Mediated Ratiometric Raman Imaging Analysis of Hydrogen Peroxide in Live Cells. *Anal. Chim. Acta*, **2019**, *1057*, 1–10.

[160] Raj, A.; Raju, K.; Varghese, H.T.; Granadeiro, C.M.; Nogueira, H.I.S.; Panicker, C.Y. IR, Raman and SERS Spectra of 2-(Methoxycarbonylmethylsulfanyl)-3,5-Dinitrobenzene Carboxylic Acid. *J. Braz. Chem. Soc.*, **2009**, *20*, 549–559.

[161] Aksoy, C.; Severcan, F. Role of Vibrational Spectroscopy in Stem Cell Research. *J. Spectrosc.*, **2012**, *27*, 513286.

[162] Unal, M.; Ahmed, R.; Mahadevan-Jansen, A.; Nyman, J.S. Compositional Assessment of Bone by Raman Spectroscopy. *The Analyst*, **2021**, *146*, 7464–7490.

[163] Ahmadi, A.; Shoushtari, M.Z.; Farbod, M. Photoelectrochemical Application of WS2 Nanosheets Prepared via a Low-Temperature CVD Method. *J. Mater. Sci. Mater. Electron.*, **2019**, *30*, 6342–6349.

[164] Duncan, K.M.; Kellis, D.L.; Huff, J.S.; Barclay, M.S.; Lee, J.; Turner, D.B.; Davis, P.H.; Yurke, B.; Knowlton, W.B.; Pensack, R.D. Symmetry Breaking Charge Transfer in DNA-Templated Perylene Dimer Aggregates. *Molecules*, **2022**, *27*, 6612.

[165] Sun, J.; Sekhar Jena, H.; Krishnaraj, C.; Singh Rawat, K.; Abednatanzi, S.; Chakraborty, J.; Laemont, A.; Liu, W.; Chen, H.; Liu, Y.-Y.; Leus, K.; Vrielinck, H.; Van Speybroeck, V.; Van Der Voort, P. Pyrene-Based Covalent Organic Frameworks for Photocatalytic Hydrogen Peroxide Production. *Angew. Chem. Int. Ed Engl.*, **2023**, *62*, e202216719.

[166] Bregnhøj, M.; Westberg, M.; Minaev, B.F.; Ogilby, P.R. Singlet Oxygen Photophysics in Liquid Solvents: Converging on a Unified Picture. *Acc. Chem. Res.*, **2017**, *50*, 1920–1927.

[167] Yang, Z.-S.; Gao, S.; Zhang, J.-L. Magnetic Manipulation of the Reactivity of Singlet Oxygen: From Test Tubes to Living Cells. *Natl. Sci. Rev.*, **2024**, *11*, nwae069.

[168] Pérez, E.M.; Martín, N. π–π Interactions in Carbon Nanostructures. *Chem. Soc. Rev.*, **2015**, *44*, 6425–6433.

[169] Kozhemyakina, N.V.; Englert, J.M.; Yang, G.; Spiecker, E.; Schmidt, C.D.; Hauke, F.; Hirsch, A. Non-Covalent Chemistry of Graphene: Electronic Communication with Dendronized Perylene Bisimides. *Adv. Mater.*, **2010**, *22*, 5483–5487.

[170] Maraka, H.V.R.; Al-Shammari, R.M.; Al-Attar, N.; Lopez, S.G.; Keyes, T.E.; Rice, J.H. Graphene Oxide Intercalation into Self-Assembled Porphyrin J-Aggregates. *Mater. Res. Express*, **2014**, *1*, 045038.

[171] Marciel, L.; Mesquita, M.Q.; Ferreira, R.; Moreira, B.; PMS Neves, M.G.; F Faustino, M.A.; Almeida, A. An Efficient Formulation Based on Cationic Porphyrins to Photoinactivate Staphylococcus Aureus and Escherichia Coli. *Future Med. Chem.*, **2018**, *10*, 1821–1833.

[172] Zgurskaya, H.I.; López, C.A.; Gnanakaran, S. Permeability Barrier of Gram-Negative Cell Envelopes and Approaches To Bypass It. *ACS Infect. Dis.*, **2015**, *1*, 512–522.

[173] Hurst, A.N.; Scarbrough, B.; Saleh, R.; Hovey, J.; Ari, F.; Goyal, S.; Chi, R.J.; Troutman, J.M.; Vivero-Escoto, J.L. Influence of Cationic Meso-Substituted Porphyrins on the Antimicrobial Photodynamic Efficacy and Cell Membrane Interaction in Escherichia Coli. *Int. J. Mol. Sci.*, **2019**, *20*, 134.

[174] Alves, E.; Costa, L.; Carvalho, C.M.; Tomé, J.P.; Faustino, M.A.; Neves, M.G.; Tomé, A.C.; Cavaleiro, J.A.; Cunha, Â.; Almeida, A. Charge Effect on the Photoinactivation of Gram-Negative and Gram-Positive Bacteria by Cationic Meso-Substituted Porphyrins. *BMC Microbiol.*, **2009**, *9*, 70.

[175] Vallecorsa, P.; Di Venosa, G.; Ballatore, M.B.; Ferreyra, D.; Mamone, L.; Sáenz, D.; Calvo, G.; Durantini, E.; Casas, A. Novel Meso-Substituted Porphyrin Derivatives and Its Potential Use in Photodynamic Therapy of Cancer. *BMC Cancer*, **2021**, *21*, 547.

[176] Josefsen, L.B.; Boyle, R.W. Photodynamic Therapy: Novel Third-Generation Photosensitizers One Step Closer? *Br. J. Pharmacol.*, **2008**, *154*, 1–3.

[177] Alves, E.; Santos, N.; Melo, T.; Maciel, E.; Dória, M.L.; Faustino, M.A.F.; Tomé, J.P.C.; Neves, M.G.P.M.S.; Cavaleiro, J.A.S.; Cunha, Â.; Helguero, L.A.; Domingues, P.; Almeida, A.; Domingues, M.R.M. Photodynamic Oxidation of Escherichia Coli Membrane Phospholipids: New Insights Based on Lipidomics. *Rapid Commun. Mass Spectrom. RCM*, **2013**, *27*, 2717–2728.

[178] Wiehe, A.; Ekaterina, S.; Senge, M.; Röder, B. Hydrophilicity vs Hydrophobicity - Varying the Amphiphilic Structure of Porphyrins Related to the Photosensitizer m-THPC. *J. Porphyr. Phthalocyanines*, **2001**, *5*, 758–761.

[179] Zhang, H.; Xu, L.; Gu, X.; Yu, D.; Li, S. Amphiphilic Di-Cationic Methylene Blue for Improving Antibacterial Photodynamic Efficiency through High Accumulation and Low Aggregation on Bacterial Cell Surfaces. *RSC Adv.*, **2023**, *13*, 239–250.

[180] Cyza, M.; Gut, A.; Łapok, Ł.; Solarski, J.; Knyukshto, V.; Kępczyński, M.; Nowakowska, M. Iodinated Zinc Phthalocyanine – The Novel Visible-Light Activated Photosensitizer for Efficient Generation of Singlet Oxygen. *J. Photochem. Photobiol. Chem.*, **2018**, *358*, 265–273.

[181] O'Toole, G.A. Microtiter Dish Biofilm Formation Assay. *J. Vis. Exp. JoVE*, **2011**, 2437.

[182] Grey, J.F.E.; Townley, A.R.; Everitt, N.M.; Campbell-Ritchie, A.; Wheatley, S.P. A Cost-Effective, Analytical Method for Measuring Metabolic Load of Mitochondria. *Metab. Open*, **2019**, *4*, 100020.

[183] Stewart, P.S. Antimicrobial Tolerance in Biofilms. *Microbiol. Spectr.*, **2015**, *3*, 10.1128/microbiolspec.MB-0010–2014.

[184] Macià, M.D.; Oliver, A. Antibiotic Resistance Development in Bacterial Biofilms. In: *Antibiofilm Strategies: Current and Future Applications to Prevent, Control and Eradicate Biofilms*; Richter, K.; Kragh, K.N., Eds.; Springer International Publishing: Cham, **2022**; pp. 37–58.

[185] Grooters, K.E.; Ku, J.C.; Richter, D.M.; Krinock, M.J.; Minor, A.; Li, P.; Kim, A.; Sawyer, R.; Li, Y. Strategies for Combating Antibiotic Resistance in Bacterial Biofilms. *Front. Cell. Infect. Microbiol.*, **2024**, *14*.

[186] Lahiri, D.; Nag, M.; Ghosh, A.; Das, D.; Dey, A.; Mukherjee, D.; Garai, S.; Ray, R.R. Biofilm and Antimicrobial Resistance. In: *Biofilm-Mediated Diseases: Causes and Controls*; Ray, R.R.; Nag, M.; Lahiri, D., Eds.; Springer: Singapore, **2021**; pp. 183–208.

[187] Laganenka, L.; Colin, R.; Sourjik, V. Chemotaxis towards Autoinducer 2 Mediates Autoaggregation in Escherichia Coli. *Nat. Commun.*, **2016**, *7*, 12984.

[188] Wang, Q.; Shi, Q.; Li, Y.; Lu, S.; Xie, X. Visible Light-Regulated Cationic Polymer Coupled with Photodynamic Inactivation as an Effective Tool for Pathogen and Biofilm Elimination. *J. Nanobiotechnology*, **2022**, *20*, 492.

[189] Lo, S.-F.; Wang, S.-Y.; Tsai, M.-J.; Lin, L.-D. Adsorption Capacity and Removal Efficiency of Heavy Metal Ions by Moso and Ma Bamboo Activated Carbons. *Chem. Eng. Res. Des.*, **2012**, *90*, 1397–1406.

[190] El-Shafey, E.-S.; Naheed Furqan, S.; Al Busafi, S.; Al Lawati, H. Preparation and Characterization of Surface Functionalized Activated Carbons from Date Palm Leaflets and Application for Methylene Blue Removal. *J. Environ. Chem. Eng.*, **2016**, *4*, 2713–2724.

[191] Wang, G.; Wang, S.; Sun, W.-H.; Sun, Z.; Zheng, S. Oxygen Functionalized Carbon Nanocomposite Derived from Natural Illite as Adsorbent for Removal of Cationic and Anionic Dyes. **2017**, *28*, 1943–1953.

[192] Milošević, M.D.; Logar, M.M.; Poharc-Logar, A.V.; Jakšić, N.L. Orientation and Optical Polarized Spectra (380–900 nm) of Methylene Blue Crystals on a Glass Surface. *Int. J. Spectrosc.*, **2013**, *2013*, 1–6.

[193] Ibupoto, A.S.; Qureshi, U.A.; Ahmed, F.; Khatri, Z.; Khatri, M.; Maqsood, M.; Brohi, R.Z.; Kim, I.S. Reusable Carbon Nanofibers for Efficient Removal of Methylene Blue from Aqueous Solution. *Chem. Eng. Res. Des.*, **2018**, *136*, 744–752.

[194] Bayomie, O.S.; Kandeel, H.; Shoeib, T.; Yang, H.; Youssef, N.; El-Sayed, M.M.H. Novel Approach for Effective Removal of Methylene Blue Dye from Water Using Fava Bean Peel Waste. *Sci. Rep.*, **2020**, *10*, 7824.

[195] Atta, A.M.; Moustafa, Y.M.; Al-Lohedan, H.A.; Ezzat, A.O.; Hashem, A.I. Methylene Blue Catalytic Degradation Using Silver and Magnetite Nanoparticles Functionalized with

a Poly(Ionic Liquid) Based on Quaternized Dialkylethanolamine with 2-Acrylamido-2-Methylpropane Sulfonate- *Co* -Vinylpyrrolidone. *ACS Omega*, **2020**, *5*, 2829–2842.

[196] Yang, C.; Zhang, M.; Dong, W.; Cui, G.; Ren, Z.; Wang, W. Highly Efficient Photocatalytic Degradation of Methylene Blue by PoPD/TiO_2 Nanocomposite. *PLOS ONE*, **2017**, *12*, e0174104.

[197] Velasco, L.F.; Parra, J.B.; Ania, C.O. Role of Activated Carbon Features on the Photocatalytic Degradation of Phenol. *Appl. Surf. Sci.*, **2010**, *256*, 5254–5258.

[198] Houas, A.; Lachheb, H.; Ksibi, M.; Elaloui, E.; Guillard, C.; Herrmann, J.-M. Photocatalytic Degradation Pathway of Methylene Blue in Water. *Appl. Catal. B Environ.*, **2001**, *31*, 145–157.

[199] Zhu, K.; Fu, H.; Zhang, J.; Lv, X.; Tang, J.; Xu, X. Studies on Removal of NH_4^+-N from Aqueous Solution by Using the Activated Carbons Derived from Rice Husk. *Biomass Bioenergy*, **2012**, *43*, 18–25.

[200] Ota, K.; Amano, Y.; Aikawa, M.; Machida, M. Removal of Nitrate Ions from Water by Activated Carbons (ACs)—Influence of Surface Chemistry of ACs and Coexisting Chloride and Sulfate Ions. *Appl. Surf. Sci.*, **2013**, *276*, 838–842.

[201] Salman, M. Removal of Sulfate from Waste Water by Activated Carbon. *Al-Khawarizmi Eng. J.*, **2009**, *5*, 72–76.

[202] Acevedo, S.; Giraldo, L.; Moreno-Piraján, J.C. Adsorption of CO_2 on Activated Carbons Prepared by Chemical Activation with Cupric Nitrate. *ACS Omega*, **2020**, *5*, 10423–10432.

[203] Aguinaco, A.; Pocostales, J.P.; García-Araya, J.F.; Beltrán, F.J. Decomposition of Hydrogen Peroxide in the Presence of Activated Carbons with Different Characteristics. *J. Chem. Technol. Biotechnol.*, **2011**, *86*, 595–600.

[204] Gomes, H.T.; Miranda, S.M.; Sampaio, M.J.; Silva, A.M.T.; Faria, J.L. Activated Carbons Treated with Sulphuric Acid: Catalysts for Catalytic Wet Peroxide Oxidation. *Catal. Today*, **2010**, *151*, 153–158.

[205] Baffoun, A.; Ghali, A.E.; Hachani, I. Decolorization Kinetics of Acid Azo Dye and Basic Thiazine Dye in Aqueous Solution by UV/H_2O_2 and UV/Fenton: Effects of Operational Parameters. *Autex Res. J.*, **2017**, *17*, 85–94.

[206] Li, C.; Wang, X.; Meng, D.; Zhou, L. Facile Synthesis of Low-Cost Magnetic Biosorbent from Peach Gum Polysaccharide for Selective and Efficient Removal of Cationic Dyes. *Int. J. Biol. Macromol.*, **2018**, *107*, 1871–1878.

[207] Anielak, A.M.; Grzegorczuk-Nowacka, M. Significance of Zeta Potential in the Adsorption of Fulvic Acid on Aluminum Oxide and Activated Carbon. *Pol. J. Environ. Stud.*, **2011**, *20*, 1381–1386.

[208] Ostolska, I.; Wiśniewska, M. Application of the Zeta Potential Measurements to Explanation of Colloidal Cr_2O_3 Stability Mechanism in the Presence of the Ionic Polyamino Acids. *Colloid Polym. Sci.*, **2014**, *292*, 2453–2464.

[209] Triquet, T.; Tendero, C.; Latapie, L.; Richard, R.; Andriantsiferana, C. The Use of Composite TiO_2/Activated Carbon Fibers as a Photocatalyst in a Sequential Adsorption/Photocatalysis Process for the Elimination of Ciprofloxacin. *Catal. Res.*, **2022**, *2*, 1–34.

[210] Mukherjee, I.; Cilamkoti, V.; Dutta, R.K. Sunlight-Driven Photocatalytic Degradation of Ciprofloxacin by Carbon Dots Embedded in ZnO Nanostructures. *ACS Appl. Nano Mater.*, **2021**, *4*, 7686–7697.

[211] Bartolomeu, M.; Reis, S.; Fontes, M.; Neves, M.G.P.M.S.; Faustino, M.A.F.; Almeida, A. Photodynamic Action against Wastewater Microorganisms and Chemical Pollutants: An Effective Approach with Low Environmental Impact. *Water*, **2017**, *9*, 630.

[212] Milović, N.M.; Wang, J.; Lewis, K.; Klibanov, A.M. Immobilized N-Alkylated Polyethylenimine Avidly Kills Bacteria by Rupturing Cell Membranes with No Resistance Developed. *Biotechnol. Bioeng.*, **2005**, *90*, 715–722.

[213] Hao, X.; Huang, L.; Zhao, C.; Chen, S.; Lin, W.; Lin, Y.; Zhang, L.; Sun, A.; Miao, C.; Lin, X.; Chen, M.; Weng, S. Antibacterial Activity of Positively Charged Carbon Quantum

Dots without Detectable Resistance for Wound Healing with Mixed Bacteria Infection. *Mater. Sci. Eng. C*, **2021**, *123*, 111971.

[214] Chai, S.; Zhou, L.; Chi, Y.; Chen, L.; Pei, S.; Chen, B. Enhanced Antibacterial Activity with Increasing P Doping Ratio in CQDs. *RSC Adv.*, **2022**, *12*, 27709–27715.

[215] Li, M.; Mai, B.; Wang, A.; Gao, Y.; Wang, X.; Liu, X.; Song, S.; Liu, Q.; Wei, S.; Wang, P. Photodynamic Antimicrobial Chemotherapy with Cationic Phthalocyanines against Escherichia Coli Planktonic and Biofilm Cultures. *RSC Adv.*, **2017**, *7*, 40734–40744.

[216] George, S.; Hamblin, M.R.; Kishen, A. Uptake Pathways of Anionic and Cationic Photosensitizers into Bacteria. *Photochem. Photobiol. Sci.*, **2009**, *8*, 788–795.

[217] Chen, Y.; Huang, Z.-H.; Yue, M.; Kang, F. Integrating Porphyrin Nanoparticles into a 2D Graphene Matrix for Free-Standing Nanohybrid Films with Enhanced Visible-Light Photocatalytic Activity. *Nanoscale*, **2014**, *6*, 978–985.

APPENDICES

Appendix A: MS, ^{1}H NMR and FTIR spectra of Chloroindium (III) 5,10,15,20-*tetrakis*(4-acetamidophenyl) porphyrin (**1a)**.

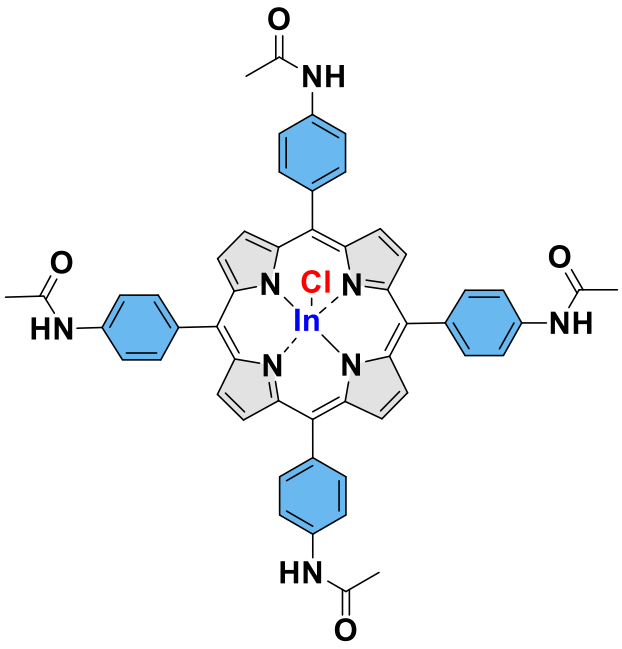

1a

MS Spectrum for 1a

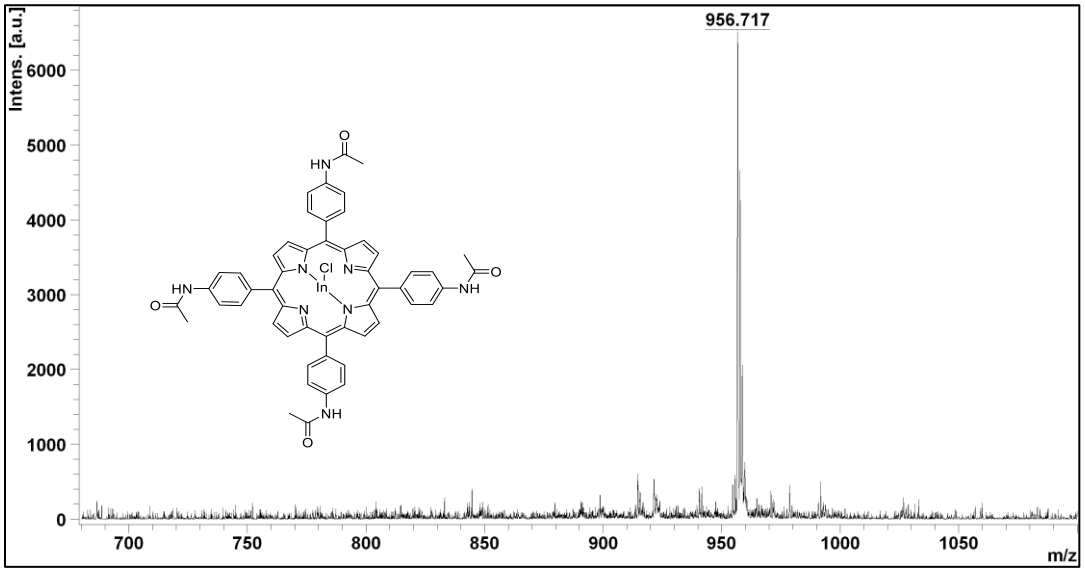

^{1}H NMR spectrum for 1a

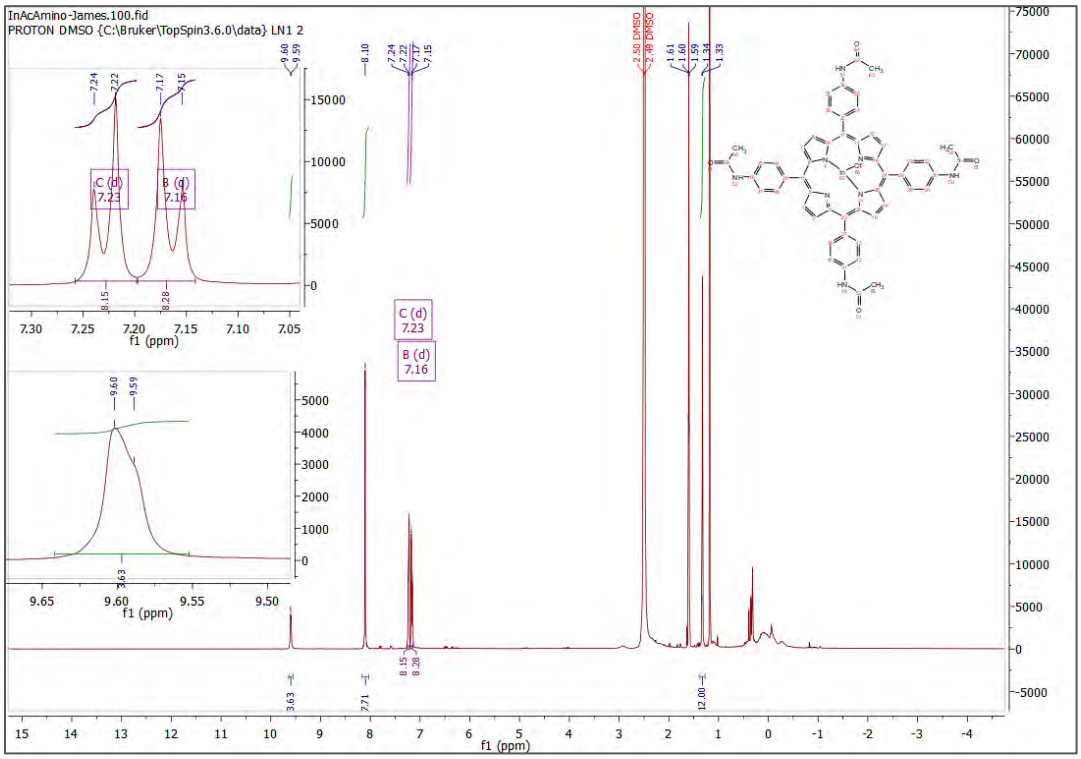

FTIR spectrum for **1a**

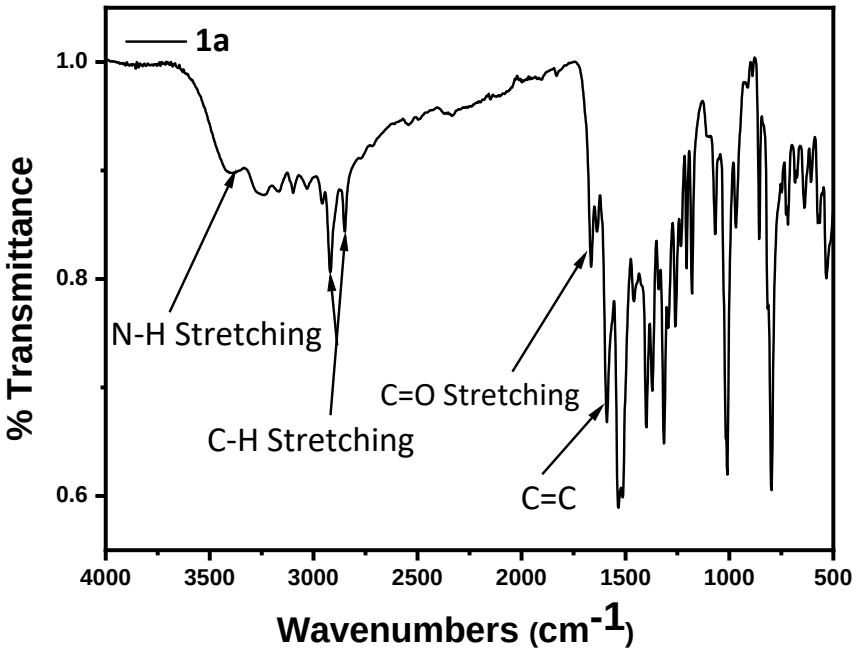
1a
1.0
0.8
0.6
% Transmittance
N-H Stretching
C-H Stretching
C=O Stretching
C=C
4000
3500
3000
2500
2000
1500
1000
500
Wavenumbers (cm-1)

Appendix B: MS, ^{1}H NMR and FTIR spectra of chloroindium (III) 5,10,15,20-tetrakis[4-(prop-2-yn-1yloxy) phenyl] porphyrin **(2a)**.

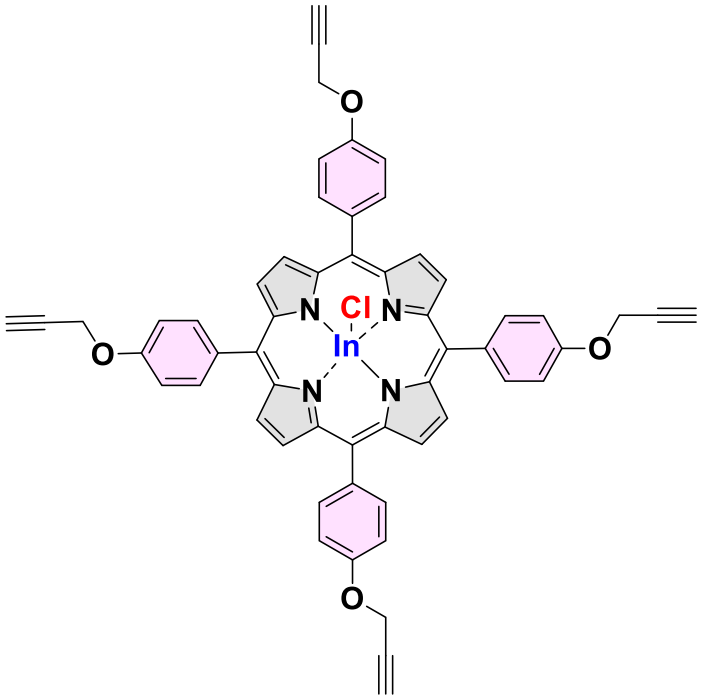

2a

MS Spectrum for **2a**

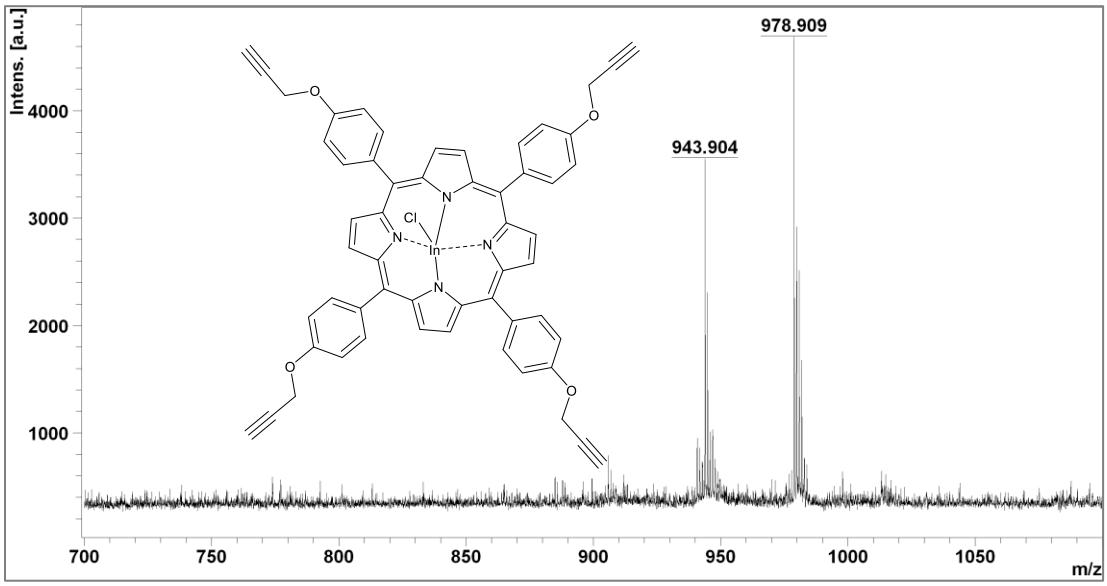

^{1}H NMR spectrum for **2a**

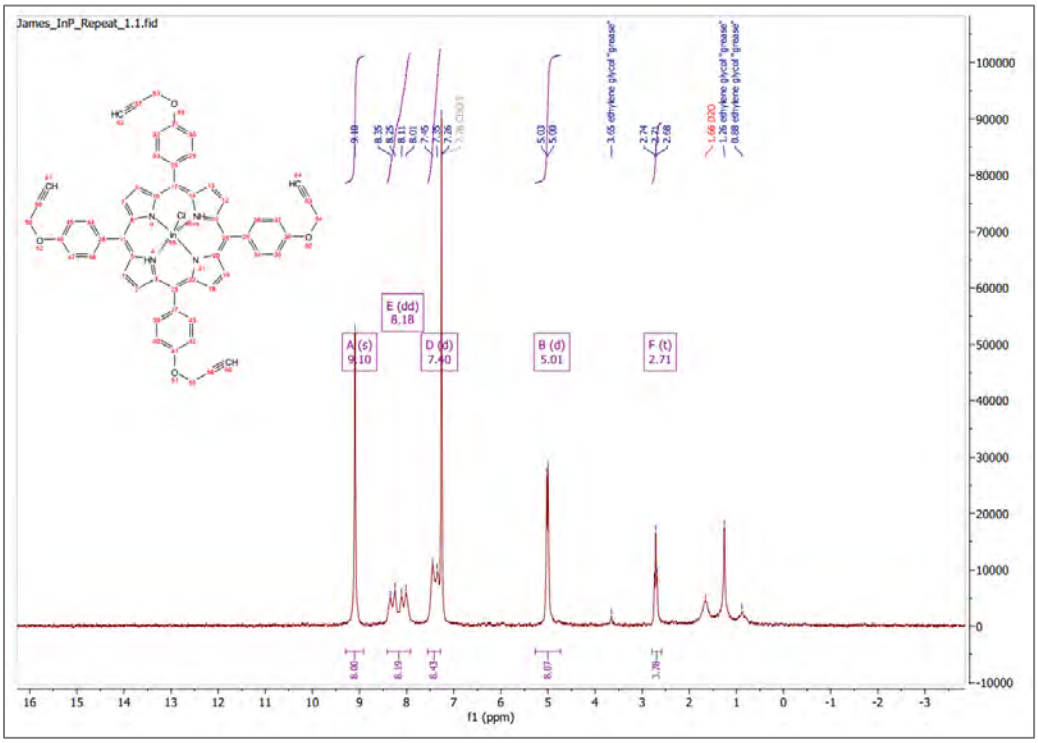

FTIR spectrum for **2a**

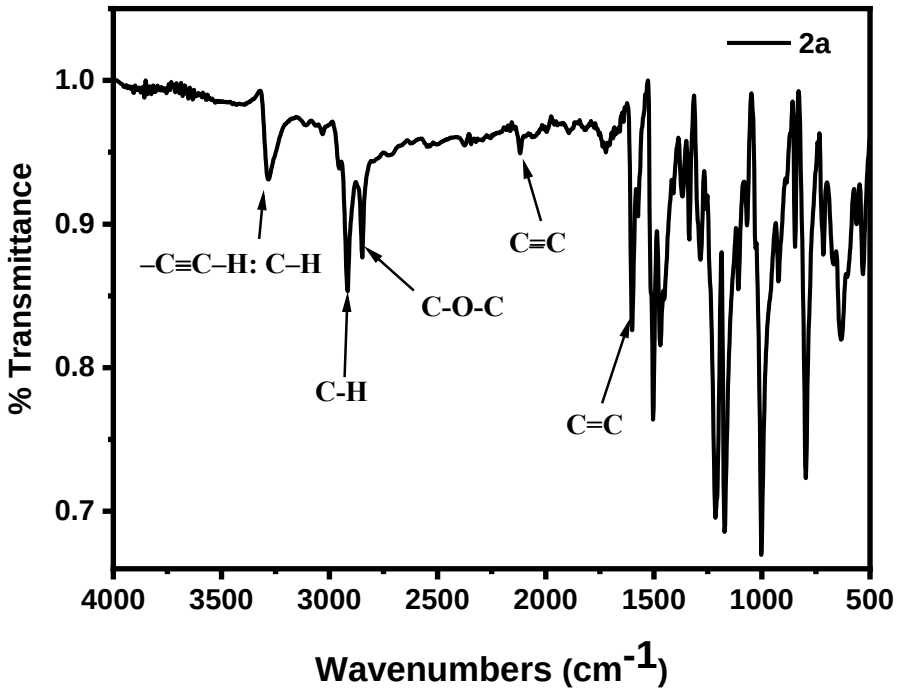

Appendix C: MS, ^{1}H NMR and FTIR spectra of 5,10,15-Tri-4-aminophenyl-20-(pyren-1-yl)porphyrin **(3)** , and Chloroindium (III) 5,10,15-tri-4-acetamidophenyl 20-(pyren-1-yl) porphyrin **(3a)**.

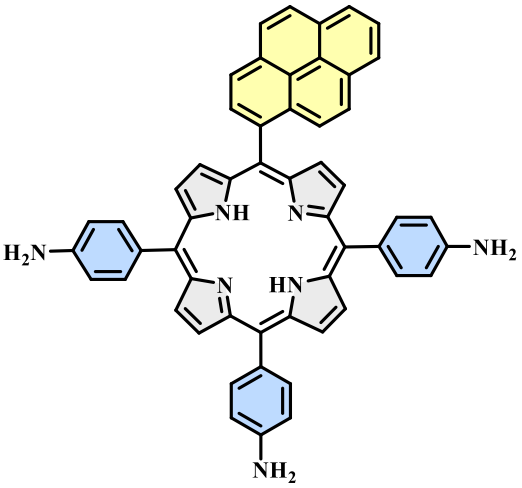

3

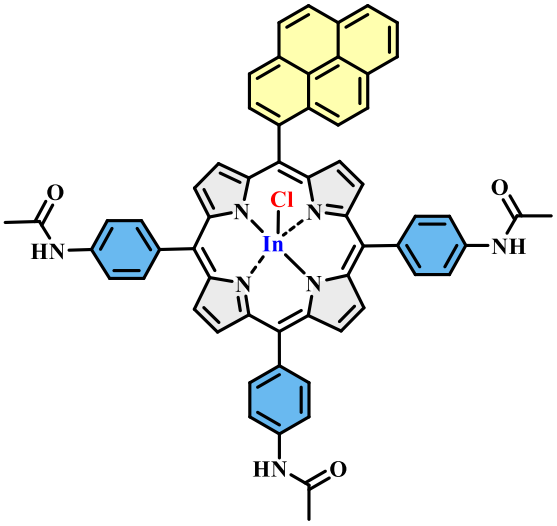

3a

Mass spectrum for **3**

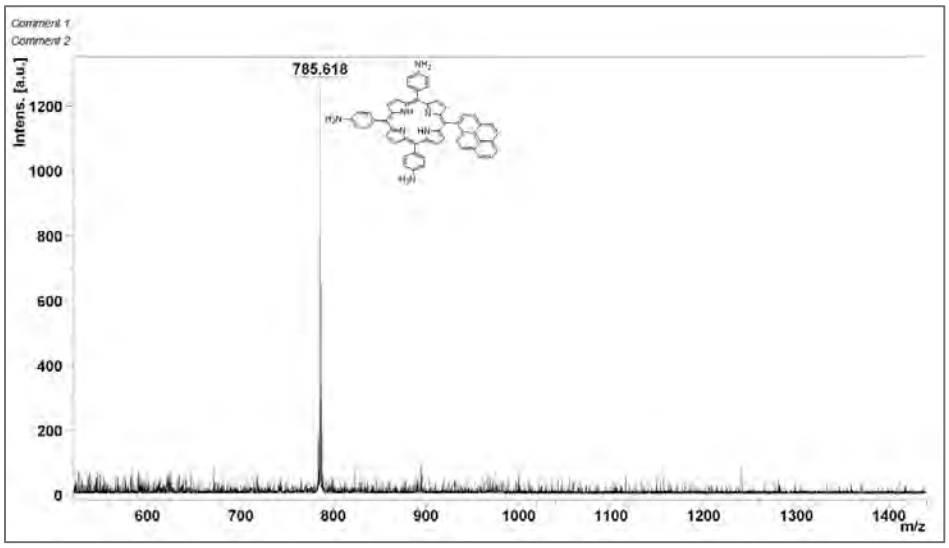

^{1}H NMR spectrum for **3**

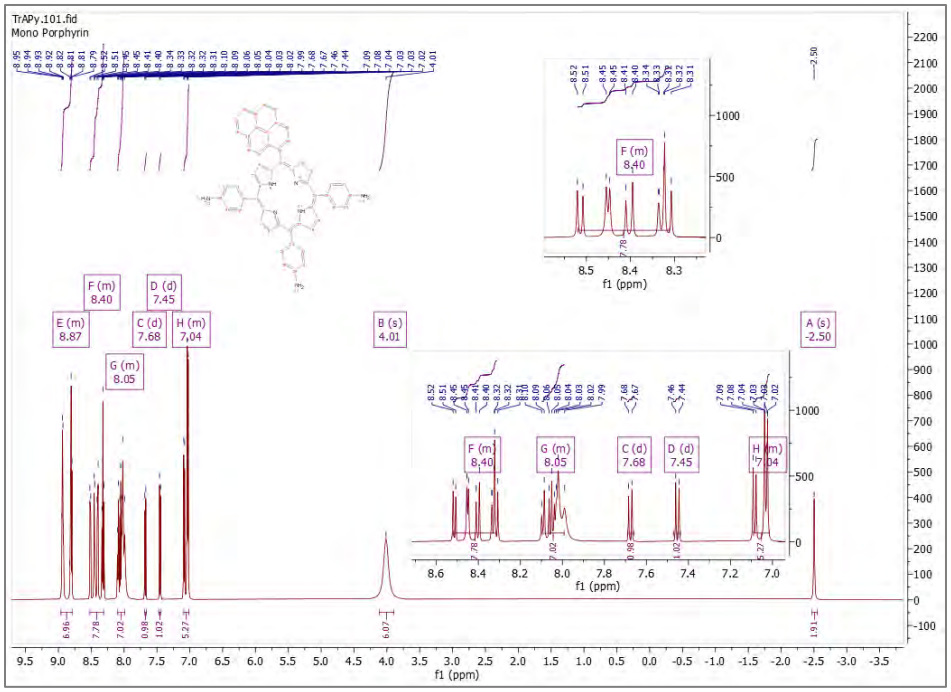

Mass spectrum for complex **3a**

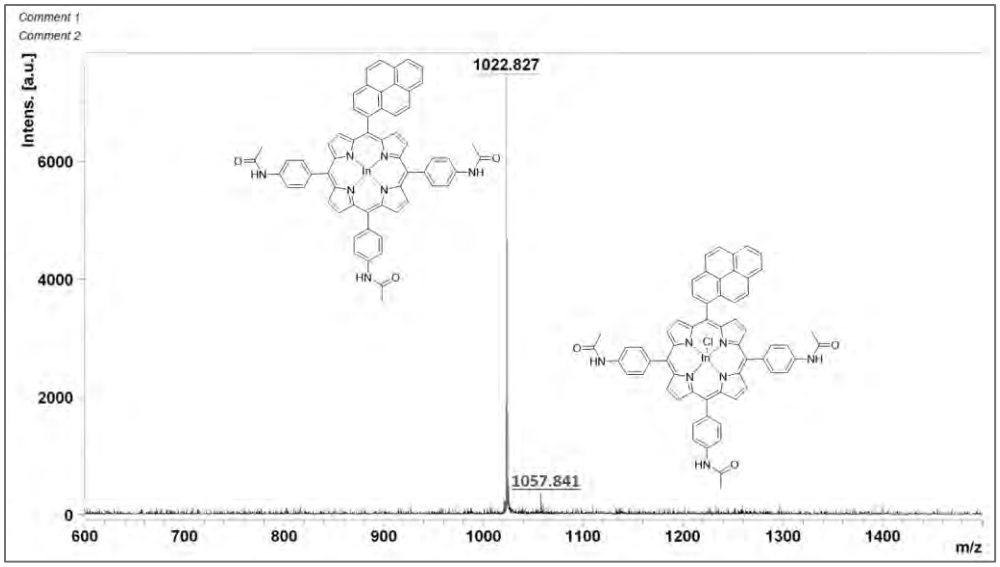

^{1}H NMR spectrum for complex **3a**

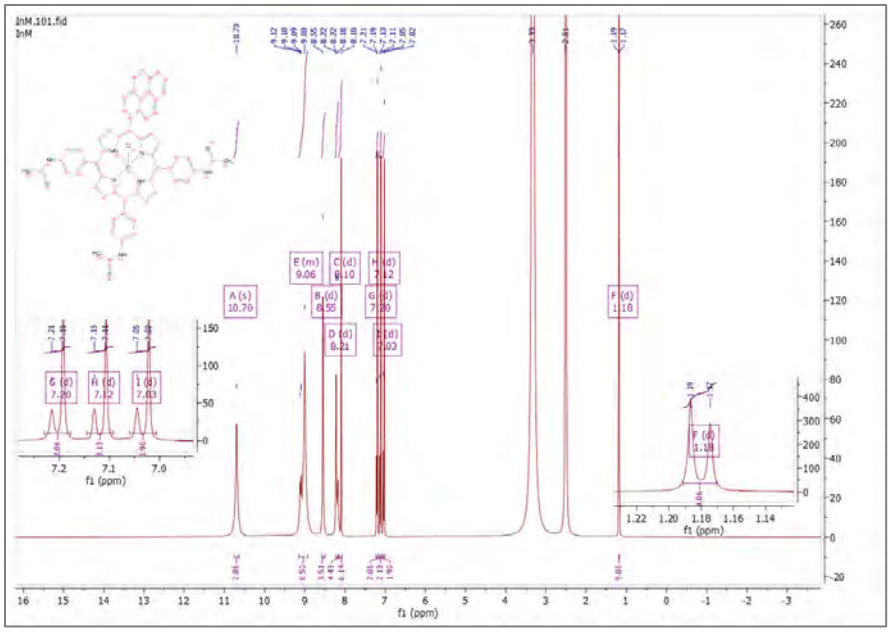

FTIR spectrum for **3** and **3a**

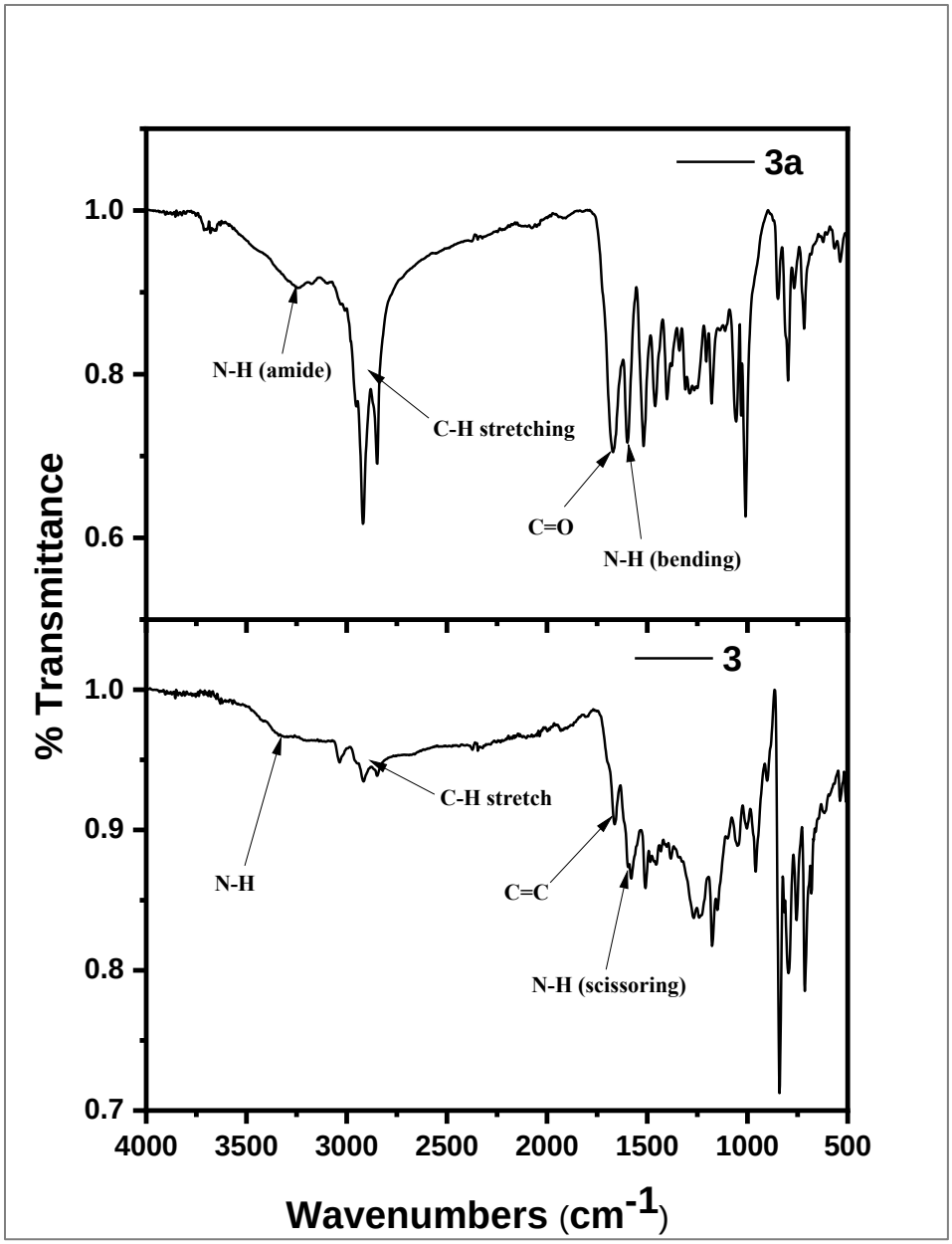
3a
1.0
0.8
0.6
N-H (amide)
C-H stretching
C=O
N-H (bending)
3
1.0
0.9
0.8
0.7
C-H stretch
N-H
C=C
N-H (scissoring)
% Transmittance
4000
3500
3000
2500
2000
1500
1000
500
Wavenumbers (cm-1)

Appendix D: MS, ^{1}H NMR and FTIR spectra of 5,15-bis(4-(*tert*-butyl)phenyl)-10,20-di(pyridin-4-yl)porphyrin **(4)**, Chloroindium (III) 5,15-bis(4-(*tert*-butyl)phenyl)-10,20-di(pyridin-4-yl) porphyrin **(4a)**, Chloroindium (III) 5,15-bis(4-(*tert*-butyl)phenyl)-10,20-bis(*N*-methylpyridinyl) porphyrin iodide **(4b)**, 5,15-di(pyridin-4-yl)-10,20-di(thiophen-2-yl)porphyrin **(5)**, Chloroindium (III) 5,15-di(pyridin-4-yl)-10,20-di(thiophen-2-yl)porphyrin **(5a)**, Chloroindium (III) 5,15-bis(*N*-methylpyridinyl)-10,20-di(thiophen-2-yl) porphyrin iodide **(5b)**.

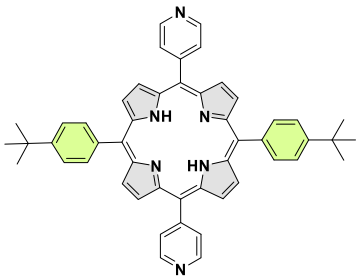

4

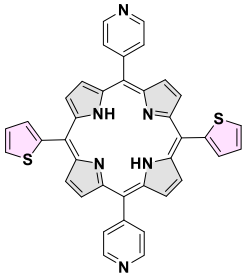

5

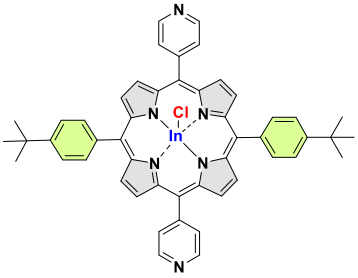

4a

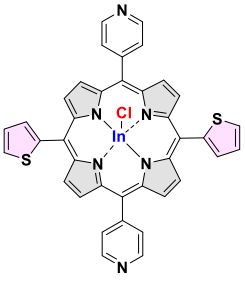

5a

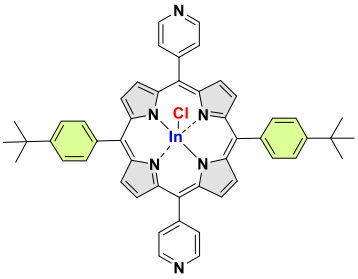

4b

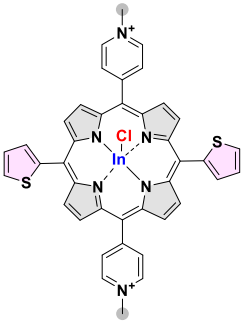

5b

Mass spectrum for **4**

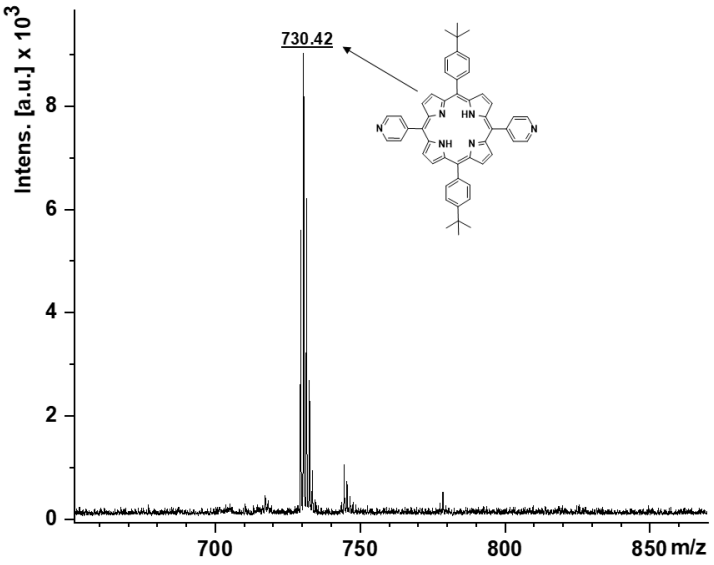

^{1}H NMR Spectrum for **4**

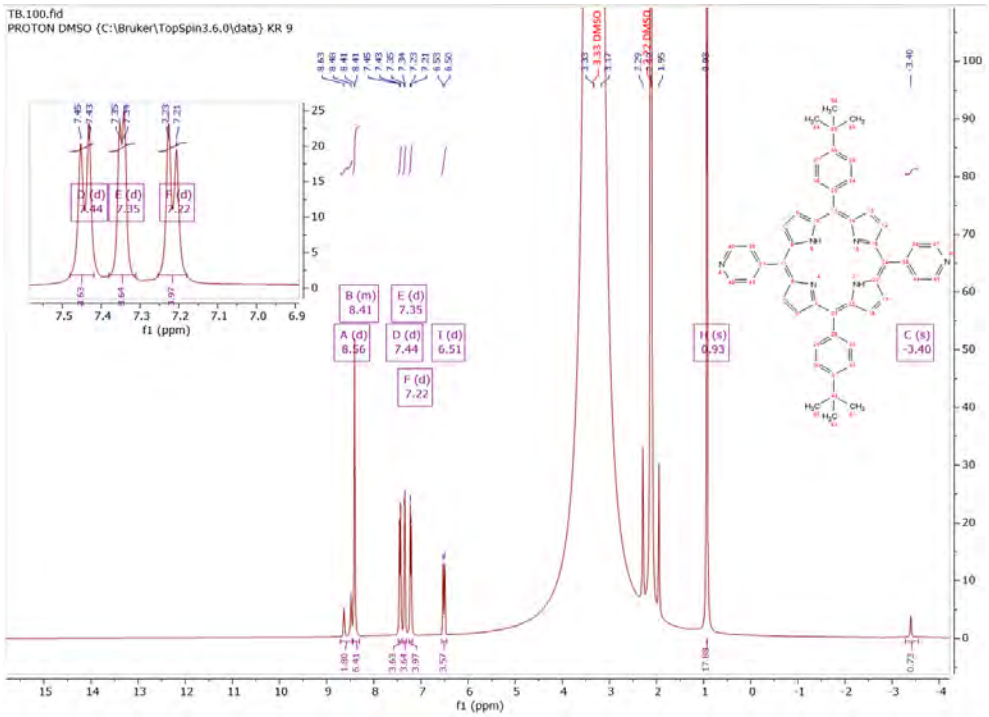

Mass spectrum for **4a**

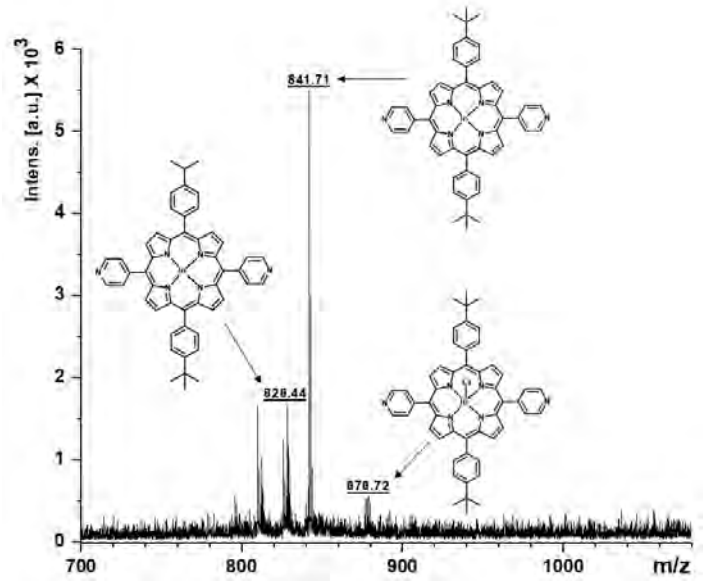

^{1}H NMR Spectrum for **4a**

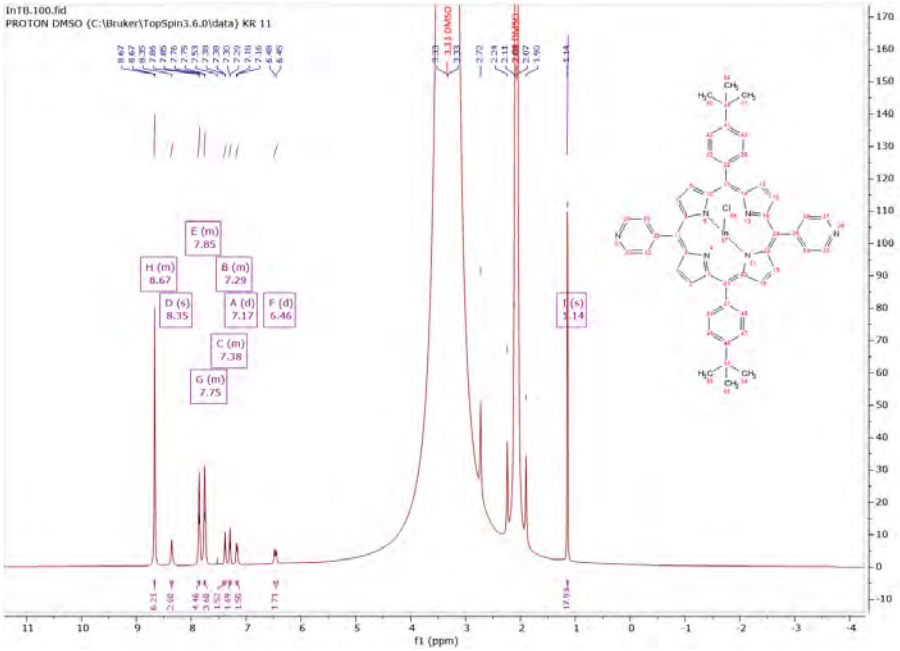

Mass spectrum for **4b**

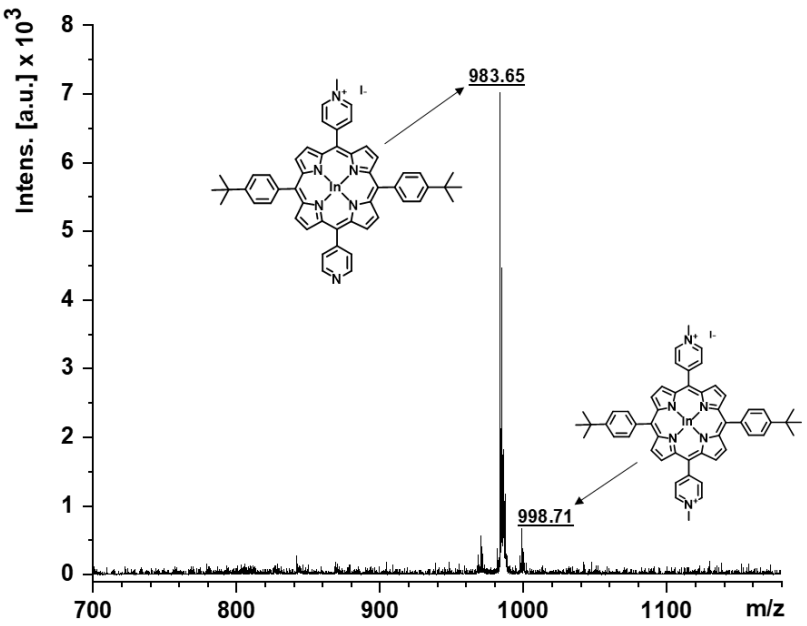

^{1}H NMR Spectra for **4b**

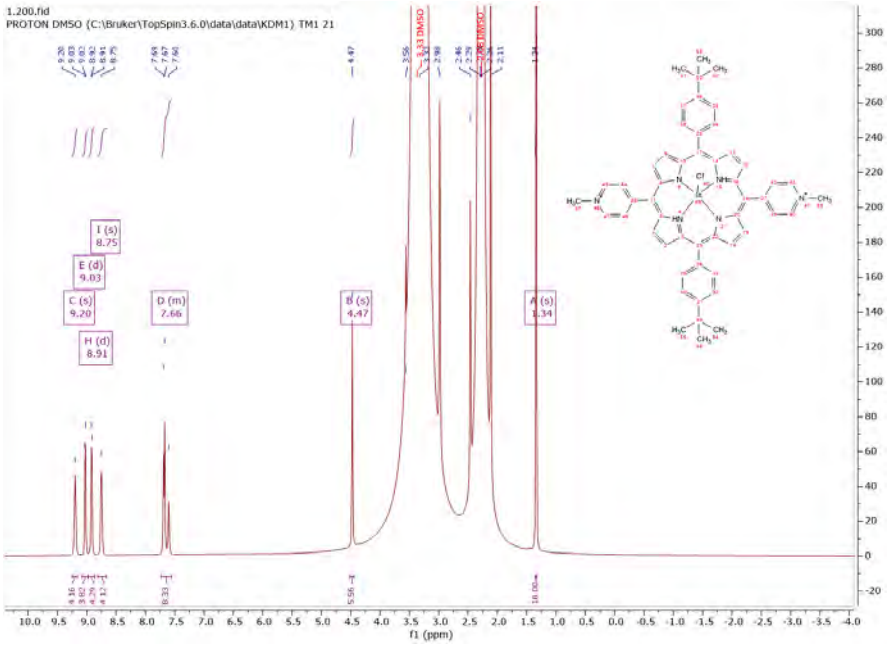

Mass spectrum for **5**

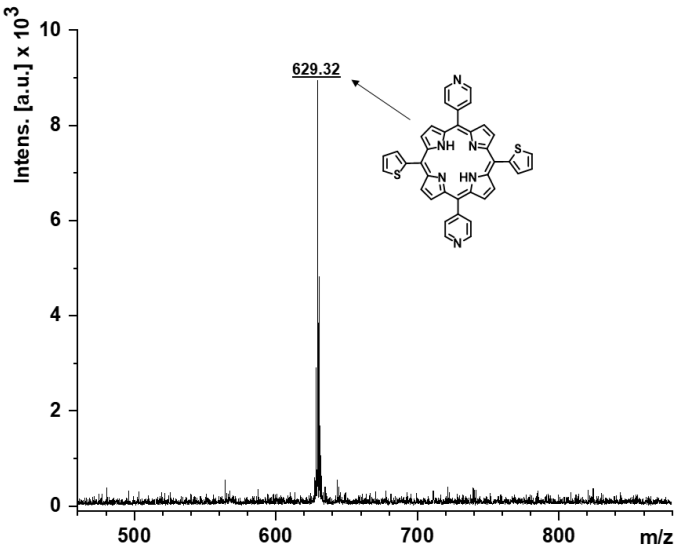

^{1}H NMR Spectra for **5**

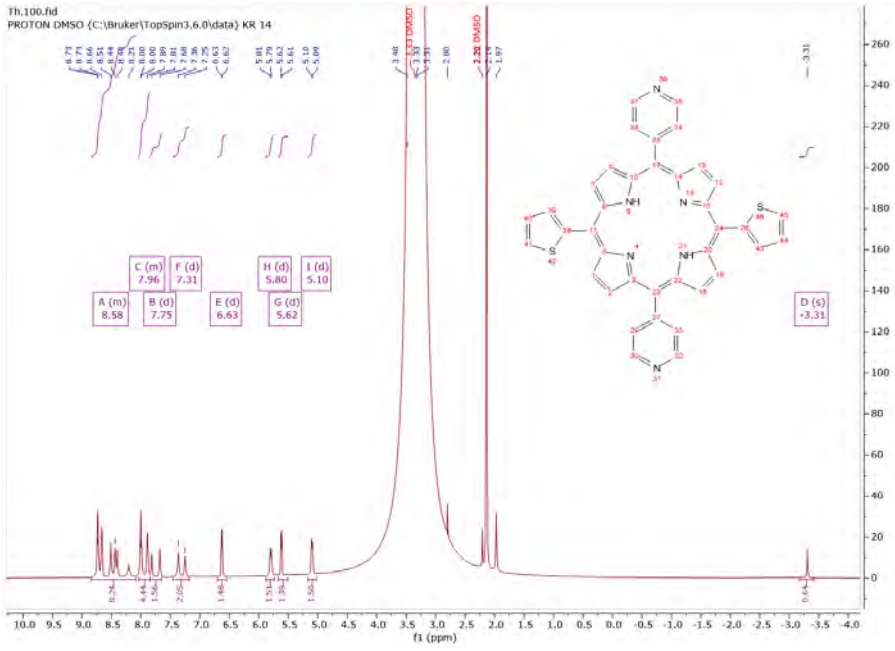

Mass spectrum for **5a**

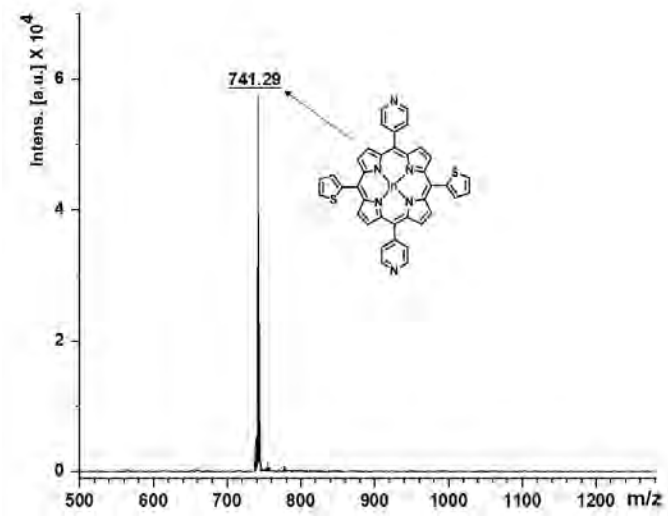

^{1}H NMR Spectra for **5a**

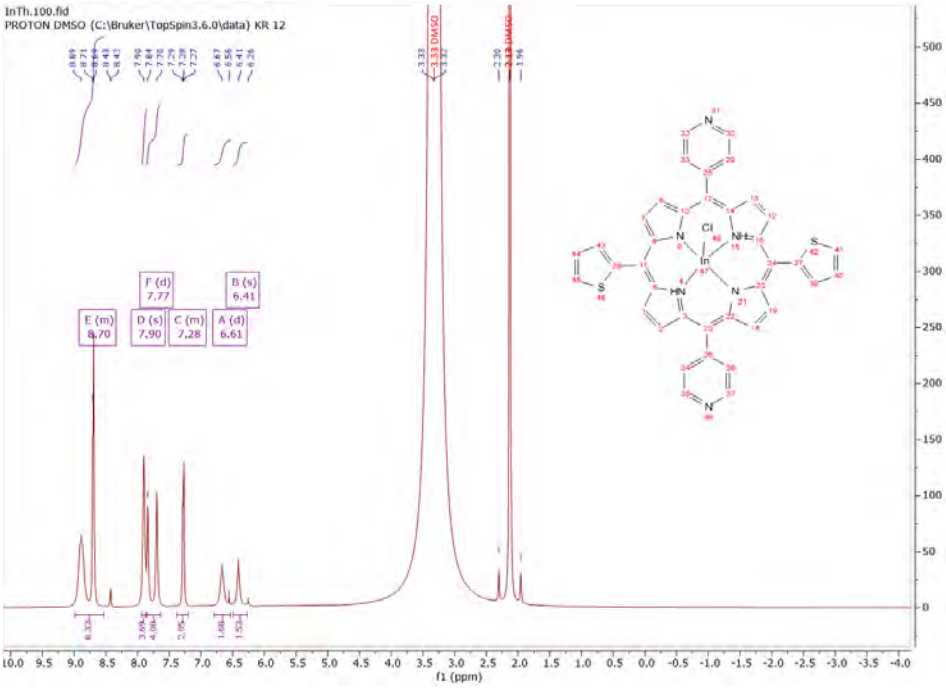

Mass spectrum for **5b**

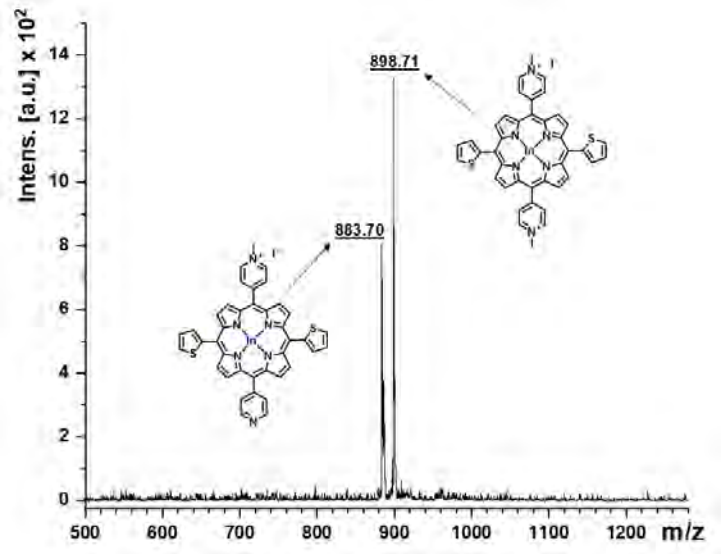

^{1}H NMR Spectrum for **5b**

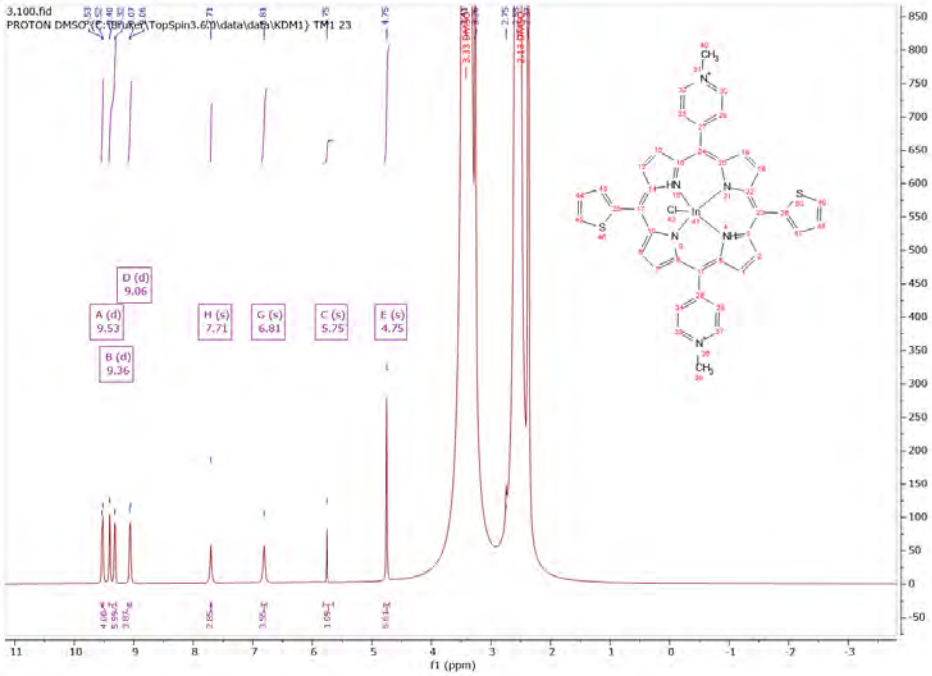

FTIR spectra for **4**, **4a**, **4b**, **5**, **5a** and **5b**